Investigation of Turbine Blade Trailing Edge Cooling and Thermal Mixing Characteristics

by
Marwan Effendy

Thesis submitted for the degree of Doctor of Philosophy
of Kingston University London

School of Aerospace Engineering
Kingston University London
2014

Investigation of Turbine Blade Trailing Edge Cooling and Thermal Mixing Characteristics

by MARWAN EFFENDY

ABSTRACT

The present computation investigates a turbine blade with trailing-edge cutback coolant ejection designs, aiming for a comparison study of aerothermal performances such as discharge coefficient and film cooling effectiveness due to the change of trailing-edge geometries and blowing ratios.

The shear-stress transport (SST) $k-\omega$ turbulence model is adopted and numerical studies are carried out by two-stage investigations:- firstly, validation of an existing cutback blade model with staggered circular pin-fins array inside the cooling passage that has been extensively studied by other researchers and predicted internal passage discharge coefficient and film-cooling effectiveness along the cutback surface are compared to experimental measurements. RANS/URANS and DES are applied during this stage; secondly, further investigation of four main cases considering different key design parameters such as the ratio of lip thickness to slot height (t/H = 0.25, 0.5, 1.0 and 1.5), the design of internal features (i.e. circular pin-fin array, elliptic pin-fin array, and empty duct), the coolant ejection angle (α = 5°, 10° and 15°). In addition, a trailing-edge cutback model with suction-side (SS) – pressure-side (PS) walls and lands is considered to create a more realistic blade design.

The results show that both steady and unsteady RANS predictions are able to produce discharge coefficients in fairly good agreement with test data, but not the film-cooling effectiveness on cutback surfaces which over-predicts in far-field wake region. Further prediction improvements can be made by using unsteady DES approach.

In terms of film-cooling effectiveness and shedding frequency, computational results indicate a strong dependency on those aforementioned key design parameters. This film-cooling effectiveness is strongly affected by turbulent flow structures along the cutback region, which is representing the dynamic mixing process between the mainstream flow and the ejecting coolant from the slot-exit. The use of elliptic pin-fin inside the cooling passage and thin lip thickness could improve the effectiveness of film-cooling. The increase of ejection angle yields almost near unity cooling effectiveness along the protected wall. Significant improvements on cooling performance are also achieved with higher blowing ratios. Computations of the trailing-edge cutback cooling with pressure-side (PS) and suction-side (SS) wall demonstrates that performance of the case without lands is better than that of the case with lands by discrepancy up to 18% in terms of overall-averaged film-cooling effectiveness. The blade trailing-edge design with lands causes a rapid decay of the averaged film-cooling effectiveness near the downstream region and an increase of discharge coefficient up to 20%, respectively.

To my mother and my father,

my wife "Murti",

my son "Zaki",

my daugthers "Khansa and Safira"

and our parents

I certify that I have read this dissertation and that, in my opinion, it is fully adequate in scope and quality as a dissertation for the degree of Doctor of Philosophy.

(Professor Yufeng Yao)
Supervisor

ACKNOWLEDGMENTS

This research has been carried out with financial support from the Ministry of Education Indonesia through the programme of "Beasiswa Luar Negeri DIKTI" under grant no. 149/D4.4/PK/2010. I would like to thank my colleagues in Muhammadiyah University of Surakarta for their help and support. Partial support from bursaries programme of Kingston University London is also greatly appreciated.

I would like to give thanks to my supervisor, Professor Yufeng Yao. He possesses an incredible amount of knowledge and experience regarding flow physics and computational methods. I have been given numerous helpful and enlightening comments. He greatly helped me with finishing this thesis. In addition, I would like to express gratitude to Mr. Marchant for his help and valuable support on this project.

Thanks to Jackie as Faculty research coordinator who guides me during my study program, and in addition to all of my friends incorporated in Aerospace Research Group (ARG) Kingston University London. Thanks to our friends Abram Perdana, Aditya Pradana, Bernadi Pranggono, Hari Prasetyo, Sarjito, Patna Partana, Tri Widodo, Joko Sedyono, Deni Vitasari and others close friends for support and encouragement towards the completion of the thesis.

Special thanks to my mother, my father, my brothers, my beloved wife "Murti", my daughters "Khansa and Safira", my son "Zaki" and my whole families for their support and patience, and always being there to pray for the success of my study far from home country.

Finally, all praises are due to God Almighty for his Endless bless and guidance that I have the strength and determination to overcome all difficulties.

LIST OF CONTENTS

Abstract ii
Acknowledgements v
List of Contents vi
List of Figures xii
List of Tables xvi
Nomenclature xvii

Chapter 1: Introduction

1.1 Background and Motivation 1
1.2 Aims, Objectives and Case Study Descriptions 5
1.3 Contributions of this study 8
1.4 Structure of the Thesis Report 9
1.5 Papers Published 12

Chapter 2: Literature Review and Terminology

2.1 Introduction 13
2.2 Cooling System of Gas Turbine Blade 14
2.3 Trailing-Edge of Gas Turbine Blade 15
2.4 Film-Cooling Effectiveness and Trailing-Edge Cutback 18
2.5 Literature Review 19
2.5.1 Previous Analytical Studies 19
2.5.2 Previous Experimental Studies 21
2.5.2.1 Experimental studies of TE cutback without pin-fin cooling: 21
2.5.2.2 Experimental studies of the blade TE cutback with pin-fin cooling: 22
2.5.3 Previous Numerical Studies 25
2.5.4 The Limitation of Previous Numerical Studies 30
2.6 Terminology on the blade TE Cutback Cooling 31
2.6.1 Discharge Coefficient 31
2.6.2 Blowing Ratio 31
2.6.3 Adiabatic Film-Cooling Effectiveness and Isothermal Condition 32
2.6.4 Heat-Transfer Coefficient 32
2.6.5 Relation between Surface Heat Flux and Non-Dimensional Temperature 33

2.7 Vortex-Shedding and Strouhal Number 33
2.8 Fast Fourier Transform (FFT) 35
2.9 Summary 37

Chapter 3: Turbulence Modelling

3.1 Governing Equations 38
3.1.1 Mass Conservation (Continuity Equation) 38
3.1.2 Momentum Conservation 39
3.1.3 Energy Conservation 39
3.1.4 State Equation 40
3.1.5 Interrelationships of Conservation Equations 40
3.2 Turbulence Modelling 41
3.2.1 Turbulence 41
3.2.2 Favre-Averaged Navier-Stokes (FANS) 42
3.2.2.1 Eddy-viscosity models: 42
3.2.2.2 Reynolds-stress models: 43
3.2.3 Hypothesis of Boussinesq Approximation 44
3.2.4 Two-Equations Turbulence Model 44
3.2.5 Standard $k-\omega$ Models 45
3.2.6 Steady and Unsteady RANS 46
3.2.7 Large Eddy Simulation (LES) 48
3.2.7.1 Subgrid-Scale: 49
3.2.7.2 Smagorinsky-Lilly model: 51
3.2.8 Detached Eddy Simulation (DES) 51
3.3 Shear-Stress Transport $k-\omega$ Models 52
3.3.1 Transport Equation 53
3.3.2 Modelling the Effective Diffusivity 54
3.3.2.1 Correction factor for a low Reynolds number: 54
3.3.2.2 The blending factors: 55
3.3.3 Modelling the Turbulence Production 55
3.3.3.1 The production of k : 55
3.3.3.2 The production of ω : 56
3.3.4 Modelling the Turbulence Dissipation 56
3.3.4.1 The dissipation of k : 56
3.3.4.2 The dissipation of ω : 57
3.3.5 Compressibility Correction 57
3.3.6 Modification of Cross-Diffusion 58

3.3.7 Model Constants 58
3.4 DES Models 58
3.4.1 The Spalart-Allmaras based DES Models 58
3.4.2 The Realisable $k-\varepsilon$ based DES Models 59
3.4.3 The SST $k-\omega$ based DES Models 59
3.5 Summary 60

Chapter 4: Computational Details

4.1 Previous Experiment and Geometries 61
4.1.1 Mainstream flow conditions 63
4.1.2 Coolant flow conditions 63
4.2 Present Computational Domain 64
4.3 Flow and Boundary Conditions 67
4.4 Mesh Generation 68
4.5 Incompressible Flow and Air Properties 70
4.6 Turbulence Models 71
4.7 Algorithm and Time Stepping 71
4.8 Scenario of Numerical Studies 71
4.8.1 Verification and Validation 72
4.8.2 Simulation Cases 73
4.9 Summary 76

Chapter 5: Verification and Validation

5.1 The Concept of Laterally Averaged Data 78
5.2 Grid Refinement Studies 79
5.2.1 Meshing 79
5.2.2 Precursor Simulation 80
5.2.3 Grid Refinement Studies 84
5.2.4 Effect of flow-through time studies 85
5.2.5 Effect of Time-step Sizes (TSS) 86
5.2.6 Single-pitch versus Double-pitch Domain 87
5.3 Steady and Unsteady Simulations 88
5.3.1 Film-cooling Effectiveness 89
5.3.2 Wall-bounded Flow (Δy^+) 91
5.3.3 Internal Cooling Passage 92
5.3.4 Discharge Coefficient (C_D) 95
5.3.5 Flow Structures 97

5.4 Film-cooling Effectiveness at Various Blowing Ratios 99
5.5 Shedding Frequency 100
5.6 Summary 104

Chapter 6: CASE I - Blade Trailing-edge Cutback Cooling with Various Lip-Thicknesses

6.1 Blade TE Cutback Cooling with various t/H ratios 105
6.2 Triangle Area and Mixing Region 106
6.3 Computational Grids 108
6.4 History of Simulations 110
6.5 Results and Discussion 111
6.5.1 Cooling Passage 111
6.5.1.1 Discharge coefficient: 112
6.5.1.2 Properties at the pin-fins surface: 113
6.5.1.3 Coolant flow behaviour inside the cooling passage: 115
6.5.2 Coolant Properties at the Slot Exit 117
6.5.3 Turbulence Characteristics 119
6.5.4 Adiabatic Wall Surface along the TE Cutback 121
6.5.4.1 Film-cooling effectiveness: 121
6.5.4.2 Film-cooling effectiveness at a low-blowing ratio: 122
6.5.4.3 Film-cooling effectiveness at high-blowing ratio: 123
6.5.4.4 Temperature at the protected wall surface for case with high blowing ratio: ... 124
6.5.4.5 Coefficient of Δy^+ and C_f at the protected surface for case with high-blowing ratio: 125
6.5.5 Dynamic Mixing Process at the Breakout Region 128
6.5.5.1 Distribution of temperature: 128
6.5.5.2 Turbulent flow structures: 131
6.5.6 Instantaneous and Time-averaged Temperature 133
6.5.7 Velocity and Turbulence Kinetic Energy 135
6.5.8 Shedding Frequency 137
6.6 Summary 141

Chapter 7: CASE II - Blade Trailing-edge Cutback Cooling with Various Internal Cooling

7.1 Internal Features inside the Cooling Passage 142
7.2 Computational Domain and Grids 146
7.3 History of Simulations 147
7.4 Results and Discussion 148
7.4.1 Internal Cooling Passage 149

7.4.1.1 Discharge coefficient: 149
7.4.1.2 Pin-fins cooling: 150
7.4.1.3 Coolant flow behaviour inside the cooling passage: 152
7.4.2 Turbulence Characteristics 154
7.4.3 Protected Wall / Cutback Surface 156
7.4.3.1 Laterally averaged film-cooling effectiveness: 156
7.4.3.2 Film-cooling effectiveness at the z/H position: 158
7.4.4 Mixing Region 160
7.4.4.1 Turbulent flow structures: 161
7.4.4.2 Temperature distributions: 164
7.4.4.3 Velocity distributions: 165
7.4.4.4 Turbulence kinetic energy: 167
7.4.5 Shedding Frequency 169
7.5 Summary 171

Chapter 8: CASE III - Blade Trailing-edge Cutback Cooling with Various Coolant Ejection Angles

8.1 Blade Trailing-edge Cutback Cooling with Various Ejection Angles 172
8.2. Geometries and Meshes 174
8.3 Evaluation of Blowing Ratios 176
8.4 History of Simulations 177
8.5 Results and Discussion 178
8.5.1 Cooling Passage 179
8.5.1.1 Discharge coefficient: 179
8.5.1.2 Coolant properties at the pin-fin surfaces: 180
8.5.1.3 Coolant properties inside cooling passage: 182
8.5.2 Turbulence Characteristics 185
8.5.3 Protected Wall/Cutback Surface 187
8.5.3.1 Laterally averaged film-cooling effectiveness: 187
8.5.3.2 Film-cooling effectiveness on various z/H position: 188
8.5.4 Mixing Region 189
8.5.4.1 Turbulent flow structures: 189
8.5.4.2 Distribution of velocity (U/U_{hg}): 191
8.5.4.3 Turbulence kinetic energy: 193
8.5.5 Shedding Frequency 195
8.6 Summary 197

Chapter 9: CASE IV - Blade Trailing-edge Cutback Cooling with Pressure-Side (PS) and Suction-Side (SS) Configuration

9.1 Blade Trailing-edge Cutback Model with PS-SS Walls and Lands 199
9.2 Computational Domain and Grids 201
9.3 Boundary Conditions and Numerical Treatments 204
9.4 Results and Discussion 206
9.4.1 Internal Cooling Passage 207
9.4.1.1 Discharge coefficient: 207
9.4.1.2 Heat transfer coefficient of the pin-fins array: 208
9.4.1.3 Heat transfer coefficient at the coolant wall duct: 211
9.4.1.4 Nusselt number for the pin-fins surfaces: 214
9.4.1.5 Coolant flow velocity: 215
9.4.2 Turbulence Characteristics 218
9.4.3 Film-cooling Effectiveness 221
9.4.4 Mixing Region 225
9.4.4.1 Turbulent flow structures: 225
9.4.4.2 Transverse velocity profiles: 227
9.4.4.3 Transverse temperature profiles: 234
9.4.4.4 Turbulence kinetic energy profiles: 237
9.4.4.5 Temperature contour: 239
9.4.4.6 Turbulence kinetic energy: 240
9.4.5 Shedding Frequency 242
9.5 Summary 245

Chapter 10: Conclusions and Future Work

10.1 Conclusions 247
10.2 Future Work 249
References 251
Appendix A-1 266

THE LIST OF FIGURES

Figure 1–1: Cooling of gas turbine blade. (a) External cooling; (b) Internal cooling. 2
Figure 1–2: A turbine blade with trailing-edge cutback design. 3
Figure 1–3: A scheme of trailing-edge cutback design. 5
Figure 2–1: Heat-flux distribution of a cooled vane and blade. 14
Figure 2–2: Cutting process of trailing-edge. 16
Figure 2–3: Types of blade trailing-edge cooling. 17
Figure 2–4: Trailing-edge cutback slot. 18
Figure 2–5: Vortex-shedding. 34
Figure 2–6: An example of time domain and frequency domain based on sampled data..36
Figure 3–1: Time-average and fluctuating velocity 47
Figure 4–1: A trailing-edge cooling of gas turbine blade. 62
Figure 4–2: Computational domain 66
Figure 4–3: Initial and boundary conditions. 68
Figure 4–4: Fine mesh C for the baseline model. 69
Figure 4–5: Present mesh and those of previous works. 70
Figure 4–6: TE cutback with four various t/H ratios. 73
Figure 4–7: Layout of staggered pin-fin array inside the cooling passage. 74
Figure 4–8: Sketch of three various ejection angles. 74
Figure 4–9: A blade TE cutback model with pressure-side (PS) – suction-side (SS) walls. ..75
Figure 5–1: Laterally averaged concept. 78
Figure 5–2: Three types of mesh 79
Figure 5–3: Precursor simulation. 83
Figure 5–4: Grid refinement studies. 84
Figure 5–5: Effect of flow time 86
Figure 5–6: Effect of time-step sizes. 87
Figure 5–7: Single-pitch versus double-pitch domain. 88
Figure 5–8: Laterally averaged data at the protected wall. 90
Figure 5–9: Resolution at the protected wall. 91
Figure 5–10: Position of pin-fins row and cross-section area at the cooling duct. 92
Figure 5–11: Δy^+ and skin friction coefficient. 93
Figure 5–12: Heat transfer coefficient and temperature. 94
Figure 5–13: Coolant flow behaviour inside the cooling passage. 95

Figure 5–14: Discharge coefficients. 96
Figure 5–15: Flow structures. 98
Figure 5–16: Cooling-film effectiveness at various blowing ratios. 100
Figure 5–17: Time history of velocity components (u, v, w) 101
Figure 5–18: FFT spectrum. 103
Figure 6–1: Triangle area 107
Figure 6–2: Mesh comparison. 109
Figure 6–3: History of simulations. 111
Figure 6–4: Discharge coefficients. 112
Figure 6–5: Coolant flow behaviour at the surface of pin-fin array. 114
Figure 6–6: Coolant flow behaviour inside the cooling passage. 116
Figure 6–7: Position of the slot exit. 117
Figure 6–8: Coolant flow behaviour at the slot exit. 118
Figure 6–9: Turbulence levels. 120
Figure 6–10: Laterally averaged film-cooling effectiveness at the protected wall. 122
Figure 6–11: Temperature at the protected wall. 125
Figure 6–12: Grid resolution effect at the protected wall. 126
Figure 6–13: Mixed-air properties at the y-y_{aw} = 0.1mm. 127
Figure 6–14: The position of laterally averaged data. 128
Figure 6–15: Temperature distribution at the mixing region (T_{hg} = 500 K, T_c = 293 K) 130
Figure 6–16: Turbulent flow structures. 132
Figure 6–17: Non-dimensional temperature distribution. 134
Figure 6–18: Normalised velocity and turbulent kinetic energy. 136
Figure 6–19: Shedding frequencies. 139
Figure 7–1: Local 2-D structured meshes for circular and elliptic pin-fin. 146
Figure 7–2: History of iterations. 148
Figure 7–3: Discharge coefficient. 150
Figure 7–4: Coolant flow behaviour at the surface of the pin-fins row. 151
Figure 7–5: Coolant flow behaviour inside the cooling passage. 153
Figure 7–6: Turbulence levels. 155
Figure 7–7: Laterally averaged film-cooling effectiveness at the protected wall. 157
Figure 7–8: Film-cooling effectiveness at the z/H position. 159
Figure 7–9: Turbulent flow structures. 163
Figure 7–10: Distribution of non-dimensional temperature at the x-y plane of z/H = 0. .165
Figure 7–11: Velocity distributions at the x-y plane of z/H = 0. 166
Figure 7–12: Turbulence kinetic energy distribution at the x-y plane of z/H = 0. 168

Figure 7–13: Shedding frequencies.....170
Figure 8–1: Mesh comparison.....175
Figure 8–2: History of simulations.....178
Figure 8–3: Discharge coefficients.....180
Figure 8–4: Coolant flow behaviour at the surface of the pin-fins row.....181
Figure 8–5: Coolant properties inside the cooling passage.....184
Figure 8–6: Turbulence levels.....186
Figure 8–7: Properties at the protected wall.....188
Figure 8–8: Laterally averaged film-cooling effectiveness.....189
Figure 8–9: Turbulent flow structures.....191
Figure 8–10: Distribution of velocity magnitude (U/U_{hg}) at the x-y plane of z/H = 0.....192
Figure 8–11: Distribution of turbulence kinetic energy at the x-y plane of z/H = 0.....194
Figure 8–12: Shedding frequencies.....196
Figure 9–1: Domains and meshes.....202
Figure 9–2: Discharge coefficients.....208
Figure 9–3: HTC at the pin-fin surfaces.....210
Figure 9–4: HTC contour at the pin-fin surfaces.....210
Figure 9–5: Spanwise-averaged HTC at the coolant passage walls.....212
Figure 9–6: HTC map at the coolant passage walls for the TE cutback with PS-SS.....213
Figure 9–7: HTC map at the coolant passage walls for the TE cutback with PS-SS and lands.....214
Figure 9–8: Nusselt number at the pin-fin surfaces.....215
Figure 9–9: Coolant flow velocity inside the cooling passage.....216
Figure 9–10: Coolant flow velocity (U/U_{hg}) contour around the pin-fins array inside the cooling passage.....217
Figure 9–11: Turbulence levels for the cases without lands.....219
Figure 9–12: Turbulence levels for the cases with lands.....220
Figure 9–13: Laterally averaged film-cooling effectiveness.....221
Figure 9–14: The comparison of the averaged film-cooling effectiveness.....223
Figure 9–15: Film-cooling effectiveness map at the protected wall.....224
Figure 9–16: Turbulent flow structures.....226
Figure 9–17: Normalised u velocity profiles at different downstream locations for the case without lands.....229
Figure 9–18: Normalised u velocity profiles on four various blowing ratio for the case without lands.....230
Figure 9–19: Normalised v velocity profiles at different downstream locations for the case without lands.....231

Figure 9–20: Normalised v velocity profile on four various blowing ratio for the case without lands. 232
Figure 9–21: Normalised *w* velocity profiles at different downstream locations for the case without lands. 233
Figure 9–22: Normalised *w* velocity profiles on four various blowing ratio for the case without lands. 234
Figure 9–23: Normalised temperature profiles on four various blowing ratio for the case without lands. 235
Figure 9–24: Normalised temperature profiles at different downstream locations. 236
Figure 9–25: Normalised turbulence kinetic energy profile at different downstream locations. 238
Figure 9–26: Normalised turbulence kinetic energy profile for four blowing ratio. 239
Figure 9–27: Distribution of non-dimensional temperature (θ) at the *x-y* plane of $z/H = 0$ 240
Figure 9–28: Distribution of turbulence kinetic energy (k/U_{hg}^2) at the *x-y* plane of $z/H=0$. 241
Figure 9–29: Shedding frequencies for the blade TE cutback without lands. 244
Figure 9–30: Shedding frequency comparison for the selected blowing ratio of 1.35. 245

LIST OF TABLES

Table 3–1: Eddy-viscosity and coefficient on development of the $k-\varepsilon$ model. 43
Table 3–2: Eddy-viscosity and coefficient on development of the $k-\omega$ model 44
Table 3–3: Eddy-viscosity and coefficient on development of the $k-\omega$ model 44
Table 3–4: Performance comparison between $k-\varepsilon$ and $k-\omega$ model 45
Table 4–1: Experimental test conditions [5][20] 64
Table 4–2: Properties of air [127][128] 70
Table 5–1: Mesh statistics 80
Table 6–1: Key dimensions of triangle area. 107
Table 6–2: Mesh statistics. 110
Table 6–3: Record of sampling data 137
Table 6–4: Strouhal number. 140
Table 7–1: Investigation of the pin-fin cooling. 144
Table 7–2: Investigation of the TE cooling with pin-fin inside cooling passage. 145
Table 7–3: Mesh statistics. 147
Table 7–4: h_{PIN}/h_{EW} ratio 152
Table 7–5: Coolant temperature at the middle point of the slot exit. 160
Table 7–6: Coolant velocity at the middle point of the slot exit. 160
Table 7–7: Record of sampling data 169
Table 8–1: Key dimensions of the shadow-triangle area 174
Table 8–2: Mesh statistics. 176
Table 8–3: Calculation of blowing ratio before tuning of the inflow coolant velocity. 177
Table 8–4: Calculation of blowing ratio after tuning of the inflow coolant velocity. 177
Table 8–5: h_{PIN}/h_{EW} ratio. 182
Table 8–6: Record of sampling data 195
Table 9–1: Mesh statistics. 203
Table 9–2: Setting-up of simulation. 204
Table 9–3: Calculation of blowing ratios (TE without lands) 205
Table 9–4: Calculation of blowing ratios (TE with lands) 206
Table 9–5: Iteration data for the case without lands. 242

NOMENCLATURE

Greeks

θ	Non-dimensional temperature	[-]
ρ	Density	[kg/m^3]
ρ_c	Density of coolant	[kg/m^3]
ρ_{hg}	Density of mainstream (hot gas) flow	[kg/m^3]
δ	Displacement thickness	[mm]
δ_{cg}	Boundary layer of the coolant wall	[mm]
δ_{hg}	Boundary layer of the mainstream wall	[mm]
μ	Dynamic viscosity [Ns/m^2]	[Pa s] or [k/m.s]
μ_t	Eddy viscosity [Ns/m^2]	[Pa s]
η	Film-cooling effectiveness	[-]
η_{aw}	Adiabatic film cooling effectiveness	[-]
υ	Kinematic viscosity	[m^2/s]
λ	Thermal conductivity	[W/mK]
λ_2	Intermediate eigenvalue of the symmetric tensor	
κ	Ratio of specific heat, ($\kappa = c_p / c_v$)	[-]
α	Inclination angle of test plate	[deg] or [°]
ε	Turbulent eddy dissipation	[m^2/s^3]
ω	Specific turbulence dissipation	[1/s]
Δ	Maximum local grid spacing (=max (Δ_x, Δ_y, Δ_z)) in case of a Cartesian grid	
ϕ	Dissipation function due to the viscous forces	
$\overline{\Omega}_{ij}$	Vorticity tensor	
$\overline{\overline{\tau}}$	Viscous stress tensor	
Γ_k	Effective diffusivity of k	
Γ_ω	Effective diffusivity of ω	
σ_k	Turbulent Prandtl numbers for k	
σ_ω	Turbulent Prandtl numbers for ω	

Capital Letters

D	Diameter of bluff body	[mm]
H	Slot height	[mm]
L	Distance in horizontal direction	[mm]
M	Blowing ratio, $M = \frac{\overline{(\rho_c u_c)_{slot}}}{\rho_{hg} u_{hg}} = \frac{\dot{m}_c}{A_{slot} \rho_{hg} u_{hg}}$	[-]
P	Pressure	[Pa]
Q	Local measure of excess rotation-rate relative to strain-rate; $Q = \frac{1}{2}\left(\lvert\overline{\Omega}\rvert^2 - \lvert\overline{S}\rvert^2\right)$	
R	Ideal gas constant, (287.22 for air)	[J/kgK]]
S	Modulus of the mean rate-of-strain tensor	
T	Temperature	[K]
U	Velocity	[m/s]

Small letters

d	Distance of the throat section to the slot exit	[mm]
f	Frequency	[1/s]
h	Specific enthalpy	[kJ/kg]
k	Turbulent kinetic energy	
n	Number of data	
t	Lip thickness	[mm]

Symbols

A_{slot}	Overall slot area at the slot exit	[mm^2]
C_D	Discharge coefficient	[-]
C_f	Skin friction coefficient	[-]
C_p	Specific heat at constant pressure	[J/kg.K]
C_υ	Specific heat at constant volume	[J/kg.K]
C_{DES}	Calibration constant used in the DES model (= 0.65)	
D_ω	Cross-diffusion term	
D_ω^+	Positive portion of the cross-diffusion term	
f_s	Shedding frequency	[1/s]
$\vec{f}$	Body force per unit mass	
$\tilde{G}_k$	Generation of turbulence kinetic energy due to the mean velocity gradients	
G_ω	Generation of ω	

h_f	Heat transfer coefficient	[W/m^{2}K]
h_{PIN}	Heat transfer coefficient at the pin-fin surface	[W/m^{2}K]
h_{EW}	Heat transfer coefficient at the end wall surface	[W/m^{2}K]
L_s	Mixing length for subgrid-scale	
L_t	Turbulent length scale	
Ma	Mach number	[-]
M_w	Molecular weight of the gas	[kg/kmole]
$\dot{m}_c$	Coolant mass flow rate	[kg/s]
$\dot{m}_{c,\,real}$	Coolant mass flow rate at real condition	[kg/s]
$\dot{m}_{c,\,ideal}$	Coolant mass flow rate at ideal condition	[kg/s]
p_{1t}	Total pressure of coolant upstream of L1 region	[Pa]
p_2	Static pressure at the slot exit	[Pa]
p_{hg}	Static pressure of hot gas	[Pa]
q_{conv}	Convective heat flux	[W/m^2]
q_w	Wall heat flux	[W/m^2]
q_{rad}	Radiative heat flux	[W/m^2]
q_{conv}	Convective heat flux	[W/m^2]
Re	Reynolds number	[-]
St	Strouhal number	[-]
s	Spanwise pitch (Lateral pitch between two pin fin)	[mm]
s_x	Streamwise pitch	[mm]
$\overline{S}_{ij}$	Strain rate tensor	
S_k	Source terms	
S_ω	Source terms	
T_w	Wall temperature	[K]
T_{aw}	Temperature at the adiabatic wall/protected wall	[K]
T_{1t}	Total temperature of coolant upstream of L1 region	[K]
T_c	Coolant temperature at the inflow section	[K]
$T_{c'}$	Coolant temperature at the slot exit	[K]
T_{hg}	Static temperature of hot gas at inflow section	[K]
Tu	Turbulence level	[-]
Tu_{hg}	Hot gas turbulence intensity	[-]
Tu_c	Coolant turbulence intensity	[-]
u_i	velocity components	
u_c	Coolant velocity	[m/s]
u_{hg}	Hot gas velocity (mainstream)	[m/s]
$\overline{u}$	Mean velocity (average)	[m/s]
u'	Fluctuating velocity components	[m/s]

Y_k Characterizes the dissipation of k

Y_ω Characterizes the dissipation of ω

$\rho\vec{g}$ gravitational body force

Abbreviations

AITEB Aerothermal Investigation of Turbines Endwalls and Blades
CFD Computational Fluid Dynamic
DES Detached-eddy Simulation
DFT Discrete Fourier Transform
DNS Direct Numerical Simulation
EW End-wall
EVM Eddy-viscosity model
FANS Favre-averaged Navier-stokes
FFT Fast Fourier Transform
HP High pressure
HTC Heat-transfer coefficient
IR Infra-red
LCS Large coherent structures
LES Large-eddy Simulation
LP Low pressure
MP Mixing point
MRI Magnetic resonance imaging
PIN Pin-fin
PS Pressure-side
PSP Pressure-sensitive paint
P_{op} Operating pressure
RANS Reynolds-Averaged Navier-Stokes
RSM Reynolds-stress model
SS Suction-side
SA Spalart-Allmaras
SAS Scale-adaptive Simulation
SST Shear-stress transport
TE Trailing-edge
TSS Time step sizes
TRANS Transient Reynolds-Averaged Navier-Stokes
URANS Unsteady Reynolds-Averaged Navier-Stokes
WALE Wall-Adapting Local Eddy-viscosity

CHAPTER 1:

INTRODUCTION

This chapter contains the background and motivation for this numerical study. A brief synopses of the literature related to trailing-edge cooling of gas turbines blades is given concisely in order to deliver the importance of this research. Thereafter, the problem and knowledge gap in this field of research are specified by considering four main aspects, which influence a performance of the trailing-edge (TE) cutback cooling. Four cases are proposed in this computational study in an effort to realise the research objectives. The outline of the thesis is explained in this chapter, followed by a list of publications related to this research at the end of the chapter.

1.1 Background and Motivation

Gas turbines and its variants are widely used for aircraft and marine propulsion, power of locomotives, land-based power generation, and other industrial applications. For example, in the petroleum industry, gas turbines have been applied to transport gas or oil through pipelines and to drive generators to produce electricity. Other civil and military applications of gas turbines include modern utilities such as helicopters, tanks, buses, cars, and motorcycles, etc.

One of the main driving forces behind gas turbine design and development is to achieve the highest possible overall engine performance in terms of power output and thermal efficiency. Due to this reason, modern gas turbines often operate at very high inlet temperatures up to 1,200 – 1,500°C [1][2][3]. Recent developments in gas turbine engines for aero-propulsion applications require an overall compressor pressure ratio of more than 50 and turbine inlet temperatures in excess of 1,727°C [4][5]. However, these conditions and requirements will cause serious issues for key components such as liners,

vanes and blades as the engine operation temperature is far beyond their critical working temperature [3]. Furthermore, higher turbine inlet temperatures could lead to other adverse effects such as simply melting, oxidation, corrosion, erosion [6] and degradation of structural strength [7]. An extremely high convective heat flux around a blade trailing-edge causes cracks [6], thermal-fatigue [6][8][9], and buckling [9] thus risking turbine blade failure.

In order to overcome these problems, turbine blades need to be cooled down by keeping the surface temperature below the melting point of a metal blade for safety and durability of engine operations [7][10][11]. The complete engine cooling design includes both platform and blade, and for the latter it includes leading-edge impingement cooling, mid-span film-cooling and trailing-edge injection cooling. Figure 1–1 illustrates various techniques of the external and internal cooling for a gas turbine blade.

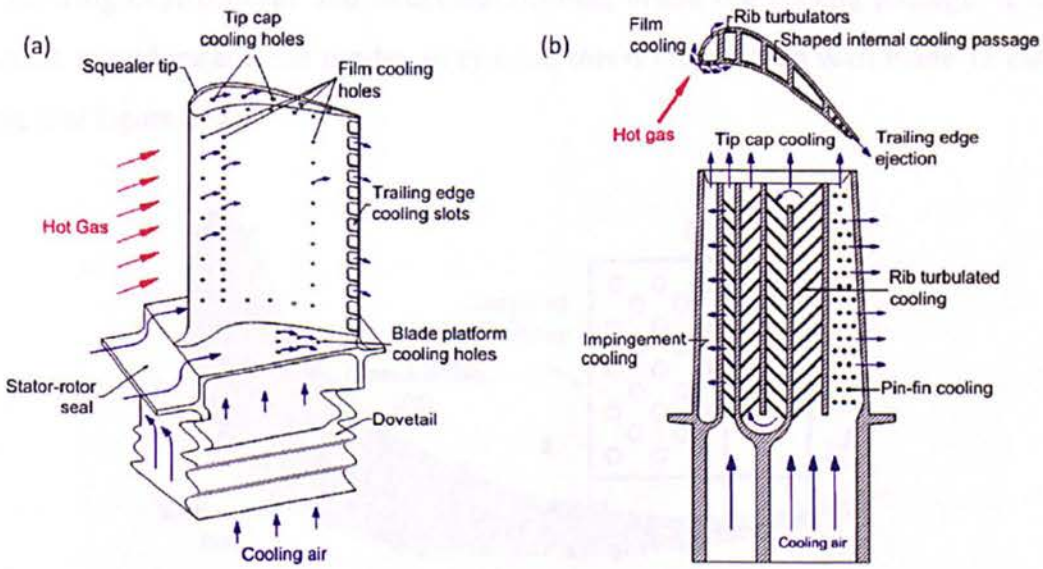

Figure 1–1: Cooling of gas turbine blade. (a) External cooling; (b) Internal cooling [10][12].

Among the various blade/vane cooling designs, the trailing-edge is one of the key areas that have been addressed by designers not only because of the high local thermal loadings [13], but also due to the very thin blade trailing-edge geometry necessary to meet the aerodynamic performance requirements. Furthermore, a modern cutback blade configuration aiming to reduce aerodynamic losses requires careful consideration for the need of sufficient coolant gas streams for safe and long-life operation [8], besides their

reliability [11] as well as the challenges of applying an internal cooling slot inside such a thinner trailing-edge domain. An effective trailing-edge cooling mechanism should maintain the material of gas turbine blade/vane under its critical temperature by considering key aspects such as mechanical strength and aerodynamic losses. Hence, the blade trailing-edge cooling has increasingly become an area of research focus in recently years.

A previous study carried out by Krueckels *et al.* [14] suggested that the pressure-side coolant ejection design could be employed in order to maximise efficiency of the cooling system of a gas turbine blade. Trailing-edge cooling with pressure-side bleed is an alternative mechanism, which is capable of achieving efficient cooling of thin trailing-edges with lower aerodynamic losses. In this system, the coolant is injected from slots to cool down the uncovered trailing-edge. This is commonly coupled with the pin-fin cooling for enhancing heat-transfer and structural stiffness inside the cooling passage. It is also important to understand the pin-fin array since this is interrelated with blade TE cutback cooling (see Figure 1–2).

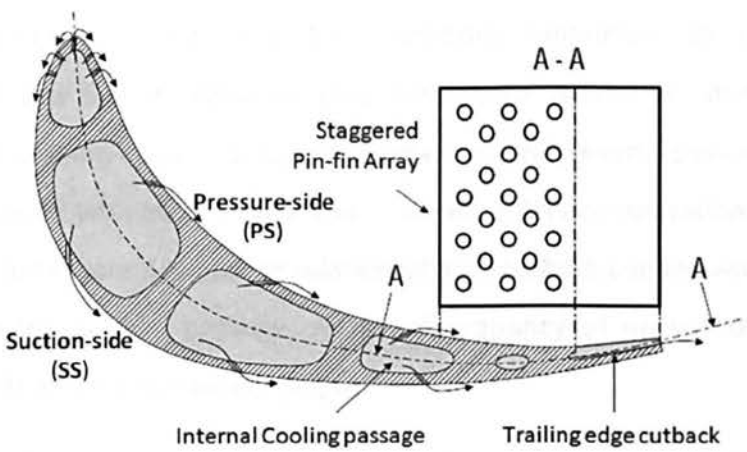

Figure 1–2: A turbine blade with trailing-edge cutback design. [15][16]

Trailing-edge blades become one of the most interesting topics due to the conflict of interest between the need of cooling and aerodynamic requirements. Moreover, the heat-transfer enhancement around the downstream of trailing-edge and thermal-shield by film-cooling behind the lip creates more complicated issues. The blade TE cutback cooling with several design parameters has been studied analytically [17][18],

experimentally and numerically for many years. In terms of Computational Fluid Dynamic (CFD) study, some published results, particularly on the film-cooling effectiveness have shown clear discrepancies between the numerical prediction and the experimental measurement. The discrepancy was seen in both steady and unsteady RANS (Reynolds-Averaged Navier-Stokes). For example, numerical study using steady RANS predicted almost ideally the film-cooling effectiveness without decay as reported by Holloway *et al.* [19], Martini *et al.* [20], and Effendy *et al.* [21]. Those findings were in agreement with those of using steady RANS with SST [22] and the $k-\omega$ turbulence model [23][24], respectively. Unfortunately, steady RANS failed to capture turbulent flow structures.

As studied by various researchers, an unsteady RANS calculation provided a better prediction for capturing turbulent flow structures at the mixing region. Nevertheless, this computation did not simulate optimally their interaction between the mainstream flow and the coolant. Consequently, the CFD prediction of the film-cooling effectiveness was inconsistent with the experimental data (see Holloway *et al.* [25], Egorov *et al.* [22], Medic *et al.* [26], and Joo *et al.* [27]).

Through a numerical approach using Detached-Eddy Simulation (DES), Martini *et al.* [23][24] applied the Spalart-Allmaras (SA) turbulence model to study an in-house laboratory blade trailing-edge cooling configuration. The results showed much better agreement compared with both steady and unsteady RANS computation. Unfortunately, under-predicted data were seen for simulation of a TE cutback cooling with double in-line rib arrays inside the cooling passage, with a discrepancy of up to 10% between the prediction [23][24] and measurement [4][5].

In continuation of the numerical work studied by Martini *et al.* [23][24], the Scale-Adaptive Simulation (SAS) of the shear-stress transport (SST) turbulence model has been employed by Egorov *et al.* [22] in their simulations. They found a significant under-prediction of the film-cooling effectiveness, in agreement with that obtained by Martini *et al.* [23][24]. So far, the cause of this discrepancy has been unclear, but various researchers have tried to relate it with the dynamic mixing process over the breakout region. It is conjectured to be related to large coherent structures (LCS) as proposed by Schneider *et al.* [28][29].

With respect to the work of Martini *et al.* [23][24] and Horbach *et al.* [30], the present study focuses on the numerical study of blade trailing-edge cutback cooling, which is particularly important and challenging for the susceptibility of the blade damage due to higher local thermal loadings and a relatively thinner structure. The study concentrates on the interaction between the internal cooling and the TE cutback cooling as the effect of shape and configuration of the pin-fin array, lip-thickness to slot-height ratio (t/H), coolant ejection angle (α), and the influence of both mainstream flows from the pressure-and-suction side. All of these parameters are illustrated as in Figure 1–3. Problems and descriptions of case studies are described as below.

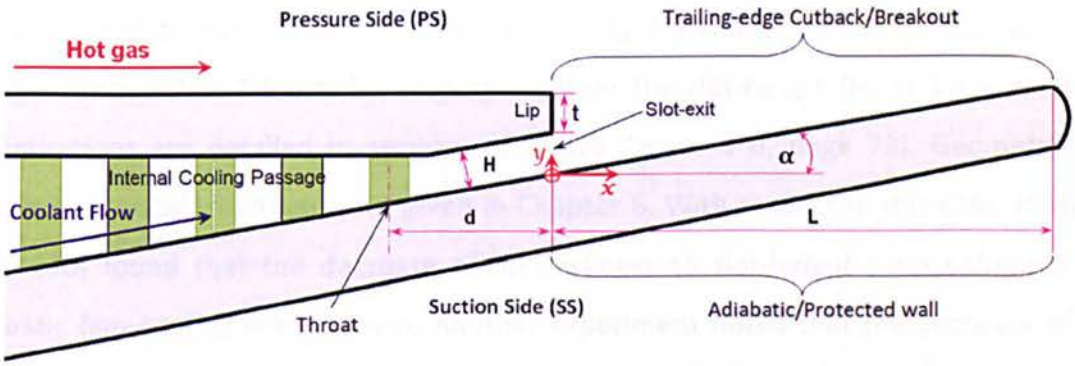

Figure 1–3: A scheme of trailing-edge cutback design.

1.2 Aims, Objectives and Case Study Descriptions

The main objective of this thesis is to investigate the computationally derived performance of the trailing-edge (TE) cutback cooling of a gas turbine blade on various geometries, as given in Figure 1–3. Flow interaction between the internal cooling (i.e. pin-fin cooling) and the external cooling (i.e. TE cutback cooling) is of concern in this numerical study. Three quantities: i.e. film-cooling effectiveness (η_{aw}), discharge coefficient (C_D), and shedding frequency (f_s) are used as the parameters studies in order to assess the performance of TE cutback cooling including their cooling interactions similar to those used in experiments. Film-cooling effectiveness illustrates the performance of TE cutback cooling at the protected/adiabatic wall (see Figure 1–3). The discharge coefficient represents the global pressure losses inside the cooling passage and the shedding frequency reflects the characteristic of unsteadiness as the effect of the

dynamic mixing process between the mainstream flow and the coolant. The mixed flow over the TE cutback/breakout will be simulated numerically in an effort to present the vortex-shedding phenomena qualitatively.

The contribution of this research is realised by considering four case studies as below. Various numerical approaches such as steady RANS, unsteady RANS and DES are considered in this study. The SST $k-\omega$ turbulence model is applied for these computations. The four case studies are described as follows:

Case I : Blade TE cutback cooling on various lip-thickness to slot-height (*t/H*) ratio

For the first case, the blade TE cutback (see Figure 1–3) is varied for four different lip-thickness to slot-height ratios (i.e. t/H = 0.25, 0.5, 1.0 and 1.5). The lip thickness (t) is changed from 1.2 to 9.6 mm by keeping constant the slot-height (H) at 4.8 mm. These configurations are detailed in section 4.8.2 (see Figure 4–6, page 73). Geometry and specific numerical treatments are given in Chapter 6. With respect to this case, Horbach *et al.* [30] found that the decrease of lip-thickness to slot-height ratio enhances the adiabatic film-cooling effectiveness. Another experiment noted that the decrease of t/H ratio from 1.0 to 0.5 improves the performance up to 10% [31]. The results of preliminary research using a blade TE cutback with two rows of long-ribs inside the cooling passage agree well against both findings [32]. So far, only a few publications exist that deal with this study parameter, and they are mainly concerned with a numerical approach. Therefore, this case is important to be studied computationally.

Case II : Blade TE cutback cooling on various internal cooling designs

Internal cooling with various features designs has been studied widely in the past. For example, several researchers evaluated the performance of innovative internal trailing-edge cooling configurations comprising pentagonal arrangement [13][33], elliptical pin-fin [34], long ribs [3], and square and semi-circular ribs [7]. Unfortunately, these previous studies only focused on the internal cooling passage. Interaction between the internal cooling and the external cooling was not addressed in their studies. A recent experiment has been reported by Horbach *et al.* [30][35] who studied comprehensively both internal and external cooling. TE cutback cooling with circular and elliptical pin-fin arrays inside the cooling passage were used for these experiments. All above inspire on numerical

study of the turbine blade TE cutback with considering internal feature designs. Three different internal cooling configurations (i.e. circular pin-fin, ellipse array and empty duct) are proposed in this computational study. The five rows of the pin-fin array are located vertically at the cooling passage as in Figure 1–3. The layout of the pin-fin array is also given in section 4.8.2 (see Figure 4–7, page 74). The detail outline of the second case study, including the results and discussion are presented in Chapter 7.

Case III : Blade TE cutback cooling on various coolant ejection angles (α)

As illustrated in Figure 1–3, the position of the trailing edge cutback follows the design of the cooling ejection angle. In this case simulation, the TE cutback cooling is designed on three different ejection angles (α = 5°, 10° and 15°). So far, investigations were carried-out with a fixed ejection angle and dissimilar geometry such as Hepeng *et al.* [36] who studied experimentally a film cooling of the trailing edge within a fixed coolant ejection angle of 0°, whilst Martini *et al.* [5][20][24] and Horbach *et al.* [30][35] used 10° as the ejection angle for their experiments. Only a few publications exist which investigate TE cutback cooling with various ejection angles (α). Two decades ago, a parametric study was carried out experimentally for several ejection angles between 0° and 15° [16]. The experiment was carried out by keeping the density ratio (ρ_c/ρ_h) constant and without considering configurations inside the cooling passage. Therefore, the third case is proposed using an integrated model as in the case 1 in an effort to address TE cutback cooling performance against the ejection angle parameter. These configurations are given in section 4.8.2 (see Figure 4–8, page 74). Modelling and the results of these case studies are presented in Chapter 8.

Case IV : Blade TE cutback cooling with pressure-side (PS) and suction-side (SS)

To date, the blade cutback models have been studied by ignoring the influence of mainstream flow along the suction-side of the blade. In order to provide a proper blade TE cutback cooling with realistic design, influence of both pressure-side (PS) – suction-side (SS) wall surfaces and their flow interactions in the near wake region is proposed in the fourth case study. These configurations are described in section 4.8.2 as depicted by Figure 4–9 (see page 75). The TE cutback cooling with land extensions is also considered for another design of this numerical study. The concept is to modify Martini's model (i.e.

baseline specimen) as used for verification and validation stage. The specification of the baseline model is illustrated in chapter 4 as a reference model (see Figure 4–2, page 66). This design is added by the PS-SS wall surfaces including lands (partitions) for another design as addressed by Yang *et al.* [6][37][38] (see Figure 9–1). This modification considers more than three different designs over the previous studies such as the blade TE cooling slot with pressure-side breakout (see references [6][25][26][39]), the blade TE breakout cooling (see references [18][40][41]), and the blade TE cooling with both PS-SS wall surfaces carried out by Joo *et al.* [27]. The results and discussion for this case study are presented in Chapter 9.

1.3 Contributions of this study

According to the literature survey, deficiencies are present in the trailing-edge cutback film-cooling knowledge base. There is a lack of understanding in the unsteady phenomena associated with the ejecting coolant, no computational data relating to the four proposed studies above, and little data available in open literature, mainly regarding investigations of blade TE cutback cooling with realistic design.

Therefore, this study presents a computational investigation into the complicated physics of trailing-edge cutback film-cooling under subsonic flow conditions. The contribution of this investigation is to extend a proven computational approach for TE cutback cooling problems by pursuing the 3-D unsteady CFD simulations on various configurations in order to provide following numerical details:

1. the performance of blade TE cutback cooling at various lip-thickness to slot-height ratios (t/H = 0.25, 0.5, 1.0 and 1.5);
2. the performance of blade TE cutback cooling with various internal cooling designs (i.e. circular pin-fin array, elliptic pin-fin array and empty duct);
3. the performance of blade TE cutback cooling at various coolant ejection angles (α = 5°, 10° and 15°)

4. the performance of blade TE cutback cooling with realistic design by considering both pressure-side (PS) and suction-side (SS) wall surfaces including the existence of land extensions.

The capability of Detached-Eddy Simulation (DES) based on the shear-stress transport (SST) $k-\omega$ turbulence model is demonstrated here. Moreover, this computational study provides comprehensive information to turbine blade designers in an attempt to improve trailing-edge cutback performance, mainly for film-cooling applications.

1.4 Structure of the Thesis Report

Chapter 1: Introduction. This chapter presents the background and motivation of this numerical study. The aims, objectives and problem descriptions are given here. The contribution of this research is described by proposing four case studies. The present study solely focuses on the numerical studies of blade trailing-edge cooling, which is particularly important and challenging for the susceptibility of the blade damage due to higher local thermal loadings and a relatively thinner structure.

Chapter 2: Literature Review and Terminology. This chapter reviews the basic concept of a cooling system in a gas turbine blades trailing-edge and the previous studies relating to blade trailing-edge cooling and pin-fin cooling. The purpose of this chapter is to give a short review of research progress with regards to blade TE cutback cooling including their terminology. The Trailing-edge cutback region as the area of interest is also comprehensively explained in this chapter including terminologies such as film-cooling effectiveness, discharge coefficient, blowing ratio, vortex-shedding and Strouhal number. Theorem of fast Fourier transform (FFT) is added to provide the basic theory for shedding frequency analysis.

Chapter 3: Turbulence Modelling. This chapter describes the governing equations, turbulence modelling, the shear-stress transport (SST) $k-\omega$ turbulence model and three DES models (i.e. the Spalart-Allmaras, the realisable $k-\varepsilon$ and the SST $k-\omega$). The Reynolds-Averaged Navier-Stokes (RANS) and Large-Eddy Simulation (LES) approaches are

explained here. The SST $k-\omega$ turbulence model is described in more detail linking to the Detached-Eddy Simulation (DES) model.

Chapter 4: Computational Set-up. This chapter explains the numerical treatments of this research. This describes the previous experiment and geometries, current studies and computational domain, flow and boundary conditions, mesh generation, algorithm and time stepping. The validation stage and the scenario of numerical studies are detailed in this section. The implementation of validation is discussed in chapter 5, whilst the investigations of the four proposed case studies are described in chapters 6 to 9.

Chapter 5: Verification and Validation. This chapter gives the validation studies of the adiabatic film-cooling effectiveness including mesh refinement studies, optimisation of time-step sizes, effect of flow-time, and precursor simulation for defining wall temperature. The computational domain with a single-pitch of pin-fin arrays versus a double-pitch of pin-fin arrays is included for comparison. Validations are performed at three different blowing ratios (M = 0.5, 0.8 and 1.1) using a baseline model of the blade TE cutback with circular pin-fin configuration inside the cooling passage, the lip-thickness to slot-height ratio of 1 and the coolant ejection angle (α) of 10°. Validation performed by steady/unsteady RANS and DES based on the SST $k-\omega$ turbulence model are discussed in this section. The interaction between the internal cooling and the external cooling are presented by comparing the flow characteristic around the pin-fin array for all approach models used.

Chapter 6: CASE I - Blade TE Cutback Cooling with Various Lip-Thicknesses. This chapter shows the performance of blade TE cutback cooling due to the effect of lip-thickness to slot height ratios from 0.25 – 1.5 mm. The local structured meshes of four t/H ratios around the lip region are given here in order to show each quality of grid resolution. The performance of the TE cutback on various t/H ratios is compared with reference to the laterally averaged film-cooling effectiveness. Properties predicted at the near wall region, the evolution of gas mixing temperature, turbulence levels, wakes and vortex-shedding resulting from the mixing region are discussed in an effort to investigate the cause of differences. Coolant properties inside the cooling passage and at the slot exit are also

shown to facilitate clear comparison. Shedding frequencies are identified by the FFT spectrum to complete the analysis shedding frequencies.

Chapter 7: CASE II - Blade TE Cutback Cooling with Various Internal Cooling Designs. This chapter contains the CFD prediction for the TE cutback cooling as a result of the effect of pin-fin configuration inside the cooling passage. The simulation results of three various internal cooling features (i.e. circular pin-fin, stream wise elliptical pin-fin, and empty duct) are presented here. The discussion section in this chapter is similar to the foregoing chapter in-so-far that the discussion considers film-cooling effectiveness (η_{aw}), coefficient of discharge (C_D), and shedding frequency (f_s). The interaction between mainstream flow and coolant are visualized by turbulent flow structures at the mixing region.

Chapter 8: CASE III - Blade TE Cutback Cooling with Various Coolant Ejection Angles. This chapter presents the CFD prediction of the performance of the TE cutback cooling for three different ejection angles i.e. α = 5, 10 and 15. The results of the three different variations are presented here. As with chapters 6 and 7, the three study parameters of film-cooling effectiveness (η_{aw}), coefficient of discharge (C_D), and shedding frequency (f_s) are assessed for comparison.

Chapter 9: CASE IV - Blade TE Cutback Cooling with Pressure-Side (PS) and Suction-Side (SS) Wall Surfaces. This chapter describes the performance of the TE cutback cooling due to the influence of both pressure-side (PS) and suction-side (SS) wall surfaces and their flow interactions in the near wake region. The computational domain is modelled to be more realistically replicate the actual conditions. The concept is to produce a finite thickness of blade trailing-edge cutback plate that has the same thickness as the coolant passage height H to form the turbine blade trailing edge and suction-side wall surface. In addition, another simulation case is equipped with land extensions in order to provide a proper shape as well as a recent design of gas turbine blade. All computational domains are constructed within a double pitch pin-fin array at the z-axis direction. Simulation tests are performed identically to the previous case studies as presented in chapters 7 and 8. Initial and boundary conditions remain unchanged. The DES computations apply the SST $k-\omega$ turbulence model.

Chapter 10: Conclusions and Future Work. This chapter presents the conclusions and recommendations from this numerical study and suggests future work.

1.5 Papers Published

During this study, several papers have been published based on the preliminary computation of pin-fin cooling and the integrated design of a trailing-edge cutback whilst taking account of the existence of the pin-fin cooling. These publications may be slightly different in terms of design, geometries and boundary condition compared to the contents in the final thesis report that contains improved results with integrated design. The papers are listed as follows:

1. Effendy, M., Yao, Y., and Yao, J., "Prediction of Pressure Loss and Wall Heat Transfer in Turbine Trailing-Edge Cooling Passage", *Proceeding of THMT–12*, Vol. 0 (2012), ICHMT digital library online, ISSN 961–91393–0–5.
2. Effendy, M., Yao, Y., and Yao, J., "Effect of Mesh Topologies on Wall Heat Transfer and Pressure Loss Prediction of Blade Coolant Passage", Applied *Mechanics and Materials*, Vol. 315 (2013) pp. 216–220.
3. Effendy, M., Yao, Y., and Yao, J., "Comparison Study of Turbine Blade with Trailing-Edge Cutback Coolant Ejection Designs", *Proc. of the 51st AIAA Aerospace Sciences Meeting including the New Horizons Forum and Aerospace Exposition*, Grapevine, Dallas, Texas. [AIAA 2013–0548].
4. Effendy, M., Yao, Y., Yao, J., and Marchant, D., Predicting Film Cooling Performance of Trailing-Edge Cutback Turbine Blades by Detached-Eddy Simulation, (AIAA 2014–0279).

CHAPTER 2:

LITERATURE REVIEW AND TERMINOLOGY

Literature review and terminology related to the trailing edge of gas turbine blade is discussed in this chapter. The discussion starts from providing an overview on a modern gas turbine and its operating conditions including the requirements. Various internal and external coolings of gas turbine blade are described to illustrate the complexity of a cooling system, which needs a careful design. The review of literature is described in more detail by classifying the contents into two categories, namely the experimental and numerical studies. The trailing-edge cutback region as the area of interest is also comprehensively explained including their terminologies such as film-cooling effectiveness, discharge coefficient, blowing ratio, vortex shedding and Strouhal number. The theorem of fast Fourier transform (FFT) is added to provide support on the shedding frequency analysis.

2.1 Introduction

As explained previously in chapter 1, gas turbine engines require a very high inlet temperature in order to maximize the power output to achieve a high thermal efficiency. Modern gas turbines typically operate at temperatures of around 1,200 – 1,500°C [2][8][10]. The temperature can be up to 2,000°C for a double engine power in aircraft gas turbines [42]. It is significantly beyond the melting temperatures for turbine vane and blade materials. Figure 2–1 illustrates the heat distribution on the turbine vane and blade as the effect of high turbine inlet temperatures.

High turbine inlet temperature causes structural strength degradation that eventually results in vane and blade break down. It causes a serious implication on durability and safety. Therefore, turbine blades/vanes must be cooled down to the levels that are

significantly below the melting point of the material using internal and external cooling techniques (also see Figure 2–1). The cooling can be done by combining convection and film cooling. A comprehensive review paper by Han *et al.* [42] summarized recent advancements in this field including both internal-cooling passage and external film cooling jets.

The trailing edge is the most critical part in a vane/blade component due to its geometrical constraint, in combination with aerodynamic, thermal and structural requirements. The trailing edge is particularly vulnerable to high turbine inlet temperatures because of its thin structure, which is susceptible to heavy mechanical and thermal stress. An effective blade TE cooling system should keep vane/blade temperature within its limit without affecting both mechanical strength and aerodynamic losses.

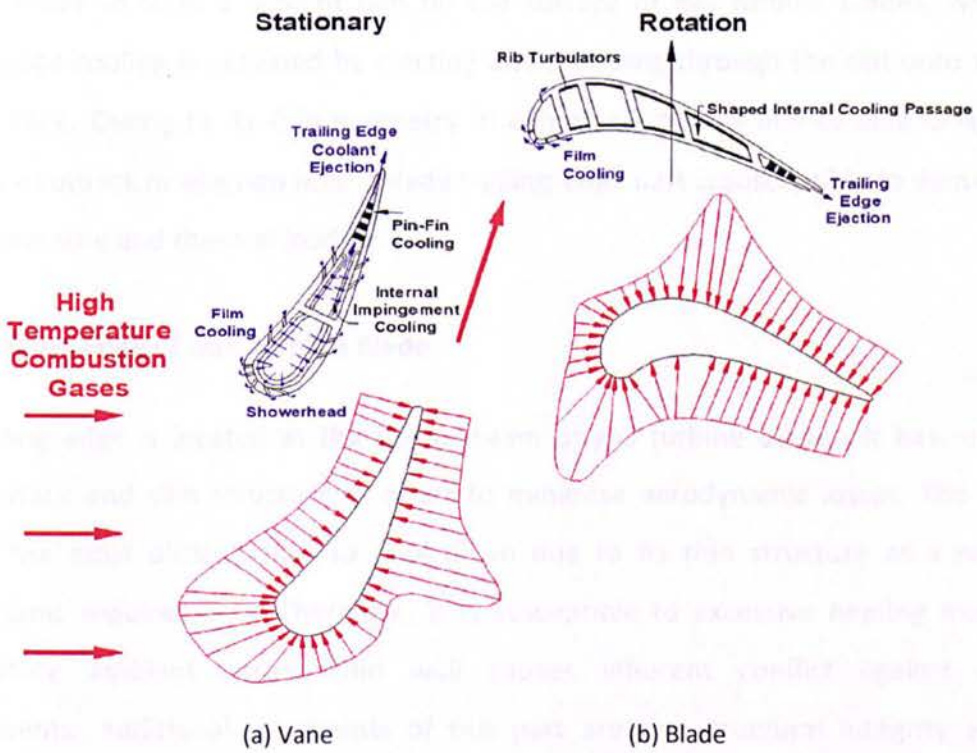

Figure 2–1: Heat-flux distribution of a cooled vane and blade [12][42].

2.2 Cooling System of Gas Turbine Blade

In most cases, a gas turbine blade surface is cooled down by discrete holes film-cooling and internal-cooling passage. Figure 2–1 depicts various internal and external coolings of

gas turbine blade (see Figure 1–1). Among the internal cooling methods are the internal-impingement cooling and the pin-fin cooling system. Internal cooling is achieved by passing the coolant gas inside the cooling passage of blade constructed by ribs. It is a common technique to insert pin-fins, ribs or other obstacles to enhance wall heat-transfer [43]. Sometimes, a dimples configuration is applied on blade inside the cooling passage in order to intensify the internal heat-transfer. A comprehensive experimental data can be found in references [44][45][46], which are focused on a matrix of cylindrical pin-fins inserted in a staggered arrangement of the internal cooling passage.

External cooling is known as film-cooling due to the involvement of a film-cooling process at the blade surfaces either at upstream, downstream, or on the surface of trailing edge. The external cooling method is achieved by injecting out internal coolant air through discrete holes to form a coolant film on the surface of gas turbine blades, while the trailing-edge cooling is obtained by ejecting a film cooling through the slot onto trailing-edge surface. Owing to its thin geometry in combination with film-cooling design that requires a cutback or ejection holes, blade trailing-edge part is susceptible to damage due to high pressure and thermal loading.

2.3 Trailing-Edge of Gas Turbine Blade

The trailing edge is located at the downstream of gas turbine blades. It has relatively small surface and slim structure in order to minimise aerodynamic losses. The trailing edge is the most difficult part to cool down due to its thin structure as a result of aerodynamic requirements. Therefore, it is susceptible to excessive heating from high temperature ambient gases. Thin wall causes inherent conflict against cooling requirements. Additional constraints of this part are the structural integrity and the manufacturing difficulty for the internal cooling passage geometry.

Current cooling technology substantially relying on the coolant air induced from the main-body up-stream is believed to bring a TE cooling within the available design solution space. An optimum solution technique commonly used for thin trailing-edge cooling is achieved by removing material of the pressure-side wall with respect to the suction-side area. Trailing edge is cut away to provide a coolant bleed slot as shown in Figure 2–2. The

corner of the upper lip plate (pressure-side wall) is cut-off parallel to the protected surface. The breakout slot is formed in parallel with the ejection slot. Hereinafter, this region is called as a "cutback" or "breakout" of trailing edge. Pressure-side slot film-cooling cutback is a common method in the trailing-edge cooling. Cutting back a pressure-side surface at the trailing edge of blade to form a continuous ejection slot is a well-established technique as shown in Figure 2–3(d). Lee *et al.* [47] equipped blade design with land extensions. Internal-cooling passage and discrete holes film-cooling are commonly applied for blade cooling before establishing this type.

(a) Before cutting (b) After cutting

Figure 2–2: Cutting process of trailing-edge.

The trailing-edge cutback area is an interesting part as the design requires thin structure to minimise aerodynamic losses, whilst it needs enough cooling for safety and durability reasons [8]. It is worth noting that the cooling air is associated with loss in engine efficiency. Therefore, a compromised solution is needed to minimize the coolant flow rate in order to keep the highest efficiency as well. All aspects should be considered simultaneously in an effort to harmonize the design and satisfy the requirements.

Gas turbine-cooling technology is complex and varies from engine manufacturer. Even the same engine manufacturer, it could be applied different cooling systems for various engine. Highly sophisticated cooling technique such as trailling-edge cooling must be utilized to maintain acceptable live and operational requirements under such extreme heat load conditions. In terms of trailing-edge cooling designs, there are several types such as (a) blade TE without internal cooling; (b) blade TE with ejection holes; (c) blade TE with centre-line slot; and (d) blade TE with slot, cutback and lands [6][18] as shown in Figure 2–3. All designs have serious stress-strain issues due to the thin thickness of trailing-edge structure. The latter have additional aero thermal issues because of large wall surfaces, which make it directly exposed to hot gas stream that needs to be precisely quantified and carefully assessed.

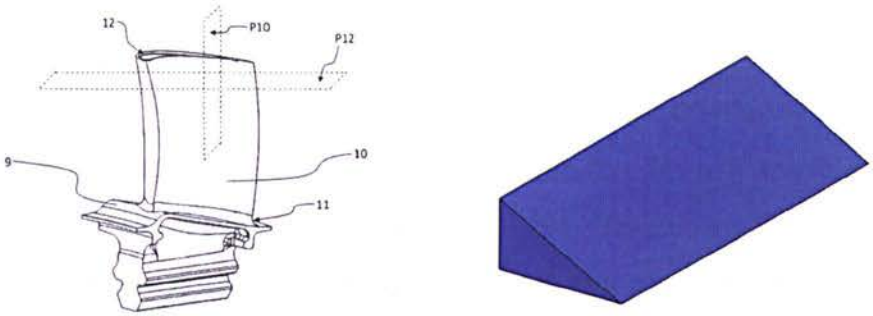

(a) Blade TE without internal cooling [48].

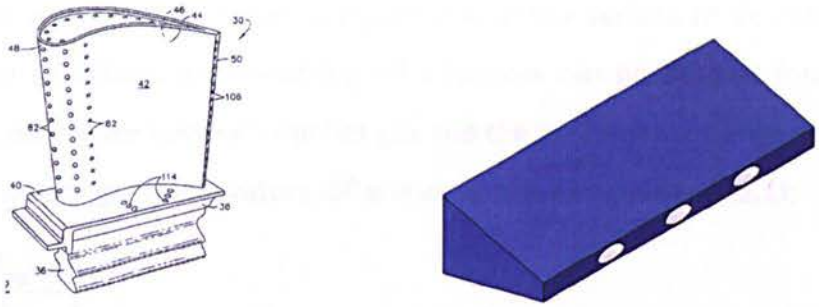

(b) Blade TE with ejection holes [49].

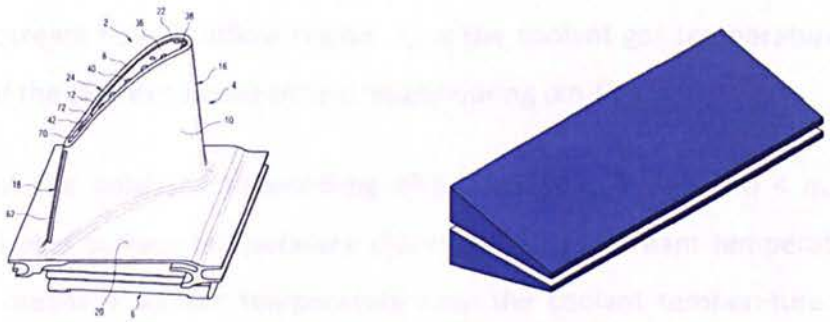

(c) Blade TE with centreline slot [50].

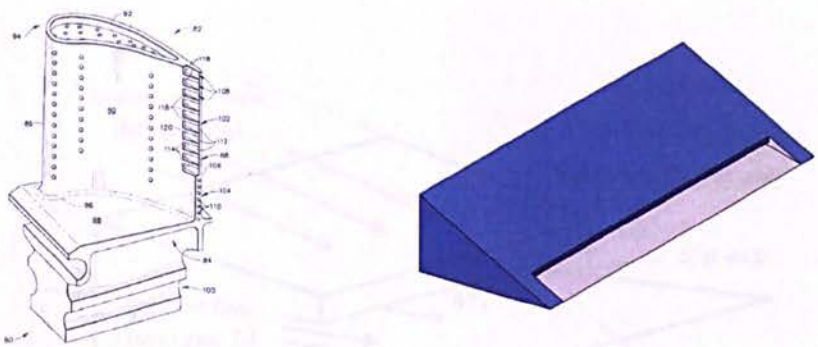

(d) Blade TE with slot, cutback and land extensions [47].

Figure 2–3: Types of blade trailing-edge cooling.

2.4 Film-Cooling Effectiveness and Trailing-Edge Cutback

The performance of a trailing-edge cutback cooling is commonly expressed by film-cooling effectiveness at the protected wall between the slot-exit and downstream of the trailing edge. According to Schneider *et al.* [29], film-cooling effectiveness is a key quantity in assessing the film-cooling performance. This is mainly affected by geometrical features of trailing-edge breakout, coolant ejection angle, blowing ratio, and mixing flow behaviour. These terminologies could be explained by a trailing-edge cutback of a gas turbine blade with land as shown in Figure 2–4. If the surface of TE cutback is on the adiabatic wall condition, a film-cooling effectiveness can be derived from the ratio of temperature difference between the hot gas and the wall surface temperature to the hot gas and the coolant gas temperature difference as given in equation (2.1);

$$\eta_{aw} = \frac{T_{hg} - T_{aw}}{T_{hg} - T_{c'}}, \tag{2.1}$$

where T_{aw} is the temperature at the adiabatic wall surfaces, T_{hg} is the hot gas temperature at the mainstream flow at inflow region, $T_{c'}$ is the coolant gas temperature measured at the centre of the slot-exit between two neighbouring pin-fins.

The range of the adiabatic film-cooling effectiveness is between $0 < \eta_{aw} < 1$. A zero number indicates surface temperature close to the mainstream temperature (hot gas), while unity means a surface temperature near the coolant temperature. According to Chen *et al.* [39], a poor value of η_{aw} means a strong mixing process between the mainstream flow and the coolant along the mixing region of the breakout slot.

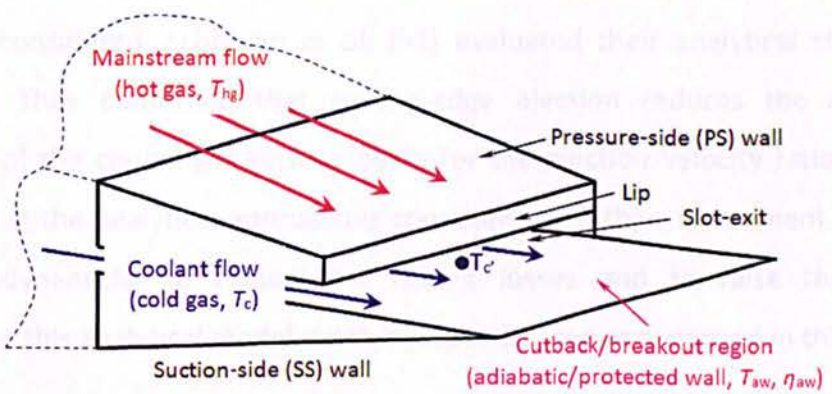

Figure 2–4: Trailing-edge cutback slot.

With respect to the film-cooling effectiveness of the trailing-edge cutback, most experimental studies indicated that the most effective film-cooling occurs near the slot exit and gradually decreases as it approaches the middle region of TE cutback. This effectiveness depends on the blowing ratio as suggested by Martini *et al.* [4][5] and Horbach *et al.* [30]. Various strategies have been done to make the film-cooling effectiveness along the blade TE cutback surface as close to unity as possible. However, various researchers found a discrepancy between the film-cooling effectiveness predicted by CFD and those demonstrated by experiments. Numerical approaches appear to result in over-prediction. So far, the origin of this discrepancy is unclear. Some suggest it may relate to the dynamic mixing process between the mainstream flow and the coolant along the breakout slot as stated by Schneider *et al.* [29].

2.5 Literature Review

The trailing-edge cutback cooling with several design parameters has been studied analytically, experimentally and numerically for many years. Numerous data have been published on cutback blade trailing-edge models, and these provide a rich database to validate CFD predictions. Brief reviews of previous studies are given as follows:

2.5.1 Previous Analytical Studies

Aerodynamic effects of trailing-edge ejection were studied theoretically by Schobeiri *et al.* [17] using one-dimensional theory. The important parameters determining the mixing losses and the efficiency of cooled blades, such as the ejection velocity ratio, the cooling mass flow ratio, the temperature ratio, the slot thickness ratios, and the ejection flow angle, were considered. Schobeiri *et al.* [51] evaluated their analytical study through experiments. They confirmed that trailing-edge ejection reduces the mixing-losses downstream of the cooled gas turbine blade for the ejection velocity ratio of 1. It was recognised that the analytical approach is consistent with their experiment, which allow turbine aerodynamicist to reduce the mixing losses and to raise the efficiency. Unfortunately, this analytical model is not in a specific area as proposed in this study.

Another analytical study of blade trailing-edge breakout cooling has been performed by Cunha *et al.* [18] in order to provide the basis for determining the geometrical effects on different configurations. The four various wedges (i.e. as solid-wedge shape without discharge, wedge with centre-line slot discharge, wedge with centre-line discrete-hole discharge, and wedge with pressure-side cutback slot discharge) were analytically investigated to advance the fundamental understanding of thermal characteristics on the trailing-edge region. One-dimensional nature of the heat-transfer verified at the airfoil of operational vanes and blades was considered to establish the external heat-transfer coefficient based on airfoil curvature and expected wall roughness. This study is expected to offer a platform for benchmarking subsequent experiment. The analytical approach reported that there are some relevant design features including size of the cooling passage, internal cooling features inside the cooling passage, trailing-edge thickness, pressure-side lip thickness, roughness on pressure-side land, and slot film coverage. All features could be used effectively for the pressure side arrangement, whereas both sizes and internal cooling features inside the cooling passage are only effective for centre-line discharge configurations. For the trailing-edge cutback design, the limitations associated with thicker trailing-edge of the centre-line are removed to allow the options of several alternative design in order to optimise the cooling configurations. Therefore, internal cooling features could be chosen to enhance the internal heat-transfer, the size of cooling passage could be increased, both trailing-edge thickness and pressure-side lip thickness could be created thinner, pressure-side land roughness could be increased to augment the coolant heat transfer, and slot film cooling effectiveness could be improved with higher coverage. The added benefit of improved aerodynamic performance is obtained by a thinner trailing-edge, and the life capability against thermal-mechanical fatigue and creep is improved as the distributions of metal temperature are more evenly distributed over the entire trailing-edge cutback. Blowing ratio (M) and lip thickness-to-slot-height ratio (t/H) are the two important key parameters to film-cooling effectiveness, which are dominant in maintaining desired it effectiveness while minimising trailing-edge cooling flow.

2.5.2 Previous Experimental Studies

Several experiments of the blade TE cutback cooling have been performed using different measurement techniques such as liquid-crystal technique [8][18][36], infra-red (IR) thermograph [4][5][30][52], magnetic resonance imaging (MRI) [53][54][55], and pressure sensitive paint (PSP) technique [6][38]. These experiments were carried out on various geometries. Brief reviews of previous experimental investigations are described as follows:

2.5.2.1 Experimental studies of TE cutback without pin-fin cooling:

Flow characteristic of the wall jet related to trailing-edge cutback cooling of turbine blades has been investigated experimentally by Yang *et al.* [6]. In this study, a TE cooling slot at pressure breakout was designed without inclination of suction-side wall similar to the one tested by Hepeng *et al.* [36], except the breakout of this specimen was equipped with lands/partitions (see Figure 2–4). This specimen had five-coolant ejections slot as the effect of land extensions. Inside the cooling passage was empty duct. The experiment was performed in a small open-circuit wind tunnel. The vast majority of the results of this experiment were presented qualitatively. Based on various blowing ratios (M = 0.43, 0.8, 1.1 and 1.6) tested, it was found that the film-cooling effectiveness could be improved by increasing the blowing ratios. The adiabatic film-cooling effectiveness with a higher intensity dominated over the protected plate. It indicated that the performance is nearly ideal along the protected wall. The existence of partition would be useful to improve the coverage of the cooling stream over the cutback surface, while the lateral expansion of the cooling stream will be restricted by the lands.

Previously, Yang *et al.* [37][38] reported a dynamic mixing process between the cooling jet stream (nitrogen) and the mainstream flows (air). The evolution of turbulent flow and vortex structures at the mixing region were quantified to examine the dynamic mixing process over the protected wall. The results showed that the optimum film-cooling effectiveness would be achieved in a range of blowing ratio between 0.6 and 0.8. Based on overall averaged performance, the film-cooling effectiveness for the blade TE breakout with lands was less than that of the blade TE without lands by discrepancy up to 10%.

2.5.2.2 Experimental studies of the blade TE cutback with pin-fin cooling:

Several TE cooling experiments have been performed by considering internal features inside the cooling passage, for example Martini *et al.* [5][16], Cunha *et al.* [18], Horbach *et al.* [30][35], Ling *et al.* [41], etc. These experiments represented an integrated model as well as currently being investigated numerically in this study. Both internal and external coolings were modelled within an integrated domain, which was possible to measure simultaneously for both performances. This approach was seen to be very useful to comprehensively study the relationship between inside the cooling passage and the TE cutback cooling. It should be noted that both are commonly coupled in real applications. The following reviews are some studies that discuss their interactions.

Hepeng *et al.* [36] investigated the heat-transfer characteristic of the blade TE cutback using an experimental approach. The lip and end-wall plate of specimen constructed the secondary flow path, which was provided by eight long ribs. The existence of land extensions along the TE cutback was not considered in their experiment. The coolant ejection was designed in parallel with the mainstream flow. This experiment was performed on three various blowing ratios of 0.5, 1.0 and 2.0. The measurement used both thermocouple and narrowband liquid crystal. The results showed that the increase of blowing ratios has a positive effect on smoothing the regular film-cooling effectiveness curve. The blowing ratio had a significant effect on film-cooling effectiveness distribution of the rib centre-line. The discrepancy of cooling effectiveness data between the two measurement methods was observed. Both film-cooling effectiveness and heat-transfer coefficient were measured by liquid-crystal technique, which showed a typical distribution for each blowing ratio tested.

A measurement of both film-cooling effectiveness and heat-transfer coefficient for turbine blade TE cooling has been performed by Choi *et al.* [8]. They varied blowing ratios at 0.3, 0.61, 1.22 and 1.83. Three different TE configurations with staggered and inline arrangement of the chord-wise rib separators with respect to the jet holes on the second blockage insert were tested experimentally in a low-speed wind tunnel. The geometry of the internal test was similar to the crossover-impingement holes design used in modern gas turbine blades. The results indicated that the internal design geometry of the trailing

edge and Reynolds number influence the heat-transfer process in the internal model with perforated blockage inserts. A wider entrance channel and a sloped land near the ejection slots yielded a higher film-cooling effectiveness from the slot ejection.

Martini *et al.* [4][5] focused on the blade TE cutback cooling with various internal cooling designs such as double in-line rib array used in low-pressure (LP) turbines, and pin-fin staggered arrays, which was predominantly found in high-pressure (HP) turbines. The ejection angle was set-up at 10° relative to the direction of the mainstream flow. This research did not consider the land design. The experiment was performed in a subsonic atmospheric open-loop wind tunnel. The results found that the internal cooling design has a strong impact on the film-cooling effectiveness near the ejection slot and high performance sustainability of a cutback blade trailing edge depends on the characteristics of the cooling channel flow. Based on the blowing ratios tested, the film-cooling effectiveness was highly dependent on the blowing ratio.

Previously, Martini *et al.* [20] noted in similar findings on the experimental investigation using a double in-line long rib of the internal cooling configuration with rib pitch (s/H = 6). The existence of ribs had a considerable influence on the local and laterally averaged adiabatic film-cooling effectiveness. In a further experiment using a small lateral pitch (s/H = 2) of internal rib array, it was found that the flow interaction between the mainstream flow and coolant jet leads to an attachment of up to three jets resulting in a distribution of characteristic temperature on the blade TE cutback. It was highly unsteady flow over trailing edges for configuration without land extensions [15][16].

A blade TE cooling with cutback lands was investigated by Cunha *et al.* [18]. The specimen used in the investigation had four-row staggered pin-fin arrays inside the cooling chamber with a convergent wedge-shaped duct. The pressure-side (PS) and suction-side (SS) wall were connected by oblong-shaped features near the duct exit. All of circular pin-fins and pedestals were placed orthogonally relative to the mainstream flow, whereas the suction-side wall was set-up at 10.5°. This design is similar to Lee's patent [47], which was equipped by the pin-fin array for internal cooling and land extensions at the breakout region. The results showed that the effective protection of heat-transfer over the cutback lands could be achieved for the blowing ratio at $M > 1.32$ [18].

A comprehensive experimental study was published by Horbach *et al.* [30]. They considered several design parameters such as the effects of various internal pin-fin configurations (e.g. circular, streamwise and spanwise ellipse), lip shapes (sharp and circular), various lip thickness ratios (t/H = 0.2, 0.5, 1.0 and 1.5) and land extensions, including experiments with and without them. Several configurations inside the cooling passage had a similar model as investigated by Martini *et al.* [23][24]. The suction-side wall was positioned at 10-deg relative to the mainstream flow. Based on various blowing ratios tested (i.e. $0.2 < M < 1.25$), the results found that a strong dependency on ejection lip thickness and minor improvements were obtained with a rounded ejection lip profile in terms of the effectiveness of film-cooling. For example, the thinnest lip thickness yielded the highest film-cooling effectiveness, whereas the rounded shape of the ejection lip caused an increase of the discharge coefficient. Furthermore, the blade TE cutback cooling with elliptical pin-fins inside the cooling passage produced a strong effect on the discharge behaviour as well as the heat-transfer and the film-cooling effectiveness. The streamwise configuration of elliptical pin-fins array generated a higher film-cooling effectiveness and a lower discharge coefficient compared to the spanwise one. A significant improvement of the adiabatic film-cooling effectiveness was attained using land extensions. Surprisingly, this finding was seen to be contradictive with previous experiment studied by Yang *et al.* [37].

Beforehand, Horbach *et al.* [35] had also evaluated the effect of lip ejection geometry for a blade TE cutback with two-row long rib inside the cooling passage. They found a similar trend in this study. The lip thickness had a pronounced effect on the mixing process between the coolant and the mainstream flow that increased the heat-transfer coefficient on thicker lip thickness. This finding was consistent with the previous experiments as done by Taslim *et al.* [31][56], Kacker *et al.* [57][58], Sivasegaram *et al.* [59], and Burns *et al.* [60].

The effect of the surface geometry on film-cooling performance of airfoil trailing-edge has been investigated experimentally by Murata *et al.* [52] for four different cutback geometries (i.e. base, diffuser, rib, dimple) and four various blowing ratios (i.e. M = 0.5, 1.0, 1.5 and 2.0). The suction-side wall was set-up at 11° relative to the mainstream flow.

Both film-cooling effectiveness and heat-transfer coefficient on the cutback and land top surfaces were measured in these studies. The results revealed that the increase of blowing ratio improves both film-cooling effectiveness and heat-transfer coefficient. The dimple surface configuration caused the enhanced heat-transfer without deteriorating the high film-cooling effectiveness. In terms of blowing ratio effects, this finding was in agreement with experiments by Martini *et al.* [4][5], Horbach *et al.* [30][35] and Yang *et al.* [6][37].

A recent experimental study was conducted by Ling *et al.* [41] in order to investigate the mean three-dimensional velocity and concentration fields on the island airfoil, TE geometry with thin straight lands and airfoil-shaped blockages in the slots. The cutback geometry consisted of rectangular slots separated by straight lands; inside each of the slots is an airfoil-shaped blockage. Four rows of staggered pin-fin array was set-up inside cooling passage chamber similar to the one tested by Cunha *et al.* [18]. The experiment was conducted at a fixed blowing ratio of 1.3. The results showed that the thinner land of the island airfoil generated a much higher spanwise averaged surface effectiveness, particularly near the slot exit. Strong horseshoe vortices were seen around the blockages in the slots as the effect of coolant non-uniformity on the airfoil breakout surface and in the wake. The existence of the islands in the slots might cause the formation of those vortices.

2.5.3 Previous Numerical Studies

Numerical investigations of blade TE cutback cooling can be found in open literature, but only little information explains the dynamic flow interaction between the internal cooling and the external cooling in a comprehensive manner. So far, most of the numerical studies employ the steady RANS approach that does not capture well in terms of the turbulent flow mixing. Therefore, the predicted data do not match with the measurement data. For instance, the use of steady RANS predicts ideal results, which ignores a decay of effectiveness as reported by Martini *et al.* [20], Effendy *et al.* [21], Egorov *et al.* [22] and Holloway *et al.* [25].

It is known that the use of unsteady RANS calculation is capable of capturing the turbulent flow structures at the mixing region as discovered by Medic *et al.* [26] and Joo *et al.* [27]. Unfortunately, it does not optimally simulate the flow interactions between the mainstream flow and the coolant. Consequently, CFD prediction of film-cooling effectiveness does not match with the experimental data as found by Holloway *et al.* [19], Egorov *et al.* [22], Medic *et al.* [26] and Joo *et al.* [27].

Other computations have been applied by unsteady simulation in order to gain a better prediction on capturing turbulent flow structures of mixing. For example, Scale-Adaptive Simulation (SST-SAS) was used by Egorov *et al.* [22], Detached-Eddy Simulation (DES) based on Spalart-Allmaras (SA) turbulence model was applied by Martini *et al.* [23][24] and Krueckel *et al.* [14], and Large-Eddy Simulation (LES) was utilized by Viswanathan *et al.* [61] and Schneider *et al.* [28][29]. Moreover, Viswanathan *et al.* [62] employed DES simulation for modelling forbody [63] and internal cooling [64]. Published papers on blade TE cutback cooling subject with various numerical methods are described below:

A pressure-side bleed on the trailing edge with realistic turbine condition was numerically studied by Holloway *et al.* [25] for both steady and unsteady RANS. A total of 2.2 million cells was constructed within a high quality grids mesh, unstructured, multi-topology and super-block mesh with average of $\Delta y^+ < 1$ at all of wall surfaces. Their steady RANS generated local centre-line effectiveness much greater than the experiments at all blowing ratio simulated, whereas unsteady RANS studies noted that vortex-shedding from the lip (case with $t/H = 0.9$) was the major driving mechanism for the mixing of main hot gas and coolant. The increase of lip thickness-to-slot height ratio caused relatively fast decay of film-cooling effectiveness due to intensified vortex-shedding. Indeed, Holloway *et al.* [25] suggested a role of unsteadiness in the pressure-side bleed on the trailing-edge cooling.

Similar to blade TE cutback as experimentally investigated by Holloway *et al.* [19] and Chen *et al.* [39], further numerical study has been undertaken by Medic *et al.* [26], using ANSYS-CFX commercial code. They applied the unsteady RANS with the shear-stress transport (SST) turbulence model computation using 1.25 million cells. In continuation of

works from Medic *et al.* [26], Joo *et al.* [27] undertook their work using the Stanford University SUMB CFD code. They applied both the SST-RANS modelling and the SST-SAS on their numerical study. Based on their studies, both Medic *et al.* [26] and Joo *et al.* [27] noted that prediction by unsteady simulation is appropriate with the available data of experiments, whereas steady RANS predicts the level of film-cooling effectiveness nearly unity along the trailing-edge surfaces, mainly for higher blowing ratios. The film-cooling effectiveness predicted by unsteady RANS was not consistent with tested data due to coolant air near the trailing-edge surface was protected from mixing process with main hot gas. A small chunk of main hot gas did not hit the bottom wall along the trailing-edge cutback. The over-prediction of film-cooling effectiveness by unsteady RANS was due to the deficiency of unsteady coherent energy at near wall of the TE cutback surfaces. Along this surface, both the total turbulence kinetic energy and the mean temperature predicted by unsteady RANS was significantly less than the SST-SAS simulation. This finding indicated that there was a strong correlation between the level of turbulence kinetic energy and the profiles of the mean temperature, which caused the degree of mixing process. This research also noted that the three-dimensional (3D) vortex-shedding caused by the upper lip is a dominant aspect that influences a mixing flow over the blade TE cooling surface. Unsteadiness in the blade TE breakout was composed by two components namely coherent and broadband components. The coherent component was due to unsteadiness and the broadband component was denoted by a closure model [27].

In parallel with their experiments, Martini *et al.* [24][23] also evaluated numerically the performance of gas turbine blade TE cutback cooling. Through studies of different TE configurations including "two-rows of long ribs" and "circular pin-fin arrays" inside the cooling passage, Martini *et al.* [20] constructed a multi-block structured mesh up to 0.89 million cells with average of $\Delta y^+ < 2$, and simulated on three different blowing ratio (i.e. M = 0.5, 0.8 and 1.1). This numerical prediction found that a highly complex turbulent mixing process was not captured correctly using $k-\omega$ model with CFX Tasc-Flow. There was a significant deviation of film-cooling effectiveness between CFD data and measurements, particularly after approaching the middle of the trailing-edge cutback region [20]. Further numerical study showed that the prediction could be improved after applying DES using Spalart-Allmaras (SA) turbulence model. This gave a detailed insight

into the unsteady film mixing on the blade TE breakout region [23][24]. The results revealed that the adiabatic film-cooling effectiveness and the heat-transfer coefficient were in a good agreement between numerical prediction and experiments at all blowing ratios. Vortex-shedding behind the lip was also captured in this DES study. The discrepancy of prediction was seen for the configuration of two-row long ribs inside the cooling passage. The CFD prediction was about 10% lower than the experimental data.

Previously, Martini *et al.* [15][16] claimed that the use of realisable $k-\varepsilon$ turbulence model predicted well on their numerical study of a trailing-edge film-cooling using circular coolant wall jets ejected from a slot with internal rib arrays, mainly for a low blowing ratio of 0.55. The deviation between CFD data and measurements was more pronounced up to 10% when increasing blowing ratios. The CFD data was over-prediction against the experiment [16]. In terms of discharge coefficient, both steady RANS and DES-SA yielded the same prediction as found by Martini *et al.* [23][24].

Further unsteady simulation was undertaken by Krueckel *et al.* [14] at a blowing ratio of 0.8. They referred to one of Martini's configuration for the blade TE cooling with circular pin-fin arrays inside the cooling passage [23][24]. A total of 1.3 M cells grid in the mixing region was constructed by Gambit 2.3 meshing tool within structured-hexahedral elements. They performed DES based on Spalart-Allmaras model similar to computational study worked-out by Martini *et al.* [23][24]. This simulation considered two different conditions of a low speed rig (Ma ≈ 0.12) and a realistic engine (Ma ≈ 0.8) which took into account a compressibility factor. The results found that CFD prediction of film-cooling effectiveness is in agreements on both conditions with under-prediction by about 5% at near the slot exit $0 < x/H < 6$ for a low speed rig, and over-prediction up to 10% between $6 < x/H < 15$ for a realistic engine.

A numerical investigation has been published by Egorov *et al.* [22] who used a similar trailing-edge cutback cooling as studied by Martini *et al.* [23][24]. They demonstrated the capability of the SST turbulence model on numerical investigation of a TE cutback with two-row long ribs. The steady/unsteady RANS and SST-SAS model were applied for these simulations. The blowing ratio was set at $M = 0.8$. A block structured mesh was employed

using hexahedral elements consist of 648,000 cells with $\Delta y^+ \approx 1$ near wall resolution. This mesh was three times less than that used by Martini *et al.* [23][24] at the same specimen. Based on the simulation using ANSYS-CFX, it was found that the use of SST-SAS turbulence model caused a significantly stronger mixing of the hot-cold streams. Unsteadiness at mixing region could be captured in this study. A course mesh influenced a relative coarseness of the resolved turbulent flow structures. In terms of film-cooling effectiveness, the results were acceptable compared to steady and unsteady RANS, with under-prediction data near the exit-slot and region at $3 < x/H < 9$.

Recently, Schneider *et al.* [28][29] investigated the interrelationship between turbulent heat-flux and large coherent structures in a film-cooled TE cutback of gas turbine blades. LES was applied on their computational study. It was found that the blowing ratio and the flow regime of the cool gas flow influence both type and the strength of large-scale structures. The change in large coherent structures had a significant consequence to the dynamic mixing process at the breakout region. Dominant clockwise-rotating flow structures existed in the region of blowing ratio in which the counter-intuitive behaviour occurred. A large coherent structure increased the upstream-and-wall-directed turbulent heat-flux. This turbulent heat-flux caused the enhanced thermal mixing process in the near wall region.

A preliminary research of this computational study note that the use of steady RANS tends to a largely over-predict against the experimental data. It has been proven by recent researches using various two-equation turbulence models such as $k-\varepsilon$, $k-\omega$, RNG $k-\varepsilon$, realisable $k-\varepsilon$ and SST [21]. Using the same domain of a TE cutback cooling as used by Martini *et al.* [20], steady RANS generates over-prediction data nearly unity.

Based on the literature reviews above, although this area has been studied by various researchers in the past such as Martini *et al.* [23][24], Krueckel *et al.* [14] and Egorov *et al.* [22], it still represents one of the most rigorous research topics in turbo-machinery studies. Computational study will focus on the use of SST $k-\omega$ turbulence model and various design of blade TE cutback cooling. In terms of turbulence model, so far, there is no published paper for the use of DES using SST $k-\omega$ turbulence model. Therefore, the

use of unsteady RANS and DES based on SST $k-\omega$ turbulence model will be realised in this numerical study.

2.5.4 The Limitation of Previous Numerical Studies

Several literature on TE cutback cooling based on numerical studies has been discussed. Among these studies, two papers by Martini *et al.* [23][24] are very useful for supporting the current computations. Both works provide great information, which are comprehensive with their experiments [4][5]. Three study parameters namely the coefficient of discharge (C_D), the effectiveness of film-cooling (η_{aw}), and the shedding frequency (f_s) are given in the literature. The chart of the adiabatic film-cooling effectiveness based on the laterally averaged data as used by Horbach *et al.* [30][35], Krueckel *et al.* [14], and Egorov *et al.* [22] are also provided here. In addition, initial and boundary conditions are clearly presented by Martini *et al.* [23][24]. Therefore, it can be adopted for the current numerical study. Unfortunately, Martini *et al.* [23][24] did not mention the boundary conditions of wall temperature at the pin-fin, the lip-end, and the end-wall. Another computational study by Schneider *et al.* [28][29] also did not explain this wall temperature, as well as Horbach *et al.* [30][35] and Krueckel *et al.* [14]. No clarifications were provided concerning this missing. Egorov *et al.* [22] used a mean temperature of the operating condition between the mainstream flow and the coolant in an effort to provide this missing information.

Other papers show clear comparison between CFD data and experiment with a significant agreement of the film-cooling effectiveness as reported by Holloway *et al.* [19][25], Medic *et al.* [26] and Joo *et al.* [27]. Unfortunately, it did not represent the laterally average film-cooling effectiveness at all surfaces of the blade TE cutback as studied by Martini *et al.* [23][24] and Horbach *et al.* [30][35]. They only presented data at the centre-line ($z/H = 0$) along a TE cutback. The three-dimensional effect of unsteadiness could not be seen in these numerical studies. In fact, both CFD and experimental data show that the adiabatic film-cooling effectiveness is not uniform over the TE cutback surface in typical blowing ratios (see references [23][24][30]). The laterally average film-cooling effectiveness is probably up-and-down depending on their distribution, mainly near the downstream

region. Besides, the TE cutback cooling used on their numerical study does not consider the existence of pin-fin cooling. Therefore, this aspect is neglected in their study.

2.6 Terminology on the blade TE Cutback Cooling

Based on the Figure 2–4 above, some terminologies on the blade TE cutback cooling can be described as follows:

2.6.1 Discharge Coefficient

The discharge coefficient, C_D, is a representation of the global pressure losses inside the cooling passage, which is defined by the measured coolant mass flow over the ideal mass flow. It is a ratio of an isentropic expansion from the total pressure measured upstream of the first rib row in the coolant passage against the static pressure of the mainstream flow as formulated below

$$C_D = \frac{\dot{m}_{c,real}}{\dot{m}_{c,ideal}}, \tag{2.2}$$

$$C_D = \frac{\dot{m}_{c,real}}{p_{1,t} \cdot \left(\frac{p_2}{p_{1,t}}\right)^{\frac{\kappa+1}{2\kappa}} \cdot A_{slot} \cdot \sqrt{\frac{2\kappa}{(\kappa-1)\cdot R \cdot T_{1,t}}\left[\left(\frac{p_{1,t}}{p_2}\right)^{\frac{\kappa-1}{\kappa}} - 1\right]}}, \tag{2.3}$$

where $p_{1,t}$ and $T_{1,t}$ are the total pressure and temperature at the coolant inlet, respectively, p_2 is the static pressure at the slot exit, A_{slot} is the area of the slot exit, κ is the specific heat capacity and R is the gas constant.

2.6.2 Blowing Ratio

The non-dimensional blowing ratio (M) is defined as a factor of slot-averaged mean density and velocity product over the density and velocity product at the main hot gas inlet plane. Clearly, this ratio is determined by comparing a pair of the fluid properties (density and velocity) at the slot exit area to the inflow region of the mainstream flow as formulated in equation (2.4). The equation can be further transformed using the mass flow rate at the slot exit, which is equal to that of the cooling inlet (i.e. mass conservation).

$$M = \frac{\overline{(\rho_c u_c)_{slot}}}{\rho_{hg} u_{hg}}, \tag{2.4}$$

Another form of blowing ratio can be expressed as follow:

$$M = \frac{\dot{m}_c}{A_{slot} \rho_{hg} u_{hg}}, \tag{2.5}$$

2.6.3 Adiabatic Film-Cooling Effectiveness and Isothermal Condition

The blade trailing-edge cooling performance along the protected wall can be expressed by an adiabatic film-cooling effectiveness (η_{aw}), which is the ratio of temperature difference between the main hot gas and the adiabatic wall surface temperature-to-the temperature difference of the hot gas and the coolant gas temperature. This ratio has been given in equation (2.1).

If the protected wall is assumed as an isothermal boundary condition, the film-cooling effectiveness (η) is calculated by referring to the wall temperature (T). The change in this definition is to differentiate between the adiabatic and the isothermal conditions.

$$\eta = \frac{T_{hg} - T}{T_{hg} - T_{c'}}, \tag{2.6}$$

2.6.4 Heat-Transfer Coefficient

The principles of the radiative heat-transfer calculation could be widely found in open literature. For this research, the convective heat-flux (q_{conv}) is obtained by subtracting the radiative heat-flux (q_{rad}) from the calculated wall heat flux (q_w) as follows:

$$q_{conv} = q_w - q_{rad} = h_f (T_{aw} - T_w), \tag{2.7}$$

where h_f is the iso-energetic heat-transfer coefficient of film-cooling, T_w is the wall temperature and T_{aw} is the adiabatic wall temperature that acquired by a wall in gas flow if the condition of thermal insulation is observed on it $q_w = 0$. It is sometimes called an *"equilibrium temperature"* and, in aerodynamics, a *"recovery temperature"*.

For determination of the adiabatic film cooling effectiveness, only convective heat transfer is of interest, which is determined as follows:

$$\eta_{aw} = \frac{T_{hg} - T_{aw}}{T_{hg} - T_{c'}} = \eta - \frac{q_{conv}}{h_{f.}\left(T_{hg} - T_{c'}\right)}, \tag{2.8}$$

where η is the diabatic film cooling effectiveness based on the actual measured wall temperatures T_w instead of T_{aw}, which is in case of the near adiabatic condition not far from η_{aw} with deviation in the range of 3 to 5% [15][16].

$$\eta = \frac{T_{hg} - T_w}{T_{hg} - T_{c'}}, \tag{2.9}$$

The iso-energetic heat-transfer coefficient (h_f) is unknown in equation (2.7), which can be derived from the superposition principles for film cooling by setting an altered wall temperature in constant flow conditions.

2.6.5 Relation between Surface Heat Flux and Non-Dimensional Temperature

The principle of superposition results in a well-known linear relationship between the surface heat-flux (q_{cond}) and the non-dimensional temperature (θ)

$$\frac{q_{cond}}{T_{hg} - T_w} = h_f\left(1 - \eta_{aw}\theta\right), \tag{2.10}$$

$$\text{where } \theta = \frac{T_{hg} - T_c}{T_{hg} - T_w}, \tag{2.11}$$

T_{aw} is the adiabatic wall temperature at the trailing-edge test plate surfaces, T_{hg} is the hot gas temperature at the main inflow plane, while T_c is the coolant gas temperature measured at the slot exit.

2.7 Vortex-Shedding and Strouhal Number

The phenomenon of vortex-shedding occurs naturally when a stream flows across a bluff body such as circular and square cylinders. It is a basic issue in fluid mechanics since the shedding frequency was measured by Strouhal in 1878 and stability analysis of von Karman Vortex Street in 1911. Several researchers noted that the mechanism of vortex

formation has not been clearly understood, despite the existence of vortex-shedding influences a vibration of structures [65], raises a resistance of fluid [66], and generates a noise [67]. Strouhal number is often used for predicting the flow around bluff body.

Among alternative methods to resolve that problem is to reduce the vortex-shedding as suggested by Hwang *et al.* [68], and Choi *et al.* [69]. The fluctuating forces on the mainstream flow could be suppressed by placing a small cylinder close to the surface of the main body. Chen *et al.* [70] evaluated a rectangular cylinder at low Reynolds numbers for reducing the vortex shedding. An improved element of suppression was proposed by Shao *et al.* [71][72]. A square cross-sectional element was placed at downstream of the main bluff body in order to reduce the vortex-shedding at high Reynolds numbers.

Figure 2–5: Vortex-shedding. [73]

In connection with reducing the vortex-shedding in a blade trailing-edge cooling, a thin thickness of this part is challenging. It is not easy to place an element close to the main body within a certain distance. A possibility model is to change the design near the trailing edge. For example, letterbox trailing-edge [40][74] or breakout slot [6][18][39] has been applied in some blades of gas turbine. It is expected to have effect on vortex-shedding formed at the mixing region. It becomes one of the interesting areas to be investigated further, mainly relating to the effectiveness of the blade TE cutback cooling.

The phenomenon of vortex-shedding can be simulated computationally using local-vortex identification criteria such as Q and λ_2 criterion [75]. The Q criterion identifies vortices with positive invariant of the velocity gradient tensor. It can be written by

$$Q = \frac{1}{2}\left(\left|\overline{\Omega}_{ij}\right|^2 - \left|\overline{S}_{ij}\right|^2 \right), \tag{2.12}$$

where $\bar{S}_{ij}$ and $\bar{\Omega}_{ij}$ are the symmetric and anti symmetric component of ∇u, respectively. $\bar{S}_{ij} = \frac{1}{2}\left(\frac{\partial \bar{u}_j}{\partial x_i} + \frac{\partial \bar{u}_i}{\partial x_j}\right)$ = the strain rate tensor, and $\bar{\Omega}_{ij} = \frac{1}{2}\left(\frac{\partial \bar{u}_j}{\partial x_i} - \frac{\partial \bar{u}_i}{\partial x_j}\right)$ = the vorticity tensor.

The Q criterion has been applied by Egorov *et al.* [22] to simulate some turbulent flow structures such as rotating cavities of gas turbines, chemical mixers, internal combustion engines, car mirrors, etc. The same Q criterion was also used by You *et al.* [76] for showing the dependency of turbulent flow structures in the instantaneous shear layer around the base flows under subsonic free stream conditions.

The characteristic of vortex-shedding can be identified by Strouhal number and frequency. Strouhal number is a non-dimensionless parameter that represents the shedding of vortices in the wake region of flow. The relation between Strouhal number and the frequency of vortex-shedding is written by

$$St = \frac{f_s \cdot D}{u}, \tag{2.13}$$

Where f_s = the shedding frequency; D = the diameter of bluff body; u = the velocity. In case of the TE cutback, the diameter is replaced by the block length of bluff body that is equal to the lip thickness (t). The displacement thickness of the boundary layer on both sides of the coolant wall (δ_{cg}) and the mainstream wall (δ_{hg}) are considered for correction of the lip thickness.

2.8 Fast Fourier Transform (FFT)

The Fourier transform of the original signal *x(t)* is given by:

$$X(i\omega) = \int_{-\infty}^{+\infty} x(t) e^{-i\omega t} dt, \tag{2.14}$$

If *x(t)* is a continuous signal which is the source of data, and N samples are denoted by $x[0], x[1], x[2], \ldots\ldots, x[k], \ldots\ldots, x[N-1]$, it can be written using the Discrete Fourier Transform (DFT) as follows:

$$X(i\omega)=\int_0^{(N-1)T} x(t)e^{-i\omega t}dt\,, \tag{2.15}$$

$$X(i\omega)=x[0]e^{-i0}+x[1]e^{-i\omega T}+\ldots+x[k]e^{-i\omega kT}+\ldots+x[N-1]e^{-i\omega(N-1)T}\,, \tag{2.16}$$

$$X(i\omega)=\sum_{k=0}^{N-1}x[k]e^{-i\omega kT}\,, \tag{2.17}$$

where

$k=0,1,2,....N-1$ and $x[kT]=x[k]$

If $e^{-i\omega kT}=W_N$, it can be rewritten $X(i\omega)=\sum_{k=0}^{N-1}x(k)\cdot W_N^{nk}$, (2.18)

where $x(k)$ = input; $X(i\omega)$ = frequency bin; W = twiddle factors

The DFT is a mathematical operation, and the FFT is an efficient *algorithm* for the evaluation of that operation. Figure 2–6 gives an example of sampled signal in the time domain (left figure), and after analyzed by the FFT in frequency domain (right figure). The peak level in frequency domain is the dominant frequency representing the characteristic of the system. Hence, this concept is very useful to identify the shedding frequencies of the dynamic mixing process between the mainstream flow and the coolant for a blade TE cooling system.

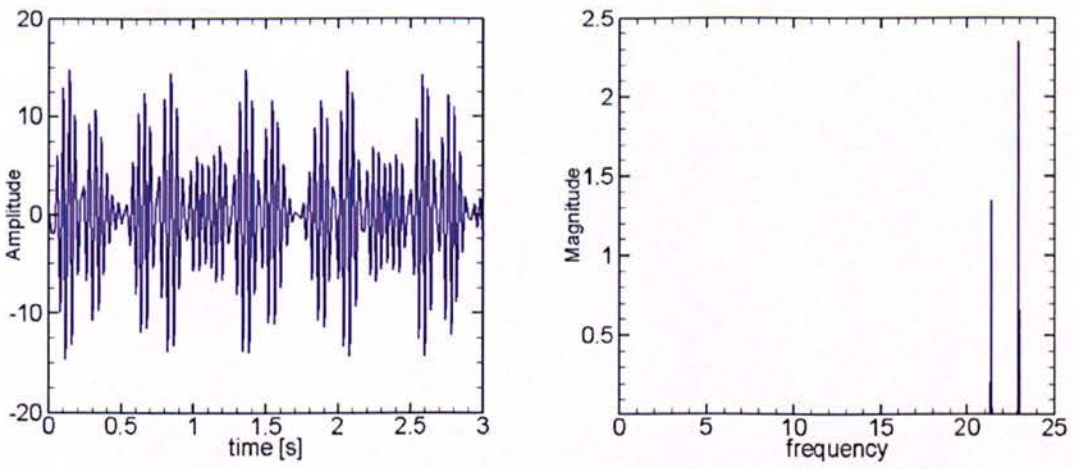

(a) Sampled signal (b) Frequency domain

Figure 2–6: An example of time domain and frequency domain based on sampled data.

2.9 Summary

Literature review and terminology related to the trailing-edge cooling of gas turbine blade have been described above. Trailing-edge cutback is an interesting region due to its geometrical constraint, in combination with aerodynamic, thermal and structural requirements. The trailing edge is particularly vulnerable to high turbine inlet temperatures because of its thin structure, which is susceptible to heavy mechanical and thermal stress. An effective TE cooling system should keep vane/blade temperature within its limit without affecting mechanical strength and aerodynamic losses. The pressure-side slot film-cooling cutback is a common method in the trailing-edge cooling.

The performance of the trailing-edge cutback cooling is usually expressed by the film-cooling effectiveness (η_{aw}) at the protected/adiabatic wall. The adiabatic film-cooling effectiveness is a key quantity that is influenced by the geometrical features inside the cooling passage, the coolant ejection angle (α), the blowing ratio (M) and the mixing flow behaviour.

The interval of the adiabatic film-cooling effectiveness is within the range of $0 < \eta_{aw} < 1$. A zero level indicates the surface temperature is close to the mainstream temperature (hot gas), while unity means the surface temperature is near the coolant temperature. A poor value of η_{aw} illustrates a strong mixing process between the mainstream flow and the coolant along the mixing region.

CHAPTER 3:

TURBULENCE MODELLING

This chapter elucidates mathematical model and turbulence modelling for this computational study. The chosen detached-eddy simulation (DES) model is given here referring to several literature. The shear-stress transport (SST $k-\omega$) turbulence model is described in more detail linking to DES.

3.1 Governing Equations

The governing equations of fluid flow represent mathematical model of the conservation laws. The governing equation is formed by the continuity equation, the energy conservation and a set of partial differential equations known as Navier-Stokes equations (see reference [77]). The three fundamental principles of conservation consist of mass, momentum and energy is given as follows:

3.1.1 Mass Conservation (Continuity Equation)

The continuity equation is based on the law of mass conservation. The general equation of the mass conservation, which is valid for incompressible as well as compressible flows, is provided by

$$\frac{\partial \rho}{\partial t}+\nabla\cdot\left(\rho\vec{U}\right)=0 \quad , \tag{3.1}$$

This equation is known to be the conservative form of mass conservation. In case of constant density, equation (3.1) could be simplified with divergence free as follow

$$\nabla\cdot\vec{U}=0, \tag{3.2}$$

3.1.2 Momentum Conservation

The momentum equation is derived from the Newton's second law of motion. The equation for the conservation of linear momentum is known as the Navier-Stokes equation. In computational fluid dynamics (CFD) literature, it is commonly used to incorporate both the momentum and the continuity equations, including the energy equation. The mathematical model of momentum conservation in conservative form is given by equation (3.3).

$$\frac{\partial}{\partial t}\left(\rho\vec{U}\right)+\nabla\cdot\left(\rho\vec{U}\vec{U}\right)=-\nabla p+\nabla\cdot\left(\overline{\overline{\tau}}\right)+\rho\vec{g}+\vec{F}, \tag{3.3}$$

where p is the static pressure, $\overline{\overline{\tau}}$ is the stress tensor, $\rho\vec{g}$ is the gravitational body force and $\vec{F}$ is the external body force per unit mass.

The stress tensor is formulated by

$$\overline{\overline{\tau}}=\mu\left[\left(\nabla\vec{U}+\nabla\vec{U}^{T}\right)-\frac{2}{3}\nabla\cdot\vec{U}I\right], \tag{3.4}$$

where μ is the molecular viscosity, I is the unit tensor

For incompressible flows, the term of the viscous stress tensor given in equation (3.4) is zero due to the incompressibility constraint given in equation (3.2), therefore equation (3.3) can be written as follows:

$$\frac{\partial}{\partial t}\left(\rho\vec{U}\right)+\nabla\cdot\left(\rho\vec{U}\vec{U}\right)=-\nabla p+\rho\vec{g}+\vec{F}, \tag{3.5}$$

3.1.3 Energy Conservation

According to the first law of thermodynamics, the rate of energy change is equal to the net rate of work done on a particle due to the surface forces, heat and body forces including gravitational effect. The energy conservation is given by

$$\frac{\partial}{\partial t}(\rho E)+\nabla\cdot\left(\vec{U}(\rho E+p)\right)=-\nabla\cdot\left(\sum_{j}h_{j}J_{j}\right)+S_{h}, \tag{3.6}$$

where h is the specific enthalpy, which is related to specific internal energy

3.1.4 State Equation

The equation of state is a mathematical model representing the physical properties of gases under pressure and temperature conditions. This equation states the relationships between one-dependent and two-independent thermodynamic properties in the unit mass system. For example, the special relation between pressure (p), temperature (T) and density (ρ) for ideal gas is given by

$$p = \rho R T, \tag{3.7}$$

where $R = c_p - c_v$ is the gas constant (R = 287.1 [J/kg K] for air).

Reynolds averaging in equation (3.7) gives

$$\bar{p} = \bar{\rho} R \tilde{T}, \tag{3.8}$$

The relation of enthalpy and internal energy to temperature can be used for ideal gas as given in equations (3.9) and (3.10), respectively.

$$dh = c_p dT \tag{3.9}$$

$$de = c_v dT \tag{3.10}$$

For compressible fluids, the equation of state makes available the relationships between the energy equation, the conservation and the momentum equations. For instance, density will be different due to the change of pressure and temperature. In case of incompressible flow, it is impossible to use the equation of state.

3.1.5 Interrelationships of Conservation Equations

In computational fluid dynamics (CFD), all conservations equations i.e. mass, momentum, and energy are coupled to be resolved simultaneously. These are connected by the equations of state for the compressible flows. Three scalar unknown i.e. density, pressure, three-velocity components, and temperature are generated by resolving six-scalar equations i.e. mass conservation, 3 components of the momentum conservation, the energy conservation, and the equations of state.

It is noted that the equation of state does not exist for the incompressible flow. Therefore, the relationships of the governing equations are not coupled by the equations of state. In practice, both the continuity and the Navier-Stokes equations are solved first in order to compute the unknown velocity and pressure without knowing temperature, and then the energy equation can be solved by itself to find temperature.

Computational solution of the incompressible flows is more complex compared to the compressible flows. Incompressible flow pressure cannot be linked to density or temperature via the equation of state. It establishes itself instantaneously in the flow field. Hence, the velocity field remains divergence free. There is no pressure term in the continuity equation, and there is only the derivative of pressure in the momentum equation. It means that the actual pressure is not important here. However, it is noted that the change of pressure in the space is highly important.

3.2 Turbulence Modelling

3.2.1 Turbulence

The motion of turbulent fluid (eddies) is an unspecified flow condition in which the diverse quantities exhibit a random variant, in space and time. The eddy of turbulent flow is influenced by Reynolds number and the existence of obstacles within flow path. A turbulent flow is commonly illustrated by the mean values and the statistical properties of their oscillations. For instance, a velocity (U) is separated into an averaged element ($\bar{u}$) and a varying time element (u') as given in equation (3.11).

$$U(\chi,t)=\bar{u}(\chi)+u'(\chi,t), \tag{3.11}$$

where the position vector $\chi=(x,y,z)$, U symbolizes the instantaneous operator, $\bar{u}$ is the mean velocity (average), and u' is the fluctuating velocity components.

Similarly, scalar quantities such as energy and pressure are expressed by

$$\phi=\bar{\phi}+\phi', \tag{3.12}$$

3.2.2 Favre-Averaged Navier-Stokes (FANS)

In engineering, the Favre-averaged Navier-Stokes (FANS) equation is commonly coupled with an eddy viscosity turbulence models. The Reynolds averaging of the instantaneous Navier-Stokes (RANS) equations results in unknown terms known as Reynolds stress. The Reynolds stress should be modelled and the process to do this known as a turbulence modelling. The RANS models are usually used in almost all numerical simulations including turbulent flows. The computational cost decreases significantly with a RANS approach.

The RANS is the motion equation of fluid flow based on time-averaged. Reynolds decomposition is a basic needed for the derivation of the RANS equations from Navier-Stokes equations which points to the separation of the flow variable and the fluctuating component. The Cartesian tensor form of the RANS equations is given by:

$$\frac{\partial \rho}{\partial t}+\frac{\partial}{\partial x_i}(\rho u_i)=0 \tag{3. 13}$$

$$\frac{\partial}{\partial t}(\rho u_i)+\frac{\partial u}{\partial x_j}(\rho u_i u_j)=-\frac{\partial P}{\partial x_i}+\frac{\partial}{\partial x_j}\left[\mu\left(\frac{\partial u_i}{\partial x_j}+\frac{\partial u_j}{\partial x_i}-\frac{2}{3}\delta_{ij}\frac{\partial u_i}{\partial x_i}\right)+\frac{\partial}{\partial x_j}\left(-\rho\overline{u_i' u_j'}\right)\right] \tag{3. 14}$$

These equations have the same general form as the instantaneous Navier-Stokes equations, where the velocities and other solution variables represent time-averaged values or ensemble-averaged. For variable-density flows, Equation (3.13) and Equation (3.14) can be interpreted as Favre-averaged Navier-Stokes equations with the velocities representing mass-averaged values.

According to Bredberg [78], RANS can be categorised into two models, the eddy-viscosity models (EVMs) and Reynolds-stress models (RSM).

3.2.2.1 Eddy-viscosity models:

The EVMs include the commonly well-known two-equation model, such as $k-\varepsilon$ model of Yang *et al.* [79] and Abe *et al.* [80]. The averaging procedure is modelled by flow

parameter (S_{ij}, Ω_{ij}) and eddy viscosity. Then, the $k-\varepsilon$ model has been expanded for new generation of the $k-\tilde{\varepsilon}$ models as known as model of Jones-Launder [81], Chien [82], Launder-Sharma [83], Hwang-Lin [84], and Rahman-Siikone [85] on typical models, respectively. Other two-equation EVMs are $k-l$ of Wolfshtein [86] and $k-\tau$ of Speziale model [87]. Further, the non-linear EVMs are developed in an effort to improve upon the deficiencies of standard EVMs. This involves higher order flow parameters such as the $k-\varepsilon-\upsilon^2-f$ model developed by Durbin [88] and the $k-\varepsilon-A_2$ model used by Suga *et al.* [89].

3.2.2.2 Reynolds-stress models:

The generation of RSMs are differential models, algebraic models, and explicit algebraic models. Numerically, RSMs are more demanding and difficult to converge, compared to EVMs.

Table 3–1: Eddy-viscosity and coefficient on development of the $k-\varepsilon$ model.

$k-\varepsilon$ models	Eddy-viscosity[a]	C_μ	C_{ε_1}	C_{ε_1}	σ_k	σ_ε
Yang-shih [79]	$\mu_t = C_\mu f_\mu k T_t$	0.09	1.44	1.92	1.0	1.3
Abe-Kondoh-Nagano[80]	$\mu_t = C_\mu f_\mu \frac{k^2}{\varepsilon}$	0.09	1.5	1.9	1.4	1.4
Jones-Launder, standard [81],	$\mu_t = C_\mu f_\mu \frac{k^2}{\tilde{\varepsilon}}$	0.09	1.55	2.0	1.0	1.3
Chien [82]	$\mu_t = C_\mu f_\mu \frac{k^2}{\tilde{\varepsilon}}$	0.09	1.35	1.8	1.0	1.3
Launder-Sharma-Yap, [83],	$\mu_t = C_\mu f_\mu \frac{k^2}{\tilde{\varepsilon}}$	0.09	1.44	1.92	1.0	1.3
Hwang-Lin [84],	$\mu_t = C_\mu f_\mu \frac{k^2}{\tilde{\varepsilon}}$	0.09	1.44	1.92	-	-
Rahman-Siikonen [85]	$\mu_t = C_\mu f_\mu k T_t$	0.09	1.44	1.92	1.0	1.3

[a]Detail derivation of the eddy viscosity including other variables are available on their reference, respectively.

Table 3–2: Eddy-viscosity and coefficient on development of the $k-\omega$ model.

$k-\omega$ models	Eddy-viscosity[b]	β^*	γ	β	σ^*	σ
Wilcox, HRN	$\mu_t = \frac{k}{\omega}$	0.09	5/9	0.075	0.5	0.5
Wilcox, LRN	$\mu_t = \alpha^* \frac{k}{\omega}$	0.09	5/9	0.075	0.5	0.5

[b]Detail derivation of the eddy viscosity including other variables are available on their reference, respectively.

Table 3–3: Eddy-viscosity and coefficient on development of the $k-\omega$ model.

$k-\omega$ models	Eddy-viscosity[c]	C_k	C_μ	$C_{\omega 1}$	$C_{\omega 2}$	C_ω	σ_k	σ_ε
Peng-Davidson-Holmberg	$\mu_t = C_\mu f_\mu \frac{k}{\omega}$	0.09	1.0	0.42	0.075	0.75	0.8	1.35
Bedberg-Peng-Davidson	$\mu_t = C_\mu f_\mu \frac{k}{\omega}$	0.09	1.0	0.49	0.072	1.1	1.0	1.8

[c]Detail derivation of the eddy viscosity including other variables are available on their reference, respectively.

3.2.3 Hypothesis of Boussinesq Approximation

The concept of eddy-viscosity is based on similarity reason, with turbulence related to the viscosity. Turbulence corresponds to the dissipation, diffusion and mixing process. Therefore, the Reynolds stress can be linked to the viscous term.

The Boussinesq hypothesis assumes that the Reynolds stress can be presented with velocity gradients. Thus, a model for the Reynolds stress could be written as:

$$-\rho\overline{u_i'u_j'} = \mu_t\left(\frac{\partial u_i}{\partial x_j}+\frac{\partial u_j}{\partial x_i}\right)-\frac{2}{3}\left(\rho k+\mu_t\frac{\partial u_k}{\partial x_k}\right)\delta_{ij} \qquad (3.15)$$

where μ_t is the eddy viscosity, and k is the turbulent kinetic energy

3.2.4 Two-Equations Turbulence Model

A two-equation turbulence model is one of the most common types of turbulence models that commonly employed by industry. These models solve two transport equations in order to obtain turbulent properties and eddy viscosity. The two standard models (i.e.

$k-\varepsilon$ and $k-\omega$) are the famous turbulence models in engineering applications with their advantage and disadvantage. The most commonly used transported variable is the turbulent kinetic energy (k), and the second transported variable is depending on the type of two-equation model, which is either the turbulent dissipation (ε) or the specific dissipation (ω). The first variable, (k), influences the energy in turbulence, whereas the second variable determines the turbulence scale within the length-scale or the time-scale.

Table 3–4: Performance comparison between $k-\varepsilon$ and $k-\omega$ model.

Two equation turbulence models	Sub-layer	Log-layer	Free-stream
$k-\varepsilon$	Robustious precise Simple	precise	Inaccurate near free shear layer
$k-\omega$	Rigid Less accurate Complicated	Length scale too large	Well-defined

The $k-\varepsilon$ model has become well known among the RANS models because it has robust formulation, it is one of the earliest two-equation models, widely documented, reliable and affordable. It also requires less computational efforts. Unfortunately, this model poses some difficulties such as over-prediction of turbulence near the stagnation point, large length scale in adverse pressure gradient flow including less capability of resolving swirling flows and curved boundary layer. Therefore, Wilcox *et al.* [90][91][92] proposed the $k-\omega$ model in an effort to resolve the deficiency of $k-\varepsilon$ model. Further, the $k-\omega$ model is developed by Peng *et al.* [93] and Bredberg *et al.* [78]. In terms of performance, Table 3–4 gives the comparison for both standard models.

3.2.5 Standard $k-\omega$ Models

From Table 3–1, the $k-\varepsilon$ model is able to predict better results in the shear layer flow, while the $k-\omega$ model is capable of generating excellent result near to the wall. This leads to development of the shear-stress transport (SST) model by considering the typical advantages of both models. The combined positive feature of both models is introduced by Menter *et al.* [94]. The $k-\omega$ model is magnified by blending function F_1, and the $k-\varepsilon$ model is added using $(1-F_2)$. The F_1 blending function would be 1 near wall region,

and switches to zero at the boundary layer where $k-\varepsilon$ model is regained. In connection with this numerical study, the shear-stress transport (SST) $k-\omega$ model is described in more detail in section 3.3.

A modification of the turbulent eddy-viscosity function is also done for the transport of the turbulent shear stress inside the boundary layer. The aim is to enhance the accuracy of flow prediction within a strong adverse pressure gradient. The SST turbulence model has shown a better prediction for flow separation compared to both $k-\varepsilon$ and $k-\omega$ models. Unfortunately, it is less capable of predicting for flow with unsteadiness such as vortex shedding.

3.2.6 Steady and Unsteady RANS

Steady RANS, often-denoted RANS, is a steady computation approach that is commonly used in engineering. In RANS, the flow properties are disintegrated into their mean and fluctuating components and integration over time (i.e. time averaging). It is different against unsteady RANS (URANS) or transient RANS (TRANS) that add an unsteady term for the momentum equation. Further details of the modelling techniques can be found in the reference texts [77] and FLUENT user manual [95].

For URANS, the usual Reynolds decomposition is employed

$$\overline{U}=\frac{1}{2T}\int_{-T}^{T}U(t)dt\,,\ U=\overline{U}+u'' \tag{3. 16}$$

The URANS equations are the usual RANS, but the transient term is added onto equations. For incompressible form

$$\frac{\partial\overline{U}_i}{\partial t}+\frac{\partial}{\partial x_j}\left(\overline{U}_i\overline{U}_j\right)=-\frac{1}{\rho}\frac{\partial\overline{P}}{\partial x_i}+\upsilon\frac{\partial^2\overline{U}_i}{\partial x_j\partial x_j}-\frac{\partial\overline{u_i''u_j''}}{\partial x_j}\,, \tag{3. 17}$$

$$\frac{\partial\overline{U}_i}{\partial x_i}=0\,, \tag{3. 18}$$

Therefore, the dependent variables are now not only a function of the space coordinates, but also a time function as follows

$$\overline{U}_i = \overline{U}_i(x,y,z,t),\ \overline{P}_i = \overline{P}_i(x,y,z,t), \text{ and } \overline{u_i''u_j''} = \overline{u_i''u_j''}(x,y,z,t) \tag{3. 19}$$

If we have the time-averaged velocity $\langle \overline{U} \rangle$, a resolved fluctuation u', and the modelled turbulent fluctuation u'', it can be derived the relationships as follows

$$U = \overline{U} + u'' = \langle \overline{U} \rangle + u' + u'' \tag{3. 20}$$

Albeit the simulation resulted by URANS are unsteady, the time-averaged flow is an interesting part.

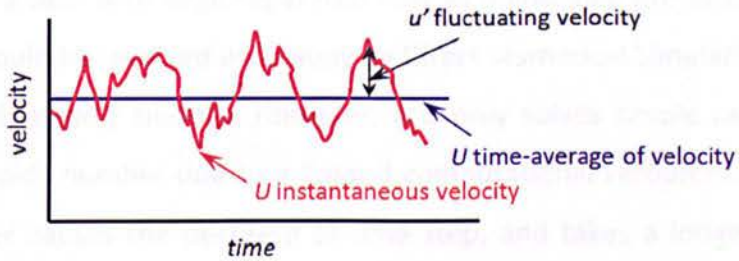

Figure 3–1: Time-average and fluctuating velocity

It is known that both steady and unsteady RANS with a proper turbulence model predict well in case of attached flow, thin shear flow, and airfoils flow. However, adverse streamwise pressure gradients probably cause small separated regions. Nevertheless, both models fail to simulate accurately in case of a massive flow separation with unsteadiness. For example, the mechanical power of a wind turbine rotor could be predicted well at high wind speeds, but not for higher wind speeds. This is due to RANS simulation produced too much viscosity that caused a delay of separation leading to a region of attached flow which is too large and the turbulence model does not correctly calculate the transport of momentum in the far-field as mentioned by Sorensen and Michelsen [96].

The capability of both steady and unsteady RANS has been applied for simulation of the trailing-edge cutback cooling, similar to the current numerical study. Several researchers reported the limited capability of steady RANS on modelling cases with unsteadiness and separation (see Holloway *et al.* [19], Martini *et al.* Martini *et al.* [20], Effendy *et al.* [21],

and Egorov *et al.* [22]). Further, various publications also noted that the unsteady RANS calculation simulated vortex shedding on the numerical study of trailing-edge cutback cooling (see Medic *et al.* [26], and Joo *et al.* [27]). Unfortunately, this achievement does not quantitatively match their experiment. Consequently, there is a gap between CFD prediction data and the experimental data as reported by Egorov *et al.* [22], Holloway *et al.* [25], Medic *et al.* [26], and Joo *et al.* [27].

3.2.7 Large Eddy Simulation (LES)

Since all turbulent scales must be modelled through a turbulence model, the steady RANS fails to simulate a case with large separated flow as mentioned previously. The scales of turbulent flow could be resolved accurately by Direct-Numerical Simulation (DNS) as long as the grid is adequately smooth. However, this only solves simple case configuration within low Reynolds number due to a limited computational resources. The increase of Reynolds number causes the decrease of time step, and takes a longer computational time.

Large-eddy simulation (LES) is seen as a compromised technique to address this issue, which is capable of overcoming the disadvantages of the RANS model. LES is spatial averaging or filtering of the Navier-Stokes equations, where the large-eddies are resolved and only the smaller-eddies are modelled by assuming isotropic turbulence. LES resolves directly when the filter length is smaller than the scales. In this situation, it is modelled using sub-grid scale (SGS) assuming that the small-eddies are more homogeneous than the larger. The governing equation is spatially filtered within the numerical grid scale. The large energy and scale is directly simulated. The small scale eddies which are generally more homogeneous and universal are modelled. The large-eddies are strongly influenced by the flow field geometry boundaries. Therefore, the computation of large-eddies by LES is more precise than the RANS modelling.

LES is widely employed in the past to simulate turbulent flow including separation. For example, the LES method has been utilized to study a subcritical flow passing a circular cylinder [97]. The focus of this computational study was to work out an extensive inspection on modelling aspects affecting the quality of LES solutions. The results noted

that two aspects, i.e. the near-wall model and the sub-grid scale model, play an important role on the modelling side.

Furthermore, the LES were carried out to investigate flow and heat-transfer for a complicated model, which was not captured on experiments. Watanabe *et al.* [98] used LES for a fully developed ribbed channel, and Viswanathan *et al.* [99] applied for a duct with rounded skewed ribs. Sewall *et al.* [100][101][102][103] evaluated the LES on developing flow and heat-transfer of a stationary/rotating ribbed internal turbine blade cooling channel, with and without considering the centrifugal buoyancy forces. Abdel-Wahab *et al.* [104][105] validated the LES Dynamic Smagorinsky model for a ribbed duct with Coriolis, buoyancy forces, and rotation. The hydrodynamic and turbulent flow phenomena were highlighted in this computational study. It was concluded that the numerical approach provides a comprehensive knowledge of the major flow structure in the flow-field. Both their computations and experiments were considered acceptable.

Similar to one of the current case study, a TE cutback with circular pin-fin inside the cooling passage has been simulated by Schneider *et al.* [28][29]. The LES method was employed for this numerical study. Both large-and-small scale structures could be captured using the LES simulation. The interrelationship between turbulent heat-transfer and large coherent structures (LCS) were visualized through well-resolved LES.

Unfortunately, similar to the DNS, the LES becomes too resource consuming when used in flow calculations involving high Reynolds numbers. The computational resource required by the LES is not significantly less when compared to the DNS. In order to overcome this deficiency, Spalart *et al.* [106] developed a new generation of eddy simulation by combining the advantages of both RANS and LES, which is known as Detached-Eddy Simulation (DES).

3.2.7.1 Subgrid-Scale:

In ANSYS Fluent, the subgrid-scale turbulence models employ the Boussinesq hypothesis as used in the RANS models,

$$\tau_{ij} - \frac{1}{3}\tau_{kk}\delta_{ij} = -2\mu_t \bar{S}_{ij} \qquad (3.21)$$

where μ_t is the subgrid-scale turbulent viscosity. The isotropic part of the subgrid-scale stresses τ_{kk} is not modeled, but added to the filtered static pressure term. $\bar{S}_{ij}$ is the rate-of-strain tensor for the resolved scale given by

$$\bar{S}_{ij} \equiv \frac{1}{2}\left(\frac{\partial \bar{u}_i}{\partial x_j} + \frac{\partial \bar{u}_j}{\partial x_i}\right) \tag{3. 22}$$

In case of compressible flows, it is fit to introduce the density-weighted filtering operator:

$$\tilde{\phi} = \frac{\overline{\rho\phi}}{\bar{\rho}} \tag{3. 23}$$

The subgrid stress tensor is formulated as follow:

$$\tau_{ij} = \bar{\rho} u_i \tilde{u}_j - \bar{\rho} \tilde{u}_i \tilde{u}_j \tag{3. 24}$$

It is split into its isotropic and deviatoric parts:

$$\tau_{ij} = \underbrace{\tau_{ij} - \frac{1}{3}\tau_{kk}\delta_{ij}}_{\text{deviatoric}} + \underbrace{\frac{1}{3}\tau_{kk}\delta_{ij}}_{\text{isotropic}} \tag{3. 25}$$

The deviatoric part of the subgrid-scale stress tensor is modeled using compressible form of the Smagorinsky model:

$$\tau_{ij} - \frac{1}{3}\tau_{kk}\delta_{ij} = -2\mu_t\left(\bar{S}_{ij} - \frac{1}{3}\tau_{kk}\delta_{ij}\right) \tag{3. 26}$$

The term of τ_{kk} can be added to the filtered pressure for incompressible, which can be re-written as:

$$\tau_{kk} = \gamma M_{sgs}^2 \bar{p} \tag{3. 27}$$

where M_{sgs} is the subgrid scale Mach number.

3.2.7.2 Smagorinsky-Lilly model:

This is a simple model, which is first proposed by Smagorinsky. The eddy-viscosity is given by

$$\mu_t = \rho L_s^2 |\bar{S}| \tag{3. 28}$$

where L_s is the mixing length for subgrid scales and $|\bar{S}| \equiv \sqrt{2\bar{S}_{ij}\bar{S}_{ij}}$.

In ANSYS Fluent L_s is computed by

$$L_s = \min(\kappa d, C_s \Delta) \tag{3. 29}$$

where κ is the von Karman constant, d is the distance to the closest wall, C_s is the Smagorinsky constant and and Δ is the local grid scale which is influenced by the volume of computational cell ($\Delta = V^{\frac{1}{3}}$).

Other models for μ_t are the Smagorinsky-Lilly model, the dynamic Smagorinsky-Lilly model, the wall-adapting local eddy-viscosity (WALE) model and the dynamic kinetic energy subgrid-scale model.

3.2.8 Detached Eddy Simulation (DES)

DES is a hybrid RANS-LES method that firstly used to resolve a turbulent flow at high Reynolds number including separated flows. This method is feasible to simulate cases with boundary layer separation, for example laminar and turbulent. This technique was first proposed by the research group of Phillipe Spalart in 1997 in an effort to overcome the limitation of the LES models [107][108][109]. The DES has been implemented to solve the near wall problem relating to eddying in shear layers.

The fundamental concept of the DES refers to one-equation model formulated by Spalart-Allmaras (SA) based on the grid resolution. The DES is a three-dimensional and unsteady numerical solution within a single turbulence model. This is a function of a sub-grid scale (SGS) model in regions where the grid density is fine enough for the LES, and as a RANS-model in regions where the turbulent length scale is less than the maximum grid size. The

unsteady RANS computed near the solid surface within the wall boundary layer, and away from the wall surface is automatically computed by the LES [110][111]. The blending factor (F) is used to control the switch between RANS and LES with a criterion as follows:

$$F = \frac{L_t}{C_{DES}\Delta}, \tag{3.30}$$

$$\text{RANS,} \quad \text{if } C_{DES}\Delta > L_t, \tag{3.31}$$

$$\text{LES,} \quad \text{if } C_{DES}\Delta \le L_t, \tag{3.32}$$

where L_t is the turbulent length scale, $C_{DES} = 0.61$, and $\Delta = \max(\Delta_x, \Delta_y, \Delta_z)$ is the maximum of local grid spacing.

Although the DES method is relatively new compared to both RANS and LES models, this approach had already been applied widely for predicting simple cases such as flow over a circular cylinder [112][113][114][115][116], airfoils [110], supersonic flow [117], and aircraft fore-bodies [63]. Further, Viswanathan *et al.* [62][64] employed the approach for investigating flow and heat-transfer in a fully developed rotating internal cooling channel. Squires *et al.* [118] applied the approach for turbulent flow over a sphere, an aircraft body, and a fighter aircraft. The DES approach gives a suitable compromise between the physical model and CPU efficiency.

As discussed in the literature reviews, the DES approach is capable of capturing the flow physic over various complex geometries [119][120]. Flow and heat-transfer in a fully developed rotating internal cooling channel was successfully simulated by Viswanathan *et al.* [64][121][122], and Martini *et al.* [23][24] used for trailing-edge cutback cooling. A strategy of meshing has also been exampled by Spalart [123].

3.3 Shear-Stress Transport $k-\omega$ Models

In the the SST $k-\omega$, the definition of turbulent viscosity is modified to account for the transport of the principle turbulent shear stress. The SST $k-\omega$ model has been developed by Menter *et al.* [94] years ago in order to integrate the robust and accurate formulation of the $k-\omega$ model in the near wall region with free stream independence of

the $k-\varepsilon$ model in the far field. The $k-\varepsilon$ model is transformed into a $k-\omega$ model with refining for the blending function, modification of turbulent viscosity, and model constant.

Near-wall treatment can be formulated for the ω equations. It changes automatically from the viscous sub-layer to wall function depending on the grid construction. In ANSYS FLUENT the value of $k-\omega$ at wall is calculated as follow:

$$\omega_w = \frac{\rho(u^*)^2}{\mu}\omega^+, \tag{3. 33}$$

Solutions of wall value, ω, can be defined analytically for both regions i.e.:

$$\omega^+ = \frac{6}{\beta_i (y^+)^2} \quad \text{, (the laminar sub-layer)} \tag{3. 34}$$

$$\omega^+ = \frac{1}{\sqrt{\beta_\infty^*}} \frac{du_{turb}^+}{dy^+} \text{, (the logarithmic region)} \tag{3. 35}$$

3.3.1 Transport Equation

In the SST $k-\omega$, the definiton of turbulent viscosity is modified to account for the transport of the principal turbulent shear-stress. The SST $k-\omega$ is similar to that of a standard $k-\omega$ model, i.e. the transport equation of turbulent kinetic energy (k) and the specific turbulent dissipation rate (ω) are formulated as follows:

$$\underbrace{\frac{\partial}{\partial t}(\rho k)}_{\text{production}} + \underbrace{\frac{\partial}{\partial x_i}(\rho k u_i)}_{\text{diffusion}} = \underbrace{\frac{\partial}{\partial x_j}\left(\Gamma_k \frac{\partial k}{\partial x_j}\right)}_{\text{prod}} + \underbrace{\tilde{G}_k - Y_k}_{\text{dissipation}} + \underbrace{S_k}_{\text{user defined}}; \tag{3. 36}$$

$$\underbrace{\frac{\partial}{\partial t}(\rho \omega)}_{\text{production}} + \underbrace{\frac{\partial}{\partial x_i}(\rho \omega u_i)}_{\text{diffusion}} = \underbrace{\frac{\partial}{\partial x_j}\left(\Gamma_\omega \frac{\partial \omega}{\partial x_j}\right)}_{\text{prod}} + \underbrace{G_\omega - Y_\omega + D_\omega}_{\text{diss cross-diff}} + \underbrace{S_\omega}_{\text{user defined}}, \tag{3. 37}$$

where ρ is the density, u_i are the velocity components, $\tilde{G}_k$ represents the generation of turbulence kinetic energy due to the mean velocity gradients, G_ω symbolizes the

generation of ω, Γ_k and Γ_ω denotes the effective diffusivity of k and ω, respectively, Y_k and Y_ω characterizes the dissipation of k and ω, D_ω indicates the cross-diffusion term, and S_k and S_ω are source terms.

3.3.2 Modelling the Effective Diffusivity

The effective diffusivities are calculated by:

$$\Gamma_k = \mu + \frac{\mu_t}{\sigma_k}, \tag{3. 38}$$

$$\Gamma_\omega = \mu + \frac{\mu_t}{\sigma_\omega}, \tag{3. 39}$$

where σ_k and σ_ω are the turbulent Prandtl numbers for k and ω, respectively. The turbulent viscosity (μ_t) is calculated by involving both k and ω as follows:

$$\mu_t = \frac{\rho k}{\omega} \frac{1}{\max\left[\frac{1}{\alpha^*}, \frac{SF_2}{a_1 \omega}\right]}, \tag{3. 40}$$

where S is the strain rate magnitude

$$\sigma_k = \frac{1}{\frac{F_1}{\sigma_{k,1}} + \frac{(1-F_2)}{\sigma_{k,2}}}, \tag{3. 41}$$

$$\sigma_\omega = \frac{1}{\frac{F_1}{\sigma_{\omega,1}} + \frac{(1-F_2)}{\sigma_{\omega,2}}}, \tag{3. 42}$$

3.3.2.1 Correction factor for a low Reynolds number:

The coefficient α* is correction factor due to low Reynolds-number correction as formulated below:

$$\alpha^* = \alpha_\infty^* \left(\frac{\alpha_0^* + \frac{\mathrm{Re}_t}{R_k}}{1 + \frac{\mathrm{Re}_t}{R_k}} \right), \tag{3. 43}$$

where

$$\mathrm{Re}_t = \frac{\rho k}{\mu \omega}, \tag{3.44}$$

$$R_k = 6, \tag{3.45}$$

$$\alpha_0^* = \frac{\beta_i}{3}, \tag{3.46}$$

$$\beta_i = 0.072, \tag{3.47}$$

$$\alpha^* = \alpha_\infty^* = 1, \text{ for high Reynolds number} \tag{3.48}$$

3.3.2.2 The blending factors:

The blending functions, F_1 and F_2, are given by

$$F_1 = \tanh\left(\Phi_1^4\right), \tag{3.49}$$

$$\Phi_1 = \min\left[\max\left(\frac{\sqrt{k}}{0.09\omega y}, \frac{500\mu}{\rho y^2 \omega}\right), \frac{4\rho k}{\sigma_{\omega,2} D_\omega^+ y^2}\right], \tag{3.50}$$

$$D_\omega^+ = \max\left[2\rho \frac{1}{\sigma_{\omega,2}} \frac{1}{\omega} \frac{\partial k}{\partial x_j} \frac{\partial \omega}{\partial x_j}, 10^{-10}\right], \tag{3.51}$$

$$F_2 = \tanh\left(\Phi_2^2\right), \tag{3.52}$$

$$\Phi_2 = \max\left[2\frac{\sqrt{k}}{0.09\omega y}, \frac{500\mu}{\rho y^2 \omega}\right], \tag{3.53}$$

where y is the distance to the next surface and D_ω^+ is the positive portion of the cross-diffusion term.

3.3.3 Modelling the Turbulence Production

3.3.3.1 The production of k :

The term $\tilde{G}_k$ represents the production of turbulence kinetic energy, and is defined as

$$\tilde{G}_k = \min\left(G_k, 10\rho\beta^* k\omega\right), \tag{3.54}$$

where G_k is defined in the same manner as in the standard $k-\omega$ model.

$$G_k = -\rho\overline{u_i'u_j'}\frac{\partial u_j}{\partial u_i}, \tag{3.55}$$

G_k is evaluated for consistence with the Boussinesq hypothesis following this equation

$$G_k = \mu_t S^2, \tag{3.56}$$

where S is the modulus of the mean rate-of-strain tensor, $S \equiv \sqrt{2S_{ij}S_{ij}}$

3.3.3.2 The production of ω:

The term G_ω represents the production of ω and is given by

$$G_\omega = \frac{\alpha}{\nu_t}\tilde{G}_k, \tag{3.57}$$

where α is given by

$$\alpha = \frac{\alpha_\infty}{\alpha^*}\left(\frac{\alpha_0 + \frac{\mathrm{Re}_t}{R_\omega}}{1+\frac{\mathrm{Re}_t}{R_\omega}}\right), \tag{3.58}$$

where α^* is referring to formulation for a low Reynolds number correction, whereas for the SST $k-\omega$ model, α_∞, is evaluated by

$$\alpha_\infty = F_1\alpha_{\infty,1} + (1-F_1)\alpha_{\infty,2}, \tag{3.59}$$

$$\alpha_{\infty,1} = \frac{\beta_{i,1}}{\beta_\infty^*} - \frac{\kappa^2}{\sigma_{\omega,1}\sqrt{\beta_\infty^*}}, \tag{3.60}$$

$$\alpha_{\infty,2} = \frac{\beta_{i,2}}{\beta_\infty^*} - \frac{\kappa^2}{\sigma_{\omega,2}\sqrt{\beta_\infty^*}}, \tag{3.61}$$

3.3.4 Modelling the Turbulence Dissipation

3.3.4.1 The dissipation of k:

The term Y_k represents the dissipation of turbulence kinetic energy, and is calculated by

$$Y_k = \rho\beta^* f_{\beta^*} k\omega, \tag{3.62}$$

In the standard $k-\omega$ model f_{β^*} is evaluated by piecewise function, and the SST $k-\omega$ model, f_{β^*} is set to be 1. Hence, it can be written $Y_k = \rho\beta^* k\omega$ for the SST $k-\omega$ model.

3.3.4.2 The dissipation of ω:

The term Y_ω represents the dissipation of ω, and is defined in a similar manner as in the standard $k-\omega$ model

$$Y_\omega = \rho\beta f_\beta \omega^2 \tag{3.63}$$

Similar to the dissipation of k, the coefficient of f_β is a constant equal to 1 for the SST $k-\omega$ model. It can be simplified by

$$Y_\omega = \rho\beta\omega^2 \tag{3.64}$$

where $\beta = \beta_i\left[1-\frac{\beta_i^*}{\beta_i}\zeta^* F(M_t)\right]$, (3.65)

For incompressible case, $\beta^* = \beta_i^*$ and for high Reynolds number, $\beta_i^* = \beta_\infty^*$

where β_i is given by

$$\beta_i = F_1\beta_{i,1} + (1-F_1)\beta_{i,2}, \tag{3.66}$$

3.3.5 Compressibility Correction

The SST $k-\omega$ model is developed by involving the standard $k-\omega$ model and the standard $k-\varepsilon$ model. It generated the diffusion term as formulated below:

$$F(M_t) = \begin{cases} 0 & M_t \le M_{t0} \\ M_t^2 - M_{t0}^2 & M_t > M_{t0} \end{cases}, \tag{3.67}$$

where

$$M_t^2 \equiv \frac{2k}{a^2}, \tag{3.68}$$

$$M_{t0} = 0.25, \tag{3.69}$$

$$a = \sqrt{\gamma RT}, \tag{3.70}$$

3.3.6 *Modification of Cross-Diffusion*

The SST $k-\omega$ model is developed by involving the standard $k-\omega$ model and the standard $k-\varepsilon$ model. It generated the diffusion term as formulated below:

$$D_{\omega} = 2(1-F_1)\rho \frac{1}{\omega \sigma_{\omega,2}} \frac{\partial k}{\partial x_j} \frac{\partial \omega}{\partial x_j}, \tag{3.71}$$

3.3.7 *Model Constants*

The constant models are:

$\sigma_{k,1}$	$\sigma_{\omega,1}$	$\sigma_{k,2}$	$\sigma_{\omega,2}$	a_1	$\beta_{i,1}$	$\beta_{i,2}$	κ	β_{∞}^{*}
1.176	2.0	1.0	1.168	0.31	0.075	0.0828	0.41	0.0828

α_1^{*}	α_{∞}	α_0	β_1^{*}	β_i	R_{β}	R_k	R_{ω}	ζ^{*}	M_{t0}	σ_k	σ_{ω}
1	0.52	1/9	0.09	0.072	8	6	2.95	1.5	0.25	2	2

3.4 DES Models

The DES concept has been studied for years by research groups as well as Boeing Commercial Airplane [107] and ANSYS-CFX [124]. At the same time, Spalart [107] used a one–equation model for developing Spalart-Allmaras model and Menter *et al.* [124] employed SST $k-\omega$ model by an adding extra blending factor in order to anticipate the activation of LES at near wall. The DES based on the SST $k-\omega$ model was tested for flow prediction of a circular cylinder, a cube and a car body [114]. Another type of DES model was developed from $k-\varepsilon$ namely DES based on realisable $k-\varepsilon$. All types DES models are available in ANSYS Fluent.

3.4.1 *The Spalart-Allmaras based DES Models*

This model is developed in an effort to replace d everywhere with a new length scale $\tilde{d}$ as formulated bellow:

$$\tilde{d} \equiv \min(d, C_{DES}\Delta) \tag{3.72}$$

C_{DES} = 0.65 is a calibration constant used in the DES model, and Δ is the maximum local grid spacing (=max(Δ_x, Δ_y, Δ_z)) in case of a Cartesian grid.

The DES length scale is redefined as follow

$$\tilde{d} \equiv d - f_d \max(0, d - C_{DES}\Delta), \tag{3.73}$$

where $f_d \equiv 1 - \tanh([8r_d]^3)$ and $r_d = \dfrac{\nu_t + \nu}{\kappa^2 d^2 \sqrt{U_{i,j}U_{i,j}}}$ (3.74)

3.4.2 The Realisable $k-\varepsilon$ based DES Models

The dissipation term of the turbulent kinetic energy (k) is modified as follow

$$Y_k = \frac{\rho . k^{\frac{3}{2}}}{l_{DES}}, \tag{3.75}$$

where $l_{DES} = \min(l_{RKE}, l_{LES})$ with $l_{RKE} = \dfrac{k^{\frac{3}{2}}}{\varepsilon}$, and $l_{LES} = C_{DES}\Delta$ (3.76)

where C_{DES} = 0.61 is a calibration constant used in the DES model, and Δ is the maximum local grid spacing (=max(Δ_x, Δ_y, Δ_z)) in case of a Cartesian grid.

In order to preserve the RANS model throughout the boundary layer, the DES length (l_{DES}) is redefined as follow

$$l_{DES} = l_{RKE} - f_D \max(0, l_{RKE} - C_{DES}\Delta), \tag{3.77}$$

In case where, $l_{DES} = l_{RKE}$, the dissipation term of the turbulent kinetic energy (k) is following the standard realisable $k-\varepsilon$ for calculating k .

3.4.3 The SST $k-\omega$ based DES Models

The turbulence dissipation term of the turbulence kinetic energy (k) is modified as described by Menter *et al.* [125]. It can be written as follow:

$$Y_k = \rho\beta^* k\omega F_{DES}, \tag{3.78}$$

where β^* is a constant (for incompressible, $\beta^* \cong \beta_i^*$ and for high Reynolds number, $\beta_i^* \cong \beta_\infty^* = 0.09$). Details equation of β_i^* and other terms can be found in reference papers by Menter *et al.* [125] and theory guide of ANSYS Fluent [95].

F_{DES} is calculated by

$$F_{DES} = \max\left(\frac{L_t}{C_{des}\Delta}, 1\right), \tag{3.79}$$

where C_{DES} = 0.61 is a calibration constant used in the DES model, and Δ is the maximum local grid spacing (=max(Δ_x, Δ_y, Δ_z)) in case of a Cartesian grid.

The turbulence length scale is defined as

$$L_t = \frac{\sqrt{k}}{\beta^* \omega}, \tag{3.80}$$

For delayed options, F_{DES} is modified as follow

$$F_{DES} = \max\left(\frac{L_t}{C_{des}\Delta}(1 - F_{SST}), 1\right), \tag{3.81}$$

where F_{SST} = 0, F_1, and F_2 are the blending function of the SST model.

3.5 Summary

The mathematical model and turbulence modelling relating to this computation has been described. The three fundamental principles of conservation and the equation of state are presented here. The RANS models are also reviewed by showing the development of two-equation models (i.e. $k-\varepsilon$ and $k-\omega$) including their advantages and disadvantages. The experience from several researchers is mentioned in terms of the capability of modelling based on steady and unsteady RANS simulation, including Large-eddy simulation (LES).

Detached-Eddy Simulation (DES) as a hybrid RANS and LES models is explained in more detail, mainly DES based on the SST $k-\omega$ model, which is applied for this numerical study. Two other DES models (i.e. Spalart-Allmaras and realisable $k-\varepsilon$) are included as comparison.

CHAPTER 4:

COMPUTATIONAL DETAILS

This chapter describes computational details including initial and boundary conditions considered in this study. Computational domain and mesh preparation are presented with key main dimensions. A blade trailing-edge (TE) cutback cooling with cylindrical pin-fin inside the cooling passage as experimentally studied by Martini *et al.* [4][5][23][24] is adopted as the computational domain. Hereinafter, this is so-called as the baseline model that made with a double-pitch distance of pin-fin array as shown in Figure 4–2. However, it is noted that the use of domain width is flexible depending on simulation case studies as mentioned in Chapter 1, considering computational costs. For example, a blade TE cutback cooling with single-pitch domain is applied for validation in chapter 5 and case studies 1 – 3 (see Chapters 6, 7 and 8), whilst a blade TE cutback cooling with double-pitch domain is considered for simulation case study 4 (see Chapter 9). Specific mesh treatments due to geometries change is described in each case as presented in Chapters 5 - 8, respectively.

4.1 Previous Experiment and Geometries

As previously mentioned in Chapter 1, this computational study refers to an experimental investigation carried out by researchers at the Institute für Thermische Strömungs-Maschinen, Baden Würtlemberg Germany. This experiment was carried out in a subsonic test facility. It was performed on a scaled-up half a blade trailing-edge model (i.e. pressure-side geometry only) integrated in an atmospheric hot wind tunnel. The specimen was scale-up by a factor of 10. It should be noted that this experiment was conducted as part of the European research project Aerothermal Investigations of Turbine Endwalls and Blades (AITEB-2) [28]. All geometries and boundary conditions were

defined by a consortium of both gas turbine manufacturers and universities in an effort to match with the engineering relevance.

Figure 4–1 gives a cross sectional view of the enlarged trailing-edge model with all main geometry dimensions. This model only considered the blade pressure-side (PS) wall as investigated by Martini *et al.* [4][5][23][24]. It had an equilaterally staggered array of pin-fins, which was predominantly used in high-pressure turbines (HP). The cooling slot had an overall width of 180 mm with the lateral pitch (S) between two pin-fins being 12 mm. In the coolant passage, the pin-fin array consisted of five rows that located in the L_1 region, whilst the L_2 region was an empty duct. The arrays were fitted in a wedge-shape duct, representing the typical trailing-edge shape. The L_3 region was the cutback area where the test plate was placed at a fixed ejection angle (α) of 10°. A nose section in the L_0 region was designed to separate the upstream near wall mainstream flow. Both the circular pin-fin diameter (D) and the cooling slot-height (H) were kept at the same value of 4.8 mm. Spanwise pitch (S) was 2.5D and streamwise pitch (S_x) was 2.167 D. This array was made by equilateral triangles.

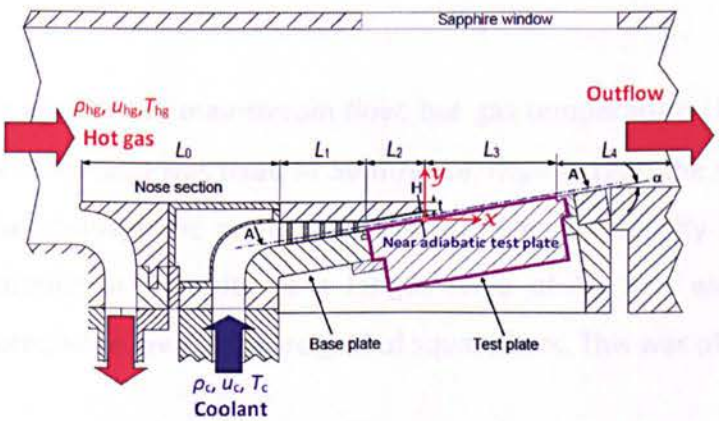

(a) side view of domain.

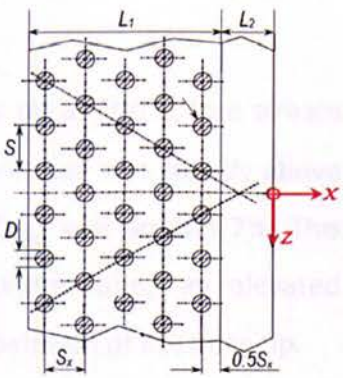

(b) section A - A

Dimension	L_0	L_1	L_2	L_3	S	S_x	t	H	D
mm	92	52	14.4	60	12	10.4	4.8	4.8	4.8

Figure 4–1: A trailing-edge cooling of gas turbine blade [4][24].

In order to obtain similar Biot number between the real engine configuration and the investigated model, both the pin-fin and the blade pressure-side (PS) wall were fabricated with high-grade steel of thermal conductivity of λ = 14 W/mK. Two different test plates

were used for the determination of film-cooling effectiveness and heat-transfer coefficients along test plate at the L_3 region. In the first test, a plastic material of low thermal conductivity of λ = 0.25 W/(mK) was used as a test plate for the blade cutback region to provide near adiabatic thermal wall conditions (i.e. L_3 region) in order to investigate the adiabatic film-cooling effectiveness [4][5]. This plate was also extended into the L_2 region in an attempt to keep the suction side (SS) wall at an adiabatic condition as well. The second test plate was made from Titanium (TiAl6V4) for the heat-transfer experiments. This extends over the L_3 region, and it was heated from the back by a temperature controlled cylinder heater [4][5][30].

4.1.1 Mainstream flow conditions

In the previous experiments [15][16], Reynolds number of hot gas mainstream flow, Re_{hg}, was fixed at 250,000. This was estimated with the density (ρ_{hg}), the free stream velocity (u_{hg}), and the viscosity (μ_{hg}) of mainstream flow. This was calculated as follow:

$$Re_{hg} = \frac{u_{hg} \cdot \rho_{hg} \cdot L}{\mu_{hg}} = \frac{u_{hg} \cdot \rho_{hg} \cdot (L_0 + L_1 + L_2 + L_3)}{\mu_{hg}}, \tag{4.1}$$

At inlet of the mainstream flow, hot gas temperature (T_{hg}) was set at 500 K, free stream velocity (u_{hg}) was fixed at 56 m/s (i.e. M_a = 0.125), the static pressure was slightly above the atmospheric at 105 kPa, and turbulence intensity level (Tu_{hg}) was around 7%. This turbulence intensity at a length scale of 10 mm was generated using an elevated turbulence level a square grid of square bars. This was placed upstream of the nose tip.

4.1.2 Coolant flow conditions

In the coolant passage, coolant air entered the inlet cavity at T_c = 293 K and turbulence intensity level (Tu_c) was around 5%. This turbulence intensity at a macroscopic length scale of 1 mm was provided by inserting a turbulence grid in the rectangular duct at the L_1 inlet region. In the tests, the coolant temperature was measured at two locations, i.e. at the inlet section of L_1 (T_c) and at the slot exit ($T_{c'}$). The references coolant of $T_{c'}$ (measured at the centre point of the slot-exit) was in a range of 295 – 330 K, depending on mass flow

rate of the coolant inlet. This coolant core temperature was referred to compute for any film cooling effectiveness presented on their work.

The density ratio (ρ_c/ρ_{hg}) was in a range of 1.5 and 1.7. Eight different blowing ratios ($M = \rho_c u_c/\rho_{hg} u_{hg}$) from 0.2 up to 1.25 were tested, resulting in a coolant Reynolds number (Re_c) of approximately 6,000 to 13,000. This was calculated using the hydraulic diameter of the ejection slots formed by the last ribs row in the cooling passage, following equation below:

$$Re_c = \frac{u_{hg} \cdot \rho_{hg} \cdot M \cdot D_{hg}}{\mu_c}, \tag{4.2}$$

where M is the blowing ratio and D_{hyd} is the hydraulic diameter of the ejection slots.

Table 4–1 gives the experimental test conditions, applied in the present work. During the tests, infrared measurement technique using IR-Thermograph was used to measure temperature at the adiabatic/protected wall surface in order to calculate the adiabatic film-cooling effectiveness.

Table 4–1: Experimental test conditions *[5][20]*

Mainstream flow		Coolant flow	
Re_{hg}	= 250,000	$T_{c'}$, $L_{2\,exit}$	= 295 – 330 K
Ma_{hg}	= 0.125	T_c, $L_{1\,inlet}$	= 293 K
u_{hg}	= 56 m/s	Tu_c	= 5%
Tu_{hg}	= 7%	M	= 0.2 – 1.25
T_{hg}	= 500 K		
P_{hg}	= 105 kPa		

4.2 Present Computational Domain

The present study is based on an experimental configuration investigated by Martini *et al.* [4][5][23][24], as shown in Figure 4–1. The computational domain includes main hot gas domain of streamwise length (L_1+L_2+L_3) as shown in Figure 4–2. This domain does not include L_4 region, which has a length of 60 mm (downstream of L_3 region) for the baseline. The coolant passage contains five rows of staggered-array cylindrical pins located at L_1

region. The arrays are fitted in a 10^{o} wedge-shaped duct, representing the shape of trailing edge that follows the angle of the coolant ejection slot. Spanwise pitch (S/D) and streamwise pitch (S_x/D) are kept the same as in the experiment. The blade trailing-edge model has a lip-thickness (t) of 4.8 mm, same as the coolant passage height (H), thus the ratio of lip thickness to coolant passage height (t/H) is 1 for this computational domain. The same t/H ratio of a trailing-edge model has been tested and simulated in previous studies using Detached-eddy Simulation (DES) based on Spalart-Allmaras model [23][24].

The coolant ejection area that known as the slot-exit (A_{slot}) is located under the lip position. This section area is depending on the slot height (H) and the width of domain in spanwise direction (see z-axis direction).

As shown in Figure 4–1, the experimental domain has a wider length in the lateral z-direction with multi-rows to reserve periodicity of the flow. It may cause a high computational cost, if using the full domain. Therefore, the computation domains only consider single-pitch (S) up to double-pitch ($2S$) in the spanwise z-direction. Figure 4–2 illustrates a computational domain for the blade TE cutback cooling with double-pitch distance of pin-fin array. Due to symmetric feature of the hot gas mainstream domain (i.e. a plain channel in the test), only half a domain height (H_{hg} = 52.5 mm) is considered in the vertical y-direction [16], same as the previous computational studies [23][24].

The 3-D computational domain associated with boundary conditions can be found in Figure 4–2(a). The key dimensions are shown in the inserted table in Figure 4–2. For this computational study, hereinafter, this configuration is named as a "baseline" of turbine blade TE cutback cooling. This domain will be used as a reference to develop other case studies. The domain, mesh and specific numerical treatments are presented in chapters 5 – 9, respectively.

With regard to the analysis of vortex-shedding frequency, two monitoring points at the same locations as the works of Martini *et al.* [23][24] are provided [x/H = 4, y/H = 1.5, z/H = 1.25] and [x/H = 4, y/H = 1.5, z/H = 0], respectively. Both points, S_1 and S_2, are illustrated with key dimensions in Figure 4–2(c). It is designed to record the mixing flow velocity (based on time domain) as a representation of unsteadiness/vortex shedding at the

mixing region. The recorded data in time domain is transformed to frequency domain using fast Fourier transform (FFT) as suggested in references [23][24][26][27].

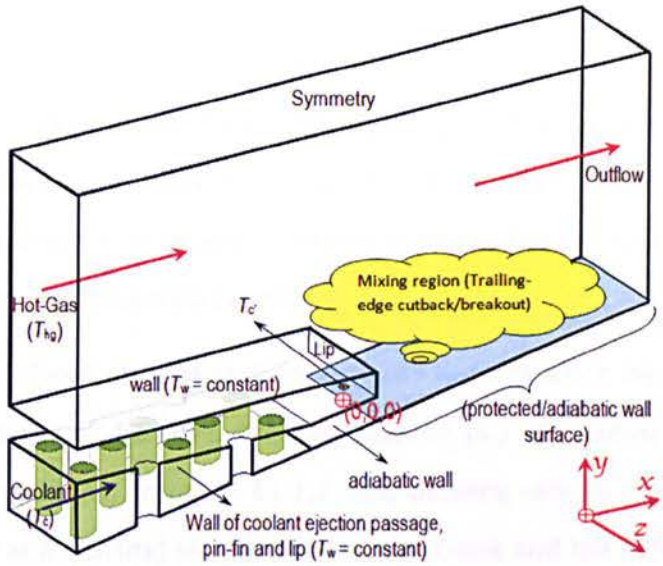

(a) The 3-D domain

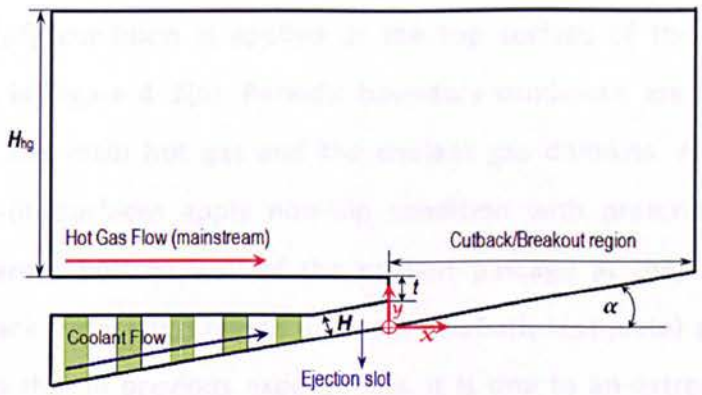

(b) The view of x-y plane

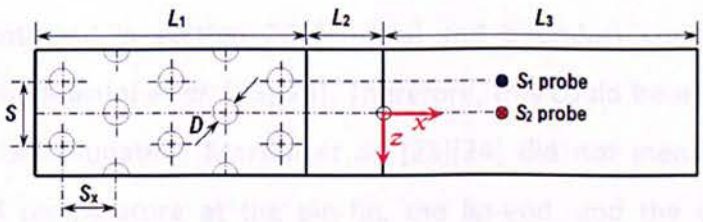

(c) The view of x-z plane

Dimensions	L_1	L_2	L_3	S	S_x	t	H	D	α
mm	52	14.4	60	12	10.4	4.8	4.8	4.8	10°

Figure 4–2: Computational domain

4.3 Flow and Boundary Conditions

All simulations of this computational study consider the same flow and boundary conditions as those of the previous researches carried out by Martini *et al.* [4][5][23][24]. The mainstream flow is set at a fixed velocity (u_{hg}) of 56 m/s (equal to Re_{hg} = 250,000), temperature (T_{hg}) of 500 K, turbulence intensity (Tu_{hg}) of 7%, and turbulence length scale of 10 mm. The operating pressure P_{hg} is set at 105 kPa slightly above the atmospheric pressure. These parameters were also used in a previous DES numerical study by Martini *et al.* [23][24] using Spalart-Allmaras model.

The coolant inflow is fixed at temperature T_c = 293 K, turbulence intensity Tu_c = 5%, and turbulence length scale of 1.5 mm. Coolant velocity (u_c) are varied from 4 to 15 m/s, subject to blowing ratio (M) from 0.5 to 1.1. The blowing ratio is calculated by the flow properties (velocity and density) measured at the slot-exit and the inflow of main hot gas. For this study, validation test is started from a lower blowing ratio of 0.5.

Symmetric boundary condition is applied at the top surface of the mainstream flow domain as shown in Figure 4–2(a). Periodic boundary conditions are employed for two sidewalls of both the main hot gas and the coolant gas domains. All of wall surfaces including the pin-fin surfaces apply non-slip condition with prescribed constant wall temperature, whereas bottom wall of the coolant passage at the L_2 region and the trailing-edge cutback surface (L_3) region (i.e. near adiabatic test plate) are assumed to be adiabatic, same as that in previous experiments. It is due to an extremely low thermal conductivity for both surfaces leading to almost adiabatic conditions [5].

As previously mentioned in section 2.5.4, initial and boundary conditions have been clearly presented by Martini *et al.* [23][24]. Therefore, this could be adopted for current numerical study. Unfortunately, Martini *et al.* [23][24] did not mention the boundary conditions of wall temperature at the pin-fin, the lip-end, and the end-wall. Another computational study by Schneider *et al.* [28][29] also did not explain this wall temperature, as well as Horbach *et al.* [30][35] and Krueckel *et al.* [14]. So far, no clarifications were provided concerning this missing. Egorov *et al.* [22] used a mean temperature of operating condition between the mainstream flow and the coolant in an

effort to provide this missing information. Precursor trial calculations are also necessary in an attempt to define a suitable wall temperature.

The initial and the boundary conditions are simplified in Figure 4–3.

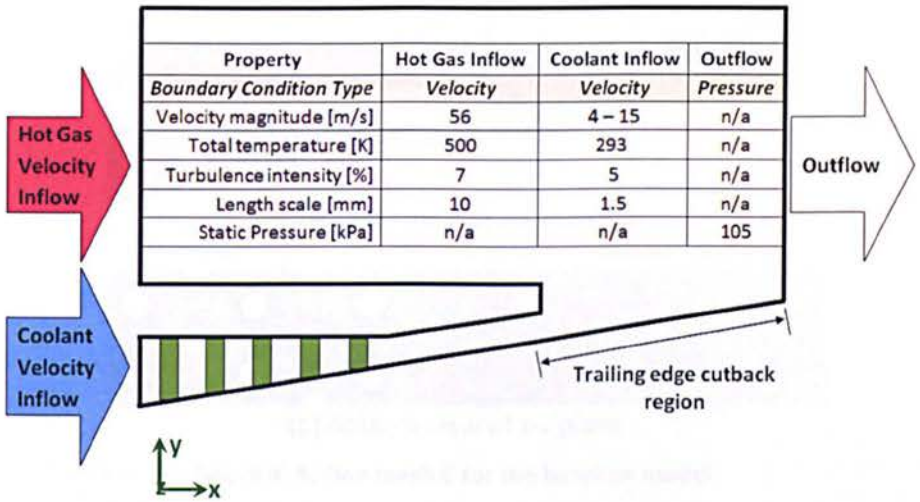

Figure 4–3: Initial and boundary conditions.

4.4 Mesh Generation

Due to the complexity of configuration inside the cooling passage of the baseline specimen, CATIA designing tool is utilized on preparing a wire-frame design of computational domain. Once the domain is created, Gambit meshing tool is used to generate block-structured meshes for both internal coolant flow and external mainstream flow domains.

Figure 4–4 gives an example of structured mesh for the computational domain as shown in Figure 4–2. A total of fifty-eight blocks are defined with forty-six blocks inside the coolant passage, and further twelve blocks in the main hot gas stream domain corresponding to L_1+L_2+L_3 regions and downstream trailing-edge region above the cutback surface. In the main hot gas domain, grid points are clustered in the near-wall of pressure-side (PS) wall surface, trailing-edge end-wall and wake region. In the coolant passage domain, grid points are also clustered around upper and bottom walls and pin-fin surfaces. It is an improvement of meshes used on the preliminary research using a blade trailing-edge model with double in-line rib array inside the cooling passage [21][32].

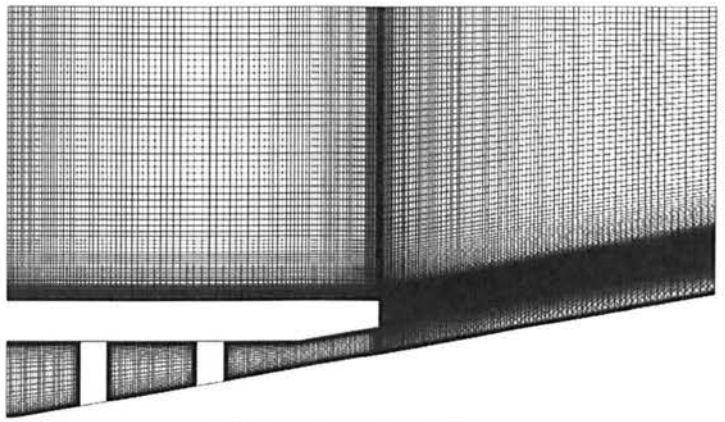

(a) Side view of *x-y plane*

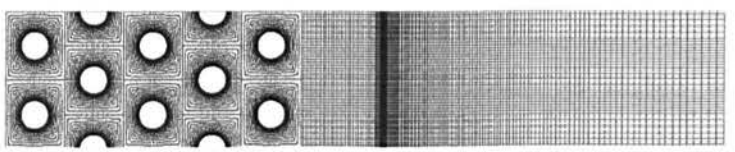

(b) Bottom view of *x-z* plane

Figure 4–4: Fine mesh C for the baseline model.

The mesh for this computation is constructed by high quality grids with $\Delta y^+ < 1$ on all surfaces. In addition, the interesting area (i.e. adiabatic/protected wall surface) is constructed in higher quality meshes with average $\Delta y^+ < 0.5$, as addressed by Nishino, *et al.* [126] in an effort to assure a sufficiently fine spatial resolution from unsteady phenomenon at the mixing region. As suggested by Spalart *et al.* [107][123] and Joo *et al.* [27], grid must be refined in each of the *x*, *y* and *z* directions in order to satisfy the blending factor as addressed by Menter *et al.* [125]. It is to be related the consistency of local grid spacing in the 3-D domain. The growth of grid spacing must be controlled linking to the requirement of blending factor (*F*) for the DES method (see chapter 3, equation (3.17) and references [110][111]).

Among many well-established wall resolution criteria, it is very important to ensure near wall viscous and thermal layers being proper resolved particularly along the cutback surface. As a comparison, Martini *et al.* [23][24] used 2.2 million hybrid structured/unstructured cells with $\Delta y_1^+ \approx 1.37$, and Egorov *et al.* [22] utilised 0.7 million structured cells with $\Delta y_1^+ \approx 1$ as shown in Figure 4–5(b) and Figure 4–5(c), respectively. As presented in Figure 4–5(a), the present mesh demonstrates a different strategy on developing mesh, which is not addressed by both researchers. It is made by structured mesh at all regions including around the pin-fins.

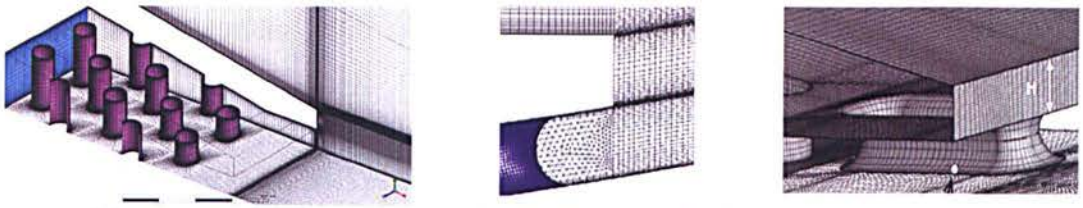

(a) Present mesh "C" (b) Martini *et al.* [23][24] (c) Egorov *et al.* [22]

Figure 4–5: Present mesh and those of previous works.

4.5 Incompressible Flow and Air Properties

A turbine blade TE cooling system could be acquired by ejecting the coolant air from the slot-exit over the TE cutback surface to form film-cooling. Simulations in this study are carried out at the same Mach number (M_a) of 0.125 as tested by Martini *et al.* [4][5][23][24] and Horbach *et al.* [30]. Due to low Mach number, it can be assumed as incompressible ideal gas behaviour. Therefore, the density only depends on the mixing gas temperature following equation (4.3).

$$\rho = \frac{P_{op}}{\frac{R}{M_w} T}, \tag{4.3}$$

where R is the universal gas constant, M_w is the molecular weight of the gas, P_{op} is the operating pressure.

Other air properties, i.e. specific heat, thermal conductivity, and dynamic viscosity, are approximated by piecewise linier functions of the temperature. This linier interpolation refers to the thermo-physical properties of air as shown in Table 4–2. The air temperature at the minimum of 293 K and the maximum of 500 K is used for the initial conditions before mixing process.

Table 4–2: Properties of air *[127][128]*.

Temperature T [K]	Specific heat Cp [J/kgK]	Thermal conductivity k [W/mK]	Dynamic viscosity μ [Ns/m^2]
293	1006.86	0.0257	1.811e-5
300	1007.00	0.0263	1.846e-5
350	1009.00	0.0300	2.082e-5
400	1014.00	0.0338	2.301e-5
450	1021.00	0.0373	2.507e-5
500	1030.00	0.0407	2.701e-5

4.6 Turbulence Models

The SST $k-\omega$ turbulence model is used for both steady/unsteady RANS and DES. A commercial CFD package, ANSYS-Fluent solver is used for these computations. A review of the SST $k-\omega$ model is described in Chapter 3. The detail of this theory can be found in reference [77].

4.7 Algorithm and Time Stepping

A finite-volume method is utilised to solve the governing equations for incompressible flow. The equations are spatially computed using second-order accuracy on multi-block structured grids, whilst it is temporally calculated with a scheme of the second-order fully implicit.

The Semi-Implicit Method for Pressure-Linked Equations Consistent (SIMPLEC) algorithm is chosen with a second-order numerical scheme applied for all flow equations (i.e. pressure, momentum, energy) of the unsteady RANS and DES calculations. Not only the grid, but also the time-step size must be small enough in an attempt to guarantee a sufficiently fine temporal resolution of the unsteady flow effects. With respect to these requirements, small time-step sizes from 5×10^{-5} to 1.25×10^{-5} seconds are applied in these computations considering the previous work carried out by Martini *et al.* [23][24].

4.8 Scenario of Numerical Studies

The trailing-edge is one area of gas turbine blades with higher heat load that needs a careful design. According to Krueckel *et al.* [14] the most important parameters for designing of trailing-edge pressure-side bleed cooling are the blockage of internal throttle feature, slot width, overhang length, pressure-side lip thickness, rotation effect and blowing rate [see Figure 1–3, page 5]. Another parameter is injection angle (α) as reported by Taslim *et al.* [31].

To address these parameters, this numerical study focuses on investigation of the blade trailing-edge cooling performance as the effect of the blowing ratio (M), the lip thickness-

to-height slot ratio (t/H), the coolant ejection angle (α), and the configuration inside the cooling passage. The existence of land extensions for both trailing-edge cutback cooling with pressure side (PS) and suction sides (SS) wall is considered here. One of Martini's models as defined in Figure 4–1 is referred to investigate these parameter changes.

In order to achieve the aim of this study as mentioned previously, this section describes the arrangement of this computational approach with the following scenarios:

4.8.1 Verification and Validation

Validation is notable on computational study in order to verify the suitability of an approach method and numerical treatments on their results compared to experimental data. A preliminary research must be valid before developing further numerical investigation on various configurations.

This research is started by grid refinement study and validation. The activities of this stage are describes as follow:

1. To prepare the baseline model of the blade TE cutback cooling as shown in Figure 4–2. In order to reduce a computational cost, this simulation only considers a single-pitch distance of pin-fins array. The use of double-pitch domain is also made for comparison. The CATIA design tool is employed for high precision design and accuracy.
2. To apply the Gambit meshing tools on constructing the structured meshes of the computational domain. Mesh is varied on three different types as illustrated using the local 2-D structured meshes around the pin-fin array (see Figure 5–2).
3. To employ the ANSYS Fluent simulation tool for verification and validation. Simulations are performed by keeping the same initial and boundary conditions as described in section 4.3 (see Figure 4–2). The shear-stress transport (SST $k-\omega$) turbulence model is applied in these computations. The assumption of working flow as explained in section 4.5 is used for this study. Several treatments such as the effect of mesh elements, the effect of wall temperature, the effect of iteration, the choice of time-step sizes (TSS), and the effect of domain size are observed here. Steady/unsteady RANS and DES are applied for those simulations. Three different

blowing ratios (M = 0.5, 0.8 and 1.1) as used by Martini *et al.* [4][5] are also used in this validation stage.

4. To assess the results of these simulations against the works of Martini *et al.* [23][24][4][5] and Horbach *et al.* [30]. The assessment is based on three criterion parameters: discharge coefficient, film-cooling effectiveness along the surface of the blade TE cutback, and vortex-shedding frequency. Numerical treatments including the results and discussion are given in chapter 5.

4.8.2 Simulation Cases

Based on the validated data, four case studies as described in chapter 1 are simulated by employing the best computation approach obtained from the validation stage. It is based on the agreement of simulation results against the experiments considering three criterion parameters mentioned above. Similarly, the CATIA design tool is used on preparation, and the Gambit meshing tools is applied on constructing the structured meshes, whilst simulations are performed using ANSYS Fluent.

The general preparation and numerical treatments for four case studies are described as follow:

Case 1 – Blade TE cutback cooling on various *t/H* ratios

1. To modify lip-thickness of the baseline model (see Figure 4–2) for providing four various t/H ratios of 0.25, 0.5, 1.0 and 1.5 (see Figure 4–6). These domains are made within a single-pitch distance of pin-fins array, and kept constant the slot height (H) of 4.8 mm.
2. To create a structured mesh for each configuration referring to the fine Mesh C as previously made for the baseline (see Figure 4–4). All are created at the same block-structured mesh as the baseline.
3. Numerical treatments including results and discussion are detailed in Chapter 6.

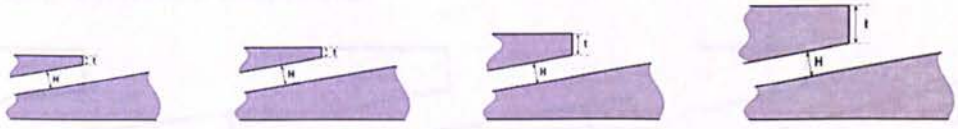

(a) t/H = 0.25 (b) t/H = 0.5 (c) t/H = 1.0 (d) t/H = 1.5

Figure 4–6: TE cutback with four various t/H ratios.

Case 2 – Blade TE cutback cooling on various obstacles inside the cooling passage

1. To modify the obstacles inside the cooling passage of the baseline model using three various designs (circular pin-fin, ellipse array, and empty duct). The variations of these pin-fins array are given in Figure 4–7. The design of the elliptical pin-fin follows the circular pin-fin in terms of layout and dimensions, meaning the coordinate systems remain unchanged. Similarly, these computational domains only consist of a single-pitch distance of pin-fins array.
2. To create a structured mesh for each configuration referring to the fine Mesh C as previously made for the baseline (see Figure 4–4).
3. Numerical treatments including results and discussion of this computation are detailed in chapter 7.

(a) Circular pin-fin (b) Streamwise elliptical pin fin

Figure 4–7: Layout of staggered pin-fin array inside the cooling passage.

Case 3 – Blade TE cutback cooling on various ejection angles (α)

1. To modify the coolant ejection angle of the baseline model with three variations at $\alpha = 5^{\circ}$, 10° and 15°. All configurations are made by keeping the cooling slot-height (H) of 4.8 mm, meaning various ejection angle is obtained by rotating the ejection slot against the reference axis of $z = 0$. Similarly, these domains are made of a single-pitch distance of pin-fins array.
2. To create a structured mesh for each configuration referring to the fine Mesh C as previously made for the baseline (see Figure 4–4).
3. Specific numerical treatments in these computations are detailed in Chapter 8, including results and discussion.

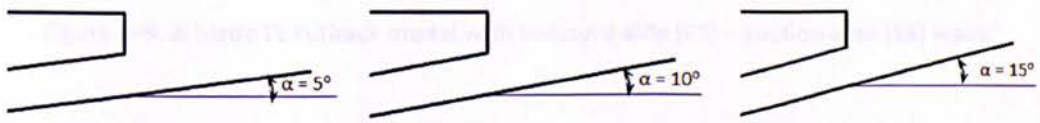

(a) $\alpha = 5^{\circ}$ (b) $\alpha = 10^{\circ}$ (c) $\alpha = 15^{\circ}$

Figure 4–8: Sketch of three various ejection angles.

Case 4 - TE cutback cooling with both PS-SS side

1. To develop a blade TE cutback model with pressure-side (PS) – suction-side (SS) side wall including land extensions. The concept is to produce a finite thickness of the blade TE cutback plate at same thickness of the coolant passage height *H* to form the turbine blade trailing edge and suction-side wall surface (see Figure 4–9). The aim is to investigate the influence of both PS and SS wall surfaces and their interactions in the near wake region. This geometry is highly dissimilar to Joo's design [26][27] that neglected the effect of internal cooling.
2. These computational domains are made of a double pitch distance of pin-fins array. It is oriented to provide a space on designing land extensions.
3. Similarly, the fine Mesh C is adopted for mesh generation.
4. Numerical treatments including results and discussion of this computation are detailed in Chapter 9.

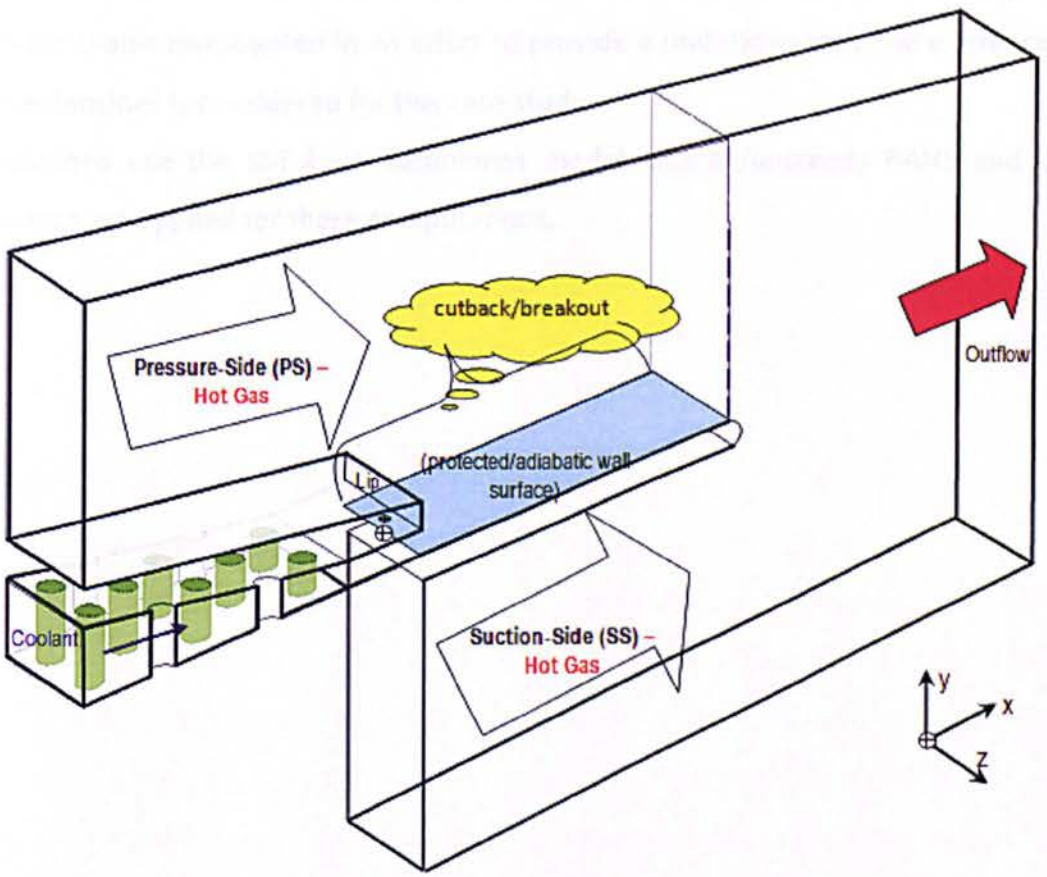

Figure 4–9: A blade TE cutback model with pressure-side (PS) – suction-side (SS) walls.

4.9 Summary

In this chapter, the initial and boundary conditions including numerical treatments have been described. It can be summarised as follows:

1. This computational study considers the same conditions as that of the works carried out by Martini *et al.* [4][5][23][24]. Due to low Mach number, in-compressible ideal gas behaviour is assumed for all of the case simulations.
2. In order to reduce the computational cost, domains of a blade trailing-edge cutback are prepared up to double-pitch distance of the pin-fin array inside the cooling passage. In addition, the structured-mesh is applied for constructing meshes.
3. Simulations are varied by considering some key parameters such as *t/H* ratios, ejection angles and internal features inside the cooling passage. Selected blowing ratios from Martini's experiments (i.e. M = 0.5, 0.8 and 1.1) are adopted as references. The influence of both pressure-side (PS) and suction-side (SS) wall surfaces is also investigated in an effort to provide a realistic model. The existence of land extensions is considered for this case study.
4. Simulations use the SST $k-\omega$ turbulence model. Steady/unsteady RANS and DES approach are applied for these computations.

CHAPTER 5:

VERIFICATION AND VALIDATION

Validation, in this regard, is notable in the context of computational studies in mind of the importance of verifying the suitability of an approach method and numerical treatments in-line with their results compared with experimental data. A preliminary research must be valid prior to developing for further numerical investigation on various configurations.

This chapter discusses the validation of computational study for a blade trailing-edge (TE) cutback cooling. The baseline domain as defined in Chapter 4 is used for verification and validation. Three types of meshes are prepared for this grid refinement study. These computations apply the same initial and boundary conditions as the previous experiments carried out by Martini *et al.* [4][5][23][24]. Simulations are performed using the SST $k-\omega$ turbulence model on three different approaches, namely steady/unsteady RANS and DES. The computations are conducted using a commercial CFD package ANSYS-Fluent. The blowing ratios as investigated by Martini *et al.* [4][5][23][24] are used in the computations.

With respect to the computational study of the blade TE cutback cooling, it is known that there are at least three key parameters, which can be assessed during validation stage, namely the adiabatic film-cooling effectiveness along the protected/adiabatic wall surface at the cutback/breakout region, the discharge coefficient and the vortex-shedding frequency. These criteria are based on the data available from the papers published by Martini *et al.* [4][5][23][24] and Horbach *et al.* [30]. During validation, the computation results are assessed against those experimental data. In terms of the adiabatic film-cooling effectiveness, post-processing is based on time-averaged data for simulations by unsteady RANS and DES.

Beside of the mesh refinement study, this validation also considers several aspects such as the choice of time-step sizes (TSS) and the effect of domain size. These aspects are observed during validation stage. The use of steady and unsteady RANS approach methods is also investigated.

5.1 The Concept of Laterally Averaged Data

In terms of the film-cooling effectiveness, the majority of analysis along the blade TE cutback/breakout in this study is based on laterally averaged calculation. This concept is needed in order to provide the same chart expression as the available measurement by Martini *et al.* [4][5][23][24] and Horbach *et al.* [30]. For example, Martini *et al.* [4][5][23][24] presented the adiabatic film-cooling effectiveness ($\overline{\eta}_{aw}$) based on an average data in *z*-axis direction along the protected/adiabatic wall surface; they also used the same methods as the paper published previously [15][16][20]. Therefore, this concept is important to be delivered here for post-processing data. The laterally averaged concept is illustrated using a sketch as shown in Figure 5–1.

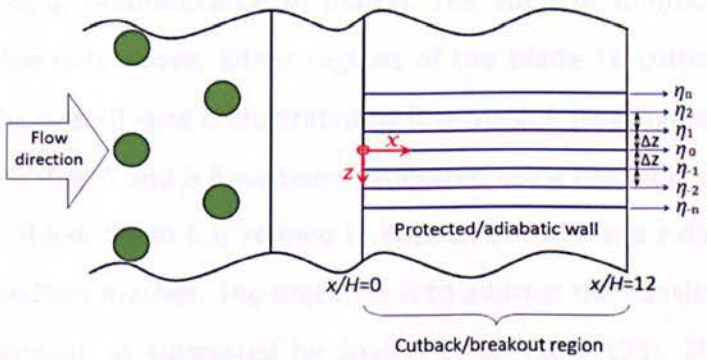

Figure 5–1: Laterally averaged concept.

Data at the protected wall surface are computed through drawing poly-lines at the same *z*-axis position along the surface with Δz = 1 mm. Distance from *x/H* = 0 to *x/H* = 12 represents the length of the protected wall surface. The number of polylines depends on the width of the domain in the *z*-axis direction. In terms of laterally averaged film-cooling effectiveness ($\overline{\eta}$), this can be formulated by equations (5.1). This would be used for other calculations of laterally averaged data, such as temperature and skin friction coefficient including other properties calculations at the mixing region.

$$\overline{\eta} = \frac{\sum_{i=0}^{n} \eta_i}{n} \tag{5.1}$$

where $\overline{\eta}$, η and n denote respectively the laterally averaged film-cooling effectiveness, the laterally film-cooling effectiveness, and the number of data.

5.2 Grid Refinement Studies

5.2.1 Meshing

As mentioned earlier, the baseline model of the blade TE cutback with circular pin-fin inside the cooling passage is chosen for validation. The validation stage is started by refinement mesh study in parallel with precursor simulation. Three types of mesh, (i.e. Mesh A, B and C), are generated to test the grid dependence.

Figure 5–2 exemplifies the local 2D structured meshes around the pin-fin array constructed by Gambit meshing tools. Both Mesh A and Mesh C have 48 and 96 elements, respectively, encircling circumference of pin-fin. The element number of Mesh B is a median of both elements above. Other regions of the blade TE cutback cooling follow these elements. The overall view is illustrated by fine Mesh C (see Figure 4–4, page 69). In similar manners, Meshes A and B have been generated using the local structured meshes as shown below. Indeed, Mesh C is refined in each of the *x, y* and *z* directions based on both coarse and medium meshes. The objective is to address the consistency of local grid spacing in a 3D domain, as suggested by Spalart *et al.* [108][123]. The growth of grid spacing must be managed linking to the requirement of blending factor (*F*) for the DES method (see Chapter 3, equation (3.30) and references [111][115]).

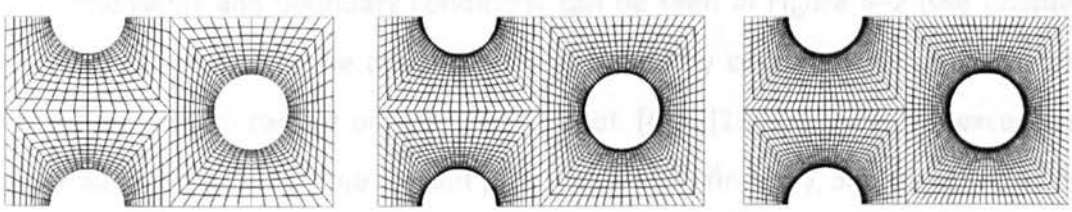

(a) mesh A (coarse) (b) mesh B (medium) (c) mesh C (fine)

Figure 5–2: Three types of mesh

Table 5–1 presents three different meshes of the baseline model, with near-wall grid resolutions in a few key areas. The grid resolution in wall units are presented for region near-wall of the pin-fin array, the end-wall of cooling passage, the pressure-side wall, the lip-end, and the protected/adiabatic wall. It has been clearly described that grid resolution is gradually refined as can be compared between them. Near the protected wall surface as a representation of the interest area is meshed by high quality grids compared to other regions. For example, Δy_1^+ is refined from 1.149 (Mesh A) to 0.257 (Mesh C) in this region.

Table 5–1: Mesh statistics

Type of Mesh	Mesh 'A'	Mesh 'B'	Mesh 'C'
Inside the cooling passage region			
pin-fin wall [a] Δy_1^+	3.764	1.098	0.907
end-wall Δy_1^+	2.776	0.861	0.749
Mainstream region			
pressure side wall Δy_1^+	4.352	1.393	0.482
lip-end wall Δy_1^+	1.501	0.746	0.607
TE cutback/breakout region			
No. of elements [b], $n_x \times n_y \times n_z$	62 × 24 × 24	93 × 36 × 36	124×48×48
protected/adiabatic wall Δy_1^+	1.149	0.401	0.257
average			
Δy_1^+	3.077	0.956	0.740

[a] an average of Δy^+ in the radial direction of pin-fins,
[b] elements at the block of TE breakout-slot/cutback region

5.2.2 Precursor Simulation

The first step of this computation is to validate an adiabatic film-cooling effectiveness along the protected/adiabatic wall. This wall surface can be viewed in Figure 5–1, whilst domain dimensions and boundary conditions can be seen in Figure 4–2 (see Chapter 4, page 66). In general, all these dimensions and boundary conditions could be obtained from the experiments carried out by Martini *et al.* [4][5][23][24], with the exception of the end-wall temperature of the coolant passage, the pin-fin array, and the lip-end. There is no specific temperature value given in their publications. They only mentioned that constant temperature boundary conditions impose on those walls and pin-fins.

As there is no wall temperature available in the literature to be used in this study, precursor simulations are carried out by considering the operating temperature of the blade TE cutback cooling tests between 293 K and 500 K (see Figure 4–3, page 68). As suggested by Egorov *et al.* [22], the mean temperature of both conditions is considered during precursor simulations. Three definitions of wall temperature (i.e. T_w = 325, 350 and 396.5 K) are applied for these computations and three types of meshes are used for mesh refinement study. Simulations are set by a small time-step size at 1.25×10^{-5} seconds in order to assure a sufficient fine temporal resolution of the unsteady effect, as suggested by Martini *et al.* [23][24]. Precursor simulations are performed at a high blowing ratio as in the experiments carried out by Martini *et al.* [23][24] and Horbach *et al.* [30].

Once numerical treatments and boundary conditions have been prepared in every case of computational domains, simulations are run with the following scenarios:

1. The first-stage simulation applies steady RANS for three types of meshes (i.e. Mesh A, Mesh B and Mesh C). One-by-one setting of wall temperature above is used in every simulation. The use of these meshes is assessed in their capability of resulting the adiabatic film-cooling effectiveness.
2. The second-stage is oriented to optimise the setting of wall temperature defined above. Similar to the first-stage, these simulations apply steady RANS.
3. Based on the mesh refinement study at the first-stage, DES is used to simulate the same variations at the second-stage.

The results are compared to available experimental data, such as those of Martini *et al.* [4][5][23][24] and Horbach *et al.* [30]. It is noted that both previous experiments use the same specimen as applied for this study.

Figure 5–3(a) provides the effect of mesh used on precursor simulations to the effectiveness of film-cooling in a selected-wall temperature (T_w) of 325 K. These charts are selected from precursor simulations on various wall temperatures and meshes, based on steady RANS. It is found that the coarse Mesh A does not produce valid data of the adiabatic film-cooling effectiveness, with both medium Mesh B and fine Mesh C resulting in a partial agreement near the slot-exit; therefore, only the adiabatic film-cooling

effectiveness data simulated using Mesh B and Mesh C could be considered for this local comparison. Both can be considered acceptable on limited prediction data between $0 < x/H < 3$ for precursor simulations using steady RANS; however, this needs to be analysed further based on Detached-Eddy Simulation (DES), as will be discussed in section 5.2.3.

Figure 5–3(b) shows the CFD prediction of the adiabatic film-cooling effectiveness ($\overline{\eta}_{aw}$) from the precursor simulations, in comparison with the measurement data by Martini *et al.* [4][5][23][24] and Horbach *et al.* [30]. Three different wall temperatures—e.g. T_w = 325, 350 and 396.5 K—have been tested using steady RANS on the fine Mesh C. The results show that the change of wall temperature has an effect to the adiabatic film-cooling effectiveness near the slot-exit, and there is almost no alteration near the downstream region. It does not predict well while setting the wall temperature (T_w) of 396.5 K. The CFD data deviate significantly near the slot-exit when compared with the measurement data. It is seen clearly that simulation by the setting of the wall temperature (T_w) of 325 K provides the correct level of the adiabatic film-cooling effectiveness near the slot-exit between $0 < x/H < 3$. It is acceptably close to experimental data, which is near unity at this limited region.

Figure 5–3(c) represents the computations of the third-stage as mentioned above. It is found that a decay of the adiabatic film-cooling effectiveness can be captured by DES. Simulation by setting wall temperature (T_w) of 396.5 K does not predict well against the experimental data, mainly near the slot-exit between $0 < x/H < 3$. This is similar to that of obtained by steady RANS in the region between $0 < x/H < 3$ (see Figure 5–3(a)). The deviation is pronounced near the slot-exit and the downstream region. The adiabatic film-cooling effectiveness is decreased by up to 10% near the slot-exit between $0 < x/H < 3$ and is over-predicted close to the downstream region between $6 < x/H < 12$, as shown in Figure 5–3(c). This implies that the adiabatic film-cooling effectiveness along the protected wall is susceptible to the change of the wall temperature at the pin-fin array, lip-end, and pressure-side including suction-side wall.

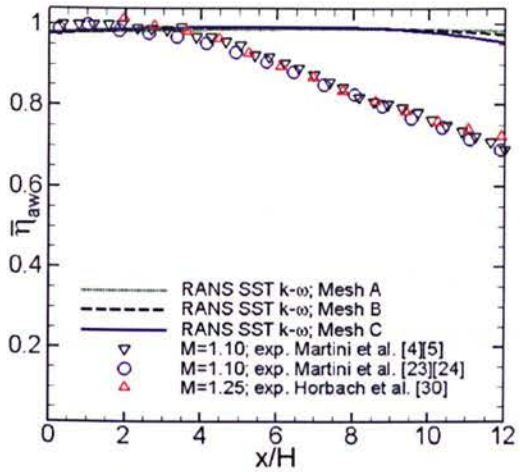

(a) Effect of mesh (steady RANS)

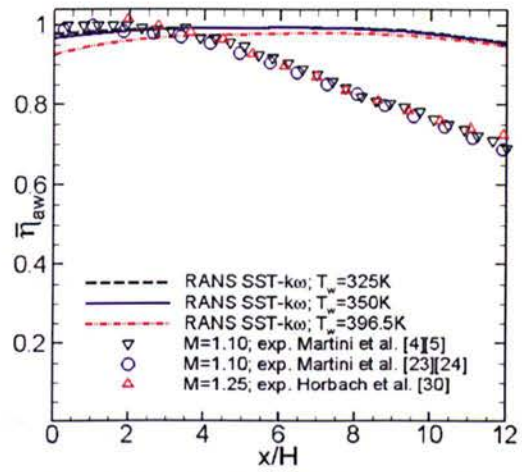

(b) Effect of wall temperature (steady RANS)

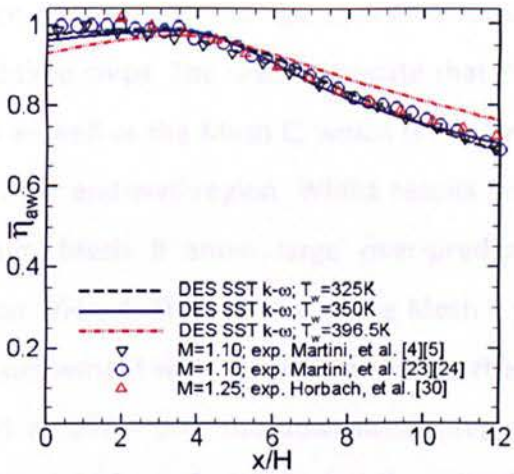

(c) Effect of wall temperature (DES)

Figure 5–3: Precursor simulation.

Based on the precursor simulations described, it can be concluded that the use of steady RANS does not predict well in terms of the adiabatic film-cooling effectiveness along the protected/adiabatic wall surface. The setting of wall temperature (T_w) has an effect to the adiabatic film-cooling effectiveness, mainly near the slot exit. DES simulation using the fine Mesh C, with a wall temperature (T_w) of 325 K, results in the correct level of the adiabatic film-cooling effectiveness, which is seen to be in good agreement with both experimental data investigated by Martini *et al.* [4][5][23][24] and Horbach *et al.* [30]. Therefore, a wall temperature at T_w = 325 K will be used for further simulations. It is noted that computations for precursor simulation only consider a high blowing ratio, which is adopted from the works of Martini *et al.* [4][5][23][24]. Further, grid refinement studies would be performed using DES by considering low and high blowing ratio as below.

5.2.3 Grid Refinement Studies

Grid refinement studies consider three successive meshes of the baseline domain from coarse to fine (see Table 5–1) at a fixed-wall wall temperature (T_w) of 325 K. The aim is to assess the adiabatic film-cooling effectiveness for three types of meshes, with considering DES simulation at low-and-high blowing ratios (M = 0.5 and 1.1). It is realised to test the grid dependence for various blowing ratios.

Figure 5–4 shows the adiabatic film-cooling effectiveness ($\overline{\eta}_{aw}$) from the grid refinement studies, in comparison with the experimental data reported by Martini *et al.* [4][5][23][24] and Horbach *et al.* [30]. These figures are based on the time-averaged data of simulations up to 3000 time steps. The results indicate that the present DES modelling requires a fine resolution as well as the Mesh C, which is fine enough to resolve the flow and heat transfer in the near end-wall region. Whilst results generated from the coarse Mesh A and the medium Mesh B show large over-prediction of the film-cooling effectiveness after position $x/H > 4$. The use of the fine Mesh C produces results that are seen to be in a very good agreement with the test data along the protected/adiabatic wall surface from the slot-exit at x/H = 0 to the downstream region of x/H = 12, with the important cooling effectiveness decay being captured successfully. The effect of mesh resolution is clear, indicated by low-blowing ratio case having largely deviation, as shown in Figure 5–4(a). The deviation is reduced for the case with a higher blowing ratio (see Figure 5–4(b)).

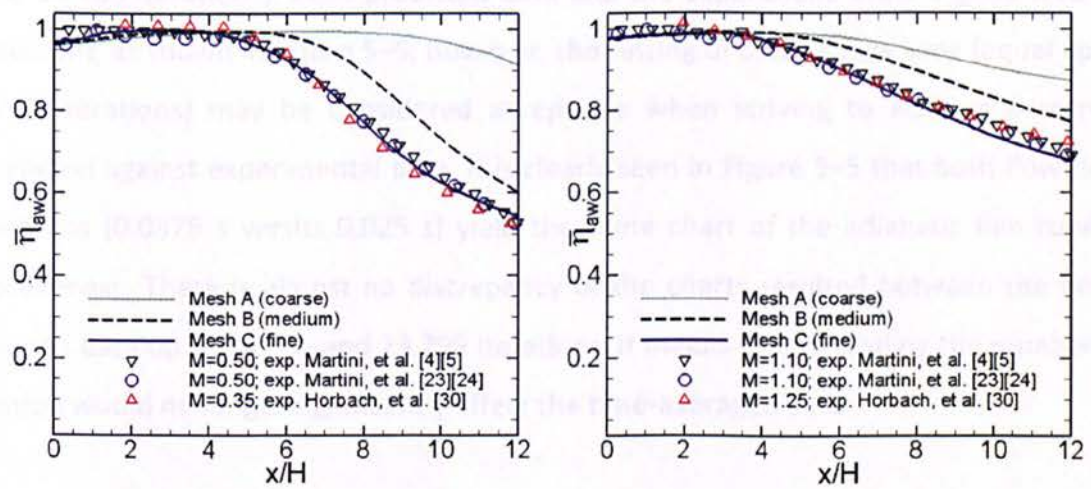

(a) Low (M = 0.5) (b) High (M = 1.1)

Figure 5–4: Grid refinement studies.

5.2.4 Effect of flow-through time studies

This section discusses the CFD data of the adiabatic film-cooling effectiveness resulting from DES for various flow time steps. The case with a low-blowing ratio as studied above is used to demonstrate an iteration effect against simulation results. Three different number of time steps (i.e. 1000, 2000 and 3000) are set in each simulation. These definitions are equal to flow time of 0.0125, 0.0250 and 0.0375 seconds with time step size of 1.25×10^{-5} seconds. It is an effort to test a simulation linking to the duration of iteration. Detached-Eddy Simulation of the baseline model indicates that a statistically stationary state condition could be achieved by setting the number of time step up to 1000, while most of these simulations are performed up to 2000 time steps. With regard to this aspect, it is important to show a reasonable iteration needed in this DES with acceptable results.

Figure 5–5 shows the CFD data on various time steps, in comparison with the experimental data carried out by Martini *et al.* [4][5][23][24] and Horbach *et al.* [30]. It has been found that a slight over-prediction data is seen at the downstream region when a case study is simulated up to 0.0125 s flow time. It is noted that this computation needs up to 12,487 iterations and a statistically stationary state condition has been achieved. This fact indicates that there is a need for more iteration when looking to improve the accumulation of time-averaged data. The trend chart of the adiabatic film-cooling effectiveness is much better after extending three times up to 0.0375 s flow time (equal up to 34,266 iterations). Both predicted data and the experiment show a good level of agreement, as shown in Figure 5–5; however, the setting of 0.025 s flow time (equal up to 23,299 iterations) may be considered acceptable when striving to achieve a correct correlation against experimental data. It is clearly seen in Figure 5–5 that both flow time definitions (0.0375 s versus 0.025 s) yield the same chart of the adiabatic film-cooling effectiveness. There is almost no discrepancy of the charts resulted between the time-averaged data up to 34,266 and 23,299 iterations. It means that extending the number of iteration would no longer significantly affect the time-averaged data.

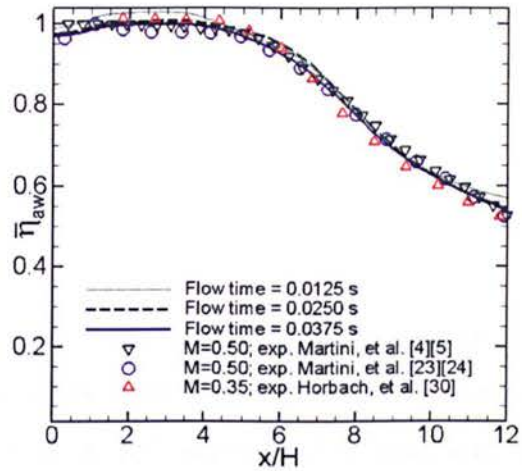

Figure 5–5: Effect of flow time.

5.2.5 Effect of Time-step Sizes (TSS)

As described in Chapter 4, a fine grid resolution is not guaranteed to obtain the correct result of unsteady simulations. A value of time-step sizes must be small enough in order to assure a sufficiently fine temporal resolution of unsteadiness. Sometimes, it is required to implement a trial-and-error process during optimisation in an attempt to achieve an exact value of time-step sizes. This aspect has been studied numerically, starting with a large time-step size of 1.0×10^{-4} up to 1.25×10^{-5} seconds in an effort to assess this effect. This range is adopted from the previous computation carried out by Martini *et al.* [23][24].

Figure 5–6 provides a comparison of the adiabatic film-cooling effectiveness for four various time-step sizes. Both numerical results using small step sizes of 2.5×10^{-5} and 1.25×10^{-5} seconds have shown a reasonable agreement against the experimental data in terms of trend and slope, with discrepancy of up to 0.62%. The use of time-step size of 5×10^{-5} seconds causes an over-prediction of the adiabatic film-cooling effectiveness by up to 2.57% at the downstream region. This is recognised due to the fact that the mode of wave flow around this region is changed owing to the effect of a larger time-step sizes. The wave flow is away over the TE cutback surface, thus causing a different mixing. Finally, wall temperature is decreased, affecting the rise of the adiabatic film-cooling effectiveness at the downstream region. The deviation widens in line with gas flow over

the TE cutback between $5 < x/H < 12$. Therefore, the discrepancy is obvious at the downstream region; however, this finding is consistent with the statement made by Martini *et al.* [23][24], where the time averaged film-cooling effectiveness on the cutback does not deviate by more than 3% for different time-step sizes between 5×10^{-5} and 1.25×10^{-5} seconds.

The use of the largest time-step size 1×10^{-4} second generates a significant over-prediction with the average deviation of up to 6.67% when compared with the use of the smallest time-step size 1.25×10^{-5} seconds. The adiabatic film-cooling effectiveness predicted is almost unity along the cutback surface. The discrepancy is very pronounced between $4 < x/H < 12$ against the experimental data; this is due to higher frequency as valuable an extent as the use of the smallest time-step sizes.

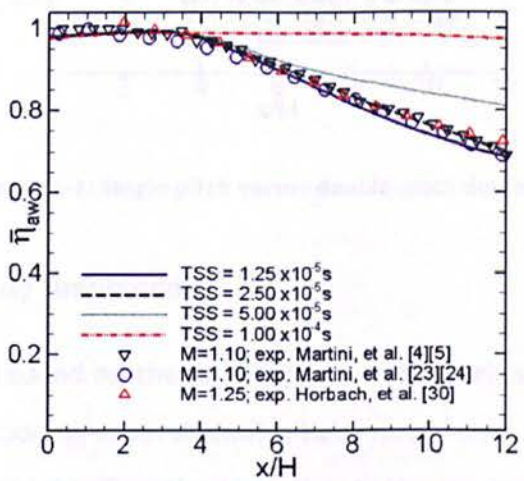

Figure 5–6: Effect of time-step sizes.

5.2.6 Single-pitch versus Double-pitch Domain

The experimental configuration has a wider length in the lateral *z*-axis direction with multi-row pin-fin inside the cooling passage arranged periodically. Using a full domain for simulation will cause a high computational cost. Two different domains of mesh, i.e. single-pitch and double-pitch of pin-fin array, have been simulated in this validation.

Figure 5–7 gives a comparison of the adiabatic film-cooling effectiveness for the use of both domains. It is found that the discrepancy is up to 1.35%. Both of them agree well against the experimental data; therefore, the use of single-pitch domain can be

considered acceptable when seeking to reduce time consumption during simulations; however, double-pitch domain will be applied for modelling the blade TE cutback cooling with the pressure-side (PS) – suction-side (SS) wall surfaces, as will be discussed in Chapter 9. This computation considers the need of design for a blade TE cutback cooling with land extensions.

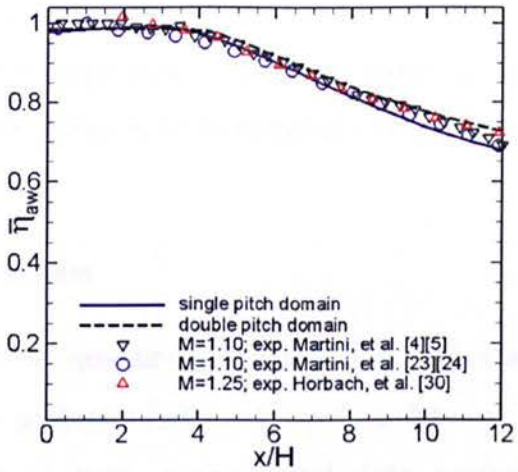

Figure 5–7: Single-pitch versus double-pitch domain.

5.3 Steady and Unsteady Simulations

Most industry CFD is still based on the RANS approach for their simulations. For example, in the case of blade TE cooling, several studies have noted that numerical analysis, using steady RANS, has tended to significantly overestimate the prediction of the adiabatic film-cooling effectiveness, as reported by various researches [20][21][22][26][27]. As simulated earlier, computations using steady RANS generate the same trend as commonly reported above. The adiabatic film-cooling effectiveness was found to be nearly unity in steady simulation, whereas laboratory test showed that it started to drops by about 0.5 near to the trailing edge at typical blowing ratio[4][5] [30]. Several researchers noted that this is to be related to in capability of steady RANS method in capturing turbulent flow structures at the mixing region. A recent study found that a better result could be achieved using unsteady RANS; however, it was a little bit sensitive in terms of inlet conditions [27].

Martini *et al.* [23][24] discovered that the DES based on Spalart-Allmaras turbulence model was capable of predicting this fluid of flow accurately; Egorov *et al.* [22], on the other hand, found a CFD prediction agreeing against test data with unsteady simulation through applying the SST-SAS turbulence model. Precursor simulations by DES simulation also yield similar correlation as those findings carried out by Martini *et al.* [23][24].

In order to show the capability of methods mentioned above, the baseline model has been simulated using three approaches i.e. steady RANS, unsteady RANS and DES. Only the case with high blowing ratios is demonstrated in this section. The simulation results are presented as follow:

5.3.1 Film-cooling Effectiveness

Figure 5–8(a) provides a quantitative comparison of the adiabatic film-cooling effectiveness along the protected/adiabatic wall surface of the blade trailing edge cutback, in comparison to both experimental data performed by Martini *et al.* [4][5][23][24] and Horbach *et al.* [30]. These charts have a direct link to temperature at the protected/adiabatic wall surface for three different methods as shown in Figure 5–8(b). DES simulation predicts well the adiabatic film-cooling effectiveness compared with both steady and unsteady RANS.

Steady RANS has significantly overestimated the adiabatic film-cooling effectiveness. The CFD data show that a film-cooling ideally protects the adiabatic wall surface. The prediction is close to 1 along with the adiabatic wall surface, with a smooth decay near the downstream region. It corresponds to the 3D steady simulation carried out by Holloway *et al.* [25], which found that the effectiveness did not fall below 1 over the length of the test plate (the adiabatic wall surface). In fact, it shows very good performance for the blade TE cutback cooling, but is not a realistic prediction against the experimental data, which decrease to approximately 0.5 near the trailing-edge at typical blowing ratios. Steady RANS only fits for predicting on partial region near the slot exit between $0 < x/H < 3$.

Over-prediction by steady RANS was established by Martini *et al.* [23][24] on their numerical studies using the $k-\omega$ model, and present author for steady RANS

computations using various turbulence models, such as $k-\varepsilon$, realisable $k-\varepsilon$, $k-\omega$ and SST. [21]. Over-predictions were also noted by Medic *et al.* [26], Joo *et al.* [27] and Egorov *et al.* [22] on their RANS studies. The reason for the large over-prediction by RANS-based modelling is probably owing to its inability to capture the dynamic process of the 'hot-cold' gas mixing that should exhibits the tendency to 'attract' the hot gas towards the wall surfaces, thus causing the rapid decay of the film-cooling effectiveness. Unsteady vortex shedding is not captured in the 3D steady simulations.

A better prediction is shown by unsteady RANS in Figure 5–8(a). It has been found that the decay of film-cooling effectiveness can be obtained from partial over-prediction between $4 < x/H < 12$, with up to 3.61% discrepancy against data predicted by DES. The predicted data near the downstream region are just over up to 10% compared with the experimental data; however, the graph trend is similar. A more intensified vortex shedding and wakes resulted by unsteady RANS may contribute to this improvement.

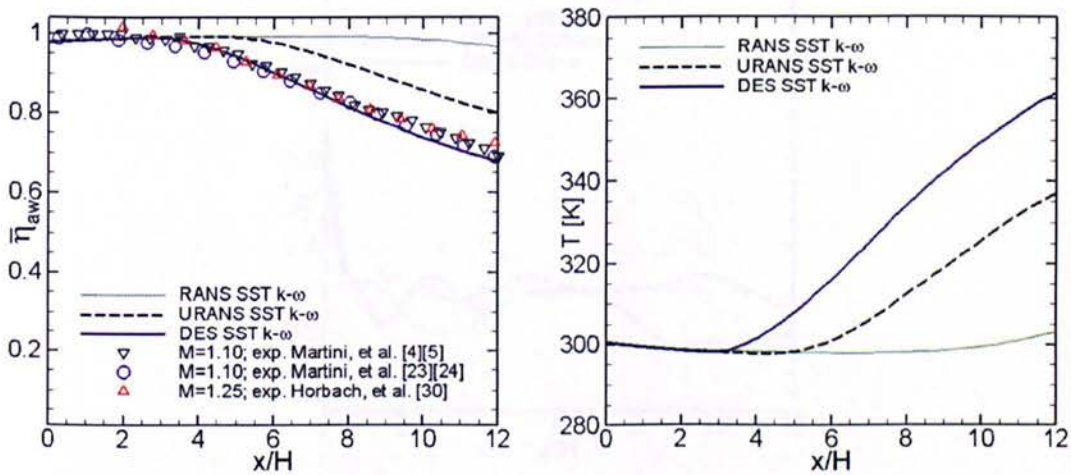

(a) Film-cooling effectiveness (b) Temperature

Figure 5–8: Laterally averaged data at the protected wall.

Another approach—the current DES—has predicted well compared to both the steady RANS and unsteady RANS. It produces a significant stronger mix of the two gas streams due to the resolved strong turbulent mixing behind the blunt pin-fin array and the lip. A strong mixing behind the lip is indicated by the turbulent flow structures (see Figure 5–15(c)). Such unsteadiness has an important role to play in the mixing process between the mainstream flow and the coolant, as stated by Holloway *et al.* [19][25]. Moreover,

Horbach *et al.* [30][35] noted that vortex shedding from the blunt ejection lip causes a decay of film-cooling effectiveness. Through Detached-Eddy Simulation (DES), wave flow can be captured more realistically—similar to the real mixing flow—whilst unsteady RANS do not simulate turbulent flow structures as well as DES computation. This is consistent with investigation performed by Krueckel *et al.* [14], where CFD using DES simulation proved to be a useful approach to back-up experimental data.

5.3.2 Wall-bounded Flow (Δy^+)

In this section, a non-dimensional wall distance for a wall-bounded flow (Δy^+) is also presented for the completion of the analysis of film-cooling effectiveness at the adiabatic wall surface. Figure 5–9(a) shows that Δy^+ predicted for all approach models is at almost similar levels along the adiabatic wall surface. The use of fine Mesh C for all models results in the characteristic of $\Delta y^+ < 1$. It proves that there is a fine grid resolution.

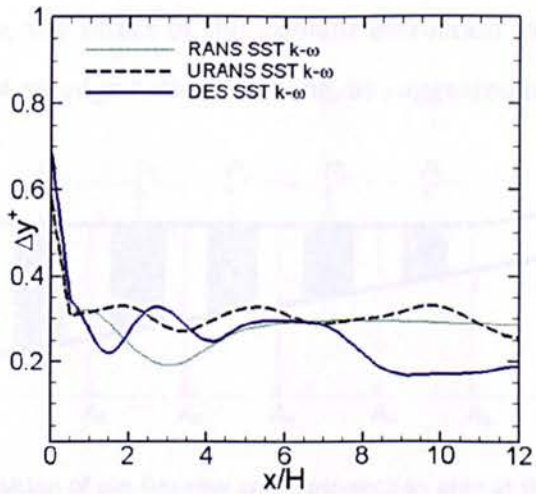

Figure 5–9: Resolution at the protected wall.

The lower value of local kinematic viscosity near the slot-exit causes a higher level of Δy^+ compared to other regions, but does not affect the predicted data from DES simulation. This is due to near the slot exit region, which is dominated by coolant gas that is far from an unsteady effect of mixing process between mainstream flow and coolant. The correlation of Δy^+ is formulated as follows:

$$\Delta y^+ \equiv \frac{u_* y}{\upsilon} \tag{5.2}$$

where u_* is the friction velocity at the nearest wall, y is the distance to the nearest wall and υ is the local kinematic viscosity of the fluid.

5.3.3 Internal Cooling Passage

The discussion of this part is aimed at assessing the heat transfer process within the cooling passage for three different methods applied in the validation stage. The dominant cause of the adiabatic film-cooling effectiveness is determined according to whether it comes from the internal passage or external region.

Figure 5–10 illustrates a side view of the internal cooling from inflow to the slot-exit region. The five rows staggered array of cylindrical pins (P_1 – P_5) and seven sections location (A_1 – A_7) are described below. These positions will be used for results comparisons, mainly to investigate the coolant flow behaviour inside the cooling passage. This information is very useful due to pin-fins array commonly being coupled with trailing-edge ejection. Therefore, the effect of this coolant extraction must be considered when investigating a blade trailing-edge cutback cooling, as suggested by Han *et al.* [12].

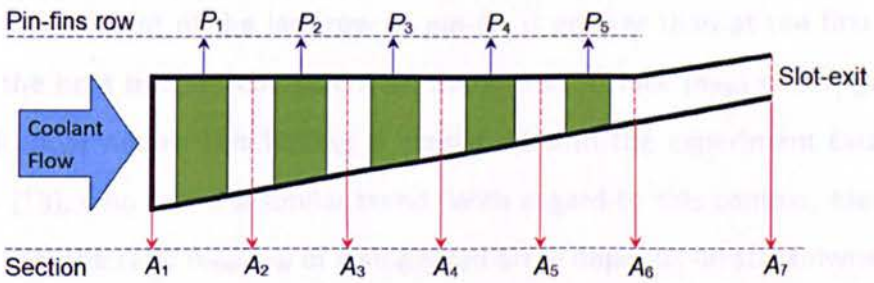

Figure 5–10: Position of pin-fins row and cross-section area at the cooling duct.

Figure 5–11 shows the characteristic comparison of the Δy^+ and skin friction coefficient (C_f) at the surface of pin-fins array (P_1 – P_5) for three numerical approaches, i.e. steady RANS, unsteady RANS and DES. Both are based on the averaged-data at the pin-fin wall surface. It has been found that all various computation methods produce the same data in each pin-fin array for both characteristics. This proves that all simulations are taken exactly at the same grid quality in an attempt to assure a correct heat transfer process within the cooling passage before ejecting coolant through the slot-exit. On the other side, both characteristics are increased following the order of pin-fins rows. The increase

of Δy^+ is caused by increasing the coolant flow velocity around the pin-fin array due to channel contraction, whereas skin friction coefficient rises by increasing the wall shear at the surface of pin-fins array, which is triggered by rising the coolant flow velocity.

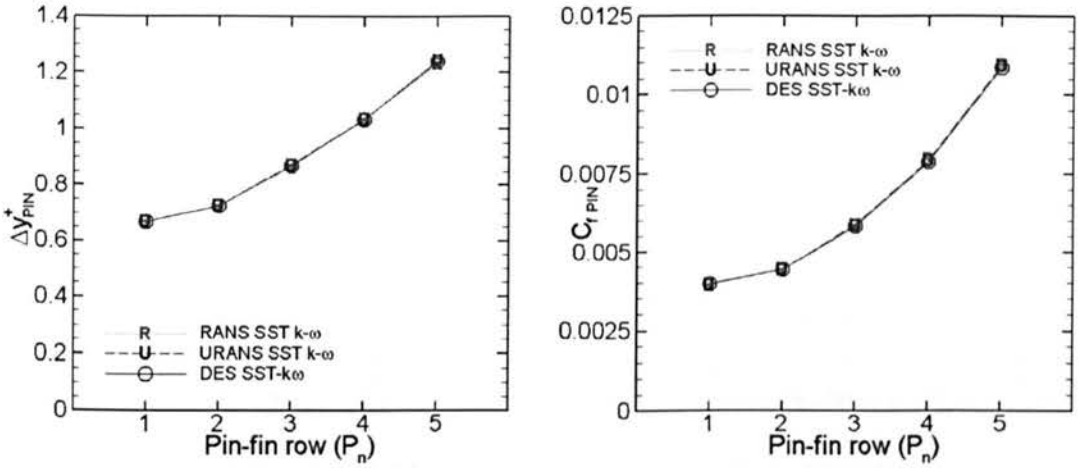

(a) Δy^+ (b) Skin friction coefficient

Figure 5–11: Δy^+ and skin friction coefficient.

Figure 5–12 shows the averaged-heat transfer and temperature of pin-fin wall surface inside the cooling passage. Slight discrepancies are witnessed for these parameters. The heat transfer coefficient of the last row of pin-fin is greater than at the first row up to 29%, whilst the heat transfer coefficient on the pin-fin surface (h_{PIN}) is 58% greater than the end wall (h_{EW}) values. This finding is consistent with the experiment carried out by Tarchi *et al.* [13], who found a similar trend. With regard to this context, Metzger *et al.* [129] noted that the ratio h_{PIN}/h_{EW} of a staggered array depends on streamwise pitch (S_x). The averaged heat transfer coefficient at the surface pin-fin inside the cooling passage is increased moderately, as shown row-by-row in Figure 5–12(a). This change is in a row with increased surface heat flux of pin-fin array and decreased temperature of surface pin-fin, which is concomitant with coolant flow inside the cooling passage (see Figure 5–12(b)). It indicates that the existence of pin-fin cooling is important in terms of keeping down temperature around this region. This also agrees well with the previous experiment done by Cunha *et al.* [18] and Tarchi *et al.* [13], which reaches a maximum of heat transfer coefficient at the last row of pin-fin array. The increase of heat-transfer coefficient is minor after the fourth row of pin-fin array. The flow velocity after the fifth

rows of pin-fins (i.e., in the throat section) tends to decelerate due to the enlarged free spacing in the L_2 region without existing ribs.

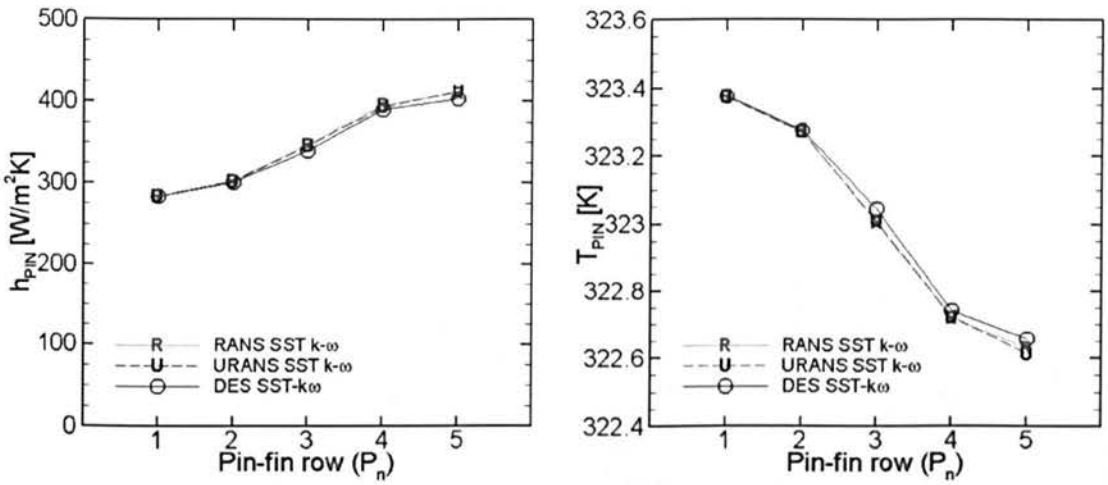

(a) Heat transfer coefficient (b) Temperature

Figure 5–12: Heat transfer coefficient and temperature.

Figure 5–13 shows the characteristic of the coolant flow inside of the cooling passage for all various methods. These values are based on the averaged data at the cross-section area ($A_1 - A_7$), as defined in Figure 5–10. It has been found that the coolant flow is more turbulent due to the combined effect of pin-fin array and converging passage. The wedge-shape duct construction influences the local coolant velocity around the pin-fin array. It implies that the motion of coolant air through pin-fin affects the near wall turbulent flow structures and its development.

By comparing Figure 5–13(a) and Figure 5–13(b), the velocity and temperature of coolant increase gradually between $A_1 - A_6$, and then decrease after reaching the peak level in the wedge channel. Both velocity and temperature decline when passing channel amongst $A_6 - A_7$. A slight discrepancy of temperature is seen on the typical method when ejecting coolant at the slot-exit (A_7). This differentiation is caused by the growth of turbulence kinetic energy, as shown in Figure 5–13(c).

Based on Figure 5–13, the coolant flow inside the cooling passage tends to show in similar behaviour for three various methods. The difference of the adiabatic film-cooling effectiveness, as discussed previously in Figure 5–8(a), is probably caused by the 3D unsteadiness formed at the mixing region. The biggest contribution comes from the

discrepancy of vortex shedding, resulting from various methods. It is obvious that there is a significant discrepancy of turbulent flow structures, as shown in Figure 5–15. However, the development of turbulence kinetic energy inside the cooling passage also cannot be negligible when ejecting coolant at the mixing region. The intensity of both aspects, as mentioned above, contributes to the intension of mixing between the mainstream flow and the coolant along the breakout region.

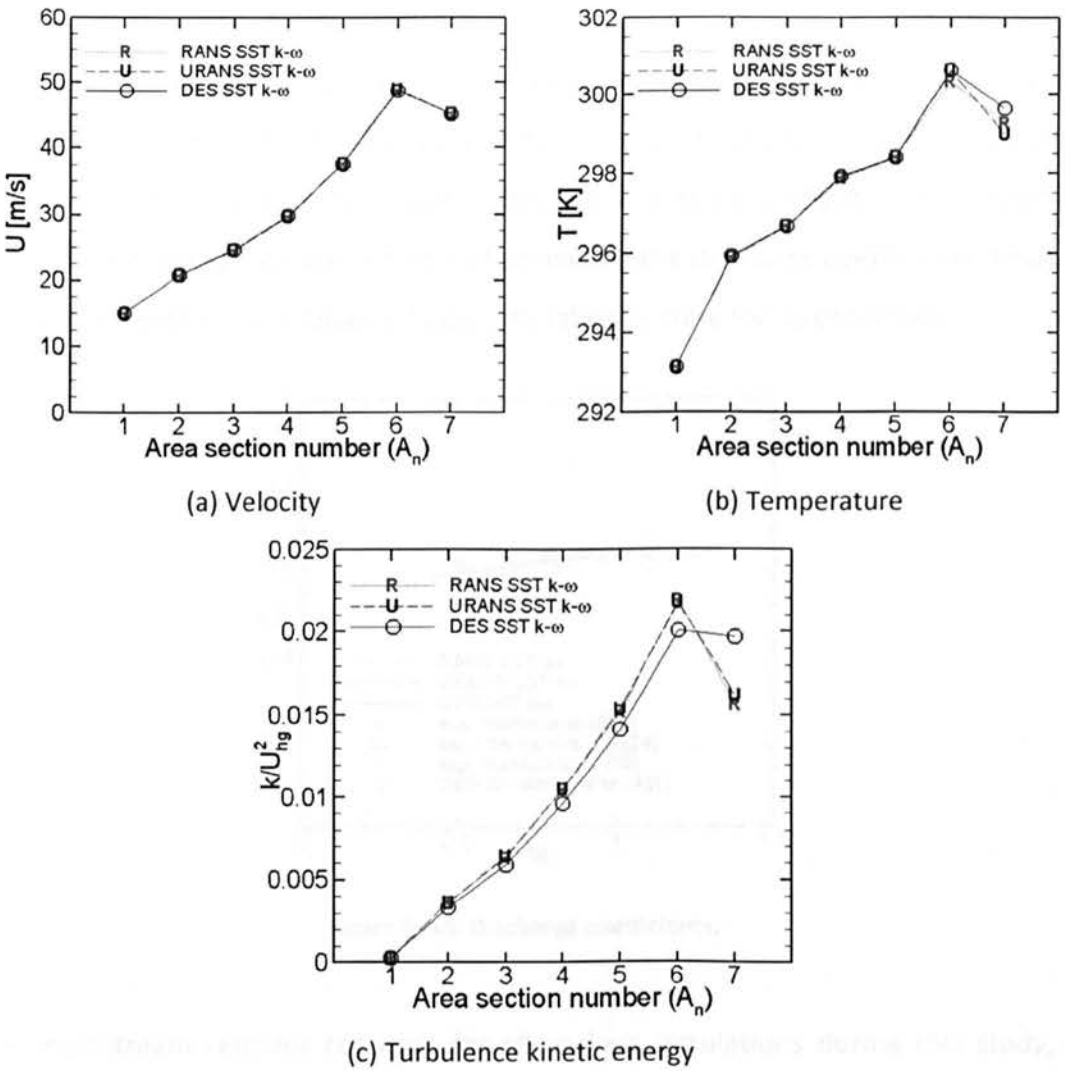

(a) Velocity

(b) Temperature

(c) Turbulence kinetic energy

Figure 5–13: Coolant flow behaviour inside the cooling passage.

5.3.4 Discharge Coefficient (C_D)

The discharge coefficient represents the discharge behaviour of the blade trailing-edge cooling slots. It quantifies the global pressure loss within the cooling passage. It reveals the actual coolant mass flux to the ideal mass flux as the effect of an isentropic expansion

from upstream region against free-stream at the ejection slot. The discharge coefficient is given in equations (2.2) and (2.3).

Figure 5–14 shows the predicted discharge coefficients (C_D) for three different blowing ratios using various methods, in comparison with the experimental measurements. The predicted data are plotted versus the blowing ratios (M). It has been found that simulation results using both steady RANS and DES are in good agreement with the experimental data. This implies that the same properties of coolant inside the cooling passage could be predicted well by both methods. The proximity data predicted for both manners justify the studies conducted by Martini *et al.* [23][24], which emphasise that there is no need for a costly DES analysis. This is due to the use of both steady RANS and DES being in a close agreement in terms of predicting the discharge coefficients; however, the prediction will be more reliable if DES simulation is done for C_D prediction.

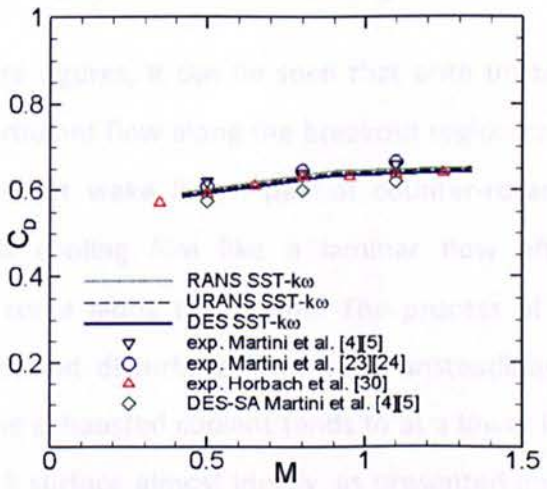

Figure 5–14: Discharge coefficients.

As the mainstream remains constant for all various simulations during this study, the increase of blowing ratio provided by raising the coolant flow velocity at the inlet causes the increase of Reynolds number at the slot-exit. The change of blowing ratio is proportional to the change of the real coolant mass flow. The discharge coefficient is increased slightly by increasing the blowing ratios. This finding is consistent with the works of Martini *et al.* [23][24], which show that the coefficient of discharge is increased by raising the Reynolds number at the coolant flow. This invention confirms the right

finding of adiabatic film-cooling effectiveness, which also has a sound suitability result, as discussed above. Hence, three case studies of validation, using the baseline, are reasonable for development for further investigation, such as blade TE cutback with various lip-thicknesses, blade TE cutback with various ejection angles, blade TE cutback with various pin-fin arrays and blade TE cutback with both pressure-side (PS) – suction-side (SS) wall surfaces.

5.3.5 Flow Structures

Figure 5–15 gives a qualitative side-view of the flow structures at the breakout region, superimposed by streamlines of main hot gas velocity and the cooling jet stream exhausted from the slot-exit. Iso-surfaces of $\Omega^2 - S^2 = 10^5$ [$1/s^2$] is used to visualise the turbulent flow structures, and is coloured by the gradation of time-averaged non-dimensional temperature (θ) distribution, with scaling as inserted in Figure 5–15.

Through comparing these figures, it can be seen that both unsteady RANS and DES are capable of simulating turbulent flow along the breakout region compared to steady RANS that only generates a short wake like a pair of counter-rotating vortex. The steady computation predicts a cooling film like a laminar flow after $x/H = 4$. Inherent unsteadiness does not come along this region. The process of heat transfer near the adiabatic wall occurs without disturbing from a big unsteadiness, such as in unsteady simulation; therefore, the exhausted coolant tends to at a lower level along the breakout that protects the cutback surface almost ideally, as presented quantitatively in Figure 5–8(a). Unfortunately, however, this is not a realistic prediction due to laboratory tests, such as Martini *et al.* [4][5][23][24] and Horbach *et al.* [30], who indicate decay by about 0.5 near the trailing edge at typical blowing ratios.

As explained previously, the unsteady computation captures the flow structures over the entire breakout of blade TE cutback. It is indicated using Figure 5–15(b) and Figure 5–15(c) for prediction using unsteady RANS and DES, respectively. Both have a different flow structures, including the mode of wavy flow and their intensity. It causes a discrepancy of temperature distribution of mixed air along the breakout region, which influences the laterally averaged film-cooling effectiveness. It can be seen clearly in Figure

5–15(b) that the scope of coolant ejection, as predicted by unsteady RANS, is greater than that of DES simulation, mainly near the downstream region. Comparing the time-averaged non-dimensional temperature of both, the cooling film is more spacious in shielding the adiabatic wall from the invasion of mainstream flow, as indicated by the domination of coolant with a lower temperature in Figure 5–15(b). Therefore, the predicted film-cooling effectiveness from unsteady RANS is greater than the prediction by DES. Unfortunately, however, this achievement is over-predicted compared against the experimental data (see Figure 5–8(a)), whilst DES predicts well against the experimental data. It is probably that the DES simulation can capture more realistically the coherent structures of the vortex shedding along the test plate of the cutback blade trailing-edge like a real phenomenon in the experiment.

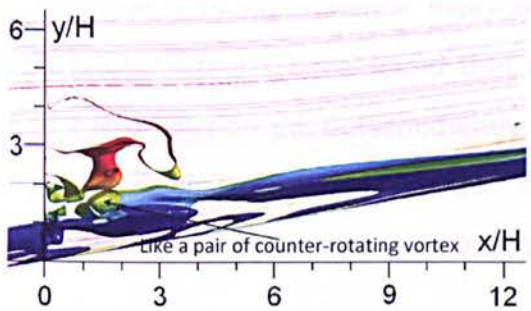

(a) Steady RANS (the 225th iteration)

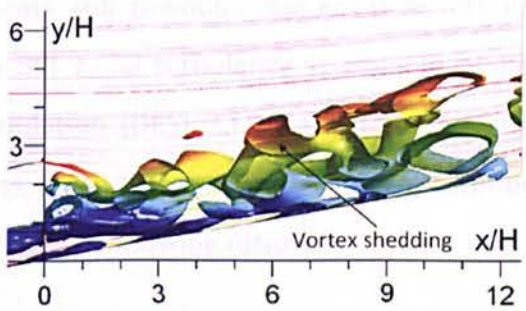

(b) Unsteady RANS (Time steps = 2000; Flow time=0.025s; 18,665th iterations)

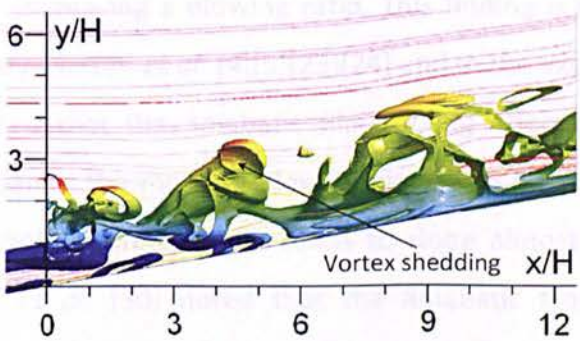

(c) DES (Time steps = 2000; Flow time = 0.025s; 24,018th iterations)

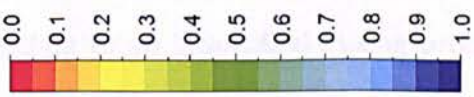

Figure 5–15: Flow structures.

In terms of flow velocity, streamlines are used to visualise the distribution of flow velocity from the mainstream flow and the ejection coolant. The flow velocity is coloured by gradation from a low value of 0 (in blue) to a high value of 1 (in red). All simulations predict vortex shedding in the wake of lip region. Flow velocity dropped significantly in this area. Streamline prediction by steady and unsteady RANS have a slight difference; this is due to the discrepancy of flow structures as the effect of mixing process along the breakout region.

5.4 Film-cooling Effectiveness at Various Blowing Ratios

Figure 5–16 presents the quantitative prediction data of the adiabatic film-cooling effectiveness ($\overline{\eta}_{aw}$) along the adiabatic/protected wall surface at various blowing ratios, in comparison with experimental measurements and previous numerical results using DES-SA [23][24]. It has been found that the SST $k-\omega$ turbulence is capable of being applied for prediction on Detached-eddy Simulation (DES). CFD data follows a strong decay of the adiabatic film-cooling effectiveness, much the same as with the experimental measurements. The decay is reduced by increasing the blowing ratio.

Anomalous phenomenon occurred when the blade TE cutback cooling is simulated around medium blowing ratio (M = 0.8). There is an opposite order of film-cooling effectiveness trend. The adiabatic film-cooling effectiveness is decreased at the downstream region by increasing a blowing ratio. This finding is similar to the previous simulation carried out by Martini *et al.* [4][5][23][24] and in the experiment by Horbach *et al.* [30], which indicated that the adiabatic film-cooling effectiveness, at the highest blowing ratio, is less than at the medium blowing ratio—mainly at the middle region $4 < x/H < 8$. A decay of cooling effectiveness tends to slope almost linier as illustrated in Figure 5–16. Horbach *et al.* [30] noted that the adiabatic film-cooling effectiveness dropped by increasing the blowing ratio from M = 0.8 to 1.25. This decrease is due to the intensified vortex shedding from the ejection lip. It occurs within a certain operating range with slot ejection, leading to an intensified mixing process between coolant and mainstream.

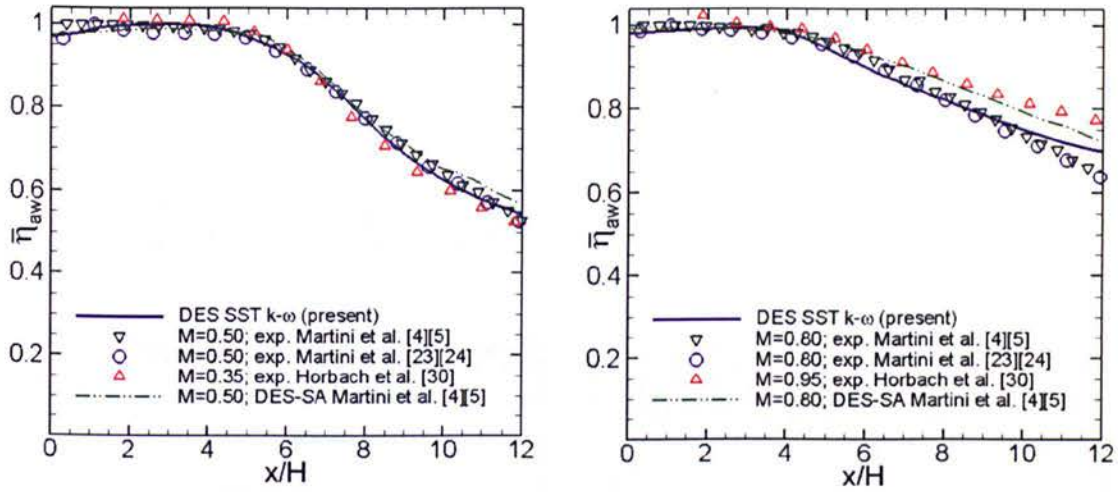

(a) Low (M = 0.5) (b) Medium (M = 0.8)

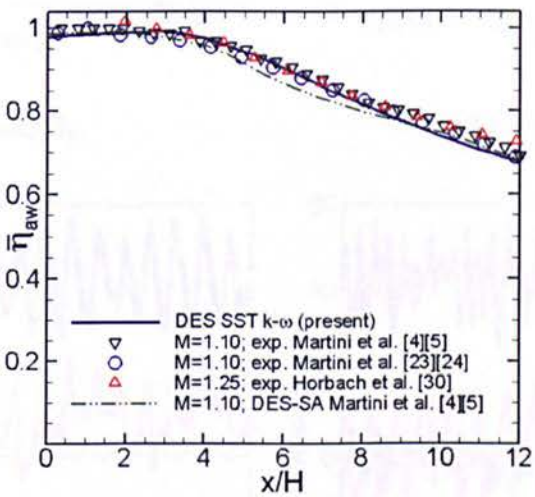

(c) High (M = 1.1)

Figure 5–16: Cooling-film effectiveness at various blowing ratios.

5.5 Shedding Frequency

As shown in Figure 5–17, vortex shedding, from the pressure-lip, is present in URANS and DES with their own characteristics. It grows up along the breakout-slot, following an intensified mixing between mainstream flow and coolant. The intensity of mixing depends on the blowing ratio used. Flow structures resulted from DES is noticeable compared to the others.

In order to complete the analysis, spectrum is necessary to quantify a dominant frequency of this vortex shedding to enable assessment using the data available. Only the case with blowing ratio of 1.1 is presented here. As explained previously, two monitoring

points have been defined identical to that of Martini *et al.* [23][24] (see Figure 4–2(c), page 66) in an effort to capture the characteristic of vortex-shedding.

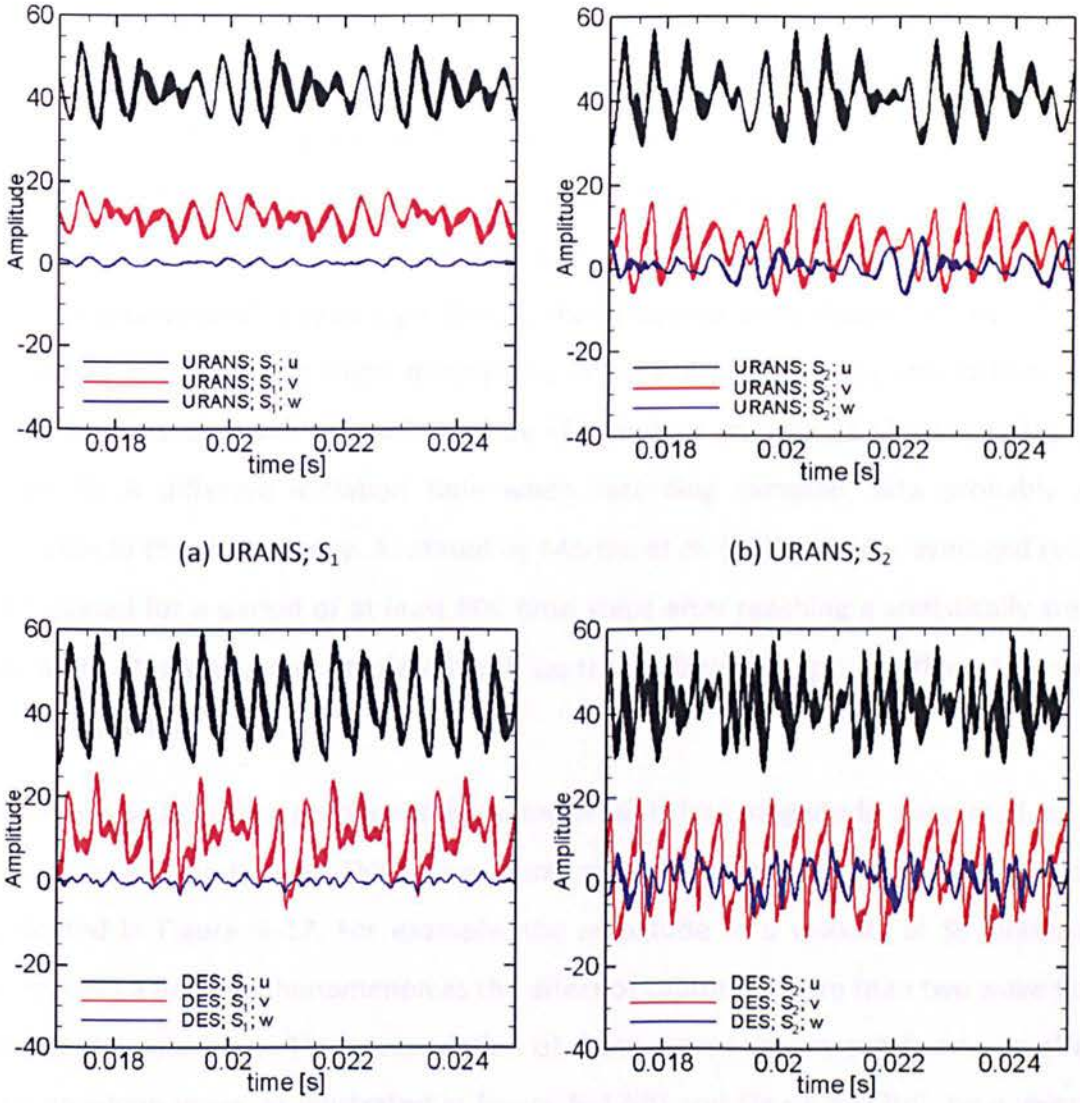

(a) URANS; S_1 (b) URANS; S_2

(c) DES; S_1 (d) DES; S_2

Figure 5–17: Time history of velocity components (u, v, w).

Figure 5–17 shows the truncated sampling data of the time variant of velocity components (u, v, w) at two different locations, as mentioned above. Sampling data are given as being between 0.017 and 0.025 seconds. It has been found that the amplitude of 'v' and 'w' velocity at the S_2 are stronger than at the S_1 location. It is probably caused by the blockage of pin-fin array inside the cooling passage. The blockages of the fifth-row pin-fin influence a different movement of local flow behind the lip; therefore, a local

airflow velocity in line with z/H = 0 is stronger than the z/H = 1.25, as can be seen in Figure 5–17(b) and Figure 5–17(d) for URANS and DES, respectively.

Figure 5–18 gives both shedding frequencies after processing by fast Fourier transform (FFT). These spectrums are based on sampling data between 0.0125 and 0.025 seconds. It has been found that the dominant frequencies are at 2.06 kHz for unsteady RANS and 2.21 kHz for DES. This finding is close to a predicted frequency f_s = 2.36 kHz by Martini *et al.* [23][24] at the blowing ratio M = 0.8. Referring to the effective lip thickness of 5 mm and the mainstream velocity at u_{hg} = 56 m/s, shedding frequency should be about 2.4 kHz if calculated analytically. A slight discrepancy is probably affected by the difference of blowing ratio used. It will be confirmed by FFT analysis on various blowing ratios (see Chapter 9). A different initiation time when recording sampled data probably also contributes to this discrepancy. As stated by Martini *et al.* [23][24], time-averaged results can be gained for a period of at least 500 time-steps after reaching a statistically steady state, whilst this study was simulated with up to 2,000 time-steps. A different range of data may have been used.

From Figure 5–18, other prominent frequencies with less magnitude compared to f_s = 2.36 kHz can be clearly seen. This is reasonable as an effect of the combined amplitudes, as indicated in Figure 5–17. For example, the amplitude of u velocity at S_2 monitoring point records a beating phenomenon as the effect of capturing more than two wave flows in typical characteristics. The accumulation of these waves causes sub-harmonic effects on the envelope wave, as illustrated in Figure 5–17(b) and Figure 5–17(d), by u velocity. Beat waves form when two waves that are close in frequency combine.

In terms of the Strouhal number, it has been recognised that a Strouhal number (S_t) of vortex shedding is approximately 0.22. This finding is suitable to previous computation study with S_t = 0.24. Sieverding *et al.* [130] report that vortex shedding of a turbulent boundary layer flow over a flat plate with a squared trailing edge is around S_t = 0.21. Boldman *et al.* [131] found that a Strouhal number of turbulent flow behind a blunt trailing edge is 0.2.

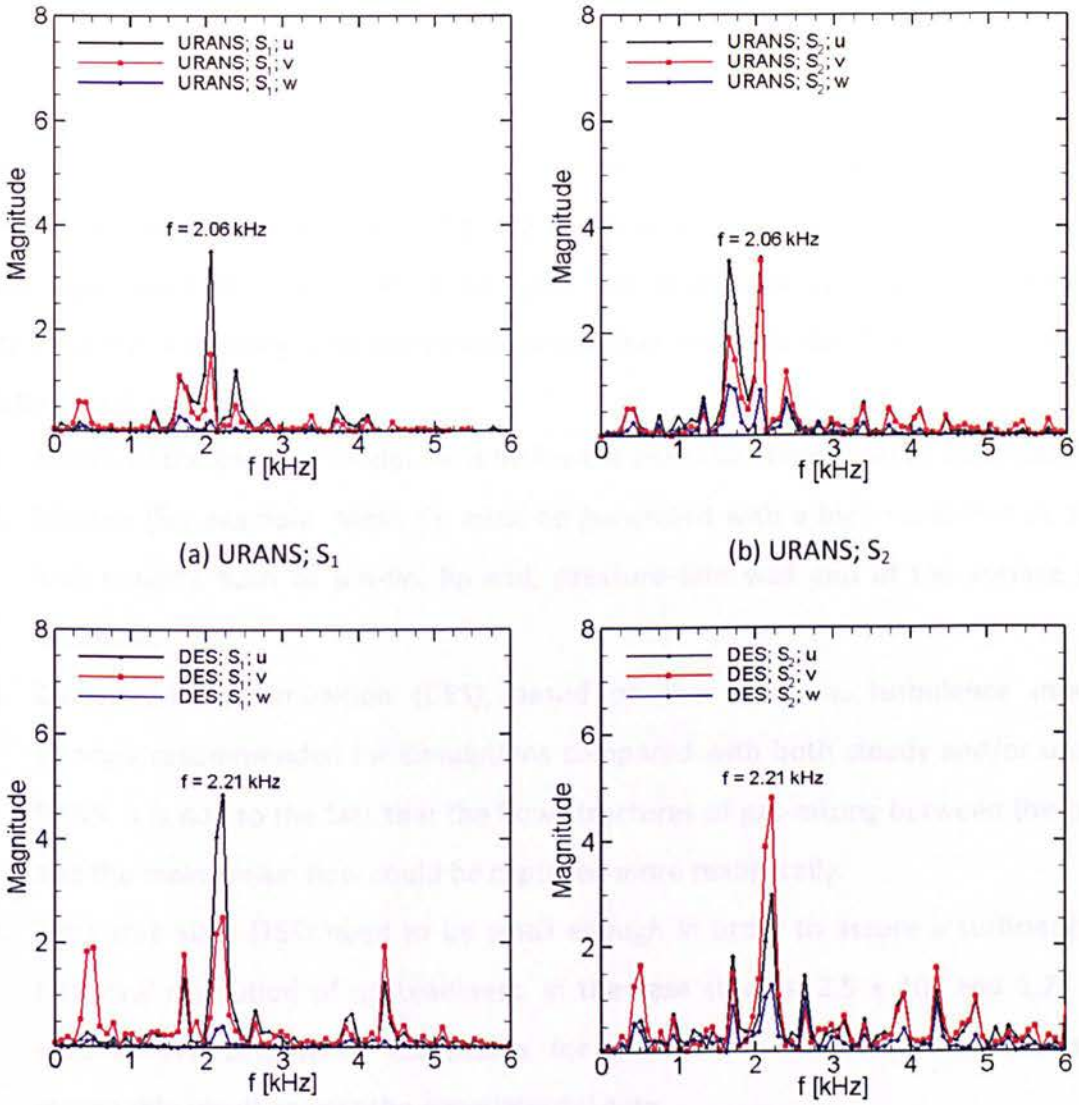

Figure 5–18: FFT spectrum.

5.6 Summary

In this chapter, grid refinement studies and the validation of the blade TE cutback cooling with circular pin-fin configuration inside the cooling passage have been performed. The operating condition of the blade TE cutback cooling at low-and- high blowing ratios, as in the experiment of Martini *et al.* [23][24], has been assessed during validation.The strategy for modelling and numerical treatments required for the baseline model is established as follows:

1. Design of the baseline model must be kept at the same dimension as the experiments.
2. Meshes (for example, Mesh C), must be generated with a high resolution at all end-wall regions, such as pin-fin, lip-end, pressure-side wall and at the surface of the breakout.
3. Detached-Eddy Simualtion (DES), based on the SST $k-\omega$ turbulence model, is strongly recommended for simulations compared with both steady and/or unsteady RANS. It is due to the fact that the flow structures of gas-mixing between the coolant and the mainstream flow could be captured more realistically.
4. Time-step sizes (TSS) need to be small enough in order to assure a sufficiently fine temporal resolution of unsteadiness. In the case studies, 2.5×10^{-5} and 1.25×10^{-5} seconds are considered acceptable for achieving a target of simulations with reasonable result against the experimental data.
5. The width of domain is not a critical issue for a blade TE cutback with periodic pin-fin configuration in lateral direction. Numerical studies using a single and double-pitch domain of pin-fin distance indicate that both domains are suitable when compared with the experimental data with full domain.

Overall, the predicted data of the adiabatic film-cooling effectiveness and the discharge coefficient are in good agreement for all various blowing ratios. It is proven by capturing well flow structures with the characteristic of shedding frequency and a Strouhal number approximately at f_s = 2.21 kHz and S_t = 0.22, respectively. Hence, these validation data can be used as a reference for further investigation in the case of other variations of these studies.

CHAPTER 6:

CASE I: BLADE TRAILING-EDGE CUTBACK COOLING WITH VARIOUS LIP THICKNESSES TO SLOT HEIGHT RATIO

This chapter describes a numerical study of the blade trailing-edge (TE) cutback cooling for four lip thickness to slot height (t/H) ratios. The baseline model as previously used for validation is modified in terms of the lip thickness (t), which is varied at 1.2, 2.4, 4.8 and 9.6 mm. The ejection slot height (H) is kept constant at 4.8 mm. All these domains only consider a single-pitch distance of pin-fin array in order to minimise the number of mesh, meaning the computational cost could be reduced. The fine Mesh 'C' tested in the validation stage is adopted. The SST k–ω turbulence model is used in DES computations. The available data of the experiments for a blade TE cutback with t/H ratio of 1.0 carried out by Martini *et al.* [4][5][23][24] and Horbach *et al.* [30] are used as a reference in comparison.

6.1 Blade TE Cutback Cooling with various t/H ratios

The trailing-edge cooling of gas turbines' blade with various lip thicknesses to slot height ratio has been studied widely in recent years. A number of experiments have been carried out to investigate the trailing-edge cooling design of turbine blades. Several publications [31][56][57][58] noted that the ratio of lip thickness to slot height has a significant influence on the blade trailing-edge cooling performance, in addition to those stated by Cuhna *et al.* [18] and Goldstein [132] in their individual experiments. Kacker *et al.* [57][58], who evaluated the film-cooling effectiveness of the impervious-wall of a two-dimensional wall jet on various t/H ratios whilst keeping lip thickness (t) constant, also confirmed the findings as described above. It can be concluded that the effectiveness of film-cooling is greatly dependent on the t/H ratios.

Taslim *et al.* [31][56] investigated the influence of different slot geometries on the film-cooling effectiveness in the surroundings of the breakout-slot region at various blowing ratio including density ratio. It was recognised that the increase of the *t/H* ratio from 0.5 to 1.0 reduced overall film-cooling effectiveness by about 10%. This finding was consistent with the previous experiments carried out by Kacker *et al.* [57][58], Sivasegaram *et al.* [59] and Burns *et al.* [60]. It can be summarised that the decrease of the *t/H* ratio is a key factor on increasing film-cooling effectiveness.

Recent experimental investigations of a blade trailing-edge cutback cooling were published by Horbach *et al.* [30][35]. Four different *t/H* ratios varied from 0.2 to 1.5. The experiment was performed at engine-realistic density ratios. It was found that the decrease of the *t/H* ratio has a potential to improve an adiabatic film-cooling effectiveness to unity. In contrast, the increase of the *t/H* ratio was seen to trigger the fast decay of the film-cooling effectiveness in the cutback region. Unsteady vortex-shedding from the blunt lip was more intensive with larger *t/H* ratios, which enhanced the mixing of the cooling film, as found by various researchers, such as Taslim *et al.* [31][56], Holloway *et al.* [25] and Martini *et al.* [23][24]. In terms of the discharge coefficient, this was also increased by raising *t/H* ratios due to an altered local pressure field in the lip's wake. The discrepancy of discharge coefficient was pronounced up to 50% for the case with blowing ratio of 0.2.

6.2 Triangle Area and Mixing Region

A 'cutback' or 'breakout' of the trailing-edge is obtained by cutting off a corner of the upper lip plate (pressure-side part) to make a lip thickness. The breakout slot is formed in parallel with the ejection slot (Figure 2–2, page 16). This design is expected to have a mixing region between the mainstream flow over the pressure-side region and the coolant from the ejection slot. As highlighted by various researchers, the lip thickness and the ejection slot height are two key parameters for performance of a blade trailing-edge cooling. The lip thickness to slot height ratio (*t/H*) is derived by comparing the lip thickness (*t*) to the ejection slot height (*H*), as illustrated in Figure 6–1.

The existence of lip, with a certain thickness, causes flow unsteadiness at the downstream of the lip when the fluid flows across the lip. This is similar to the flow around a bluff body, as described in Chapter 2. This unsteadiness grows up along the mixing region (over breakout area), depending on the lip thickness (t) and the blowing ratio (M) of a cooling system. Taslim *et al.* [56], Holloway *et al.* [25] noted that the unsteadiness is more pronounced when increasing the lip thickness to slot height ratio.

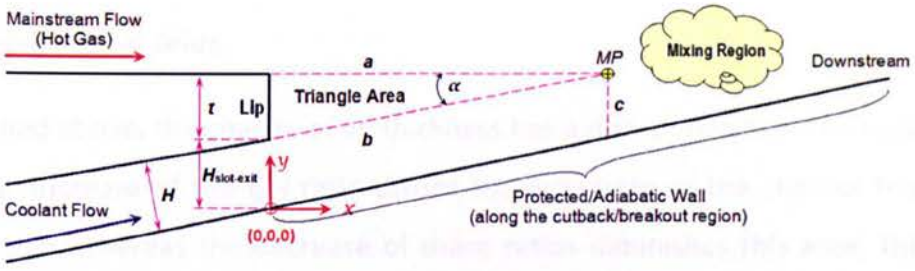

Figure 6–1: Triangle area

In order to investigate the effect of these parameters to the flow unsteadiness, four t/H ratios were proposed by providing four different lip thicknesses (t) between 1.2 and 7.2 mm, and keeping the ejection slot height (H) of 4.8 mm, as detailed in Table 6–1. For a constant slot height, it has been clearly presented that this t/H ratio only depends on the lip thickness. Any change to the lip thickness influences the region of mixing flow.

Table 6–1: Key dimensions of triangle area.

t/H	t (mm)	H (mm)	a (mm)	b (mm)	c (mm)	α (degree)
1.5	7.2	4.8	40.833	41.463	4.874	10
1.0	4.8	4.8	27.222	27.642	4.874	10
0.5	2.4	4.8	13.611	13.821	4.874	10
0.25	1.2	4.8	6.911	6.806	4.874	10

Based on Figure 6–1, a shadow triangle area is formed by a round up flow between the mainstream flow and the ejecting coolant. Two lines (i.e. 'a' and 'b') are projected in-line with both the pressure-side wall and the upper wall of coolant slot, respectively. The interconnection of both lines and the lip thickness (t) creates a triangle area and a point (MP) at the mixing region. This triangle area is located behind the lip where vortex-shedding commonly exists around this area.

For a lower *t/H* ratio, the mainstream flow and the ejecting coolant will mix readily at the mixing region. A triangle area formed by a round up flow is narrowed as the effect of a lower lip thickness (see Figure 6–1). Both the length of 'a' and 'b' are reduced if the lip thickness is decreased. In contrast, the triangle area widens when the lip thickness is increased. In an ideal condition, both vertical height of $H_{slot\text{-}exit}$ and *'c'* are the same due to the *'b'* line is parallel with the adiabatic wall.

6.3 Computational Grids

As mentioned above, the change of lip thickness has a direct impact on the region behind the lip. The increase of the *t/H* ratio causes the expansion of the shadow triangle area behind the lip, whereas the decrease of these ratios diminishes this area. This is more extensive with increasing lip thickness.

In terms of meshing, the variation of lip thickness affects a different treatment on the constructing meshes, mainly behind the lip region. On the other hand, all variations should be constructed at the same quality of mesh as the fine Mesh 'C' (see Figure 4–4, page 69). An advanced mesh strategy is needed in an effort to achieve grid dependence, as suggested by Spalart *et al.* [108][123]. Grids with all spacing much smaller than boundary-layer thickness (δ) give acceptable results. This is an important aspect in terms of ensuring a sufficient fine spatial resolution against unsteady effects behind the lip.

Figure 6–2 illustrates the local structured meshes around the lip region for four *t/H* ratios generated by the Gambit meshing tool. Only around this region are depicted here in order to highlight the mesh generation behind the lip. Other region including the cooling passage remains unchanged. All cases were constructed with the same number of blocks by developing the fine Mesh C of the baseline model. The fine Mesh C has 96 elements encircling the circumference of the pin-fin. It is known that this mesh has been used successfully on the validation stage. Very small spacing's with gradation are seen above and under the lip position within the middle region as shown in Figure 6–2. These structures might not be hindered in order to provide the mesh gradation behind the lip region, which is not be addressed by various researchers in the previous computations. These meshes were also deliberately made symmetrical between the block at L_2 and L_3

region, in an effort to avoid grid size changes that could occur unexpectedly (see the vertical gradation lines above and under the lip). It is held that these changes, if they occur, may reduce the accuracy of the calculation, as addressed by Spalart *et al.* [108].

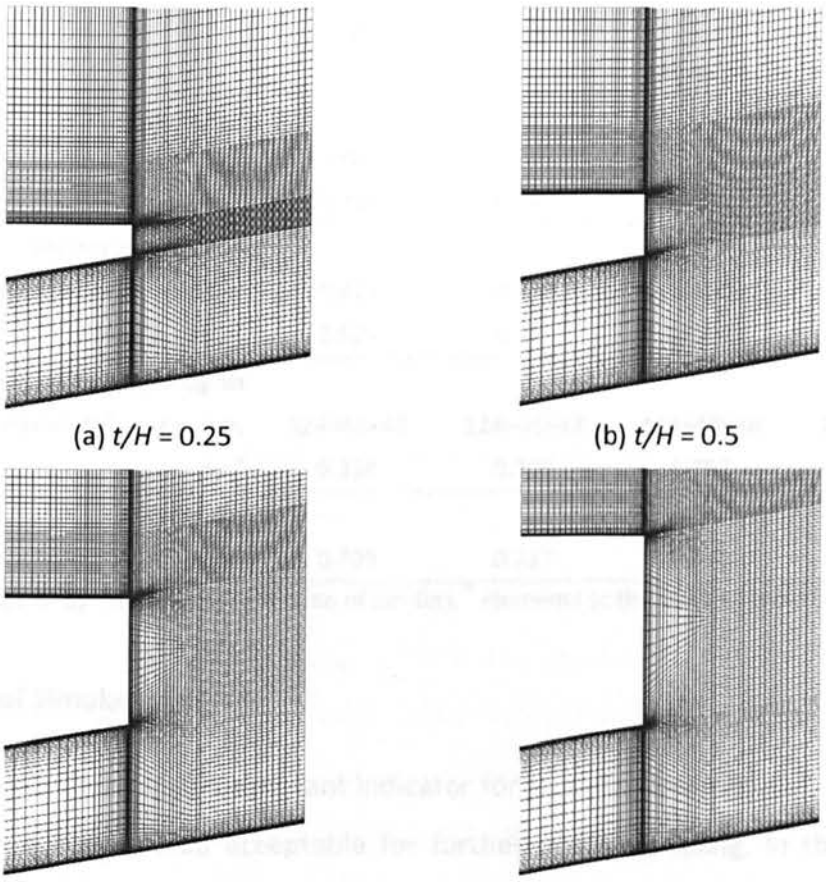

(a) $t/H = 0.25$ (b) $t/H = 0.5$

(c) $t/H = 1.0$ (baseline) (d) $t/H = 1.5$

Figure 6–2: Mesh comparison.

At the lip surface, all cases are meshed on a high-quality resolution at $\Delta y^+ < 1.0$, as detailed in Table 6–2. It is noted that all wall regions, such as inside the cooling passage, the pin-fin array, the pressure side zone and along the blade TE cutback/breakout region, were constructed at the same grid resolution with an expansion factor less than 1.2.

Table 6–2 gives a comparison of grid resolution for four cases. All t/H ratios have a very fine grid resolution, which ensures a sufficient spatial resolution of $\Delta y^+ < 1$. A slight discrepancy can be seen at the lip-end wall, the pressure-side wall and the adiabatic wall of the test plate; however, these can be considered acceptable for this study due to all variations have been kept within high-quality resolution, the same as the fine Mesh 'C'. In

fact, this grid dependence has been verified with a satisfied-result as previously proven on validation stage (see Chapter 5).

Table 6–2: Mesh statistics.

t/H ratio	0.25	0.5	1.0 (baseline)	1.5
Inside the cooling passage region				
pin-fin wall[a] Δy_1^+	0.907	0.907	0.907	0.906
end-wall Δy_1^+	0.751	0.752	0.749	0.751
Mainstream region				
pressure side wall Δy_1^+	0.475	0.478	0.482	0.488
lip-end wall Δy_1^+	0.528	0.523	0.607	0.654
TE breakout/cutback region				
No. of elements[b], $n_x \times n_y \times n_z$	124×48×48	124×48×48	124×48×48	124×48×48
Δy_1^+	0.338	0.309	0.257	0.254
average				
Δy_1^+	0.739	0.737	0.740	0.694

[a] an average of Δy^+ in the radial direction of pin-fins, [b] elements at the block of breakout-slot region

6.4 History of Simulations

A steady state condition is an important indicator for stopping a simulation, meaning the data then can be considered acceptable for further post-processing. In this numerical study, computations are realised up to 2,000 time steps, which requires up to 360 computational hours for a domain with a single-pitch distance of pin-fin array. It is equal to approximately 23,299 iterations for the baseline simulation. Each case has a typical iteration for achieving a statistically stationary state.

Figure 6–3 displays the iteration history of all simulations for both blowing ratios studied. These data are based upon the temperature ($T_{c'\text{-}2}$) at the centre point of the slot exit. The oscillations occurring for simulation at a high-blowing ratio are related to unsteadiness, while the oscillation almost does not exist for simulations at a low-blowing ratio (see Figure 6–3(a)). A lower blowing ratio is identical to a lower coolant flow velocity at the inflow region due to the boundary condition of mainstream flow velocity is kept constant at 56 m/s. The discrepancy of both oscillations is likely caused by different flow intensity inside the cooling passage.

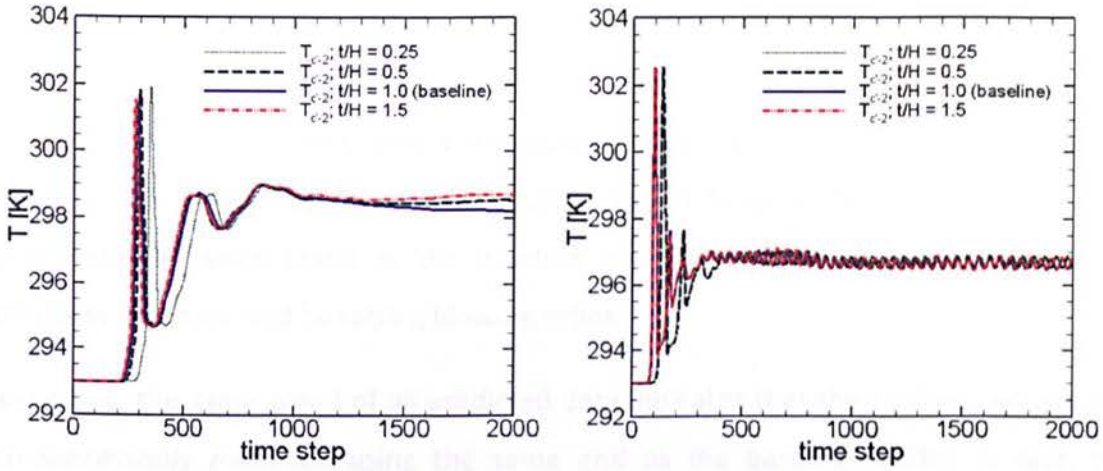

(a) Low blowing ratio (b) High blowing ratio

Figure 6–3: History of simulations.

6.5 Results and Discussion

Investigation of the blade trailing-edge cutback cooling with four *t/H* ratios has been performed computationally. The simulation results are presented below. Discussion starts by focusing on coolant flow behaviour inside the cooling passage, followed by the performance of the blade trailing-edge cutback cooling. The dynamic interaction of the mainstream flow and the coolant, including the spectrum of vortex-shedding at the mixing region, are also discussed thereafter.

6.5.1 Cooling Passage

The discussion of this part is aimed towards assessing the heat-transfer process inside the cooling passage before ejecting the coolant from the slot exit. Due to the geometries of the cooling passage remains unchanged, it is expected to have the same coolant flow behaviour along this channel. In regards to this investigation, all configurations must be kept the same grid and quality, mainly the region inside the cooling passage. The structured-mesh of the fine Mesh 'C' as in Figure 4–4 (see page 69) has been used to develop three others as seen in Figure 6–2.

6.5.1.1 Discharge coefficient:

Figure 6–4 provides the CFD prediction of the discharge coefficients (C_D) for four different varieties of *t/H* ratios, in comparison with the available data of experimental measurements. The predicted data are computed from each simulations using equation (2.3); then are plotted against blowing ratios. It has been found that the CFD data demonstrate the same trend as the baseline model for all *t/H* ratios. The discharge coefficients are increased by raising blowing ratios.

As expected, the same trend of all predicted data indicates that the cooling passage has been successfully modelled using the same grid as the baseline model. In fact, the discharge coefficients almost remain unchanged for all cases simulated. This is highly reasonably due to the cooling slot of all variations is kept at the same geometry and numerical treatments. The present computation implies that this result is considered acceptable for a comparison study of the *t/H* ratio effects. A slight discrepancy is likely caused by the recirculation effect of unsteady vortex-shedding from the mixing region, which influences the static pressure at the slot exit. Then, this gives a slight effect to the calculation of discharge coefficient.

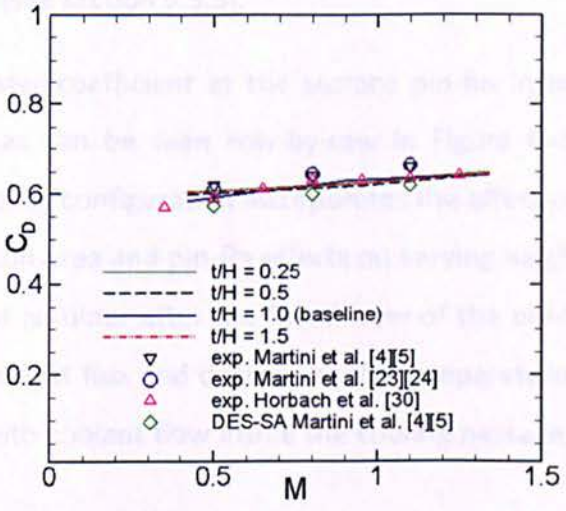

Figure 6–4: Discharge coefficients.

From Figure 6–4, the CFD data in this numerical study match that of the experiments, as well as the CFD data of Martini *et al.* [23][24]. Moreover, this finding is seen to be in-line

with the experimental data by Horbach *et al.* [30]. This means the coolant flow behaviour could be simulated well along the cooling channel.

6.5.1.2 Properties at the pin-fins surface:

As previously described in section 6.5.1.1, the coolant flow along the cooling passage for all variations would be expected to have the same properties as the baseline model. In order to ensure a former finding of the discharge coefficient, properties at the pin-fin surface are assessed in terms of those similarities and trends. Figure 6–5 denotes the quantitative comparison of properties at the pin-fins' surface for four *t/H* ratios. Only the variation at high-blowing ratio is discussed here considering a similarity of trend. However, it is expected to reflect the case at the other variety of blowing ratio. In terms of the pin-fin row (P_1 – P_5) position, refer to Figure 5–10 (see page 92), as defined previously. It has been found that the change of *t/H* ratio does not influence the characteristics at the surface of pin-fins inside the cooling passage. This fact implies that the coolant gases within the cooling passage, on four models, share similar behaviours prior to being ejected through the slot exit. This similarity is highly expected in order to make a fair investigation along the protected/adiabatic wall surface, which is a main area of interest in this study (see section 6.5.3).

The average heat-transfer coefficient at the surface pin-fin inside the cooling passage increases moderately, as can be seen row-by-row in Figure 6–5(a). The heat-transfer coefficient in such a cooling configuration incorporates the effect of flow acceleration due to the constriction section area and pin-fin effects on varying heights. The increase of the heat-transfer coefficient is minor after the fourth row of the pin-fin array. This is in-line with raising the surface heat flux and decreasing the temperature at the pin-fin surface, which is concomitant with coolant flow inside the cooling passage, as shown in Figure 6–5(b).

The resulting trend of the heat-transfer coefficient in this computation is confirmed by that of Cunha *et al.* [18] and Tarchi *et al.* [13], who studied similar subjects through staggered arrays. The peak heat-transfer occurred in the last row of the pin-fin located in a wedge duct. The increase of the heat-transfer coefficient with a contraction channel is

stronger than for the staggered pin-fin within a parallel duct. The heat-transfer difference between the peak and lowest levels, from the first rows pin-fin, is approximately 45.45% in this study. Cunha *et al.* [18] noted up to 38.46% in their experiment and Tarchi *et al.* [13] found up to 180% in their study with seven rows pin-fins, whilst Metzger *et al.* [133], who measured the heat-transfer through ten rows of staggered pin-fins within parallel duct, discovered 12% of heat-transfer discrepancy between the highest and the lowest. Similar results have been found by Lawson *et al.* [134], Chyu *et al.* [135] and Mitre *et al.* [136], all of whom investigated heat-transfer in the parallel duct with seven-row arrays. These researches noted that the heat-transfer increases through the first three rows and then decreases for the remaining rows.

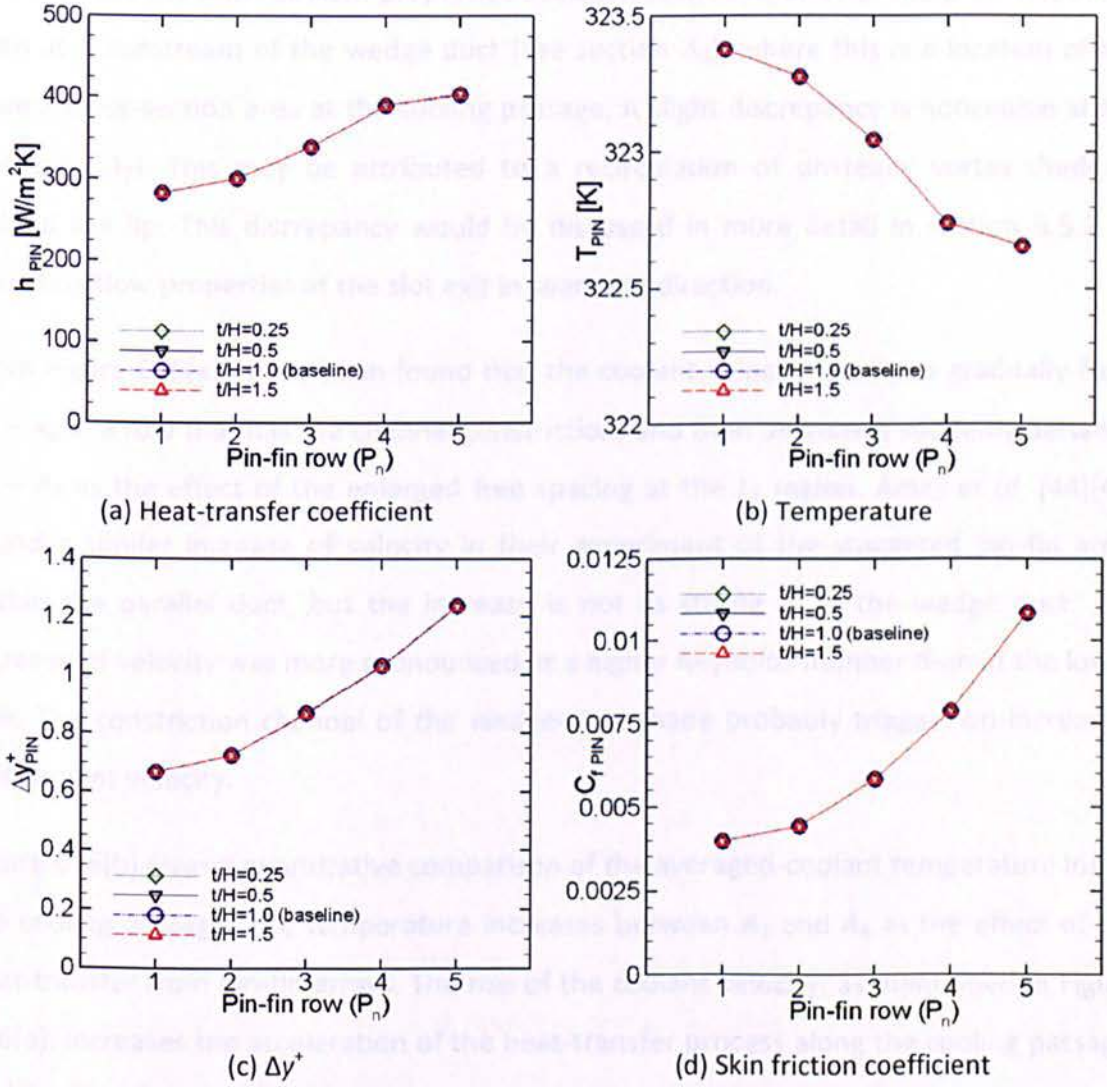

Figure 6–5: Coolant flow behaviour at the surface of pin-fin array.

Figure 6–5(c) and Figure 6–5(d) represent both the Δy^+ and the skin friction coefficient (C_f) at the pin-fin wall surface, respectively. The same values of both Δy^+ and C_f at all variations prove that all simulations took exactly the same grid quality for four cases simulated.

6.5.1.3 Coolant flow behaviour inside the cooling passage:

Similarly, these coolant flow behaviour would be expected to have the same properties along the cooling channel. Figure 6–6 shows the area-averaged values computed across the inter-pin-fins ($A_1 - A_7$) at the internal cooling passage. The measured area of $A_1 - A_7$ has been explained in Chapter 5 (see Figure 5–10, page 92). As predicted, all variations demonstrate the same coolant properties between section A_1 and A_6. The peak values are seen at downstream of the wedge duct (see section A_6), where this is a location of the lowest cross-section area at the cooling passage. A slight discrepancy is noticeable at the slot exit (A_7). This may be attributed to a recirculation of unsteady vortex-shedding behind the lip. This discrepancy would be discussed in more detail in section 6.5.2 by assessing flow properties at the slot exit in spanwise direction.

From Figure 6–6(a), it has been found that the coolant velocity increases gradually from $A_1 - A_6$ in a row that has the channel constriction, and then decreases suddenly between $A_6 - A_7$ as the effect of the enlarged free spacing at the L_2 region. Ames *et al.* [44][45] found a similar increase of velocity in their experiment of the staggered pin-fin array within the parallel duct, but the increase is not as strong as in the wedge duct. The increase of velocity was more pronounced at a higher Reynolds number than at the lower one. The constriction channel of the wedge-duct shape probably triggers on increasing this coolant velocity.

Figure 6–6(b) gives a quantitative comparison of the averaged-coolant temperature inside the cooling passage. The temperature increases between A_1 and A_6 as the effect of the heat-transfer from pin-fin arrays. The rise of the coolant velocity, as mentioned in Figure 6–6(a), increases the acceleration of the heat-transfer process along the cooling passage, and further significantly contributes in terms of raising this temperature. The combined effect of the wedge-duct shape and pin-fin arrays also triggers the increase of turbulence

kinetic energy and turbulence levels throughout the cooling channel, as shown in Figure 6–6(c). That finding agrees with the experiment carried out by Ames *et al.* [44][45], which found a similar increase of turbulence level, and then decreased at the last row of pin-fin arrays.

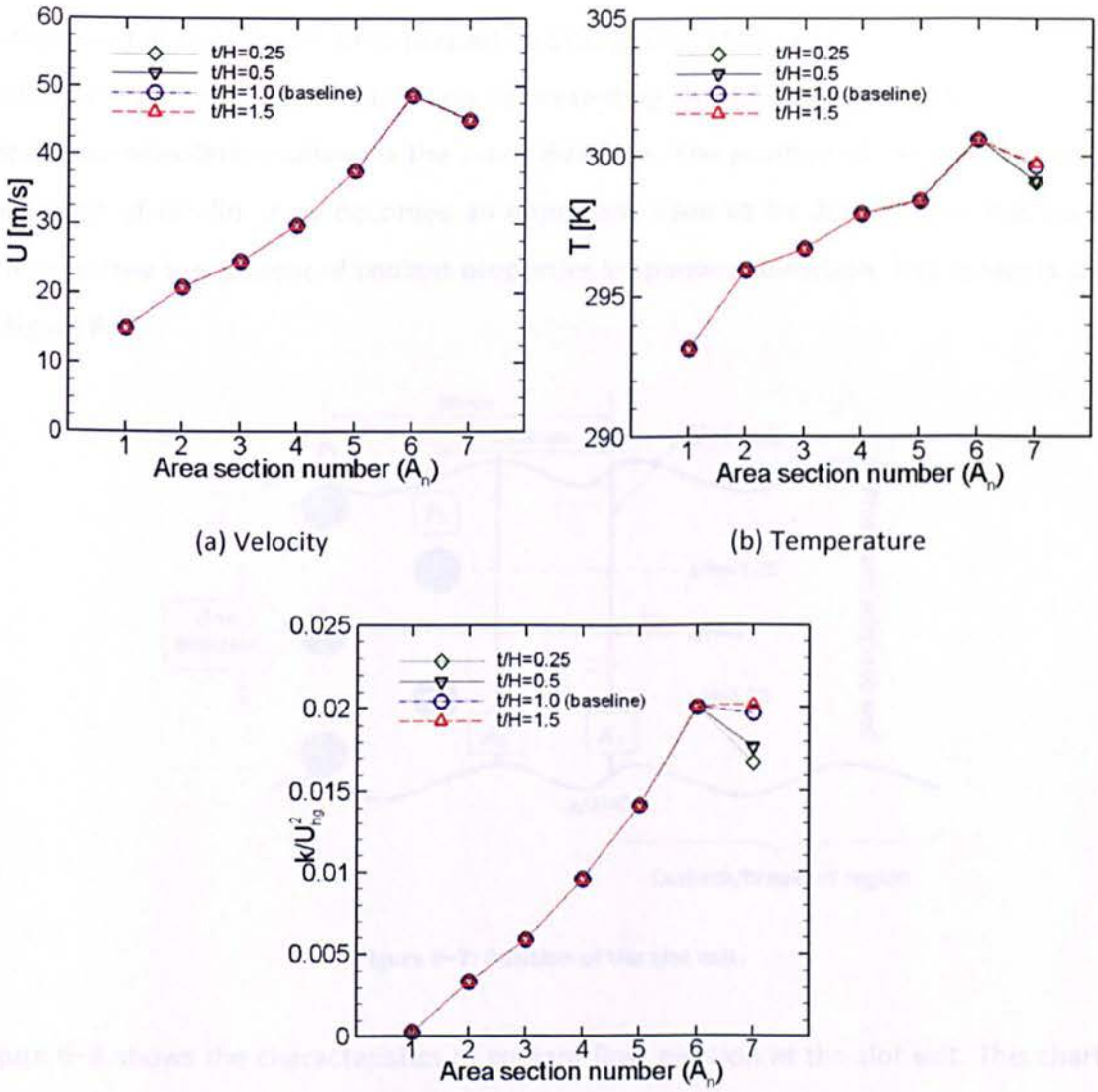

(a) Velocity

(b) Temperature

(c) Turbulence kinetic energy

Figure 6–6: Coolant flow behaviour inside the cooling passage.

Figure 6–6(b) and Figure 6–6(c) show the differences in both the coolant temperature and the turbulence kinetic energy at the slot exit, respectively. This is due to a reverse flow effect from the mixing region, which is known to influence the turbulence levels of the coolant ejection at the L_2 region. A reverse flow is triggered by recirculation effect of vortex shedding behind the lip, which commonly exists around the shadow triangle area.

In terms of the turbulence kinetic energy, it has been found that the reverse flow effect of unsteadiness from the simulation using the thickest lip thickness is stronger than when using the thinnest one, as indicated in Figure 6–6(c).

6.5.2 Coolant Properties at the Slot Exit

As discussed above, the cause of properties discrepancy at the slot exit area (A_7) has been unclear. It needs a further explanation by presenting laterally averaged properties within a spanwise orientation following the z-axis direction. The position of the slot exit against the layout of pin-fin array becomes an important issue to be described in this section before further assessment of coolant properties in spanwise direction. This layout is given in Figure 6–7.

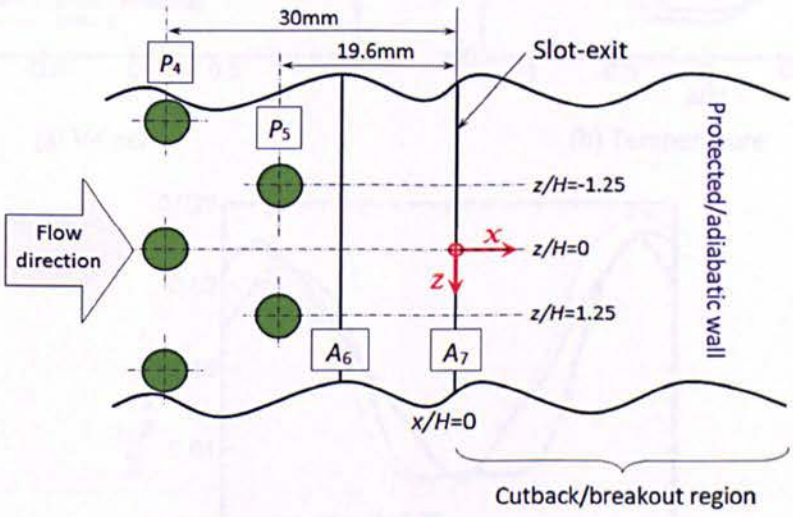

Figure 6–7: Position of the slot exit.

Figure 6–8 shows the characteristics of coolant flow ejection at the slot exit. This chart is based on the averaged properties data in spanwise direction. It has been found that all variations show similar trends with a slight discrepancy. The discrepancy is noticeable between the centre ($z/H = 0$) region and other z/H position. For example, the coolant flow velocity at the centre is greater than other z-axis, whilst other properties have an opposite trend that tends to at a lower level in the centre. It can be seen in Figure 6–8(a). This discrepancy is likely to be related to layout of pin-fin array inside the cooling passage as shown in Figure 6–7. In-line with the centre ($z/H = 0$), a higher coolant flow velocity at the slot exit is affected by the existence of the fifth row of pin-fin array that causes the

rise of ejecting cooling. In-line with the z/H = -1.25 and 1.25, a lower level of coolant flow velocity is caused by the vortices flow effect behind the fifth cylindrical pin-fins. This vortex causes recirculation in spanwise direction, and then influences the drop of ejecting coolant. It proves that this array has an important role to play in this discrepancy.

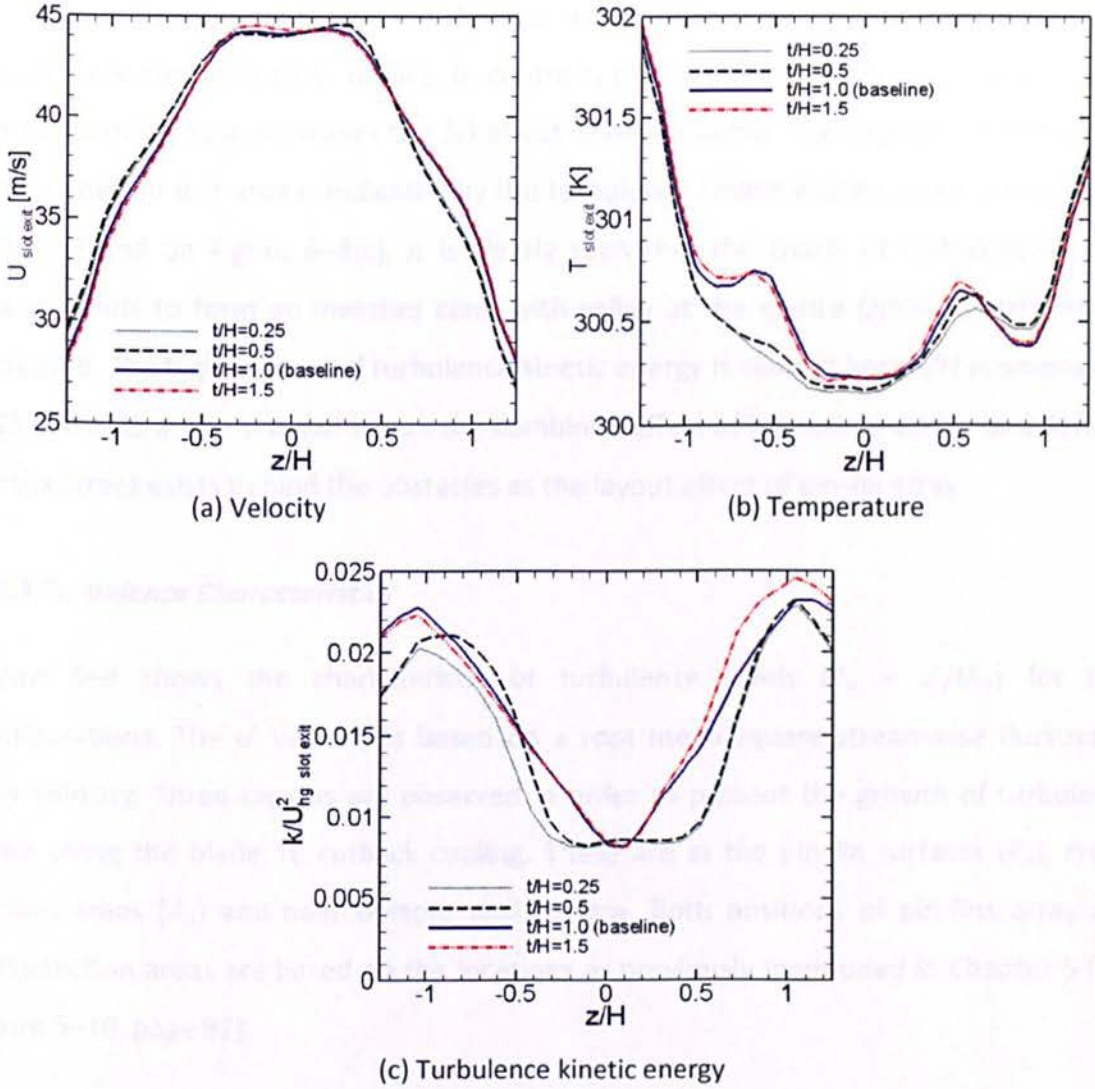

(a) Velocity

(b) Temperature

(c) Turbulence kinetic energy

Figure 6–8: Coolant flow behaviour at the slot exit.

As previously mentioned, the coolant temperature chart is opposite against the coolant flow velocity in Figure 6–8(a). The decrease of coolant temperature around the middle region is most likely triggered by the acceleration of coolant flow velocity, while the increase of coolant temperature in other regions is due to the deceleration of that velocity. Looking at Figure 6–6(b) and Figure 6–8(b), the coolant temperature for the case

with higher lip thickness is greater than the case with lower one. The discrepancy is obvious in the middle region between $-1 < z/H < 1$. The asymmetric chart is seen with discrepancy up to 1.6 K between both side regions. This increase is likely related to a larger recirculation of vortex-shedding behind the lip, which affects a dynamic thermal mixing process around this region. A larger circulation causes a strong invasion of mainstream flow (hot gas) into the slot exit region. Moreover, the 3D effect makes flow that is more complicated in nature. In contrast, the invasion is reduced within a smaller vortex shedding that decreases the 3D effect of recirculation. The degree of recirculation flow at the slot exit area is indicated by the turbulence kinetic energy, as shown in Figure 6–8(c). Based on Figure 6–8(c), it is clearly seen that the charts of turbulence kinetic energy tends to form an inverted cone with valley at the centre (z/H=0) if t/H ratio is increased. The highest level of turbulence kinetic energy is clear at both z/H positions of –1.25 and 1.25 at the slot exit where the combined effect of horseshoe vortex and Karman Vortex Street exists behind the obstacles as the layout effect of pin-fin array.

6.5.3 Turbulence Characteristics

Figure 6–9 shows the characteristic of turbulence levels ($T_u = u'/U_\infty$) for four configurations. The u' velocity is based on a root mean square streamwise fluctuation flow velocity. Three regions are observed in order to present the growth of turbulence levels along the blade TE cutback cooling. These are at the pin-fin surfaces (P_n), cross-section areas (A_n) and near bottom wall surface. Both positions of pin-fins array and cross-section areas are based on the locations as previously mentioned in Chapter 5 (see Figure 5–10, page 92).

It has been found that the turbulence levels are gradually increased along the cooling passage as clearly indicated by the averaged-turbulence levels at the cross-section areas. These levels are greater than at the pin-fin surfaces. Both locations of turbulence levels also could be treated in-line with the notation of A_n for cross-section areas and P_n for pin-fins, respectively. It is also clearly seen that there is no discrepancy for four configurations simulated, mainly inside the cooling passage. A slight discrepancy is seen at the slot-exit (A_7) as recirculation effect behind the lip region.

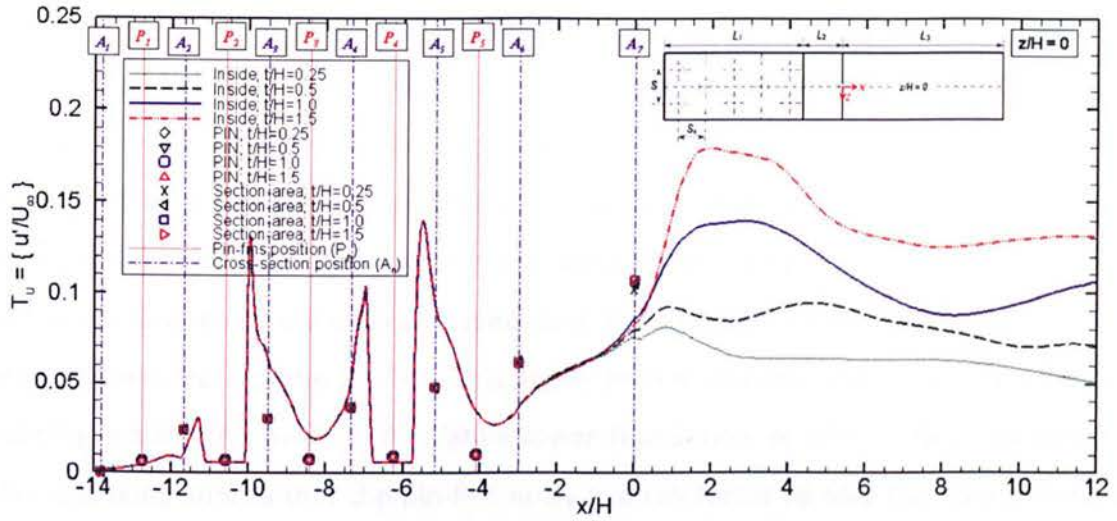

(a) $z/H = 0$

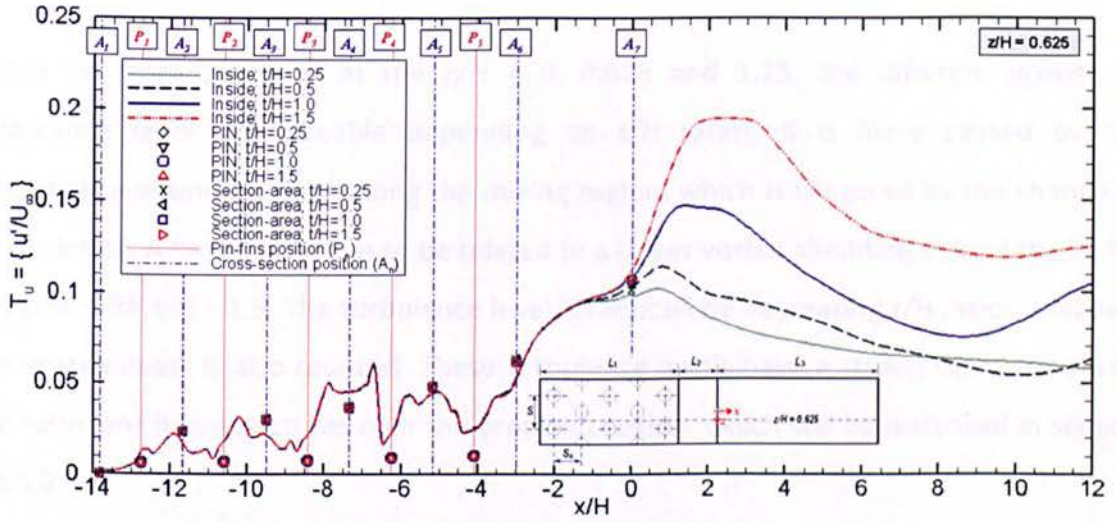

(b) z/H =0.625

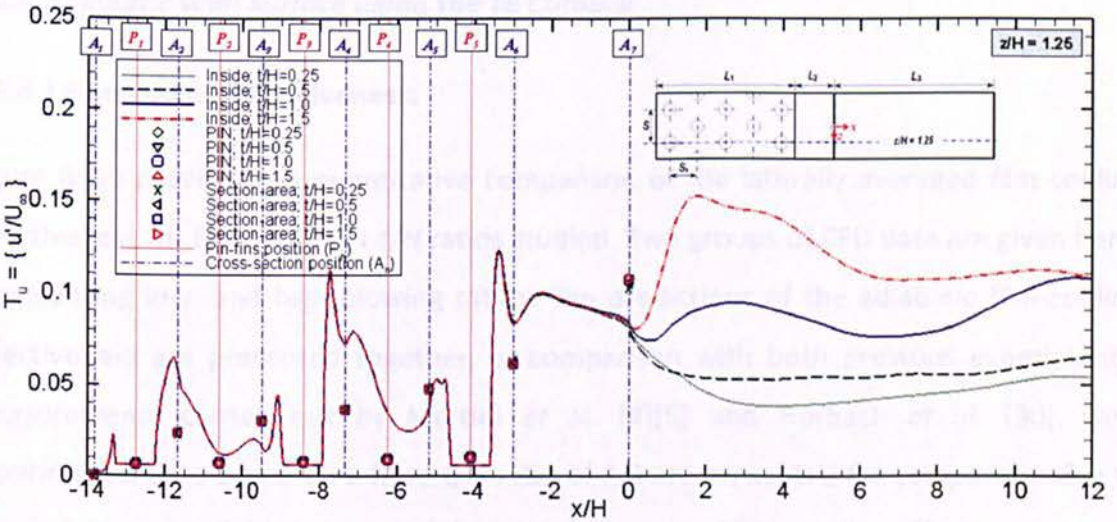

(c) z/H = 1.25

Figure 6–9: Turbulence levels.

In order to inspect the growth of turbulence levels as the effect of pin-fins array, three different positions at the z/H = 0, 0.625 and 1.25 are observed here. It is projected from turbulence levels near the bottom wall surfaces along the blade TE cutback cooling for those positions. These data are collected from 0.1 mm in parallel with the adiabatic wall. It is recognised that turbulence level is not uniform. It is more obvious concomitant with the coolant flow inside the wedge-shaped duct. The turbulence level behind the pin-fins is greater than in front of the pin-fins. This higher level is related to the existence of vortex-shedding behind the pin-fins. A relative lower fluctuation at z/H = 0.625 compared to other positions implies that the pin-fins array is a key factor to play the flow generation inside the cooling passage.

Based on three positions at the z/H = 0, 0.625 and 1.25, the different growth of turbulence level is noticeable depending on t/H ratios. It is likely caused by the discrepancy of unsteadiness along the mixing region, which is triggered by the change of lip thickness. A larger growth is to be related to a larger vortex-shedding behind the lip for the case with t/H = 1.5. The turbulence level is reduced by decreasing t/H ratios, meaning the unsteadiness is also reduced. These turbulence levels have a strong correlation with the turbulent flow structures over the breakout region, which will be discussed in section 6.5.5.2.

6.5.4 Adiabatic Wall Surface along the TE Cutback

6.5.4.1 Film-cooling effectiveness:

Figure 6–10 provides the quantitative comparison of the laterally averaged film-cooling effectiveness for four different t/H ratios studied. Two groups of CFD data are given here, representing low- and high-blowing ratios. The predictions of the adiabatic film-cooling effectiveness are presented together, in comparison with both previous experimental measurements carried out by Martini *et al.* [4][5] and Horbach *et al.* [30]. Only experimental data based on a fixed t/H ratio of 1.0 are presented for comparison due to not all data are available in terms of the laterally averaged film-cooling effectiveness.

In general, the performance of the blade TE cutback cooling is strongly dependent on the blowing ratio (M) and the lip thickness to slot-height (t/H) ratio. Simulations at all various t/H ratios predict the same level of adiabatic film-cooling effectiveness as being between $0 < x/H < 3$. The CFD data decay gradually up to 50% depending on the blowing ratio and the t/H ratio. The prediction, using the baseline model with $t/H = 1.0$, agrees well for both blowing ratios, compared to the experiments performed by Martini *et al.* [4][5] and Horbach *et al.* [30].

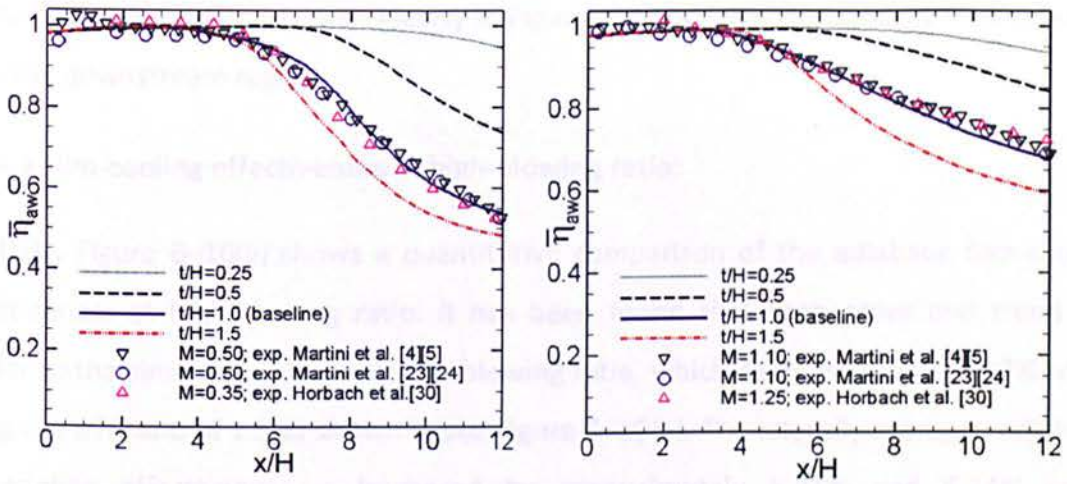

(a) Low blowing ratio (b) High blowing ratio

Figure 6–10: Laterally averaged film-cooling effectiveness at the protected wall.

6.5.4.2 Film-cooling effectiveness at a low-blowing ratio:

From Figure 6–10(a), it is found that the decrease of the t/H ratio causes an increase in the adiabatic film-cooling effectiveness near the downstream region. The blade TE cutback design, with the lowest ratio ($t/H = 0.25$), generates the highest level of cooling effectiveness nearly unity along the breakout region. It improves the performance up to 10.33% against the baseline model. A slight decay is seen near the downstream region between $8 < x/H < 12$, with a discrepancy of up to 0.05% compared to the baseline. An average of 6.58% could be improved through the application of a fixed ratio of $t/H = 0.5$. The decay is more pronounced at the downstream region with a discrepancy of up to 25% from unity. It emphasises the experimental finding by Horbach *et al.* [30], where the decrease of the t/H ratio is able to improve the adiabatic film-cooling effectiveness near

unity. Based on an experimental investigation without considering configuration inside the cooling passage, Taslim *et al.* [31] noted that the decline of the lip thickness to slot height ratio has a potential to increase an adiabatic film-cooling effectiveness by approximately 10%.

In contrast, the adiabatic film-cooling effectiveness is decreased for the case with a higher *t/H* ratio. The performance declines more rapidly when using the blade TE cutback with *t/H* = 1.5. The average discrepancy is up to 3.02% when compared with the performance of the baseline model. It is seen clearly in Figure 6–10(a), where the decay is more rapid near the downstream region.

6.5.4.3 Film-cooling effectiveness at high-blowing ratio:

Similarly, Figure 6–10(b) shows a quantitative comparison of the adiabatic film-cooling effectiveness at high-blowing ratio. It has been found that both order and trend are similar to the simulation results at low-blowing ratio, which decreased up to 3.19% when using the *t/H* ratio of 1.5 as shown in see Figure 6–10(a). The laterally averaged adiabatic film-cooling effectiveness is increased by approximately 5.21% and 6.34% when decreasing *t/H* ratio from 1 to 0.5 and 0.25, respectively. Unfortunately, however, there are no available measurement data to be included for comparison; CFD data therefore are not compared with experimental data. The agreement between CFD and experiment for the baseline model is used as a reference for this investigation. Nevertheless, Horbach *et al.* [30] stated clearly from their experiment that the thinnest lip thickness provides the highest film-cooling effectiveness. This statement was justified by comparing the averaged film-cooling effectiveness versus blowing ratio at a fixed *x/H* = 8. The results indicated that the thinner lip thickness (i.e. at *t/H* = 0.2 and 0.5) was effective within the higher blowing ratio when compared to the blade TE cutback with thicker lip thickness (i.e. at *t/H* = 1.0 and 1.5) [30]. These results were comparable to their previous experiment using the blade TE cutback with two-row long rib inside the cooling passage [35].

As discussed previously in the literature review, Taslim *et al.* [31] believed that a film-cooling effectiveness could be maximised by utilising a thin lip thickness in order to

reduce an intensified mixing along the TE cutback region. Further, the coolant jet is persistent along the lower wall surface for a longer distance. The thinnest lip thickness is oriented to minimise the intensified mixing between the mainstream flow and the coolant, and to create smaller wakes flow along the mixing region. Most likely, owing to the presence of a larger wake, this triggers the unsteadiness increase, influencing their mixing process.

Based on this study, a rapid decay of the adiabatic film-cooling effectiveness, as shown in Figure 6–10, is likely to be caused by larger wakes with unsteadiness. For example, a simulation for the case with a thicker lip thickness (i.e. t/H =1.5) generates larger wakes within typical unsteady vortex-shedding from the blunt lip (see Figure 6–16). Not only unsteadiness, but also the growth of both turbulence kinetic energy and turbulence intensity are noticeable for this computation. This finding proves that the increase of lip thickness causes the development of unsteady vortex-shedding, which in turn enhances the mixing of cooling film, as reported by Martini *et al.* [23][24], Horbach *et al.* [30][35] and Holloway *et al.* [25]. This unsteadiness will be qualitatively visualised by turbulence flow structures in section 6.5.5.2.

6.5.4.4 Temperature at the protected wall surface for case with high blowing ratio:

In order to explain the different decay of film-cooling effectiveness as discussed above, the laterally averaged data along the protected wall surface such as wall temperature (T), non-dimensional wall distance for a wall-bounded flow (Δy^+), and skin frictions coefficient (C_f) are given here. Only the high-blowing ratio case will be discussed here due to both results showing a similar order and trend; however, it is expected that this will be reflected for the case with low blowing ratio.

Figure 6–11 gives the laterally averaged temperature (T) at the protected wall surface. The result shows that the temperature starts-up at x/H = 4 for all variations. The increase of t/H ratios causes the increase of wall temperature near the downstream region. Those temperatures detailed in Figure 6–11 have a direct influence on the adiabatic film-cooling effectiveness in Figure 6–10(b), respectively. By comparing temperature at the protected wall surface in Figure 6–11 with air temperature T_1 at y-y_{aw} = 0.1mm in Figure 6–15(c), it

is seen that the change of both temperatures has a similar trend. Therefore, the air temperature T_1 at y-y_{aw} = 0.1mm could be used to represent the temperature at the adiabatic wall surface (see Figure 6–15). Moreover, these trends are similar up to a certain distance from the end wall, as illustrated in Figure 6–15(c). By looking at the air properties at y-y_{aw}=0.1mm, the relation of velocity and other properties can be linked with that the decay of the adiabatic film-cooling effectiveness.

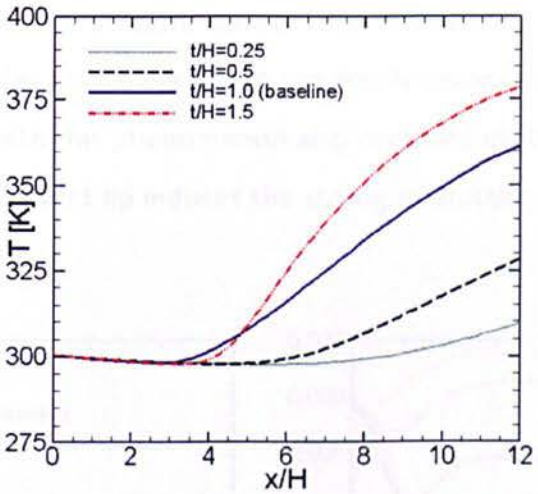

Figure 6–11: Temperature at the protected wall.

6.5.4.5 Coefficient of Δy^+ and C_f at the protected surface for case with high-blowing ratio:

In terms of both non-dimensional wall distance for a wall-bounded flow (Δy^+) and the skin friction coefficient (C_f), it is found that both coefficients fluctuate along the protected wall surface, showing a similar trend and order against both the adiabatic film-cooling effectiveness (see Figure 6–10(b)) and temperature (see Figure 6–11). Deviation is more pronounced for the blade TE cutback with a higher t/H ratio. This is due to the different velocity (see Figure 6–13(a)) for various t/H ratios. The velocity changed following the unsteadiness along the mixing region. This can be identified by drawing a comparison in each coefficient (Δy^+ and C_f) on different t/H ratios in Figure 6–12(a) and Figure 6–12(b). This finding implies that thinner lip thickness causes a smaller wake that is able to reduce the mixing process between the mainstream hot gas and the coolant. The comparison of wake and unsteadiness phenomenon over the blade TE cutback can be seen on the

visualisation of turbulence flow structures, as in Figure 6–16. It is seen clearly that a lower *t/H* ratio causes smaller wakes, whereas a higher *t/H* ratio produces larger wakes.

In their research, Holloway *et al.* [19][25] found that unsteady vortex-shedding from the pressure side lip has an important role to play in the mixing process between the coolant and the mainstream flow over at the breakout region. A larger lip thickness causes an intensified vortex-shedding, whereas thin lip thickness reduces the mixing process and creates smaller wakes; this, in turn, causes the different slope of the film-cooling effectiveness. This provides an answer to the previously unexplained experimental results by Holloway *et al.*[25], with this phenomenon also captured on DES studies by Martini *et al.* [23][24] where a thick blunt lip induces the strong interaction of air from the ejection slot and the mainstream gas.

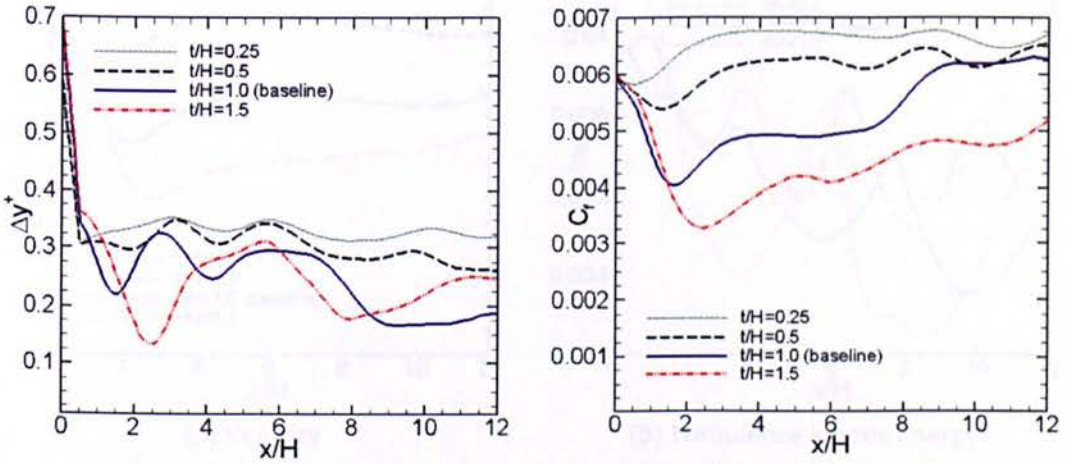

(a) Δy^+ (b) Coefficient of skin frictions

Figure 6–12: Grid resolution effect at the protected wall.

Figure 6–13 gives the laterally averaged flow velocity and turbulence kinetic energy at y-y_{aw} = 0.1mm along the cutback/breakout region. This scenario is taken into account in an effort to inspect the discrepancy along the protected wall. This is due to both velocity and turbulence kinetic energy being zero at the adiabatic wall, which causes a difficult situation to have the data to be linked with the temperature at the protected wall (see Figure 6–11) and the adiabatic film-cooling effectiveness (Figure 6–10(b)) thereafter. A similarity of trend between temperature (T) at the adiabatic wall and the air temperature (T_1) at y-y_{aw} = 0.1mm would be expected to explain those relations. As would be discussed in section 6.5.5.1, the evolution of temperature shows the same trend as the end wall

temperature within a distance of up to 0.5 mm from the adiabatic wall (see Figure 6–15). Therefore, the discrepancy of performance could be explained by investigating the mixed-air properties at y-y_{aw} = 0.1mm along the cutback region.

It has been found that the decrease of t/H ratios causes the increase of mixing flow velocity and turbulence kinetic energy along the mixing region. The fluctuation of turbulence kinetic energy is reduced by decreasing lip thickness, while it grows up with raising lip thickness as shown in Figure 6–13(b). Both are at the higher level for the case with the lowest t/H ratio of 0.25. An experimental study carried out by Horbach *et al.* [30][35] noted that a turbulence level is increased for thicker lip thickness. Unfortunately, there are no available data for comparison.

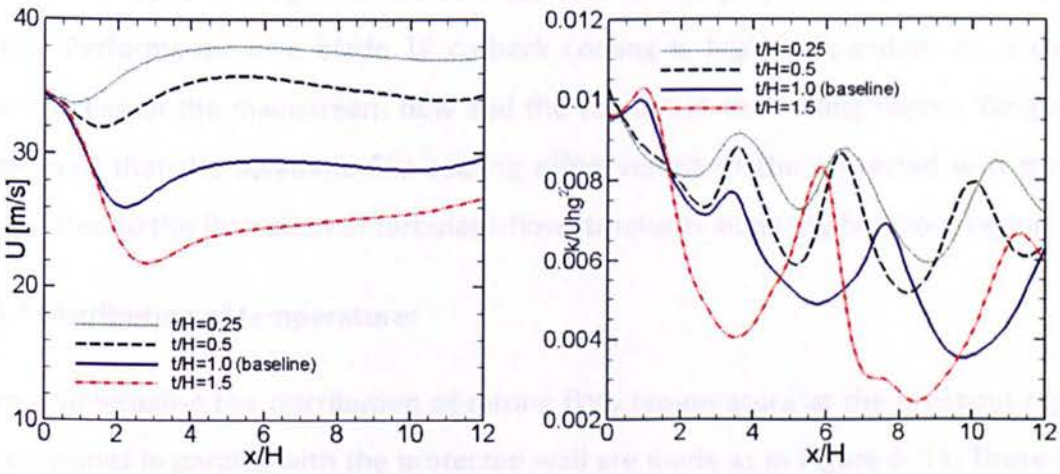

(a) Velocity (b) Turbulence kinetic energy

Figure 6–13: Mixed-air properties at the y-y_{aw} = 0.1mm.

From Figure 6–13(a), it is seen that all variations generate the same coolant flow velocity at level of 34 m/s when ejecting from the slot exit. This flow condition is changed along the cutback region depending on t/H ratios. The flow velocity is rapidly decreased at the lowest level of 22 m/s between $0 < x/H < 3$ for the case with the highest t/H ratio of 1.5, and then increased slightly after this point. The decrease is gradually reduced for other variations and followed by a reduction of peaks distance in streamwise direction concomitant with reduction of from t/H ratio of 1.0 and 0.25. This may be attributed to the vortex-shedding behind the lip. The strongest decrease for the case with the highest t/H ratio of 1.5 is likely caused by a larger wake formed at the shaddow trianlge area that give a widen resirculation flow. In contrast, a smaller vortex-shedding behind the lip

reduces that effect, as can be compared in Figure 6–13(a).The discrepancy of mixing flow velocity near the protected wall causes a different regeneration of coolant flow near this region. For example, a higher level of flow velocity for the case with lower lip thickness accelerates the regeneration of coolant from the slot exit. This process is much faster than at a lower flow velocity. Therefore, the protected wall is shielded continuously by the regeneration of coolant as an increase of flow velocity along the mixing region. Finally, the adiabatic film-cooling effectiveness is near unity for the case with the thinnest lip thickness (see Figure 6–10).

6.5.5 Dynamic Mixing Process at the Breakout Region

The unsteadiness of mixing flow has an important role to play in the local heat-transfer process. Performance of a blade TE cutback cooling is highly dependent on a mixing process between the mainstream flow and the coolant at the mixing region. Yang *et al.* [6] believed that the adiabatic film-cooling effectiveness of the protected wall is most likely related to the formation of turbulent-flow structures along the breakout region.

6.5.5.1 Distribution of temperature:

In order to visualise the distribution of mixing flow temperature at the breakout region, nine poly-lines in parallel with the protected wall are made as in Figure 6–14. These lines follow the angle of coolant ejection at 10°. Each line represents the laterally averaged temperature at the same *x-z* plane in a certain distance from the protected wall, which is computed by adopting equation (5.1). It is calculated at the same manner as the laterally averaged film-cooling effectiveness shown in Figure 6–10.

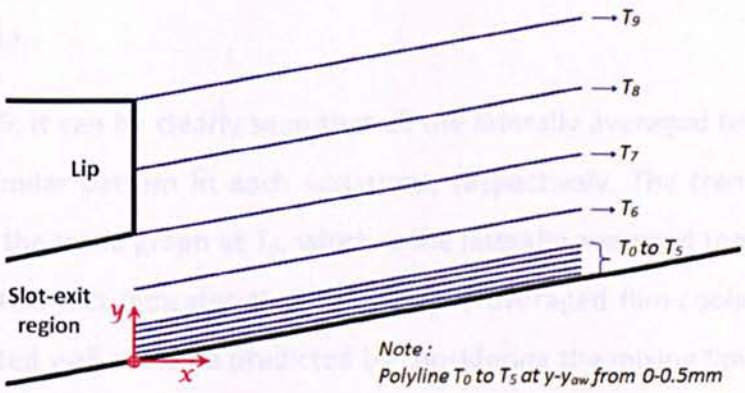

Figure 6–14: The position of laterally averaged data.

Figure 6–15 shows the distribution of mixing flow temperature as the effect of four various t/H ratios. These charts follow the nine polylines as previously defined in Figure 6–14. It is found that the change of lip thickness influences the distribution of air temperature at the mixing region. For example, all the laterally averaged temperature of T_9 tend to have a similar trend with a specific peak temperature around x/H = 1.5, depending on the lip thickness. A lower peak temperature for the case with lower lip thickness is probably caused by a smaller vortex-shedding formed behind the lip. It is reasonable due to the triangle region is smaller than the other variations. Therefore, the mainstream flow tends to have a big impact from the ejection coolant as the recirculation effect of unsteady vortex-shedding, mainly behind the lip region. After attaining a peak level, all the laterally averaged temperature of T_9 decreases gradually up to a certain temperature depending on the growth of vortex-shedding along the breakout region in each variations. This temperature distribution relates to the turbulent flow structures formed at the mixing region as the multiple effect of mixing-flow regeneration between mainstream flow and coolant.

Similarly, all the laterally averaged temperature of T_8 is dominated by main hot-gas temperature, where these temperatures are less than at T_9. The domination is more pronounced for a higher t/H ratio, mainly near the slot exit (x/H = 0).

The laterally averaged temperature of T_7 has a different trend in every case studied, especially between $0 < x/H < 2$. This implies that vortex-shedding exist behind the lip within different size, which depends on the triangle area. The increase of t/H ratio creates a bigger vortex-shedding that gives a different effect against the laterally averaged temperature of T_7, mainly near the slot exit region. This is due to the recirculation flow around this region.

From Figure 6–15, it can be clearly seen that all the laterally averaged temperature from T_0 to T_5 has a similar pattern in each variations, respectively. The trend graph at T_5 is identical against the trend graph at T_0, which is the laterally averaged temperature at the protected wall. This fact indicates that the laterally averaged film-cooling effectiveness along the protected wall could be predicted by considering the mixing flow behaviour in a range of this distance (up to 0.5 mm). However, it is fairly seen a slight discrepancy. Based

on the laterally averaged temperature from T_0 to T_5, it can be stated that near the slot exit between $0 < x/H < 4$ is dominated by the ejecting coolant, which is far away from the mainstream flow effect. As mentioned above, a bigger vortex-shedding occurs for the case with a higher t/H ratio, which is more potential to grow up with a bigger wavy. A recirculation effect of unsteady vortex-shedding causes the growth of wavy flow along the breakout region, and this becomes more bigger at the downstream region. Therefore, it influences an intensified mixing between the mainstream flow and the coolant, meaning the mainstream gas, with its higher temperature, is more able to reach the protected wall. Consequently, the increase of wall temperature near the downstream region is more noticeable for the highest t/H ratio due to a stronger magnitude and a wider flow oscillation period.

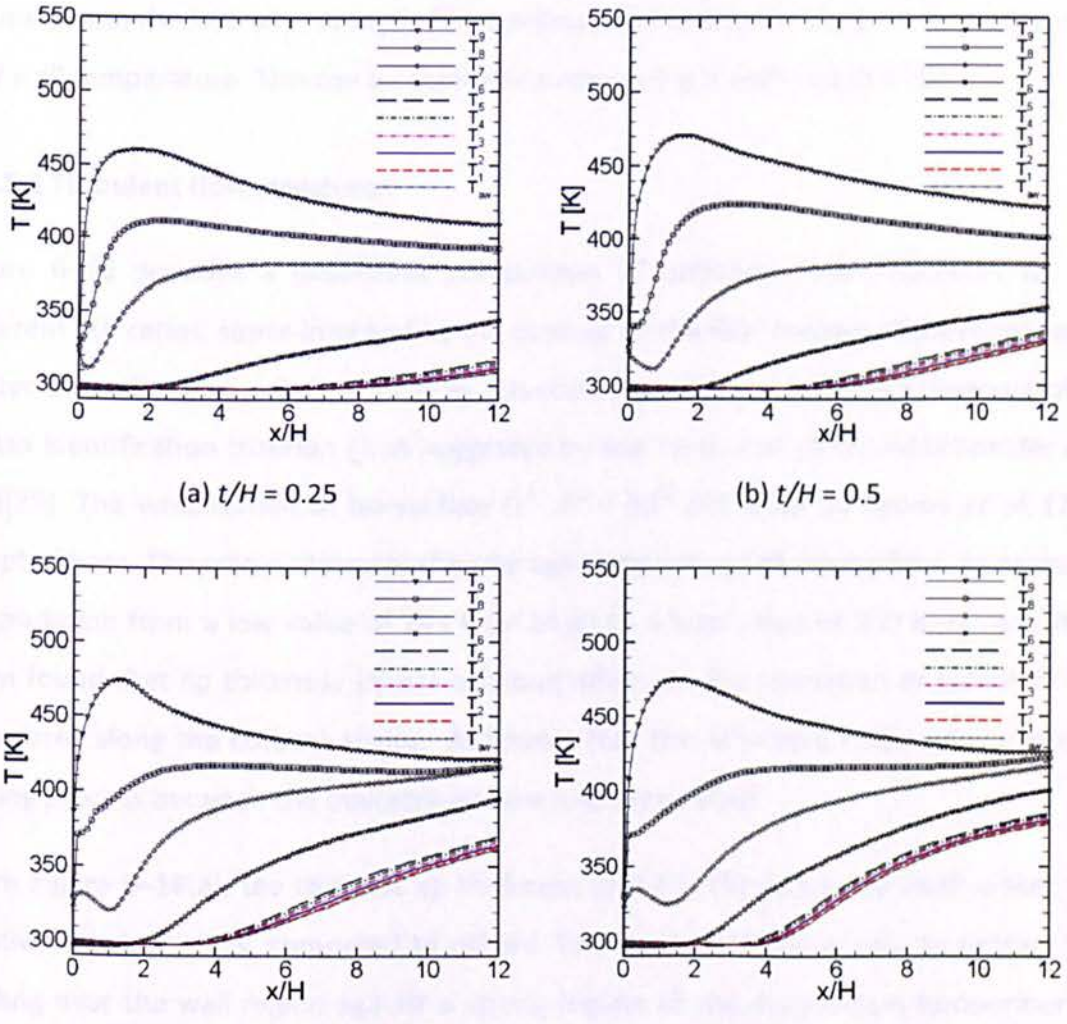

(a) $t/H = 0.25$ (b) $t/H = 0.5$

(c) $t/H = 1.0$ (baseline) (d) $t/H = 1.5$

Figure 6–15: Temperature distribution at the mixing region (T_{hg} = 500 K, T_c = 293 K)

In contrast, smaller wakes obtained by simulation from the thinnest lip thickness causes a domination of film-cooling almost across the entire surface of the adiabatic wall. Smaller wakes over the breakout region are most effective when seeking to keep the coolant at the lowest temperature level along the adiabatic wall.

By comparing Figure 6–15 with Figure 6–16, it can be seen that the distribution of air temperature is strongly influenced by unsteady vortex-shedding of mixing process at the breakout region. This finding confirms the previous experiments carried out by Martini *et al.* [23][24], Horbach *et al.* [30][35] and Holloway *et al.* [25], who studied unsteadiness at the TE breakout. Typical turbulent flow structures of each variety of *t/H* ratios affect the end wall temperature at the protected wall, as shown in Figure 6–15. Due to the adiabatic film-cooling effectiveness over the protected wall being a function of the end wall temperature, the laterally averaged film-cooling effectiveness follows the tendency of the end wall temperature. This can be seen when comparing it with Figure 6–10.

6.5.5.2 Turbulent flow structures:

Figure 6–16 provides a qualitative comparison of turbulent flow structures for four different *t/H* ratios, super-imposed by the contour of the film-cooling effectiveness at the protected wall surface. Turbulent flow structures are presented by iso-contours of the vortex identification criterion Q, as suggested by von Terzi *et al.* [137]and Schneider *et al.* [28][29]. The visualisation of iso-surface $\Omega^2 - S^2 = 10^5\ 1/s^2$ used by Egorov *et al.* [22] is adopted here. The colour indicates the average temperature of mixing flow, as expressed by gradation from a low value of 293 K (in blue) to a high value of 500 K (in red). It has been found that lip thickness (*t*) has a strong effect on the formation of turbulent flow structures along the cutback region. As known that this structure represents a dynamic mixing process between the mainstream flow and the coolant.

From Figure 6–16(a), the thinnest lip thickness (*t/H* = 0.25) generates small wakes with relative shorter waves, compared to others. This flow condition is able to protect film-cooling near the wall region against a strong impact of the mainstream temperature. In fact, the blue colour as a representation of the film-cooling almost dominates at the protected wall surface.

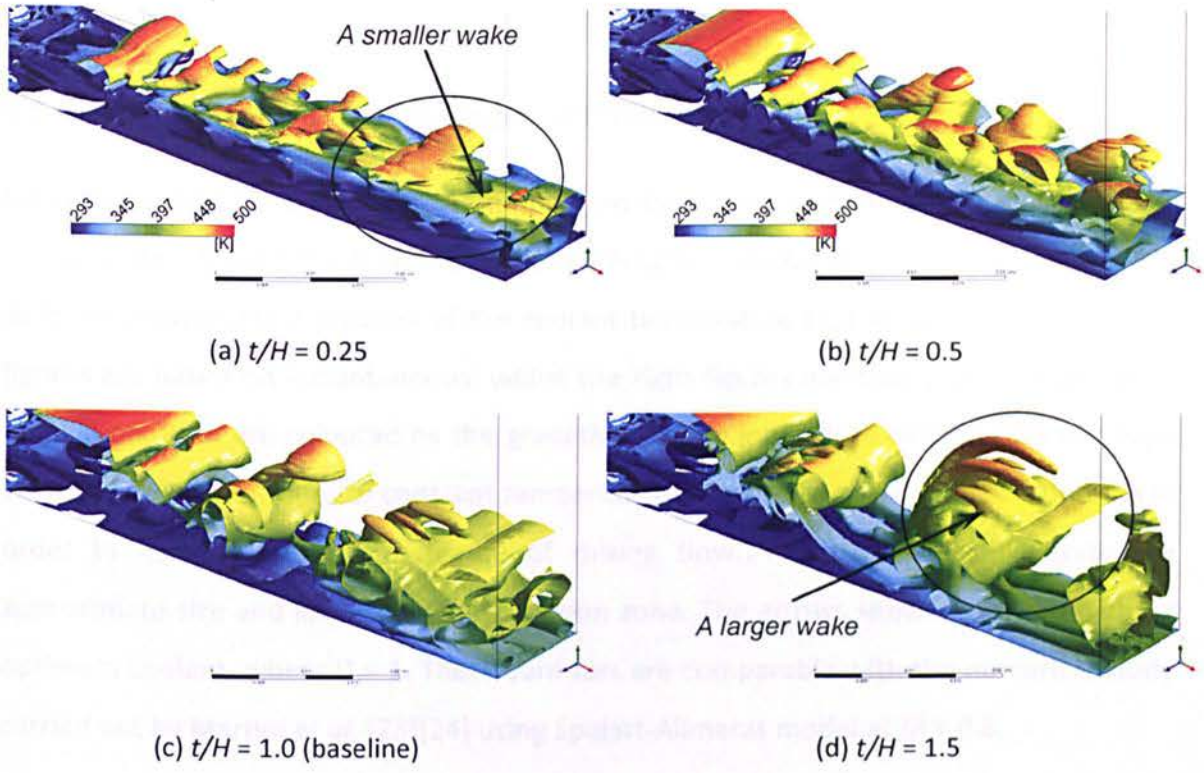

(a) $t/H = 0.25$ (b) $t/H = 0.5$

(c) $t/H = 1.0$ (baseline) (d) $t/H = 1.5$

Figure 6–16: Turbulent flow structures.

Wakes and unsteadiness are more pronounced when increasing t/H ratio. Wakes with a strong intensity grow up along the cutback region, followed by the growth of vortex-shedding with longer waves. This vortex-shedding is more-and-more stronger for the case with a higher t/H ratio, as seen clearly at the downstream region (see Figure 6–16(d)). This triggers a strong mixing between the mainstream flow and the film cooling slot jets, which degrades the adiabatic film-cooling effectiveness. Indeed, a decay of the film cooling effectiveness is obvious for a higher t/H ratio (see Figure 6–10). This finding matches with measurements carried out by Chen *et al.* [39], who found a degradation of the film cooling effectiveness due to an intensive mixing on a trailing-edge cooling.

This numerical study indicates that DES simulation could be used to predict well, such as when seeking to realise the previous experimental findings investigated by Taslim *et al.* [31][56], Krueckel *et al.* [14] and Horbach *et al.* [30][35], which maintain that a thinner lip thickness ratio produces higher film-cooling effectiveness. This also proves a forgoing research done by Holloway *et al.* [25], which identified that a larger lip thickness accelerates more film-cooling effectiveness decay due to intensified vortex-shedding.

6.5.6 Instantaneous and Time-averaged Temperature

Figure 6–17 depicts contours of the non-dimensional temperature (θ) distribution at the *x-y* plane for a fixed *z/H* = 0 on four various *t/H* ratios. The location of this plane is in-line with the measurement position of the coolant temperature ($T_{c'}$) at the slot exit. The left figures are based on instantaneous, whilst the right figures are based on time-averaged calculation. Both are coloured by the gradation from a low values of 0 (in red) to a high values of 1 (in blue). Lines of constant temperature are superimposed on both contours in order to help assessing the degree of mixing flow. The streamlines illustrate the approximate size and location of recirculation zone. The arrows show a location with an optimum coolant, where θ = 1. These contours are comparable with the numerical study carried out by Martini *et al.* [23][24] using Spalart-Allmaras model at *M* = 0.8.

Form Figure 6–17, it is recognised that the instantaneous non-dimensional temperature (left figures) express a highly unsteady mixing process between the mainstream flow and the coolant air which indicates the pattern of vortex-shedding. The periodic pattern of wakes from the lip can be clearly identified with different intensities of the instantaneous contour on each variety *t/H* ratio. The increase of lip thickness causes the growth of wave flow with greater intensity and sporadic period. The mode of wave flow most likely influences the discrepancy of film-cooling effectiveness due to a different intensity of mixing process. As recognised by Schneider *et al.* [29], the instantaneous flow field has pairs of counter-rotating vortices due to the existence effect of lip. The vortices are very pronounced when increasing *t/H* ratio, as shown on the left Figure 6–17. These vortices are similar to those discovered in a von Karman vortex street (see Figure 2–5, page 34).

As discussed earlier, temperature at the protected wall surface is most likely related to the formation of turbulent flow structures along the cutback region. This formation affects the penetration of mainstream flow towards the coolant near the protected wall. This is obvious at a higher *t/H* ratio, as illustrated in Figure 6–17(d).

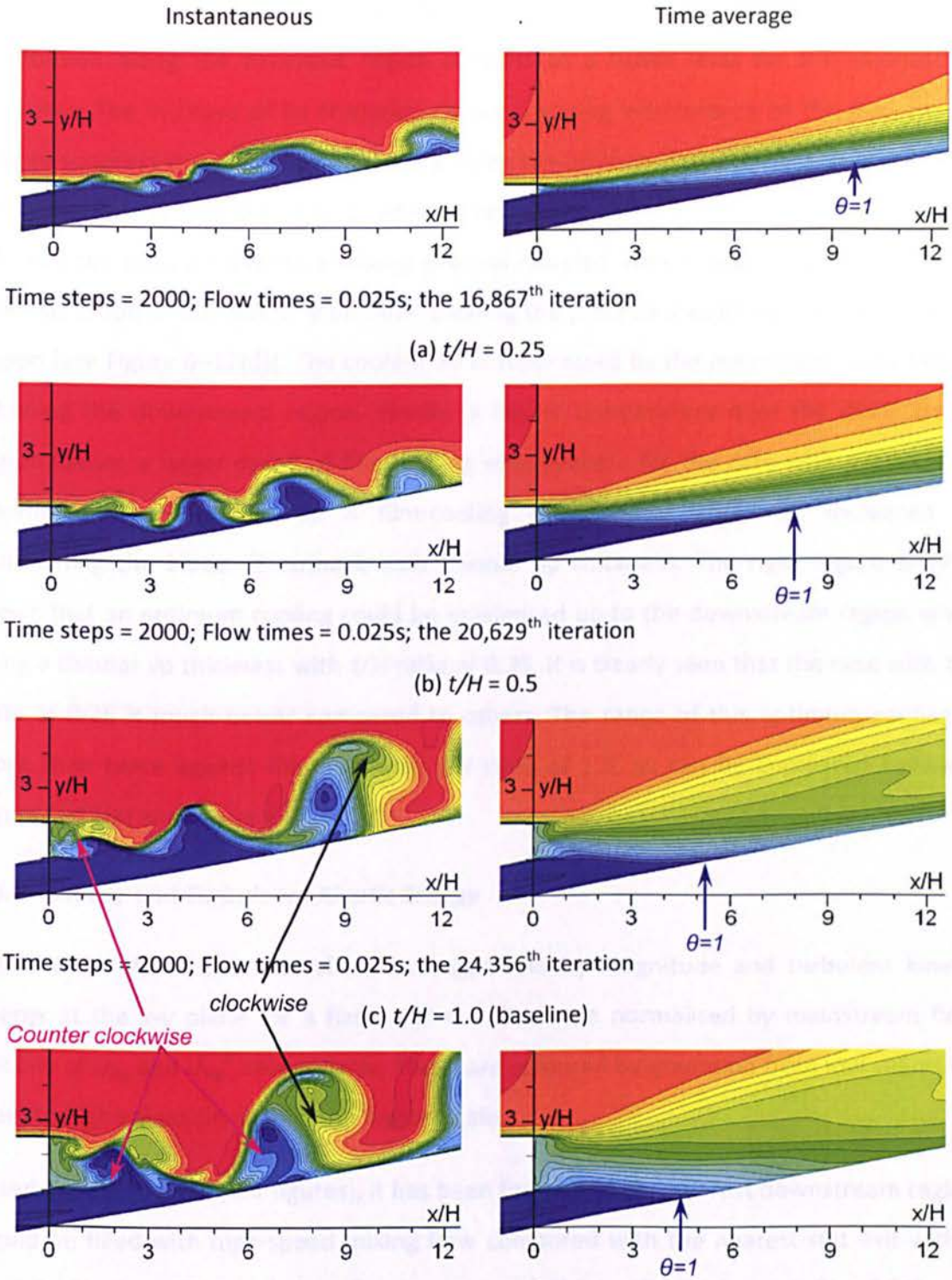

Time steps = 2000; Flow times = 0.025s; the 16,867th iteration

(a) t/H = 0.25

Time steps = 2000; Flow times = 0.025s; the 20,629th iteration

(b) t/H = 0.5

Time steps = 2000; Flow times = 0.025s; the 24,356th iteration

(c) t/H = 1.0 (baseline)

Time steps = 2000; Flow times = 0.025s; the 24,738th iteration

(d) t/H = 1.5

Figure 6–17: Non-dimensional temperature distribution ($\theta = \left[\frac{T_{hg} - T}{T_{hg} - T_{c'}}\right]$).

Based on the time-averaged contour (right figures), the non-dimensional temperature (θ) distribution along the breakout region remains at a lower level for the thinnest lip thickness. The increase of lip thickness causes a strong interference of the mainstream flow to suppress the shielded film cooling along the protected wall surface. It is indicated by the narrowing blue colour of θ, which is only up to x/H = 4.5 for a higher t/H ratio of 1.5. Besides that, an intensive mixing process coupled with a large wake influences a spacious scope of the mainstream flow reaching the protected wall near the downstream region (see Figure 6–17(d)). The coolant air is suppressed by the mainstream flow before attaining the downstream region. Finally, a higher temperature near the downstream region causes a larger decay of film-cooling effectiveness for the case with a thicker lip thickness (see Figure 6–10). A film-cooling effectiveness could be increased by maintaining the blade TE cutback with thinner lip thickness. The right Figure 6–17(a) shows that an optimum cooling could be maximised up to the downstream region when using a thinner lip thickness with t/H ratio of 0.25. It is clearly seen that the case with t/H ratio of 0.25 is much better compared to others. The range of this optimum cooling is more than twice against the case with t/H ratio of 1.5, as can be compared between Figure 6–17(a) and Figure 6–17(d).

6.5.7 Velocity and Turbulence Kinetic Energy

Figure 6–18 shows the normalised averaged-velocity magnitude and turbulent kinetic energy at the x-y plane for a fixed z/H = 0. Both are normalised by mainstream flow velocity of U_{hg} and U_{hg}^2, respectively. These are coloured by gradation from low values (in blue) to high values (in red) on the typical scale.

Based on Figure 6–18 (left figures), it has been found that the nearest downstream region would be filled with high-speed mixing flow compared with the nearest slot exit within typical t/H ratios. This is obvious for the case with thinner lip thickness (t/H = 0.25), and the mixing flow speed gradually reduces through increasing the lip thickness. Certainly, this causes a different regeneration of the coolant flow near to the protected wall. A reduction in the local air velocity along the breakout delays the regeneration of coolant flow from the ejecting slot to shield the adiabatic wall surface; therefore, local air temperature tends to be at a higher level, as seen in Figure 6–17(d) on the right image.

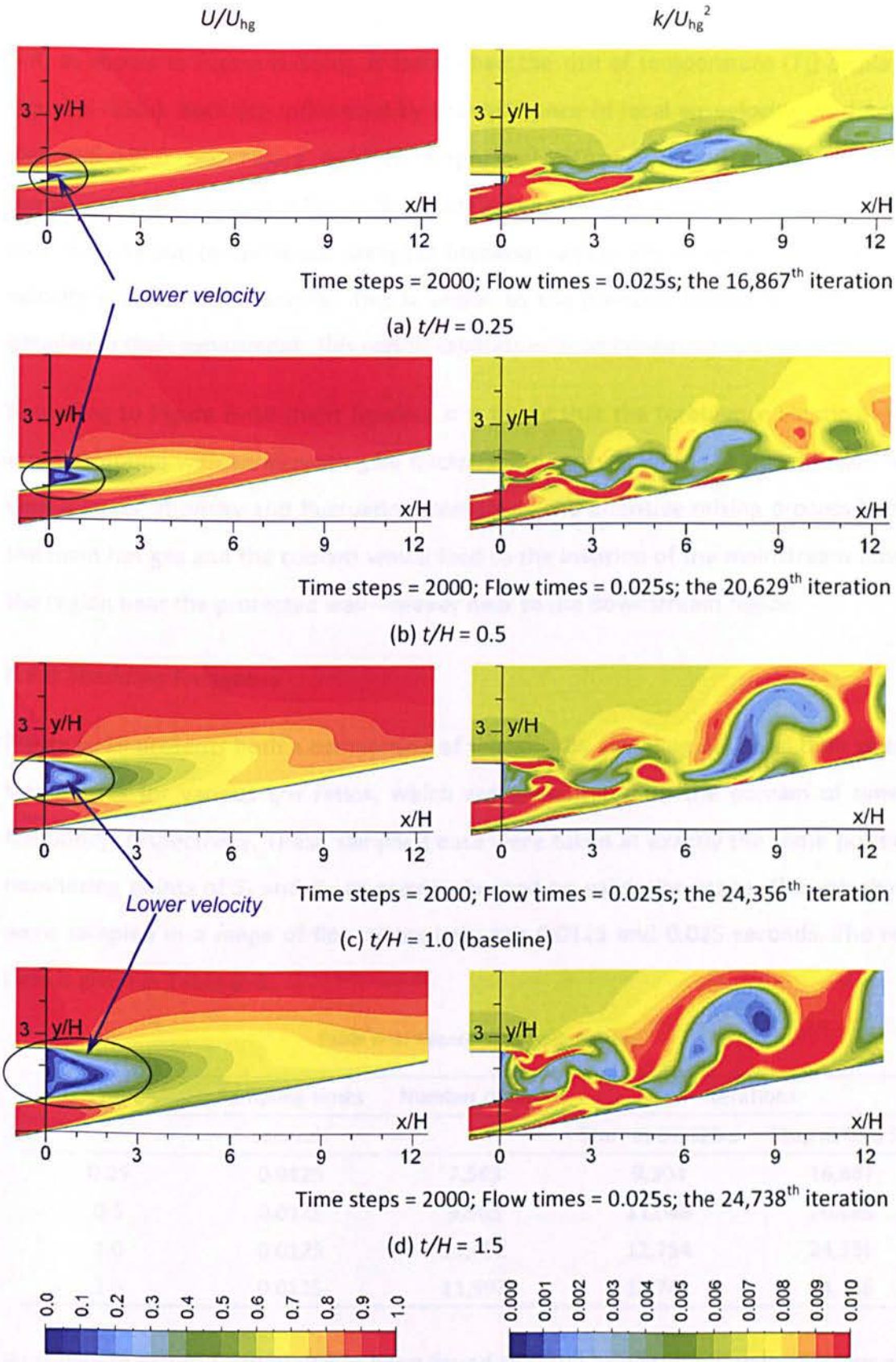

Figure 6–18: Normalised velocity and turbulent kinetic energy.

As previously presented in Figure 6–15, the increase in mixing temperature (T_1) after $x/H > 4$, as shown in Figure 6–15(d), is faster than the rise of temperature (T_1) displayed in Figure 6–15(a). Both are influenced by the difference of local air velocity, as detailed in Figure 6–18(a) and Figure 6–18(d), respectively. The gradation of non-dimensional temperature distribution in Figure 6–15 confirms a strong relation between the change of local velocity and temperature along the breakout region. Moreover, a region with lower velocity is seen behind the lip. This is similar to the previous finding of Yang *et al.* [6], detailed in their experiment. This region expands with an increasing lip thickness.

According to Figure 6–18 (right figures), it is found that the turbulence kinetic energy is more profound with an increasing lip thickness. This grows up to the downstream region with a larger intensity and fluctuation; therefore, the intensive mixing process between the main hot gas and the coolant would lead to the invasion of the mainstream flow into the region near the protected wall—mainly near to the downstream region.

6.5.8 Shedding Frequency

Figure 6–19 presents both a comparison of the velocity sampling data and their shedding frequencies for various t/H ratios, which are presented with the domain of time and frequency, respectively. These sampling data were taken at exactly the same position of monitoring points of S_1 and S_2, as previously used on validation stage. The velocity data were sampled in a range of flow times between 0.0125 and 0.025 seconds. The record data is given in Table 6–3.

Table 6–3: Record of sampling data.

t/H ratios	Sampling times	Number of data	Iterations	
	seconds		Start at 0.0125 s	Stop at 0.025 s
0.25	0.0125	7,563	9,304	16,867
0.5	0.0125	9,583	11,046	20,629
1.0	0.0125	11,602	12,754	24,356
1.5	0.0125	11,997	12,741	24,738

As shown in Figure 6–19(a), it has been found that the amplitude of velocity is increased by raising t/H ratios. This result matches the vortex-shedding, as depicted using the turbulent flow structures in Figure 6–16. The amplitude of velocity resulting from the

thickest lip thickness is more than two times that of the thinnest one. A slight difference of the amplitude for both two monitoring points at S_1 and S_2 is caused by the co-existence of the pin-fin array within the cooling passage. The blockages of the pin-fin array probably influence the distribution of the flow velocity when ejecting from the slot exit. This is very pronounced for the case with lower *t/H* ratio where the gas flow velocity at *z/H* = 0 is greater than at *z/H* = 1.25, as illustrated in Figure 6–19(a). Therefore, this discrepancy causes the different flow velocity along the mixing region. Based on Figure 6–19 (the left figures), simulation using the smallest lip thickness generates a harmonic wave pattern in typical mode. Sub-harmonic wave is captured in this case simulation, as found by Medic *et al.* [26]. The response also contains a sub-sub harmonic wave with a stronger intensity when increasing *t/H* ratios. Moreover, the beating phenomenon is pronounced for the case with higher *t/H* ratios, for example at 1.0 and 1.5. It is caused by the 3D effect of turbulent flow mixing which probably generates a similar frequency in each wave. Both mainstream flow and the ejecting coolant produce a close frequency when mixing process, as the effect of increasing *t/H* ratios. It is known that a mutual interference occurs for two or more waves with a close frequency. The accumulation of these waves causes the combined amplitudes, which results in the envelope wave of the beating phenomenon. It can be clearly seen on the left Figure 6–19(c).

In terms of frequency, it has been found (as shown in the right Figure 6–19(b)) that the increase of *t/H* ratios causes the decrease of the dominant frequency. Sequentially, the vortex-shedding frequencies are f_s = 3.69, 3.2, 2.21, and 1.49 kHz from the thinnest to the thickest lip thickness, respectively. This prediction is appropriate with the relation of frequency and period where frequency is proportionate to a reverse period. The frequency predicted by the baseline specimen with *t/H* ratio = 1.0, compared to the previous study, is also discussed in section 5.5 (see page 100). It is based on the time variant of velocity components (u, v, w) at the same position of this sampling data. The results were seen to agree well against the available data of Martini *et al.* [23][24], which reports a dominant frequency f_s = 2.36 kHz based on simulation at the blowing ratio *M* = 0.8. An analytical calculation, as suggested by Martini *et al.* [23][24] using equation (2.13), found that the shedding frequency should be approximately 2.4 kHz with reference to the effective lip thickness of 5mm and the mainstream velocity at u_{hg} = 56 m/s.

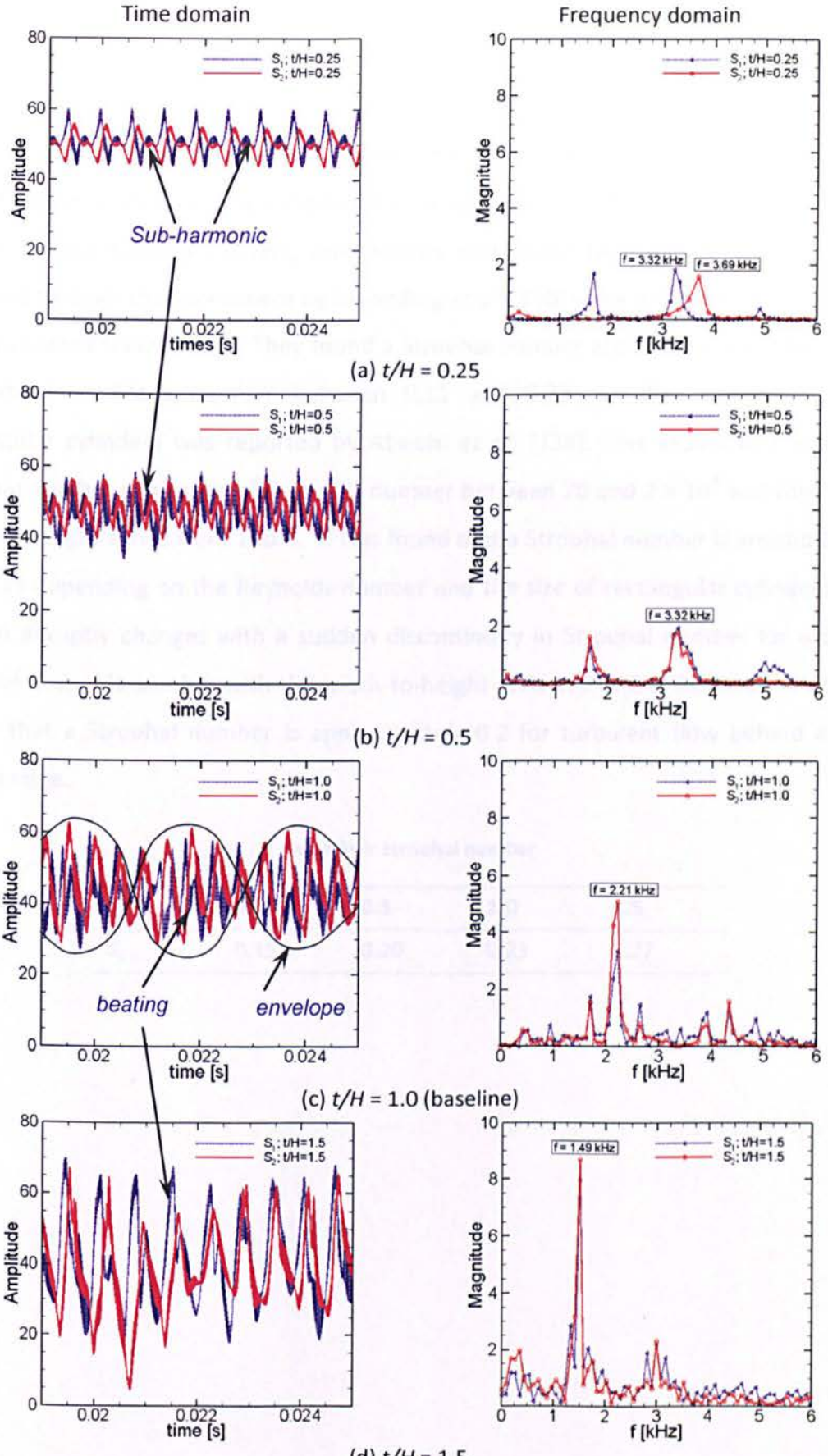

Figure 6–19: Shedding frequencies.

By using a Strouhal number equation (2.13) in Chapter 2, all dominant frequencies predicted above can be calculated in terms of Strouhal number, as presented in Table 6–4. The level of Strouhal number is around 0.15 and 0.23 for various *t/H* ratios. A lower Strouhal number for the case with the lowest *t/H* ratio is most likely to be related to their vortex shedding frequency. Comparing the Strouhal numbers for the two TE geometries with turbulent boundary layers, one notices that these findings are close to those garnered through the experiment by Sieverding *et al.* [130] using a simple flat plate model with a squared trailing-edge. They found a Strouhal number around $S_t = 0.215$ from their experiment at Mach number between 0.11 and 0.25. Another experiment using rectangular cylinders was reported by Atsushi *et al.* [138]. This experiment evaluated Strouhal number in a range of Reynolds number between 70 and 2×10^4 and the ratio of width-to-height varies from 1 to 4. It was found that a Strouhal number is around $S_t = 0.1$ and 0.15 depending on the Reynolds number and the size of rectangular cylinders. Flow pattern abruptly changes with a sudden discontinuity in Strouhal number for a certain range of Reynolds number with the width-to-height ratio of 2 and 3. Boldman *et al.* [131] report that a Strouhal number is approximately 0.2 for turbulent flow behind a blunt trailing edge.

Table 6–4: Strouhal number.

t/H	0.25	0.5	1.0	1.5
S_t	0.15	0.20	0.23	0.22

6.6 Summary

The blade TE cutback cooling for various *t/H* ratios has been studied computationally. DES, using the SST $k-\omega$ turbulence model, was applied for these simulations. The results have been presented with a good agreement against the available data of experiments. It has been proven by the agreement of predicted performance for the baseline model in terms of discharge coefficient, film-cooling effectiveness and vortex shedding frequency. Based on the results and discussion above, the following conclusions can be made:

1. The change of *t/H* ratio does not influence the heat-transfer process inside the cooling passage; it has been proven by the coolant flow behaviour at the surface of pin-fin and the coolant flow along the cooling channel, which is exactly the same in each row of pin-fin for all *t/H* ratios. A slight discrepancy at the slot exit is most likely triggered by a recirculation vortex-shedding behind the lip, which influences the ejecting coolant.
2. The increase of *t/H* ratio of the blade TE cutback cooling causes the decrease of the adiabatic film-cooling effectiveness, mainly near the downstream region. It is due to an intensified mixing process between the ejecting coolant and the mainstream gas at the mixing region. It is shown qualitatively by the growth of the turbulent flow structures when increasing *t/H* ratios, and can be seen quantitatively by an increasing of the amplitude of airflow velocity and the magnitude of shedding frequency. This finding is consistent with the experiment carried out by Horbach et al. [30] who investigated a trailing-edge cutback cooling in different geometry and internal cooling features.

3. The dominant frequency is decreased by increasing the *t/H* ratio from 0.25 to 1.5. The spectrum frequencies are f_s = 3.69, 3.2, 2.21, and 1.49 kHz from thinner to thicker lip thickness. This frequency corresponds to S_r = 0.15, 0.20, 0.23, and 0.22, respectively.

CHAPTER 7:

CASE II: BLADE TRAILING-EDGE CUTBACK COOLING WITH VARIOUS INTERNAL COOLING DESIGNS

This chapter describes the computational study of the blade trailing-edge (TE) cutback cooling with various internal cooling designs. The internal feature inside the cooling passage of the baseline model as previously used for validation is modified with three different shapes (i.e. empty duct, circular and elliptic pin-fin). Similar to previous study, the domain width for this study is devised within a single-pitch distance of pin-fin array. The generation of mesh and the use of turbulence model are similar to the computation of case 1 (see Chapter 6). The local 2D structured meshes for both circular and elliptical pin-fin are presented in this chapter, whilst the other regions have the same resolution as shown in Figure 4–4 (see page 69). The measurement data of the blade TE cutback with pin-fin cooling, as derived in the works of Martini *et al.* [4][5][23][24] and Horbach *et al.* [30], are referred to in an effort to assess the results of this investigation.

7.1 Internal Features inside the Cooling Passage

The internal feature inside the cooling passage such as pin-fin array is a key role parameter that affects the performance of the gas turbine blade trailing-edge cooling. It is known that the pin-fin cooling is commonly integrated with the trailing-edge ejection cooling. The pin-fins usually have the ratio of height-to-diameter between 0.5 and 4. This is typically applied to enhance heat-transfer from the blade wall around the pin-fin region. Heat is transferred from both the end-wall and the pin-fins array. The flow separation and wakes are shed at the pin-fin downstream, followed by horseshoe vortex. This creates additional mixing, and then enhances heat transfer. The main reason of this application is due to manufacturing constraint in the very tight trailing-edge of gas turbine blade. Han *et al.* [12] noted that the distribution of heat-transfer in the cooling

passage is strongly affected by the design of pin-fins array. They highlighted the design of internal features, such as the type of array, spacing, size and shape, for consideration when investigating the pin-fin cooling.

The blade trailing-edge cooling performance has been studied experimentally and numerically for many years, with various configurations, including staggered or in-line arrangement with cylindrical [13][33][44][45], elliptical pin-fins [13][34][139][140][141] [142], rectangular [142][143][144], diamond [145][146] and drop-shaped [147] (see Table 7–1 below). Amongst these studies, Tarchi *et al.* [13] carried out an experimental research by proposing innovative trailing-edge internal cooling designs with a pentagonal arranged circular pin-fin and staggered elliptical pin-fin. Similar configurations were further investigated by Carcasci *et al.* [34] and Bianchini *et al.* [33], involving turning flow in front of the cooling passage. Facchini *et al.* [3][7][148] also evaluated the effects of turning flow using different internal cooling designs with enlarged pedestals and square or semi-circular ribs. The results showed that the combined effect of flow acceleration and pin-fin array lead to a significant increase of the heat-transfer. The heat-transfer coefficient of pin-fin surface is always greater than that of the surrounding end wall. In terms of the pressure loss, the streamwise elliptical pin-fins orientation has a significant contribution to an overall decrease in pressure drop.

The studies as mentioned in various literatures above did not address the mixing flow interaction between the mainstream flow and the coolant from the ejection slot. The shielded film-cooling near the downstream region was not investigated here; these only emphasised the performance of the pin-fin cooling. Similar previous researches of the pin-fin cooling on various models are listed in Table 7–1.

Aside from the literature reviews detailed above, comprehensive studies of a blade TE cooling, with consideration to the internal features inside the cooling passage, as shown in Table 7–2, have been performed experimentally and numerically for in-line array [20][22][35][36] and staggered arrangements [14][23][24][30], including empty duct [19][25]. Various shapes of the pin-fin array were used in those studies, such as long ribs [4][5][15][16], cylindrical pin-fins [41][149] and elliptical pin-fins 5 with streamwise and spanwise orientation. It was found that the elliptical pin-fin configuration inside the

cooling passage causes a strong effect in terms of both discharge behaviour (C_D) and film-cooling effectiveness (η_{aw}). It should be noted that several investigations, as listed in Table 7–2, used different initial and boundary conditions, including their geometries.

Table 7–1: Investigation of the pin-fin cooling.

Investigators	Arrangement	Row	Pin shape	*S/D*	*Sx/D*	shape duct	Re
Bianchini, C. *et al.*, [33]	Staggered	7	Cylindrical	2.3	1.86	10 degree (fitted)	18,000
Ames, F.E. *et al.* [44][45]	Staggered	8	Cylindrical	2.5	2.5	-	3,000; 10,000 & 30,000
Metzger, D.E. *et al.* [133]	Staggered	10	Cylindrical	1.5-2.5		square duct	1,000<Re< 1,000,000
Lawson, SA. *et al.*,[134]	Staggered	7	Cylindrical	2	1.73	square duct	5,000 – 30,000
Lau, S.C. *et al.* [150]	Staggered	15	Cylindrical	2.5	2.5	-	10,000 - 60,000
Won, S.Y. *et al.* [151]	Staggered	12	Cylindrical	2		square duct	18,700 - 110,900
Su, G. *et al.* [152]	Staggered	12	Cylindrical	2		square duct	10,000 – 100,000
Dellibra, G. *et al.*, [153]	Staggered	8	Cylindrical	2.5	2.5	-	10,000 & 30,000
Yu, R. *et al.* [154]	Staggered	4	Cylindrical	1.5-2.5		square duct	1,678-8,500
Chyu, M.K. *et al.* [135]	Staggered In line	7 7	Cylindrical	2.5		square duct	5,000 – 25,000
Mitre, J.F. *et al.* [136]	Staggered In line	7 7	Cylindrical	1.25-2.5	1.25-2.5	square duct	7,000 – 23,000
Hwang, J.-J. *et al.*, [155][156][157]	Staggered In line	5 5	Cylindrical Cylindrical	2.5 2.5	2.5 2.5	Trapezoidal duct	6,000 - 40,000
Tarchi, L. *et al.*, [13]	Staggered	7 6	Cylindrical Elliptical	2.3 2.5	1.86 2.17	10 degree (fitted)	9,000 – 27,000
Uzol, O. *et al.*, [139] [140]	Staggered	2 2	Cylindrical Elliptical	2 2	2 2	-	10,000 & 47,000
Carcasci, C. *et al.*, [34]	Staggered	6	Elliptical	2.5	2.17	10 degree (fitted)	18,000
Li *et al.* [141]	Staggered	10	elliptical	1.1-3		square duct	1,000 – 10,000
Yang, K.S. *et al.* [142]	Staggered In line	5 5	elliptical rectangular			square duct	-
Sara, O.N. *et al.* [143]	Staggered	4-13	rectangular			square duct	10,000 – 34,000
Saha, A.K. *et al.* [144]	In line	15	rectangular	1.1-3		square duct	180-600
Jeng, T.M. [158]	Staggered In line	15	rectangular			square duct	< 20,000
Tanda, G. [145]	Staggered In line	7-14 7-13	Diamond			square duct	8,800 – 20,000
Jeng, T.M. [146]	In line	15	Diamond			square duct	
Chen, Z. *et al.* [147]	Staggered	10	Drop-shaped			square duct	900 – 9,000

Table 7–2: Investigation of the TE cooling with pin-fin inside cooling passage.

Investigators	Arrangement	Row	Pin shape	*S/D*	*Sx/D*	Wedge-shape duct
Martini, *et al.* [15][16]	In line	2	long ribs	2		10 degree (fitted)
Martini, *et al.* [20]	In line	2	long ribs	6		10 degree (fitted)
Egorov, *et al.* [22]	In line	2	long ribs	-	2.5	10 degree (fitted)
Hepeng, *et al.* [36]	In line	1	long ribs	-	2.5	0 degree
Horbach, *et al.* [35]	In line	2	long ribs	-		10 degree (fitted)
Martini, *et al.* [4][5]	In line Staggered	2 5 & 6	long ribs cylindrical	- 2.5	2.5	10 degree (fitted)
Martini, *et al.* [23][24]	In line Staggered	2 5 & 6	long ribs cylindrical	- 2.5	2.5	10 degree (fitted)
Horbach, *et al.* [30],	Staggered Staggered	5 5	Cylindrical, Elliptical	2.5	1.25	10 degree (fitted)
Krueckels, *et al.* [14]	Staggered	5	Cylindrical	2.5	2.17	10 degree (fitted)
Ling, *et al.* [41]	Staggered	4	Cylindrical	-	-	-
Telisinghe, *et al.* [149]	Staggered	5	Cylindrical	-	-	-
Holloway, *et al.* [19][25]	Empty duct	-	-	-	-	-
Medic, *et al.* [26]	Empty duct	-	-	-	-	-
Joo, *et al.* [27]	Empty duct	-	-	-	-	-
Schneider *et al.* [28][29]	Empty duct	-	-	-	-	-
Yang, *et al.* [38]	Empty duct	-	-	-	-	-
Benson *et al.* [55]	Empty duct	-	-	-	-	-
Barigozzi, *et al.* [159]	Empty duct	-	-	-	-	-

With regard to the experiments of Martini *et al.* [4][5] [23][24] and Horbach *et al.* [30], this chapter discusses the performance of the blade TE cutback model with various configurations within the cooling passage. The mixing flow interaction between the mainstream flow and the coolant from the ejection slot as the effects of those variations becomes a focus in this numerical study. This study encompasses internal and external cooling for the blade TE cooling in an effort to provide a comprehensive research using an integrated model. This is due to the pin-fin cooling (internal cooling region) is commonly adjoined with the trailing-edge ejection cooling (external cooling area).

7.2 Computational Domain and Grids

As mentioned above, all variations of this computation are devised within a single pitch distance of pin-fin array referring to the blade TE cutback cooling as previously defined in Figure 4–2 (see page 66). The internal feature inside the cooling passage is modified with circular and elliptical pin-fin array including an empty duct.

The variation of the pin-fin inside the cooling passage causes the requirement of their meshing development around the pin-fin region; therefore, it needs to show the structure of these meshes. Figure 7–1 illustrates the local 2D structured meshes for both circular and elliptical pin-fin. Both meshes are constructed within the block-structured mesh using the Gambit meshing tool. It is based on the fine Mesh C used previously for validation. Both are kept the same number of cells, with a 96-encircling circumference of the pin-fin, as shown in Figure 7–1. The expansion factor ($r < 1.2$) is applied at all regions near to the end-wall of the pin-fin, the lip-end, the pressure-side-wall area and the adiabatic wall region, which ensures a sufficient spatial resolution of $\Delta y^+ < 1$. Other regions of the blade TE cutback domain are projected from these grids. All views of the structured mesh are illustrated by the baseline configuration, as shown in Figure 4–4 (see page 69).

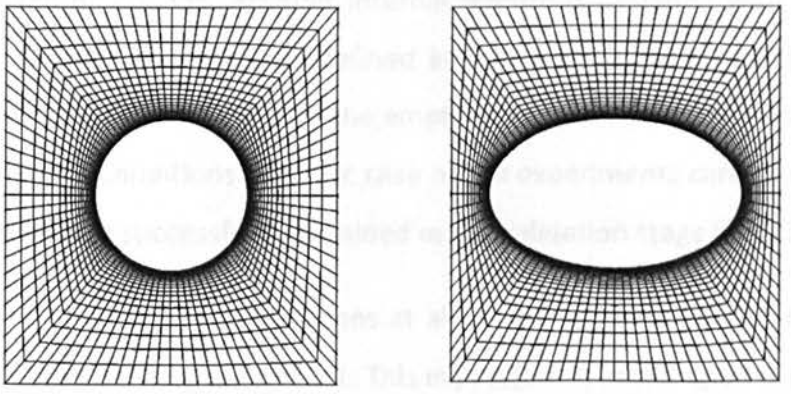

a. circular b. ellipse

Figure 7–1: Local 2-D structured meshes for circular and elliptic pin-fin.

Table 7–3 details the characteristics of the mesh for three different configurations. All simulation cases are developed on the fine grid resolution with $\Delta y^+ < 1$.

Table 7–3: Mesh statistics.

Pin-fins	Empty duct	Circular (baseline)	ellipse
Inside the cooling passage region			
pin-fin wall [a] Δy_1^+	-	0.907	0.724
end-wall Δy_1^+	0.556	0.749	0.739
Mainstream region			
pressure side wall Δy_1^+	0.484	0.482	0.484
lip-end wall Δy_1^+	0.929	0.607	0.766
breakout/cutback region			
No. of elements [b], $n_x \times n_y \times n_z$	124×48×48	124×48×48	124×48×48
Δy_1^+	0.194	0.257	0.250
average			
Δy_1^+	0.547	0.740	0.673

[a] an average of Δy^+ in the radial direction of pin, [b] elements at the block of breakout-slot region.

7.3 History of Simulations

As informed earlier, this chapter discusses the simulations of the blade trailing-edge cutback cooling with various internal cooling designs. Internal feature of the pin-fin cooling is varied in terms of its shape, i.e. circular and elliptical. The main geometry of these specimens is kept at the same dimension as the baseline, with the exception of the shape of the pin-fin cooling. Another internal feature is designed with empty duct. An internal feature of the baseline, as defined in Figure 4–2 (see page 66), is cut-off in an attempt to provide a TE cutback with the empty duct. All these case studies are simulated in exactly the same conditions as in the case of the experiments carried out by Martini *et al.* [4][5], which were successfully examined in the validation stage (see Chapter 5).

Figure 7–2 gives the history of iterations at all variations detailed above. It is presented within the selected blowing ratio of 1.1. This expression is based upon the temperature at the centre of the slot exit (A_7). Two monitoring points of the flow temperature are provided in-line with the $z/H = 0$ (Tc'_2) and at the $z/H = 1.25$ (Tc'_1). It has been found that the temperature Tc'_1 (see Figure 7–2(a)) is greater than Tc'_2 (see Figure 7–2(b)) for both the cases with pin-fin cooling. The existence of the circular pin-fin array causes a more significant oscillation of flow with sub-harmonic staggering when compared to others. Flow oscillation could be reduced by replacing the elliptical pin-fin array for the internal

cooling passage. Flow temperature remains unchanged for the case with empty duct, which are at the same level for both monitoring points (see the red colour in Figure 7–2).

Based on the history of iterations in Figure 7–2, three case studies have been sufficiently simulated up to a statistically steady state condition. Each case has a typical iteration for achieving a converged solution. Every case of simulation requires up to 360 computational hours for a domain with a single pitch distance of pin-fin array in a typical meshing above. It depends on the blowing ratio and their configuration. The simulation of the blade TE cutback, with its circular pin-fin, takes a longer time to achieve a steady state condition after the solution is converged, as shown in Figure 7–2. The oscillation within periodic sub-harmonic is more pronounced for this configuration. Both elliptical pin-fin and empty duct tend to result in a constant level when compared with the circular pin-fin array. The cause of oscillation for the case with circular pin-fin has been unclear. It is probably caused by the unsteadiness effect from the mixing region.

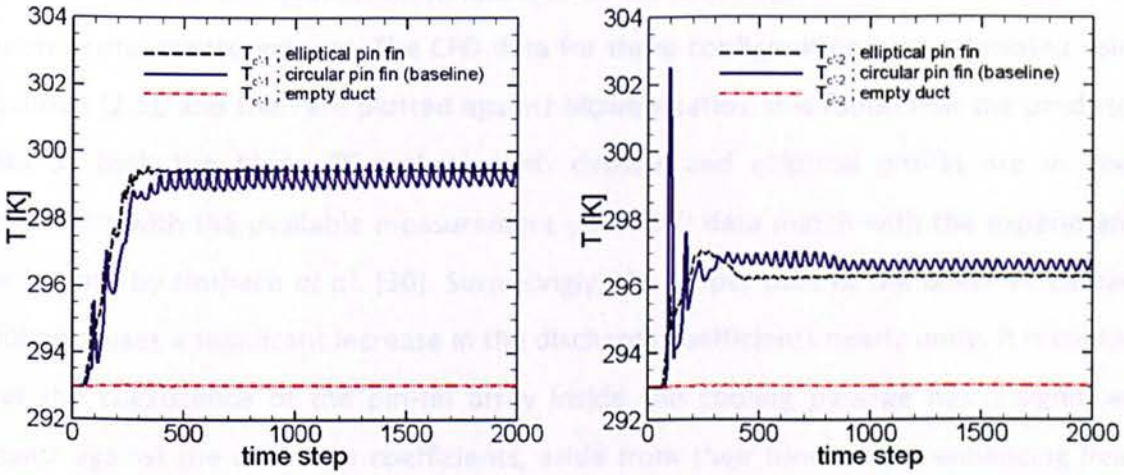

(a) Temperature at the z/H=1.25 (b) Temperature at the centre

Figure 7–2: History of iterations.

7.4 Results and Discussion

Once a proper computational domain and grids have been created, considering those variations mentioned above, DES is used to simulate each configuration. Simulation is stopped for data collection when approaching a statistically stationary state condition, as shown by the iteration history in Figure 7–2. Based on the time-averaged data, the results

are analysed and interpreted in a similar manner with the existing experiments performed by Martini *et al.* [4][5] [23][24] and Horbach *et al.* [30].

7.4.1 Internal Cooling Passage

Three types of design as mentioned above are used to vary the internal feature inside the cooling passage of a blade trailing-edge cutback cooling. Of course, these variations implicate the difference of coolant flow behaviour along the cooling channel. This becomes an important issue towards assessing the heat-transfer process inside the cooling passage before ejecting the coolant from the slot exit. The interaction between the mainstream flow and coolant at mixing region is more complicated as the effect of this coolant flow behaviour.

7.4.1.1 Discharge coefficient:

Figure 7–3 shows the qualitative comparison of the discharge coefficients alongside the experimental measurements. The CFD data for three configurations are calculated using equation (2.3), and then are plotted against blowing ratios. It is found that the predicted data of both the blade TE cutback with circular and elliptical pin-fin are in good agreement with the available measurement data. CFD data match with the experiments carried out by Horbach *et al.* [30]. Surprisingly, the empty duct of the blade TE cutback cooling causes a significant increase in the discharge coefficients nearly unity. It is evident that the coexistence of the pin-fin array inside the cooling passage has a significant impact against the discharge coefficients, aside from their function for enhancing heat-transfer along the cooling channel. A higher discharge coefficient means the pressure loss in the cooling passage is at a lower level, meaning the power need of coolant flow could be minimised. However, the benefit of this configuration must be evaluated in terms of film-cooling effectiveness.

In-line with the works of Horbach *et al.* [30], the present computation proves that the discharge coefficient could be increased up to 10% by replacing internal feature inside the cooling passage using elliptical pin-fin array into the pin-fin cooling of the baseline model.

The discrepancy of pin-fin shape causes the difference of friction losses along the cooling channel, which affects the global calculation of discharge coefficients.

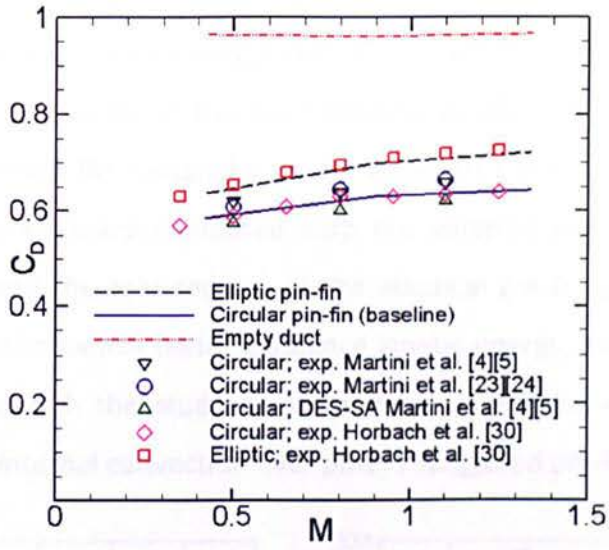

Figure 7–3: Discharge coefficient.

7.4.1.2 Pin-fins cooling:

Figure 7–4 gives the properties of the coolant air at the surface of the pin-fins' row inside the cooling passage (see positions $P_1 - P_5$ in Figure 5–10, page 92).). It illustrates the average values at the pin-fin surface. Both pressure and temperature decrease gradually along the cooling channel. The reduction of the pin-fins surface pressure indicates the pressure losses inside the cooling channel, whilst the decrease in the pin-fins' surface temperature is likely caused by the coolant flow effect, which has a lower temperature.

Based on Figure 7–4(c) and Figure 7–4(d), both heat-transfer and skin friction coefficients increase moderately. The increase of the heat-transfer coefficient is in-line with previous investigations using streamwise-staggered elliptical pin-fin with one row of fillet circular pin-fin [160]. The rise of the heat-transfer coefficient along the cooling passage has also been experimentally demonstrated by Tarchi *et al.* [13]. The average increase is more than 1.5 times in their experiment using a wedge-duct with the circular and the elliptical pin-fin array. This rise is also consistent with the work of Yang *et al.* [142], who investigated the heat-transfer coefficient of a staggered elliptic and square pin-fin within a parallel duct.

From Figure 7–4(c), the heat-transfer coefficient for the case with circular pin-fins is relatively higher than the elliptical pin-fins with an average discrepancy of up to 20.21%. Tarchi *et al.* [13] found the same trend as that of their experiment. The deviation of the heat-transfer coefficient is more pronounced after approaching the second row of the pin-fin array. The higher level of the heat-transfer coefficient is probably caused by increasing the turbulence flow intensity as the effect of the circular pin-fin array. This shape effect is more intensive compared with the elliptical pin-fin array. The stream design at the front and the rear regions of the elliptical pin-fin guide flow with lower turbulence level, then influence their turbulence kinetic energy, as shown in Figure 7–5. This finding is in-line with the study of Ames *et al.* [44], who examined a turbulent augmentation of the internal convection over pins in staggered pin-fin arrays.

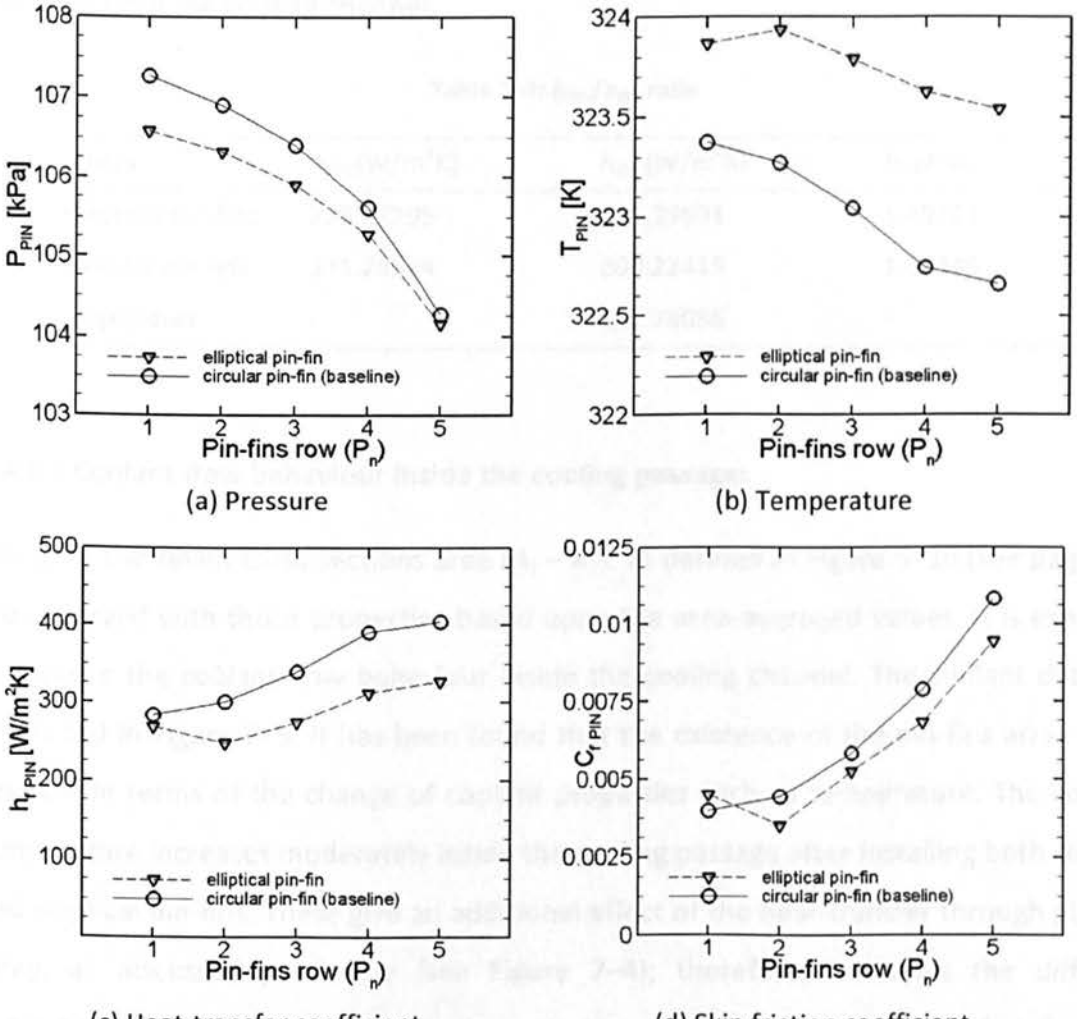

Figure 7–4: Coolant flow behaviour at the surface of the pin-fins row.

The heat-transfer coefficient on the pin-fin surface (h_{PIN}) is always higher than the end wall (h_{EW}) values, as presented in Table 7–4. This agrees well with the experimental data available, such as that obtained by Facchini *et al.* [3] and Tarchi *et al.* [13]. Van Fossen [161] found the ratio h_{PIN}/h_{EW} of 1.35 on their investigation, whilst Chyu [162] reported their findings as being between 1.1 and 1.20 using similar staggered arrays. Furthermore, the ratio h_{PIN}/h_{EW} of a staggered array depends on streamwise pitch (S_x), as addressed by Metzger *et al.* [129]. The present study notes that the blade TE cutback cooling with circular pin-fin generates a higher h_{PIN}/h_{EW} ratio of 1.58 compared with elliptical pin-fin configuration of up to 1.29. A lower turbulence intensity of the coolant flow inside the cooling passage for empty duct causes a lower heat-transfer coefficient at the end-wall. Its coefficient decreases significantly between 37% and 39% when the pin-fin arrays are removed from the cooling channel.

Table 7–4: h_{PIN}/h_{EW} ratio

arrays	h_{PIN} (W/m^{2}K)	h_{EW} (W/m^{2}K)	h_{PIN}/h_{EW}
Elliptical pin-fins	279.27295	216.19991	1.29173
Circular pin-fins	331.28574	209.22415	1.58340
Empty duct	-	131.78036	-

7.4.1.3 Coolant flow behaviour inside the cooling passage:

Similarly, the seven cross-sections area ($A_1 - A_7$), as defined in Figure 5–10 (see page 92), are observed with those properties based upon the area-averaged values. It is expected to capture the coolant flow behaviour inside the cooling channel. The coolant data are presented in Figure 7–5. It has been found that the existence of the pin-fins array has a key role in terms of the change of coolant properties such as temperature. The coolant temperature increases moderately inside the cooling passage after installing both circular and elliptical pin-fins. These give an additional effect of the heat-transfer through pin-fins array, as discussed previously (see Figure 7–4); therefore, it causes the different characteristics of the coolant air when ejecting from the slot exit, which influences external cooling performance.

From Figure 7–5(b), the coolant temperature increases up to 2.7% with the peak level at A_6 of the section area. Both the cases with the circular and the elliptical pin-fin array results showed a similar trend of temperature, whilst the case with the empty duct only increased by about 0.68% with the peak level at A_7 of the section area.

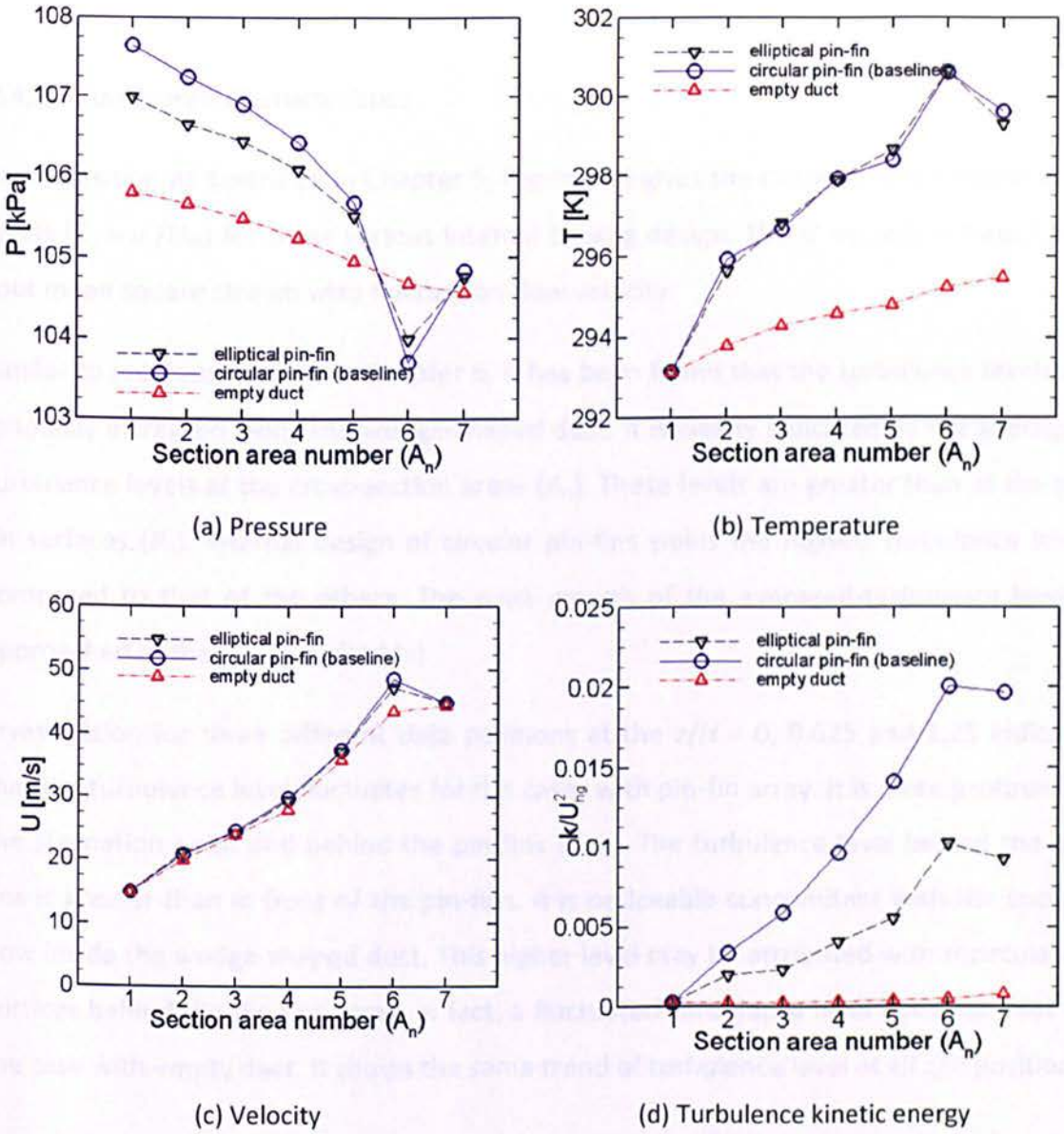

Figure 7–5: Coolant flow behaviour inside the cooling passage.

From Figure 7–5(d), the turbulence kinetic energy increases gradually in typical characteristic as the shape effect of the pin-fin array. The construction of a wedge-shaped duct inside the cooling passage is also seen to trigger their rise. In addition, the case with the empty duct shows virtually no effect on their turbulence kinetic energy, meaning their

heat-transfer process is not as effective as the case with the pin-fin array inside the cooling passage, although the coolant velocity is at an almost similar level for all variations (see Figure 7–5(c)). The higher level of velocity for both the cases with the pin-fin array is most likely caused by the reduced space in the cooling channel. Clearly, the discrepancies, as discussed above, cause the different performance.

7.4.2 Turbulence Characteristics

Same position as described in Chapter 5, Figure 7–6 gives the characteristic of turbulence levels ($T_u = u'/U_\infty$) for three various internal cooling design. The u' velocity is based on a root mean square stream wise fluctuation flow velocity.

Similar to previous findings in Chapter 6, it has been found that the turbulence levels are gradually increased along the wedge-shaped duct. It is clearly indicated by the averaged-turbulence levels at the cross-section areas (A_n). These levels are greater than at the pin-fin surfaces (P_n). Internal design of circular pin-fins yields the highest turbulence levels compared to that of the others. The peak growth of the averaged-turbulence level is approached at the ejection slot (A_7).

Investigation for three different data positions at the z/H = 0, 0.625 and 1.25 indicates that the turbulence level fluctuates for the cases with pin-fin array. It is more profound at the stagnation point and behind the pin-fins array. The turbulence level behind the pin-fins is greater than in front of the pin-fins. It is noticeable concomitant with the coolant flow inside the wedge-shaped duct. This higher level may be attributed with recirculation vortices behind the pin-fins array. In fact, a fluctuated-turbulence level does not exist for the case with empty duct. It shows the same trend of turbulence level at all z/H positions.

From Figure 7–6, it has been found that the turbulence level is increased rapidly when ejecting coolant at the slot exit (A_7), and then decreased after approaching the peak level behind the lip region. In addition, this turbulence level grows along the mixing region that depends on a dynamic interaction between the mainstream flow and the coolant ejection. It is seen that the turbulence level tends to increase near the downstream region.

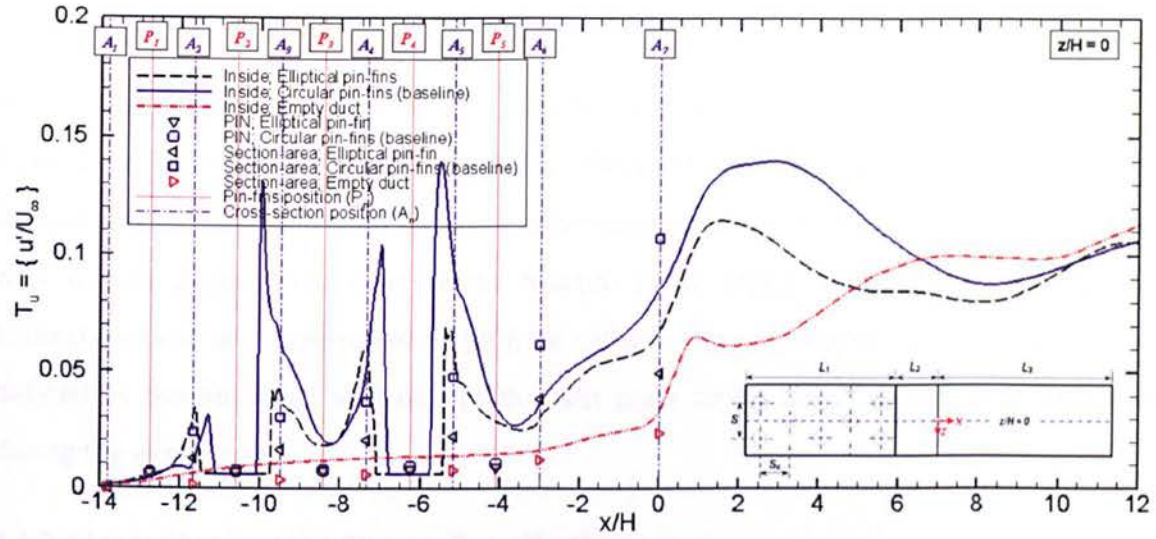

(a) $z/H = 0$

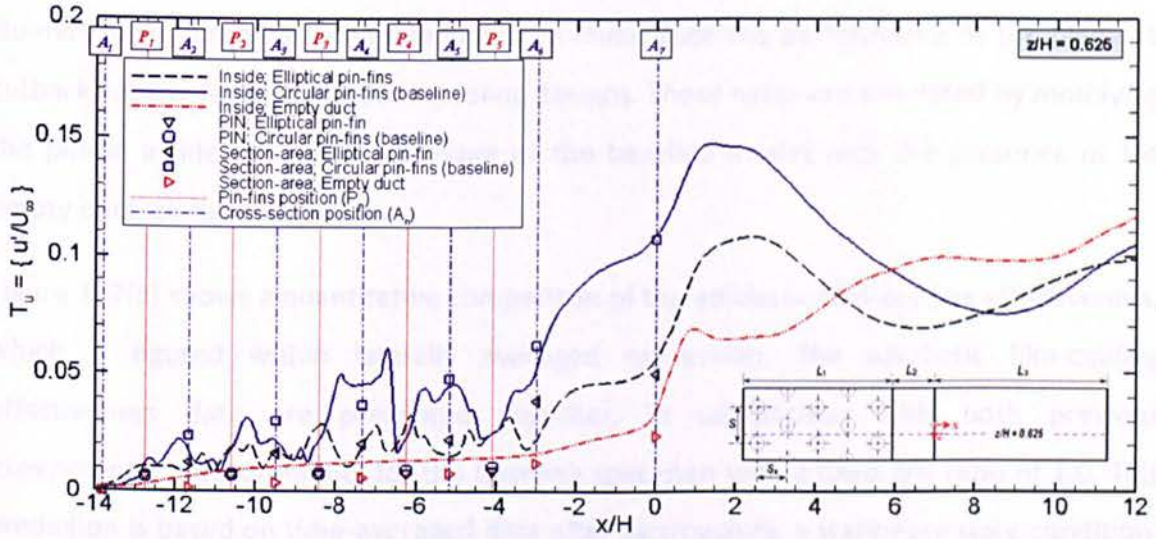

(b) $z/H = 0.625$

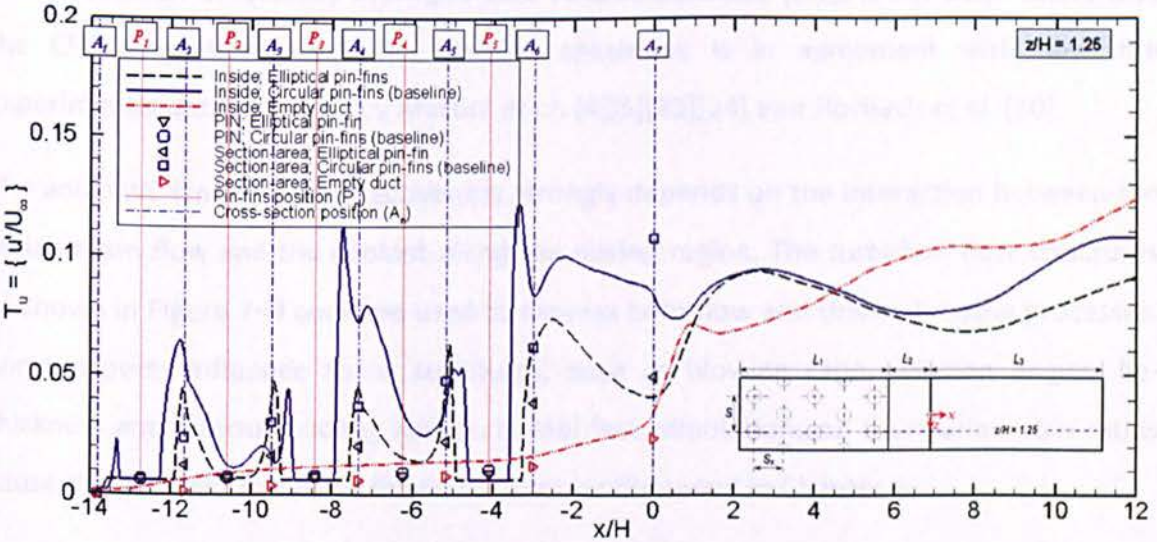

(c) $z/H = 1.25$

Figure 7–6: Turbulence levels.

7.4.3 Protected Wall / Cutback Surface

As discussed previously, the performance of the blade trailing-edge cutback cooling is commonly expressed by the film-cooling effectiveness at the protected wall surface. Several researchers have used different definitions in this case, such as Yang *et al.* [6][38], who named a protected wall, whilst Martini *et al.* [4][5] mentioned a trailing-edge cutback surface, and Horbach *et al.* [30][35] called a tested plate/surface. Sometimes, it is defined as the adiabatic wall due to the test plate being set at an adiabatic condition during the experiment.

7.4.3.1 Laterally averaged film-cooling effectiveness:

Numerical studies have been conducted to investigate the performance of the blade TE cutback cooling for three internal cooling designs. These cases are simulated by modifying the pin-fin inside the cooling passage of the baseline model with the presence of the empty duct, circular and ellipse.

Figure 7–7(a) shows a quantitative comparison of the adiabatic film-cooling effectiveness, which is figured within laterally averaged expression. The adiabatic film-cooling effectiveness data are presented together, in comparison with both previous experimental measurements for the baseline specimen with a fixed *t/H* ratio of 1.0. This prediction is based on time-averaged data after approaching a stationary state condition. The calculation of laterally averaged data follows equation (5.1). It has been found that the CFD simulation using the baseline specimen, is in agreement with both the experimental data garnered by Martini *et al.* [4][5][23][24] and Horbach *et al.* [30].

The adiabatic film-cooling effectiveness strongly depends on the interaction between the mainstream flow and the coolant along the mixing region. The turbulent flow structures as shown in Figure 7–9 could be used to express both flow and thermal mixing processes. Some aspects influence these structures, such as blowing ratio, ejection angles, lip-thickness and internal cooling design. In real fact, simulations on four various *t/H* ratios cause the different turbulent flow structures, as discussed in Chapter 6.

The second case of this computational study shows that the performance of the blade TE cutback cooling is strongly influenced by the internal cooling designs. The co-existence of the pin-fins inside the cooling passage is very important for a trailing-edge cooling in order to maintain a high effectiveness along the protected wall. It has been shown that the performance of the cases with internal pin-fin cooling is greater than the case with the empty duct. The film-cooling effectiveness for the case with the empty duct is at the lowest level throughout the breakout region, and it drops significantly after the $x/H = 4$ position. This trend is affected by the temperature at the adiabatic wall, as shown in Figure 7–7(b). The level of temperature between $0 < x/H < 4$ for the case with empty duct is slightly higher than for the two other configurations. This is due to the effect of the wall temperature at the suction side (SS) wall, which affects coolant flow near to the protected wall. The influence of their wall temperature remains at the near wall area due to a relative lower turbulence intensity inside the cooling passage, as discussed previously (see Figure 7–5(f)). The 3D effect along the coolant channel is relatively low for this configuration.

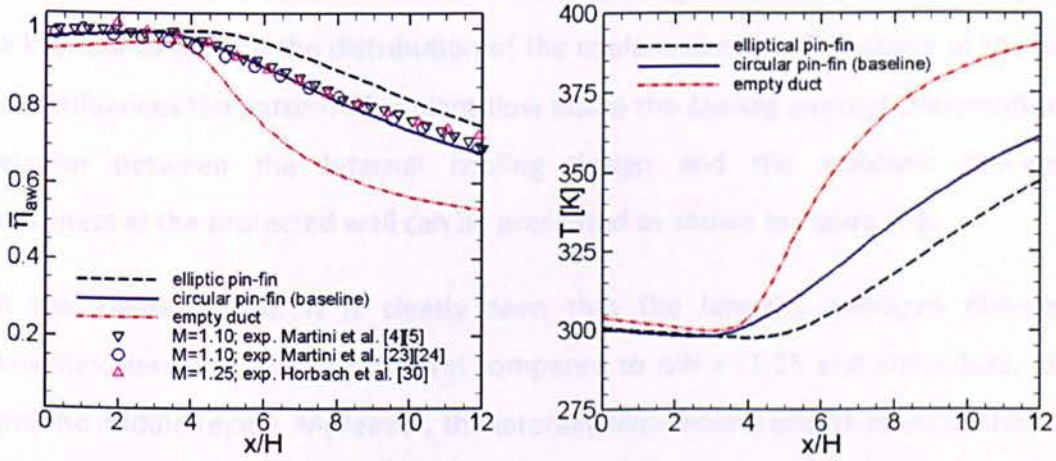

(a) adiabatic film-cooling effectiveness (b) temperature

Figure 7–7: Laterally averaged film-cooling effectiveness at the protected wall.

The performance of the case with the empty duct could be improved upon by establishing the pin-fins array inside the cooling passage. Furthermore, cooling effectiveness is increased by up to 2.53% (on average), replacing the streamwise orientation of the elliptical pin-fin array. Most likely, the film-cooling would be able to reach up to the

downstream region with better distribution, as seen in Figure 7–7(b), meaning this improves the quality of the film-cooling effectiveness, as shown in Figure 7–7(a).

7.4.3.2 Film-cooling effectiveness at the *z/H* position:

In order to complete the discussion of the adiabatic film-cooling effectiveness shown above, the cooling effectiveness along the centre line (z/H = 0), the z/H = 1.25, and the z/H = -1.25 are given here, in comparison with laterally averaged calculation. It has been found (Figure 7–8) that each configuration yields a different distribution of the adiabatic film-cooling effectiveness. The laterally film-cooling effectiveness at the centre line tends to be at the lowest level after attaining its peak point, with the exception of the blade TE cutback with elliptical pin-fin. The decay is more pronounced near the downstream region. This discrepancy between the centre line and other regions implies that the 3D flow effect exists along the mixing region. The mixing process increases in a typical turbulence flow structure, depending on its flow interaction. As the mainstream flow remains constant at the velocity of 56 m/s, the flow interaction depends upon the coolant ejection from the slot exit. In the case of a fixed blowing ratio, the internal cooling design has a key role to play on the distribution of the coolant ejection. The shape of the pin-fin cooling influences the pattern of coolant flow inside the cooling passage. Hereinafter, the correlation between the internal cooling design and the adiabatic film-cooling effectiveness at the protected wall can be presented as shown in Figure 7–8.

From the Figure 7–8(a), it is clearly seen that the laterally averaged film-cooling effectiveness tends to at a higher level compared to z/H = -1.25 and z/H = 1.25, mainly around the middle region. Moreover, the laterally film-cooling effectiveness at the centre (z/H = 0) drops rapidly after achieving x/H > 6. This is a different characteristic of trend against two other graphs in Figure 7–8(b) and Figure 7–8(c), respectively. This trend is most likely caused by the shape of the elliptical pin-fins, which triggers the formation of turbulence flow structure. In-line with the centre position, a rapid decay of the laterally film-cooling effectiveness is triggered by an intensified mixing process along this region. The observation at the region between z/H = -1.25 and z/H = 0 shows that the laterally film-cooling effectiveness is greater than the laterally averaged one, mainly at z/H = -0.625. The same fact is also found at other regions between z/H = 0 and z/H = 1.25. This

may contribute a significant increase of the laterally averaged film-cooling effectiveness compared to the others.

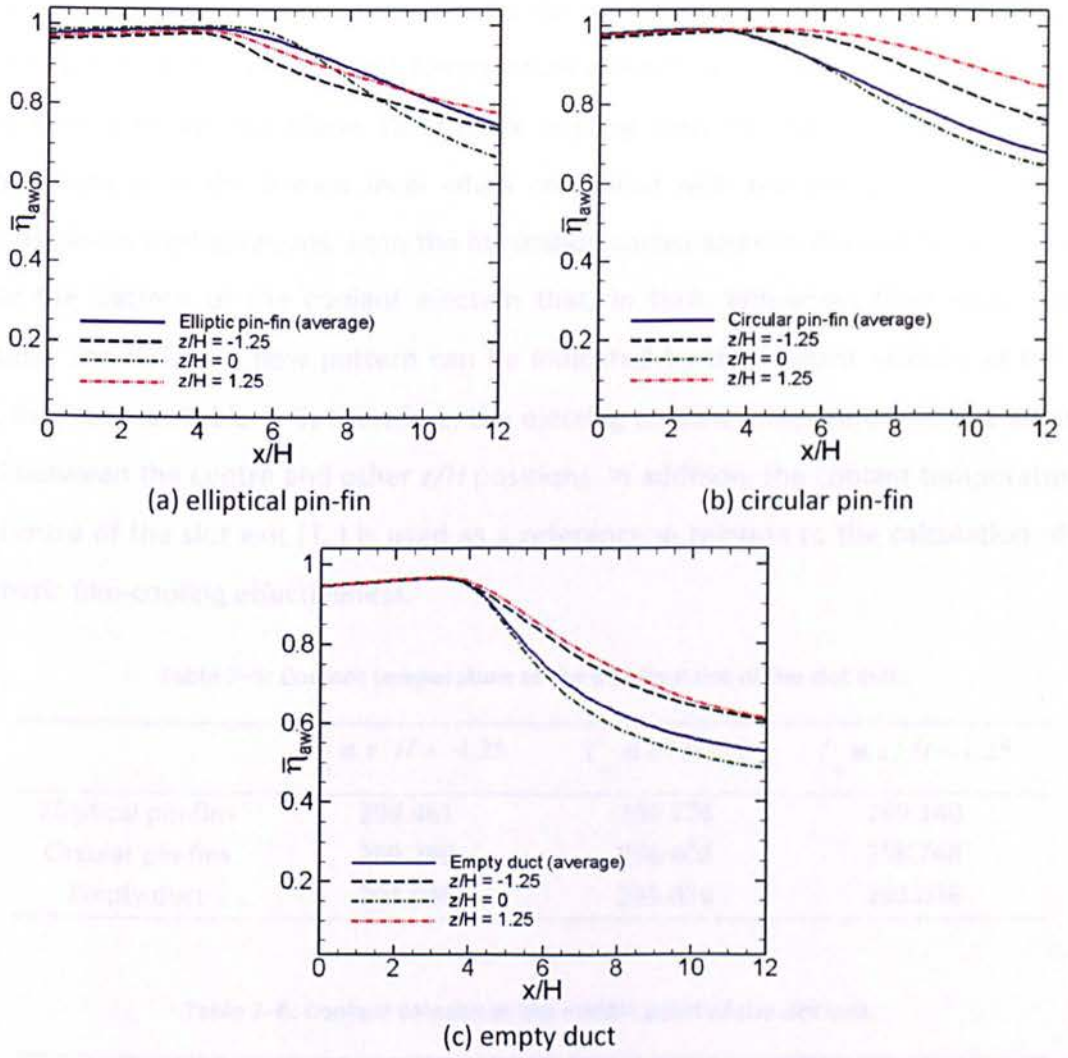

(a) elliptical pin-fin (b) circular pin-fin

(c) empty duct

Figure 7–8: Film-cooling effectiveness at the *z/H* position.

As mentioned above, the distribution of the adiabatic film-cooling effectiveness at the protected wall is most likely caused by the pattern and intensity of the turbulent flow structures at the mixing region. The fluctuation of the adiabatic film-cooling effectiveness depends on their distributions. This correlation can be seen by linking the film-cooling effectiveness in Figure 7–8 and the turbulent flow structures in Figure 7–9. Each configuration causes a typical characteristic of mixing, which influences their heat-transfer process. This proves that the turbulent flow structure has an important role to play in both flow and thermal mixing process between the mainstream flow and the coolant, and then affects the distribution of the adiabatic film-cooling effectiveness at the

protected wall. A turbulent flow structure is influenced by the coolant ejection at the slot exit, which is affected by internal shape designs.

Table 7–5 shows the coolant properties at the middle point of the slot exit. It has been clearly identified that the coolant temperature remains at the same level as the centre point (*z/H* = 0) for the blade TE cutback cooling with the empty duct. The coolant temperature is at the lowest level when compared with the other *z/H* positions for various pin-fin configurations. Both the horseshoe vortex and von Karman Street probably cause the pattern of the coolant ejection that, in turn, influences their heat-transfer process. The different flow pattern can be indicated by the coolant velocity at the slot exit, as shown in Table 7–6; therefore, the ejecting coolant temperature is at a different level between the centre and other *z/H* positions. In addition, the coolant temperature at the centre of the slot exit ($T_{c'}$) is used as a reference in relation to the calculation of the adiabatic film-cooling effectiveness.

Table 7–5: Coolant temperature at the middle point of the slot exit.

	T_{c_1} at $z/H=-1.25$	T_{c_2} at $z/H=0$	T_{c_1} at $z/H=1.25$
Elliptical pin-fins	299.461	296.276	299.140
Circular pin-fins	299.269	296.408	298.748
Empty duct	293.036	293.036	293.036

Table 7–6: Coolant velocity at the middle point of the slot exit.

	U_{c_1} at $z/H=-1.25$	U_{c_2} at $z/H=0$	U_{c_1} at $z/H=1.25$
Elliptical pin-fins	44.7187	52.4399	43.1405
Circular pin-fins	37.4698	55.1177	37.1187
Empty duct	46.2089	46.4175	46.3655

7.4.4 Mixing Region

The mixing region is an interaction zone between the mainstream flow and the ejecting coolant. This is located behind the lip throughout the breakout area. The performance of the blade TE cutback cooling is highly dependent on the mixing process between them,

whilst their mixing is strongly influenced by the blowing ratio and their geometry. Moreover, the internal cooling passage design plays an important role in their performance, as shown in this study. Martini *et al.* [23][24] noted that an unsteady mixing process is influenced by the internal slot design. In connection with the characteristics of the mixing process along the breakout region, it is important to assess this phenomenon.

7.4.4.1 Turbulent flow structures:

As discussed previously, performance of a trailing-edge cutback cooling is influenced by the intensity of mixing process between the mainstream flow and the coolant ejection, which is related to the turbulent flow structures at the mixing region. Schneider *et al.* [28] noted that a change in type and strength of the dominant coherent structures formed behind the cutback lip affect that performance. The relations between the turbulent flow structures at mixing region and the adiabatic film-cooling effectiveness at the protected wall are presented quantitatively in Figure 7–9.

Figure 7–9 (the left figures) depicts the qualitative comparison of the turbulent flow structures for three different case studies, super-imposed by the contour of the adiabatic film-cooling effectiveness at the protected wall and the non-dimensional temperature (θ) distribution at the *x-y* plane for a fixed z/H = -1.25. All visualisations are based on simulation after approaching a statistically stationary state condition at 0.025 seconds. The turbulent flow structures are presented by iso-contours of the vortex identification criterion Q, as suggested by von Terzi *et al.* [137] and Schneider *et al.* [28][29]. The visualisation of iso-surface $\Omega^2 - S^2 = 10^5\ 1/s^2$ refers to Egorov *et al.* [22]. S is the strain rate and Ω is the vorticity. The colour indicates the non-dimensional temperature (θ) distribution of mixing, which is expressed by the gradation from a low value of 0 (in red) to a high value of 1 (in blue).

These numerical studies found that the empty duct cooling passage yields a specific turbulent flow structure within typical wakes (see Figure 7–9(c)), whilst both the cases with circular and elliptical pin-fin are seen to generate similar structures of turbulent flow at the mixing region (see Figure 7–9(b) and Figure 7–9(a)). The pattern of unsteady vortex-shedding is noticeable when seen from a side view on the right Figure 7–9. It can

be clearly seen that the similarity of coherent structure for both the cases with circular and elliptical pin-fin also cause similar distribution of the adiabatic film-cooling effectiveness at the protected wall. A larger wake of coherent structure for the case with empty duct as in Figure 7–8(c) seen to trigger an intensified mixing flow, which degrades the film-cooling effectiveness mainly near the downstream region. This is obvious between $4 < x/H < 12$ compared to the others, as indicated by changing the gradation colour from blue to red in *x*-direction (see Figure 7–9(c)). This evidences that the growth of wakes has a key role in the thermal mixing as illustrated by both contours of wakes and the non-dimensional temperature (θ) distribution at a fixed $z/H = -1.25$. The non-dimensional temperature (θ) distribution decreases sharply at a level of 0.55 near the downstream region, as shown in green in Figure 7–9(c). A larger wake triggers an intensified thermal mixing flow, whilst a smaller wake reduces that process. The penetration of mainstream flow into the region near the protected wall surface is more pronounced for the case with empty duct as the effect of larger wakes formed.

Figure 7–9 (the right figures) provides the side-view of turbulent flow structures the same as the left figures, inserted by the streamline of normalised flow velocity (U/U_{hg}) from the mainstream flow and the ejecting coolant. The intensity of flow velocity is scaled by the gradation contour from a low value of 0 (in blue) to a high value of 1 (in red). Based on the streamlines gradation colour, flow velocity inside the cooling passage is relative at a lower level for the case with the empty duct, when compared with the others. It is consistent with a quantitative data inside the cooling passage as previously presented in Figure 7–5(c). The coolant flow velocity for both the cases with pin-fins is in similar level with peak level in A_6. It is seen that a bigger increase of coolant flow velocity is due to a contraction channel; however, the existence of the pin-fin array also contributes to narrowing the chamber inside the coolant channel, which causes a slight increase those coolant velocity before ejecting from the slot exit.

In fact, turbulent flow structures with larger wakes are resulted from simulation of the case with empty duct. The intensity of wakes is reduced when using pin-fin array inside the cooling passage. This may be caused by the existence of pin-fin array that trigger the growth of coolant flow in all directions. Their turbulent flow structures are more random

and chaotic. The randomness is caused by the multiple effects of the horseshoe vortex near to the end-wall and the Karman vortex street around the middle pin-fin array.

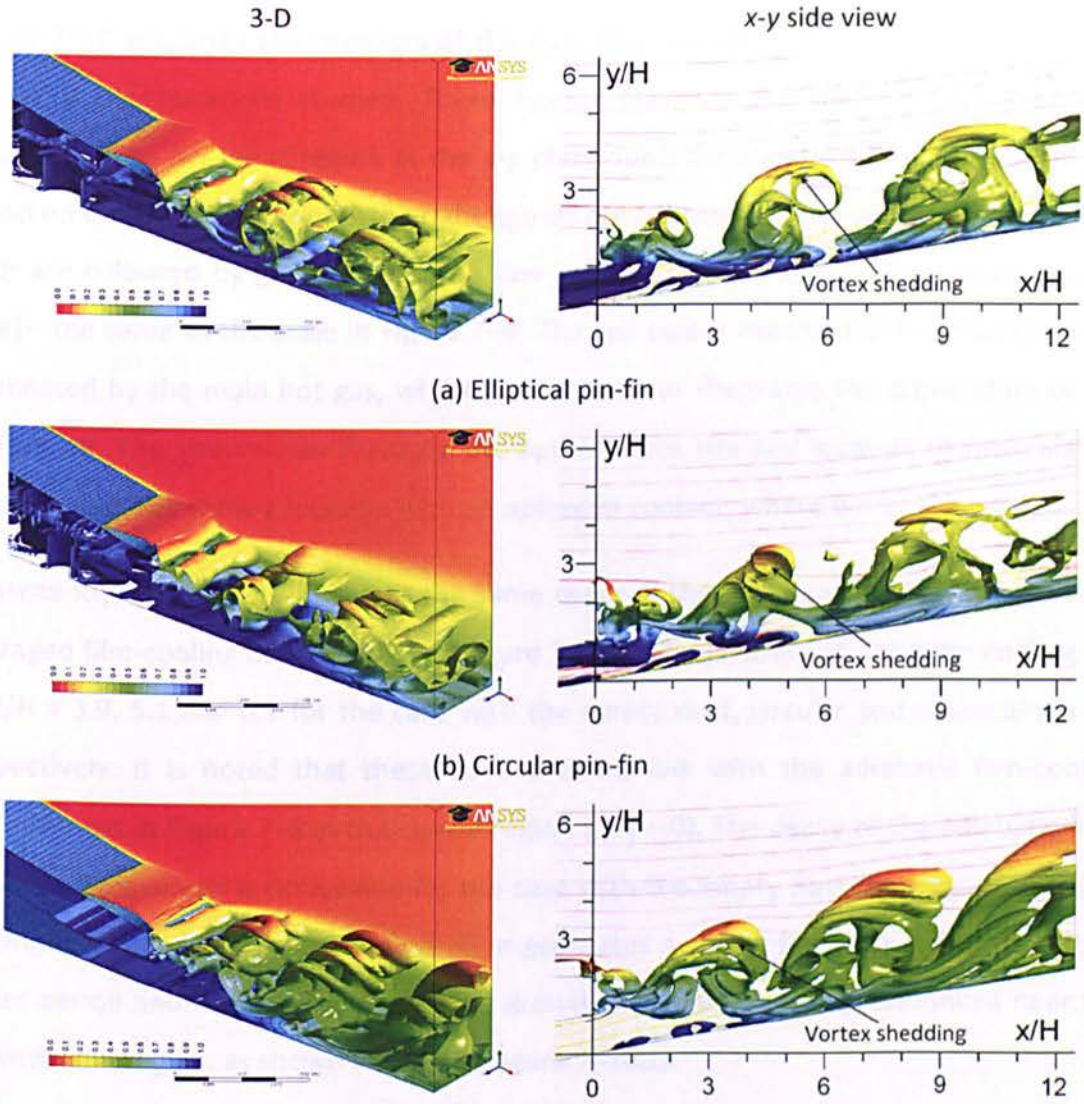

Figure 7–9: Turbulent flow structures.

Different from empty duct, the growth of wakes is seen to reduce in *z*-direction, and this is dominant in *y*-direction. This structure is almost dominated by the effect of lip construction that triggers the growth of vortex-shedding similar with in 2D case. The formation of vortex-shedding tends to remain well-ordered. Medic *et al.* [26] and Joo *et al.* [27] found a similar structure on their computational study. This increases regularly in a similar shape and period.

7.4.4.2 Temperature distributions:

Figure 7–10 visualises the contours of the non-dimensional temperature (θ) distribution on three configurations studied. These figures illustrate the thermal mixing process throughout the breakout region at the *x-y* plane for a fixed $z/H = 0$. The left figures are based on instantaneous, whilst the right figures are centred on time-averaged calculation. Both are coloured by gradation from a low value of 0 (in red) to a high value of 1 (in blue)—the same as the scale in Figure 7–9. The red colour means that the mixing flow is dominated by the main hot gas, whilst the blue colour illustrates the domination of the coolant air. The streamlines illustrate the approximate size and location of recirculation zone. The arrows show a location with an optimum coolant, where $\theta = 1$.

Consistently, Figure 7–10(b) shows the same order of the optimum cooling ($\theta = 1$) as the averaged film-cooling effectiveness in Figure 7–7(a). The location of optimum cooling are at $z/H = 3.9$, 5.1 and 6.7 for the case with the empty duct, circular and elliptical pin-fin, respectively. It is noted that these have a direct link with the adiabatic film-cooling effectiveness in Figure 7–8 at the centre region ($z/H = 0$). The decay of the adiabatic film-cooling effectiveness is noticeable for the case with the empty duct (see Figure 7–10(c)). Linking to Figure 7–9(c), this configuration generates a strong formation of wakes with a larger period and higher magnitude. The growth of wakes is more pronounced near the downstream region, as shown in the left Figure 7–10(c).

From Figure 7–10(b), it has been found that the larger wakes for the case with empty duct cause a strong invasion of mainstream flow with a hot temperature into the protected wall surface. Therefore, the optimum cooling is reduced at $z/H = 3.9$ after approaching a balance condition of thermal mixing. The optimum cooling is improved after replacing inside the cooling passage with circular or elliptical pin-fin array. Both achievements are presented on the right Figure 7–10(b) and Figure 7–10(a), respectively. It can be seen clearly that both intensities of wakes are not as strong as for the case with empty duct.

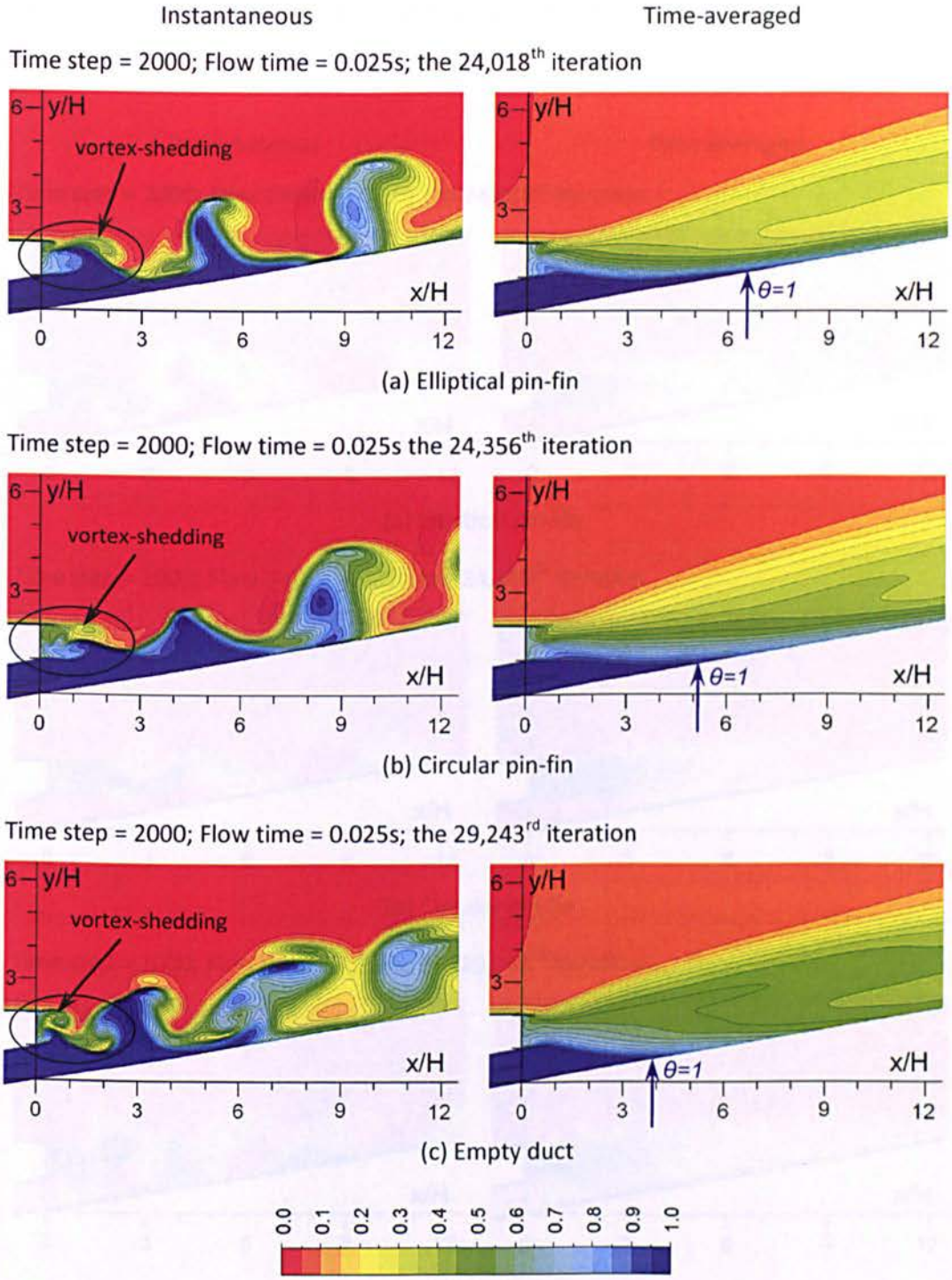

Figure 7–10: Distribution of non-dimensional temperature (θ) at the *x-y* plane of *z/H* = 0.

7.4.4.3 Velocity distributions:

Figure 7–11 shows the normalisation of instantaneous and time-averaged velocity magnitude (U/U_{hg}) along the mixing region at the same *x-y* plane as used above. These are normalised by the free-stream velocity of main hot gas flow (U_{hg}). Both are presented

with a gradation colour from a low value of 0 (in blue) to a high values of 1 (in red) on a typical scale.

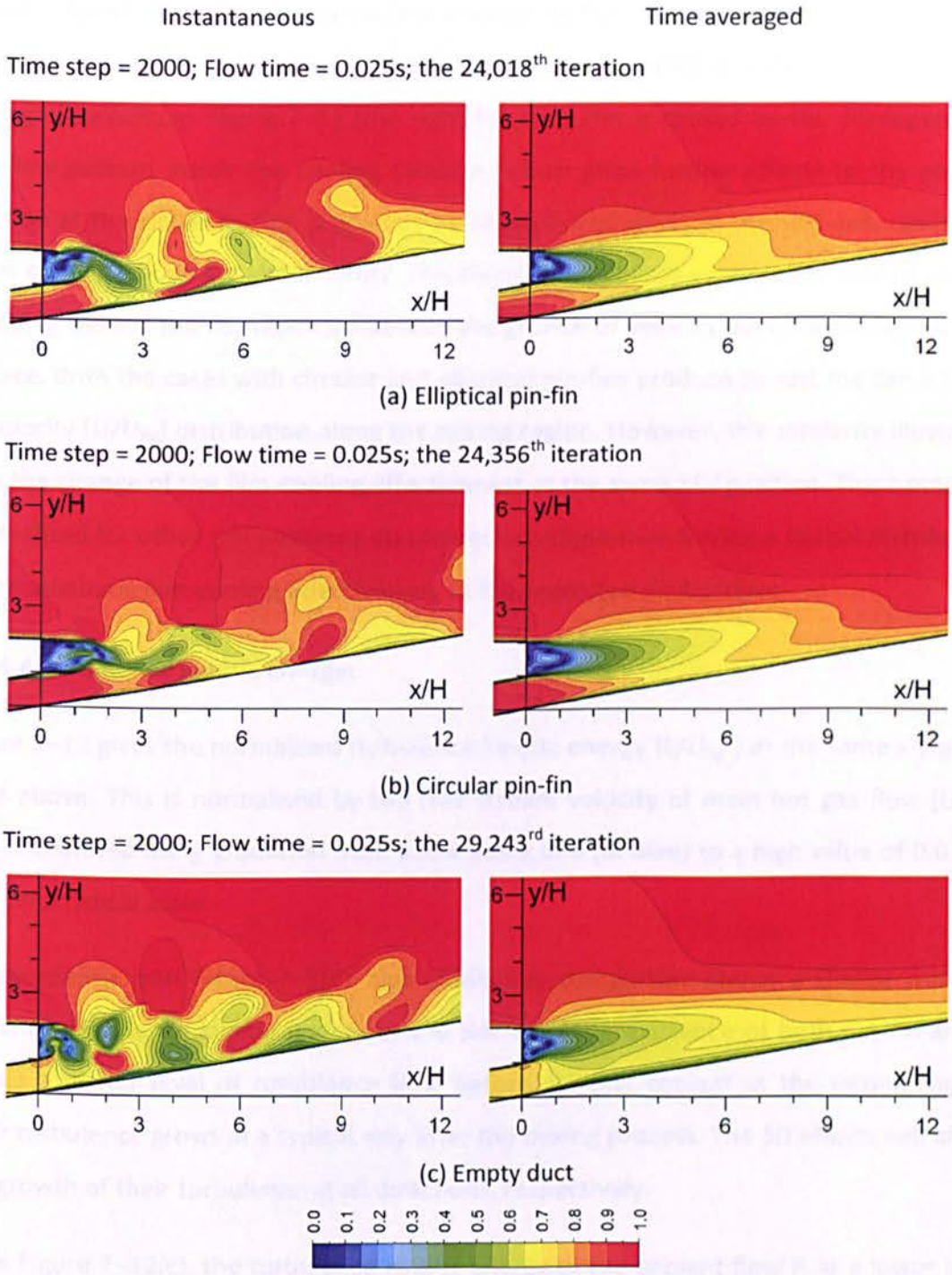

Figure 7–11: Velocity distributions at the *x-y* plane of *z/H* = 0.

In general, each configuration generates a specific pattern of unsteady vortex-shedding, as indicated by the instantaneous velocity on the left Figure 7–11. Velocity drops

significantly to the lowest level behind the lip region. This is noticeable for the case with the empty duct, as illustrated by the time-averaged-velocity on the right Figure 7–11(c).

It is also found that the ejecting coolant velocity for the case with the empty duct is less than the case with both circular and elliptical pin-fins. This is seen clearly for time-averaged velocity in Figure 7–11 (the right figures). This is caused by the discrepancy of the flow pattern inside the cooling passage, which gives further effects to the coolant ejection at the slot exit. This is obvious by about 0.7 of U/U_{hg} at the slot exit, whilst the other configurations are almost unity. This discrepancy causes a different mode of vortex-shedding behind the lip, which influences the growth of velocity over the protected wall surface. Both the cases with circular and elliptical pin-fins produce almost the same trend of velocity (U/U_{hg}) distribution along the mixing region. However, this similarity illustrates only the change of the film-cooling effectiveness at the same z/H position. This cannot be generalised for other z/H positions due to each configuration having a typical distribution of the adiabatic film-cooling effectiveness at the protected wall surface.

7.4.4.4 Turbulence kinetic energy:

Figure 7–12 gives the normalised turbulence kinetic energy (k/U_{hg}^2) at the same x-y plane used above. This is normalised by the free-stream velocity of main hot gas flow (U_{hg}^2). This is coloured using gradation from a low value of 0 (in blue) to a high value of 0.01 (in red) on a typical scale.

In accordance with Figure 7–5(d), this qualitative comparison shows a similar trend in terms of turbulence kinetic energy at the slot exit. The existence of both pin-fin arrays causes a higher level of turbulence flow before ejecting coolant at the mixing region. Their turbulence grows in a typical way after the mixing process. The 3D effects will affect the growth of their turbulence at all directions, respectively.

From Figure 7–12(c), the turbulence kinetic energy of the coolant flow is at a lower level when ejecting from the slot exit, as indicated using blue colour. This matches with the level of turbulence kinetic energy along the coolant channel in Figure 7–5(d), where it remains constant at a lower intensity. It increases after interaction with the mainstream flow in a typical mode. Two other configurations of pin-fin array causes a strong impact

on the growth of turbulence kinetic energy along the coolant passage, and then in the mixing region, as in Figure 7–12(a) and Figure 7–12(b). This qualitative visualisation is seen to be in line with the quantitative trend in Figure 7–5(d).

Time step = 2000; Flow time = 0.025s; the 24,018th iteration

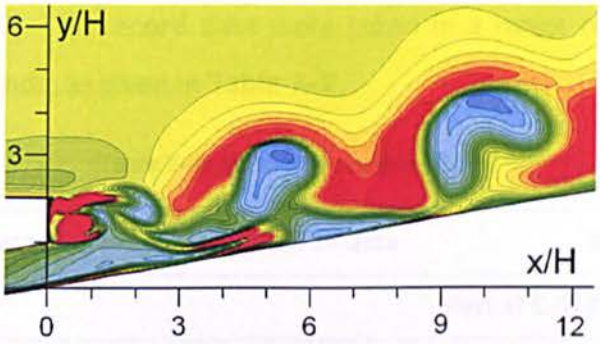

(a) Elliptical pin-fin

Time step = 2000; Flow time = 0.025s; the 24,356th iteration

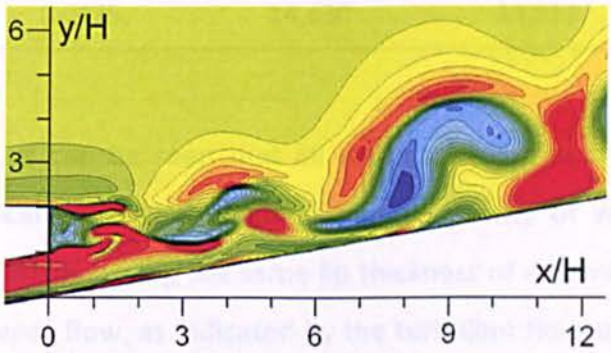

(b) Circular pin-fin

Time step = 2000; Flow time = 0.025s; the 29,243rd iteration

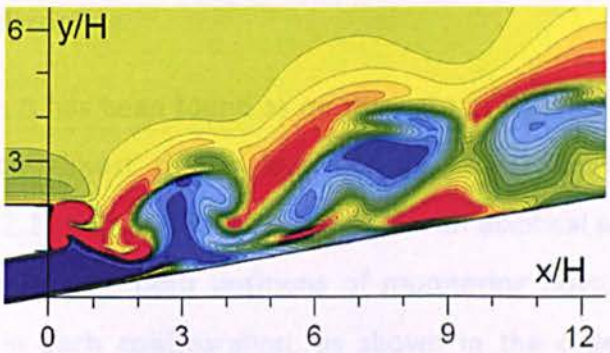

(c) Empty duct

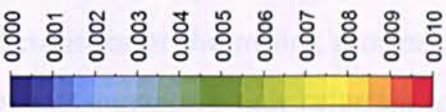

Figure 7–12: Turbulence kinetic energy distribution at the *x-y* plane of *z/H* = 0.

7.4.5 Shedding Frequency

Figure 7–13 gives the truncated record of the mixing flow velocity and their shedding frequencies at the mixing region for three different internal slot designs. These data were sampled from monitoring points S_1 and S_2, as previously applied on validation stage (see Figure 4–2(c), page 66). The record data were taken in a range of flow times between 0.0125 and 0.025 seconds, as given in Table 7–7.

Table 7–7: Record of sampling data.

Configurations	Sampling times	Number of data	Iterations	
			Start at 0.0125s	Stop at 0.025s
Elliptical pin-fins	0.0125	11,461	12,557	24,018
Circular pin-fins	0.0125	11,602	12,754	24,356
Empty duct	0.0125	14,430	14,813	29,243

From the left figures, it can be seen that all amplitudes are at a similar level of flow velocity within a typical pattern, respectively. The similarity of velocity amplitudes is reasonable for all variations having the same lip thickness of 4.8mm. The mixing process occurs within an unsteady flow, as indicated by the turbulent flow structures in Figure 7–9. The movement of mixing flow captures the beating phenomenon with sub-harmonic waves, as shown by the envelope wave on the left Figure 7–13. This happens for all types of the blade TE cutback cooling.

In terms of frequency, it has been found as on the right of Figure 7–13(b) that spectrum frequencies are at an almost similar level for all cases simulated. The dominant frequencies are 2.09, 2.21 and 2.25 kHz for the case with elliptical pin-fin, circular pin-fin and empty duct, respectively. Both positions of monitoring points produce the same dominant frequency in each configuration, as shown in the order above. Again, the similarity of these frequencies indicates that the dimension of the lip-end is a key parameter against the characteristics of the mixing process. This is plausible due to an analytical calculation of dominant frequency only referring to the effective lip thickness and the mainstream velocity, as discussed previously in chapter 5 and 6.

A slight difference of the dominant frequency is probably due to the growth effect of the turbulent flow structures at the mixing region, as previously presented in Figure 7–9. This discrepancy is likely triggered by the different coolant ejection as the influence of internal pin-fin designs. This layout causes the different characteristic of the coolant ejection at the slot exit.

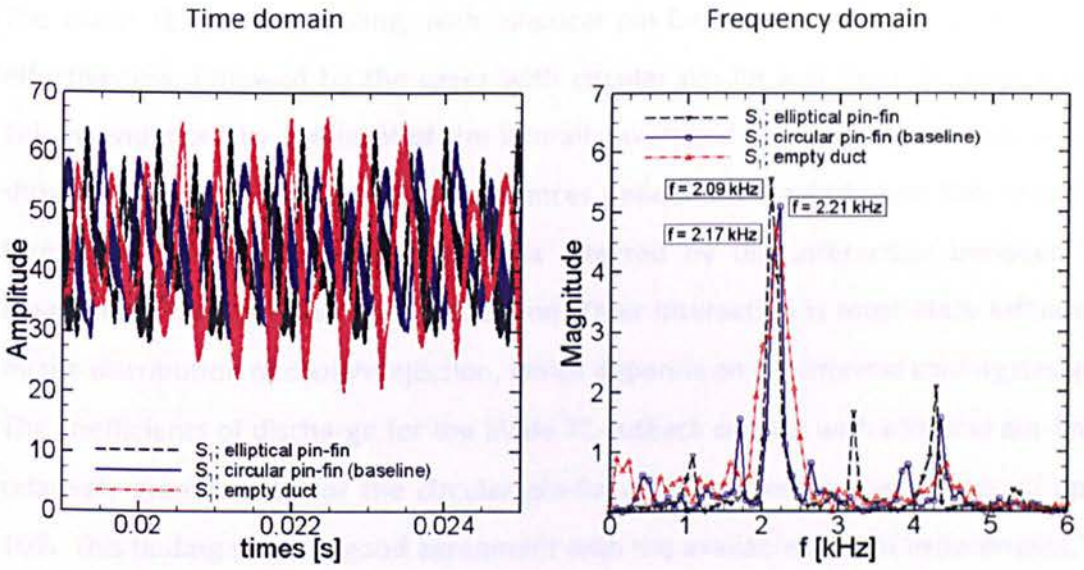

(a) S_1 monitoring point

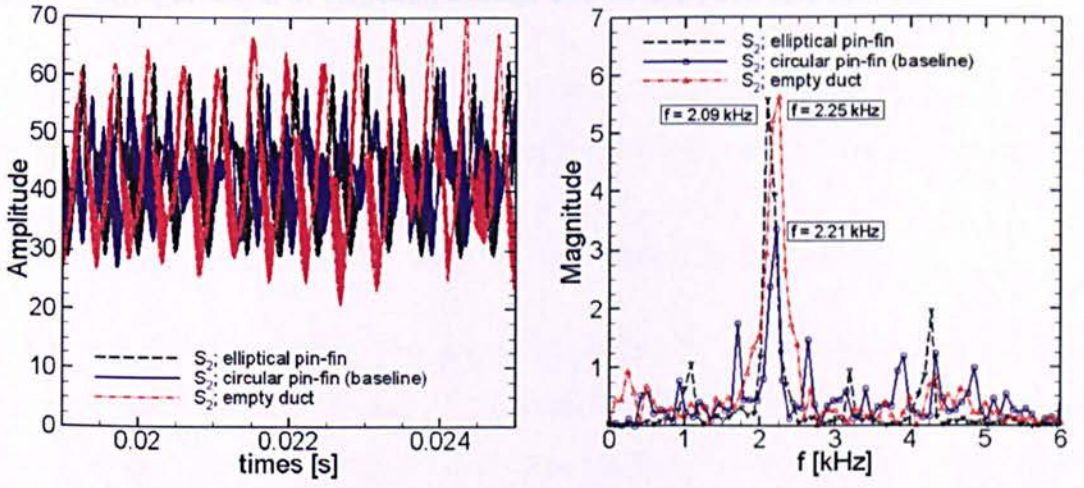

(b) S_2 monitoring point

Figure 7–13: Shedding frequencies.

7.5 Summary

The blade TE cutback cooling on various internal slot designs has been studied numerically. DES was applied for these simulations, with the SST $k-\omega$ turbulence model. The results and discussion have been presented as above. Accordingly, the following statements can be concluded:

1. The blade TE cutback cooling, with elliptical pin-fin, yields the highest film-cooling effectiveness, followed by the cases with circular pin-fin and then the empty duct. This is evidenced by the level of the laterally averaged film-cooling effectiveness, as shown in Figure 7–7(a). These performances depend on the turbulent flow structure formed at the mixing region, which is affected by the interaction between the mainstream flow and the coolant ejection. Their interaction is most likely influenced by the distribution of coolant ejection, which depends on the internal cooling designs.
2. The coefficients of discharge for the blade TE cutback cooling with elliptical pin-fins is relatively greater than for the circular pin-fin with an average discrepancy of up to 10%. This finding shows a good agreement with the available data of experiments.The dominant frequencies are 2.09, 2.21 and 2.25 kHz for the blade TE cutback model with pin-fin configurations of elliptical, circular and empty duct, respectively.

CHAPTER 8:

CASE III: BLADE TRAILING-EDGE CUTBACK COOLING WITH VARIOUS COOLANT EJECTION ANGLES

This chapter describes a computational study of the blade trailing-edge cutback cooling with various coolant ejection angles. A baseline configuration with an ejection angle of 10° has been modified to 5° and 15°, respectively and the aim is to investigate the ejection angle change on the performance of both the pin-fin cooling and the blade TE cutback cooling. The computational domain only has a single pitch distance of the pin-fin array in the spanwise direction. Mesh generation and turbulence model are the same as that of the case 1 and case 2 computations (see Chapters 6 and 7, respectively). Similarly, DES is employed to simulate all three-configuration cases. Time-averaged results are collected up to 2000 time steps, after simulation approaching a statistically stationary state. The previous experiments of a blade TE cutback cooling with 10° ejection angle carried out by Martini *et al.* [4][5][23][24] and Horbach *et al.* [30] are used as a reference for assessing the present results. The detailed computations are described as follows.

8.1 Blade Trailing-edge Cutback Cooling with Various Ejection Angles

The need for careful design of the geometry of the coolant injection region is already recognised, but not yet quantitatively understood [59]. Unfortunately, only few publications exist that deal with the injection angle of a TE cutback cooling. Most of researchers evaluated the blade TE cooling performance with a fixed ejection angle and different geometries of blade trailing edge. For example, Hepeng *et al.* [36] investigated experimentally the film-cooling of a trailing-edge within a fixed coolant ejection angle of 0°, while Martini *et al.* [15][16] [20] and Horbach *et al.* [30][35] used 10° ejection angle in

their experiments. Furthermore, each researcher utilized different model and geometry in the studies.

About two decades ago, a parametric study has been carried out to investigate experimentally the effect of an ejection angle between 0 and 15° [4][5]. However, other conditions were not in the typical range for a modern turbine blade, e.g. a constant density ratio (ρ_c/ρ_h) was kept, so as the lip thickness to slot height ratios (t/H), and the slot width to height ratios (w/H), etc. The configuration inside the cooling passage was also not considered in those experiments. Above all, the results revealed that a TE breakout cooling with 8.5° ejection angle was an optimum angle for providing a greater film-cooling effectiveness.

The importance of the lip thickness and the injection angle of a film-cooling slot were reported by Sivasegaram *et al.* [59], who studied the adiabatic-wall effectiveness in a two-dimensional case with constant flow properties. They evaluated the cooling effectiveness from three different injection angles (α = 30°, 60° and 90°) of the adiabatic-wall against the direction of free-stream. The measurements were performed with larger density ratios (ρ_c/ρ_h) and small t/H ratios at Mach number (Ma > 0.5). The results agreed qualitatively with those performed by Papell *et al.* [163] with an injection angle of 45°, 80°, and 90°, but some quantitative differences were shown. Both investigations found that the film-cooling effectiveness decreases significantly when the coolant injection angle increased with respect to the mainstream flow direction.

In terms of aerodynamic losses, Aminossadati *et al.* [164] noted that the increase of ejection angle would cause the raise of losses in particular for the case with higher coolant mass flow rates. This observation was based on investigations with various ejection angles between 0 and 45°.

In order to further study the TE cutback cooling systems as discussed above, three different ejection angles (5°, 10° and 15°) are simulated by employing ANSYS Fluent. Geometries and numerical treatments are described below. The results and discussions are included thereafter.

8.2. Geometries and Meshes

As defined earlier in Chapter 4, the baseline of the blade TE cutback cooling has a specific ejection angle of 10°. The change of the coolant ejection angle will influence several geometries such as the fitted area of wedge-shaped duct, the height of pin-fin array inside the cooling passage, the slot exit area and the inclination of the protected wall surface, including the shadow-triangle area. It is expected that the change of these geometries affect both performance of pin-fin cooling and trailing-edge cutback cooling.

Table 8–1 illustrates the change of geometries for a blade TE cutback cooling as the effect of three coolant ejection angles. These ejection angles are formed by rotating the coolant slot of L_1 region and the protected/adiabatic wall of L_3 region at the reference axis of $z = 0$ and keeping constant the slot-height (H) at 4.8 mm. These geometries are derived referring to Figure 6–1 as previously explained in Chapter 6 (see page 107). It is seen that the length of the slot-exit in vertical direction ($H_{slot\text{-}exit}$) is slightly increased by approximately 2.7% when changing an ejection angle from 5° to 15°. It means that the cross-section area of the slot-exit will widen corresponding to the increase of that ejection angle. The slot exit area reduces 1.15% if ejection angle decreases from 10° to 5°, whilst it expands up to 1.54% if ejection angle increases from 10° to 15°. Therefore, the coolant air would be ejected by few extra spaces, through the slot-exit for the case with higher ejection angle.

Table 8–1: Key dimensions of the shadow-triangle area.

α (degree)	t/H	t (mm)	H (mm)	a (mm)	b (mm)	c (mm)=H_{se} at the slot-exit	Area (mm^2) at the slot-exit
5	1.0	4.8	4.8	54.864	55.074	4.818	57.816
10	1.0	4.8	4.8	27.222	27.642	4.874	58.488
15	1.0	4.8	4.8	17.914	18.546	4.949	59.388

a; b; and c refer to Figure 6–1. The length of c is viewed vertically (parallel with y-axis)

Figure 8–1 illustrates the front views of the local structured meshes around the lip region for those ejection angles. Gambit meshing tool is employed to create the multi-block structured grids. All above are constructed by keeping the same number of blocks as

applied for the baseline model using the fine Mesh C (see Figure 4–4, page 69). These meshes are generated with the growth of spacing in all directions as suggested by Spalart *et al.* [108][123] and Joo *et al.* [27]. A boundary layer mesh is applied to all wall surfaces, which ensures a sufficient spatial resolution of $\Delta y^+ < 1$.

Table 8–2 represents the grid resolutions of the blade TE cutback configuration as depicted in Figure 8–1. The interesting area (i.e. adiabatic/protected wall surface) is constructed in higher quality meshes with average $\Delta y^+ < 0.5$, as addressed by Nishino, *et al.* [126].

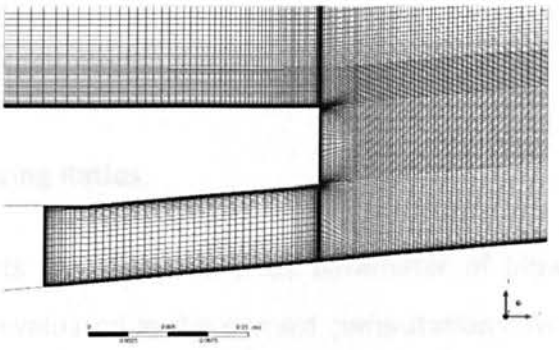

(a) $\alpha = 5°$

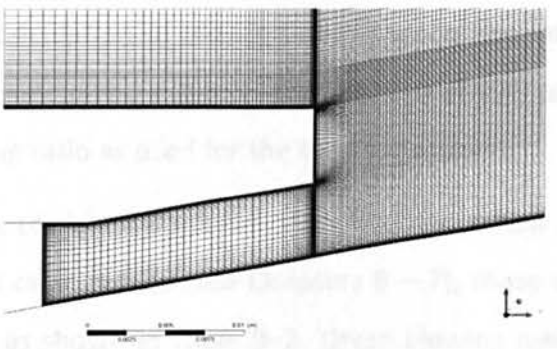

(b) $\alpha = 10°$

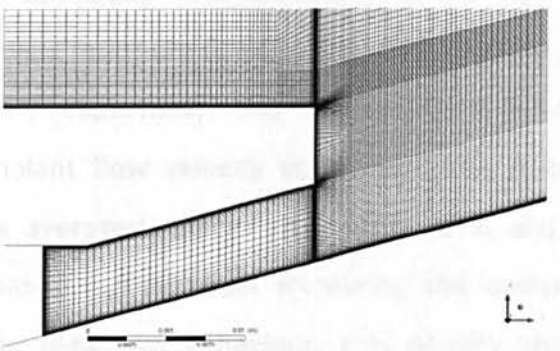

(c) $\alpha = 15°$

Figure 8–1: Mesh comparison.

Table 8–2: Mesh statistics.

Ejection angles (α)	5°	10° (baseline)	15°
Inside the cooling passage region			
pin-fin wall[a] Δy_1^+	0.784	0.907	1.010
end-wall Δy_1^+	0.555	0.749	0.984
Mainstream region			
pressure side wall Δy_1^+	0.488	0.482	0.477
lip wall Δy_1^+	0.539	0.607	0.724
TE cutback/breakout region			
No. of elements, $n_x \times n_y \times n_z$	124×48×48	124×48×48	124×48×48
protected wall Δy_1^+	0.183	0.257	0.320
average			
Δy_1^+	0.613	0.740	0.876

[a] an average of Δy^+ in the radial direction of pin-fin

8.3 Evaluation of Blowing Ratios

Before presenting results and discussion, the parameter of blowing ratio becomes an importance issue to be evaluated in the current computations. As mentioned above, the cross-section area at the slot-exit is slightly changed as the coolant ejection angles changes. It affects the calculation of blowing ratio due to this ratio is a function of the coolant velocity and density at the slot-exit. Therefore, it should be evaluated in order to provide the same blowing ratio as used for the baseline model.

By keeping constant the coolant velocity of 15 m/s at the inflow boundary condition as applied for the previous case studies (see Chapters 6 – 7), these computations yield the different blowing ratios as shown in Table 8–3. These blowing ratios are evaluated using equation (2.4) based on simulation data at the mainstream flow and the slot exit. The evaluation results of blowing ratios are 0.969, 1.345, and 1.817 for the cases with ejection angle of 5°, 10° and 15°, respectively. This discrepancy is most likely caused by the different increase of coolant flow velocity at the slot exit. It can be seen clearly by comparing between the averaged-velocity magnitude of u_c and $u_{c'}$ in Table 8–3. The density ratio also increases slightly when increasing the coolant ejection angles. By assuming incompressible ideal gas behaviour, this density change is a function of temperature following equation (4.3).

The performance comparison of blade TE cutback cooling is commonly evaluated at the same blowing ratio as used in Chapters 6 and 7, respectively. It is unfair if the simulation results as presented in Table 8–3 are used for comparison. Therefore, the coolant flow velocity at the inflow boundary condition must be tuned in an attempt to achieve the same blowing ratio as a standard on comparison. For example, in order to keep the blowing ratio at $M = 1.34$, coolant velocity should be adjusted at 21, 15 and 11 m/s for the cases with ejection angle of 5°, 10° and 15°, respectively. Table 8–4 gives the calculation of blowing ratio after tuning the coolant flow velocity.

Table 8–3: Calculation of blowing ratio before tuning of the inflow coolant velocity.

Description	notations	5°	10°	15°
Coolant inflow	u_c (m/s)	15	15	15
Slot-exit	$u_{c'}$ (m/s)	33.995419	45.142056	60.746288
	ρ_c (kg/m^3)	1.1674899	1.2210646	1.2254193
Mainstream flow	u_{hg} (m/s)	55.999996	55.999996	55.999996
	ρ_{hg} (kg/m^3)	0.7317154	0.7317154	0.7317154
Blowing ratio	$M = \rho_c u_{c'}/\rho_{hg} u_{hg}$	**0.968597**	**1.345209**	**1.816663**
Density ratio	ρ_c/ρ_{hg}	**1.595552**	**1.668769**	**1.674721**

Table 8–4: Calculation of blowing ratio after tuning of the inflow coolant velocity.

Description	notations	5°	10°	15°
Coolant inflow	u_c (m/s)	21	15	11
Slot-exit	$u_{c'}$ (m/s)	45.497204	45.142056	44.667015
	ρ_c (kg/m^3)	1.1985526	1.2210646	1.2233666
Mainstream flow	u_{hg} (m/s)	55.999996	55.999996	55.999996
	ρ_{hg} (kg/m^3)	0.7317154	0.7317154	0.7317154
Blowing ratio	$M = \rho_c u_{c'}/\rho_{hg} u_{hg}$	**1.330796**	**1.345209**	**1.333562**
Density ratio	ρ_c/ρ_{hg}	**1.638004**	**1.668769**	**1.671916**

8.4 History of Simulations

Figure 8–2 provides the iteration history of simulations for three different case studies. This history data are based upon the centre point ($T_{c'2}$) temperature at the slot-exit under

the lip, where this temperature is used to calculate the adiabatic film-cooling effectiveness. It has been found that three case studies have been sufficiently simulated up to a statistically stationary condition in order to gain time averaged-results. In addition, these computations are run up to 2000 time steps with a small time step size of 1.25×10^{-5} seconds.

It is seen that each simulation case has a typical iteration and oscillation. Harmonic oscillation is more noticeable for the simulation case with 10° ejection angle. Simulations for other case studies tend to at a constant level after approaching approximately 8,000 of iterations. This oscillation may be attributed to the growth of turbulence levels when ejected from the slot exit. This iteration history also notes that the level of temperature for the case with ejection angle of 5° is lower than that of the others.

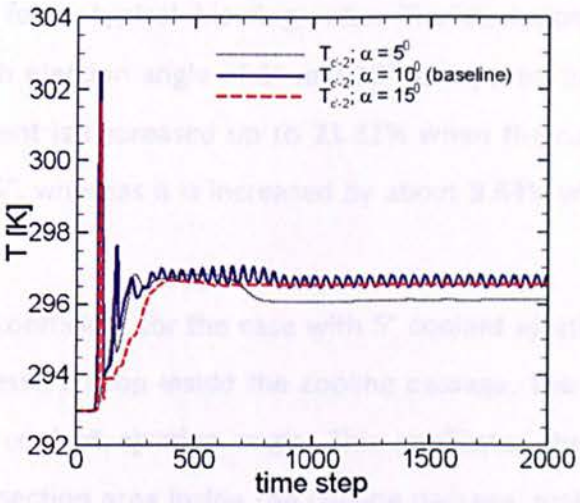

Figure 8–2: History of simulations.

8.5 Results and Discussion

The computation of the blade TE cutback cooling has been performed for three coolant ejection angles. The results and discussion are presented below with starting first for the coolant flow behaviour inside the cooling passage, followed by the performance of the blade TE cutback cooling. The dynamic interaction of mainstream flow and coolant, including the frequency spectrum, are also discussed thereafter.

8.5.1 Cooling Passage

As mentioned earlier, these variations cause the change of geometries inside the cooling passage including the inclination of the protected wall surface. Similar to the case 2 as previously presented in Chapter 7, it may affect the flow behaviour along the cooling channel. It is interesting to assess this discrepancy relating to a dynamic flow interaction at the mixing region and the film-cooling effectiveness.

8.5.1.1 Discharge coefficient:

Figure 8–3 shows the predicted data of discharge coefficient (C_D) on three configurations above, in comparison with experimental data carried out by Martini *et al.* [4][5][23][24] and Horbach *et al.* [30]. The predicted data are plotted against the blowing ratios. The results show that the increase of ejection angle (α) from 5° to 15° causes the increase of discharge coefficient for a typical blowing ratio. The deviation is more pronounced between the case with ejection angle of 5° and 10°, compared to those of 10° and 15°. The discharge coefficient is decreased up to 21.31% when the coolant ejection angle is changed from 10° to 5°, whereas it is increased by about 9.63% when modified from 10° to 15°.

The lowest discharge coefficient for the case with 5° coolant ejection angle is most likely caused by a larger pressure drop inside the cooling passage. The pin-fin height reduces when decreasing the coolant ejection angle. This implicates the reduction of pin-fins surface and the cross section area inside the cooling passage, mainly close to the inflow region. Moreover, both the inlet and the slot exit section are at the same section area when a blade trailing-edge cutback will be designed with 0°coolant ejection angle. On the other hand, the rise of coolant ejection angle causes a slight increase for the slot-exit area (see Table 8–1). This explanation indicates that the change of coolant ejection angle causes the geometries changes for the inlet region, the pin-fin height, the slot-exit height, and the inclination of the protected wall surface. The change of these geometries affect the global pressure loss inside the cooling passage then influences the discharge coefficient.

As previously stated, the CFD data for the baseline are in very good agreement with the available measurements data. It is considered reasonable due to both computation and experiment use the same design with 10° coolant ejection angle.

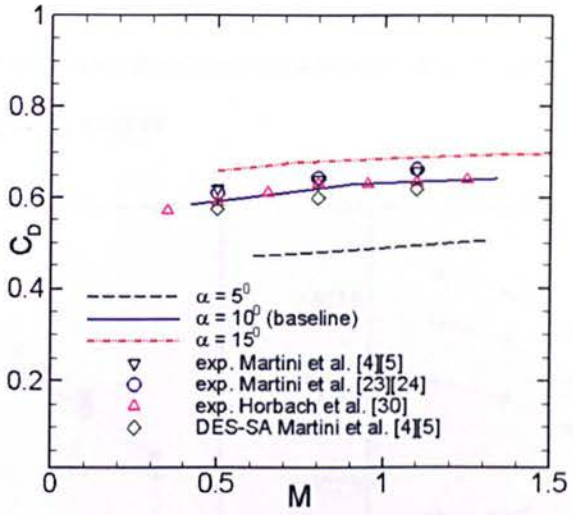

Figure 8–3: Discharge coefficients.

8.5.1.2 Coolant properties at the pin-fin surfaces:

Figure 8–4 gives the coolant properties at the surface of the pin-fins array for three cases studied. These properties are based on the averaged data at the pin-fin surfaces in each row of array. In terms of the pin-fin array ($P_1 - P_5$), the row positions refer to Figure 5–10 (see page 92) as mentioned in Chapter 5. It has been found that both pressure and temperature are gradually decreased along the pin-fin rows (see Figure 8–4(a) and Figure 8–4(b)), while both heat-transfer and skin-friction coefficient are increased moderately (see Figure 8–4(c) and Figure 8–4(d)). The heat-transfer coefficient for the case with 5° ejection angle is relative greater than others.

Based on Figure 8–4(c), an anomalous phenomenon occurs after approaching the fifth row of the pin-fin array where the heat-transfer coefficient drops suddenly less than two others. On the other hand, from Figure 8–4(b), temperature increase suddenly at the fifth row of pin-fin array for a lower ejection angle of 5° that influences directly the decay of local heat-transfer coefficient as stated above. So far, the cause of this phenomenon is unclear. It is probably caused by the increase of coolant velocity at the inflow region (see

u_c in Table 8–4) that triggers the rise of the 3-D flow effects along the cooling passage. The increase of coolant flow velocity gives a strong impact on the growth of turbulence levels inside the coolant passage. In addition, the combined effect of the pin-fin array and the increase of coolant velocity have a significant contribution on the rise of this turbulence. It is noted that the decrease of ejection angle reduces the cooling passage, mainly at the upstream of L_1 region.

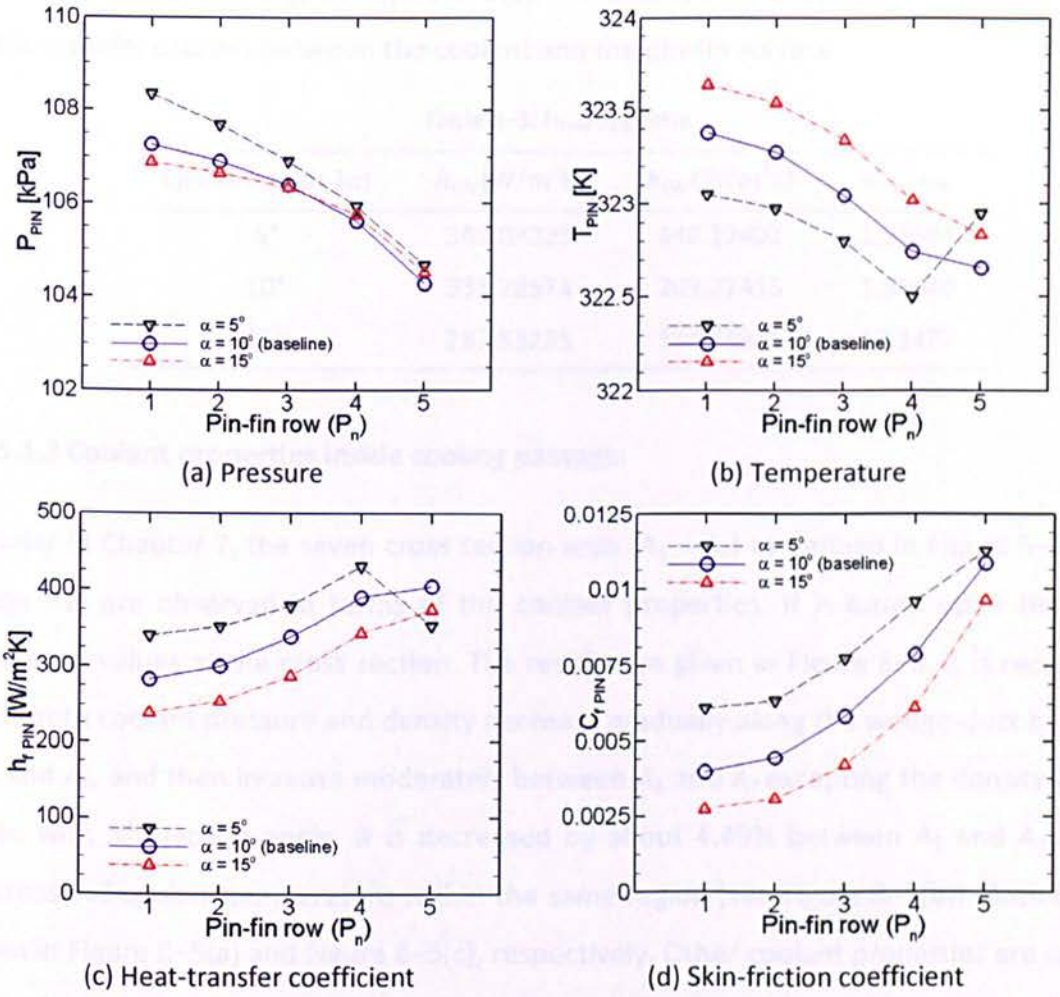

Figure 8–4: Coolant flow behaviour at the surface of the pin-fins row.

As previously discussed in Chapter 7, the heat-transfer coefficient on the pin-fin surface (h_{PIN}) is always greater than the end-wall (h_{EW}) values. The numerical results show that the h_{PIN} coefficient is around 53 – 58% higher than the h_{EW} one. The trend of this finding is seen to be in-line with the previous investigations worked out by Van Fossen *et al.* [161], Chyu [162], Facchini *et al.* [3] and Tarchi *et al.* [13]. It is noted that all researchers referred above only evaluated a pin-fin cooling model, which is totally difference compared to the

present computation in terms of design and geometries. The h_{PIN}/h_{EW} ratio of the present study are given in Table 8–5. Both heat-transfer coefficient at the pin-fin surface (h_{PIN}) and the end wall (h_{EW}) increase up to 14% when ejection angle is decreased by about 5°, whilst the ratio of h_{PIN}/h_{EW} remains in a range between 1.53 and 1.58. The increase of heat-transfer coefficient is likely caused by the different flow behaviour along the internal cooling channel. This can be confirmed by the coolant flow velocity in Figure 8–5(c), turbulence kinetic energy in Figure 8–5(e).This discrepancy is seen to trigger a different heat-transfer process between the coolant and the pin-fin surface.

Table 8–5: h_{PIN}/h_{EW} ratio.

Ejection angle (α)	h_{PIN} (W/m^{2}K)	h_{EW} (W/m^{2}K)	h_{PIN}/h_{EW}
5°	369.03223	240.12402	1.53684
10°	331.28574	209.22415	1.58340
15°	283.53235	184.73906	1.53477

8.5.1.3 Coolant properties inside cooling passage:

Similar in Chapter 7, the seven cross section area ($A_1 - A_7$) as defined in Figure 5–10 (see page 92) are observed in terms of the coolant properties. It is based upon the area-averaged values at the cross section. The results are given in Figure 8–5. It is recognised that both coolant pressure and density decrease gradually along the wedge-duct between A_1 and A_6, and then increase moderately between A_6 and A_7 excepting the density for the case with 5° ejection angle. It is decreased by about 4.49% between A_5 and A_7 as the increase of coolant temperature within the same region (see Figure 8–5(b)). Both can be seen in Figure 8–5(a) and Figure 8–5(c), respectively. Other coolant properties are seen to rise along the wedge-duct. Interestingly, the ejection angle has a key role to play the unique change of coolant properties along the cooling channel (L_2 region).

An anomalous phenomenon is seen from simulation result for the case with 5° ejection angle (see Figure 8–5 (b)). The coolant temperature increases up to 5.35% near the slot-exit after approaching the fifth cross-section area between A_5 and A_7 .It seems the property of coolant density follows this change (see Figure 8–5(d)) due to density is a function of temperature as explained in equation (4.3). The increase of temperature is

likely caused by intensifying of coolant flow along the cooling passage as the rise of coolanf flow velocity at the inlet region (A_1) and the reduction of cooling channel. This factors intensify the coolant flow velocity as seen in Figure 8–5(c) that trigger the increase of turbulent kinetic energy (see Figure 8–5(e)) and turbulence levels (see Figure 8–6). As a result, heat-transfer process is more intensive that cause a rapid increase of coolant temperature between A_5 and A_7.

A significant discrepancy of the coolant flow velocity is evident before approaching the cross-section area at A_6, as shown in Figure 8–5(c). This discrepancy is definitely caused by the different setting of coolant velocity at the inflow region in order to provide in similar blowing ratio as the baseline for M = 1.34. Therefore, the coolant flow velocity at the inflow region must be tuned as explained in Table 8–4. That discrepancy is also triggered by the geometry change of wedge-shaped duct at the L_1 region as the various effect of ejection angle. A contraction channel is reduced for a lower ejection angle, meaning the constriction duct for the case with 5° ejection angle is less than that of the others. Of course, it causes a different increase of that coolant velocity along the wedge-shaped duct.

It has been shown that turbulence kinetic energy is at higher level for the case with lowest ejection angle, compared to the others. It is most likely caused by the existence of pin-fin array inside the cooling channel, which influences the growth of turbulence kinetic energy (see Figure 8–5(e). The decrease of ejection angle causes the reduction of wedge-shaped duct, mainly at the inlet region. It affects the construction of fitted pin-fin array and coolant flow velocity, which triggers the increase of both turbulence levels. As previously discussed in Chapter 7, turbulence kinetic energy increases slightly along the empty channel. It would be increased after replacing the pin-fin array inside the cooling channel. It evidences that the pin-fin array is a key role to cause this discrepancy. With respect to this phenomenon, coolant properties inside the cooling passage would be qualitatively visualised using the fourth case in Chapter 9.

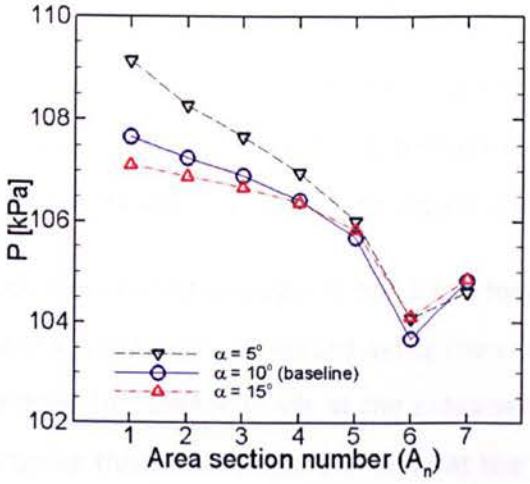

(a) Pressure

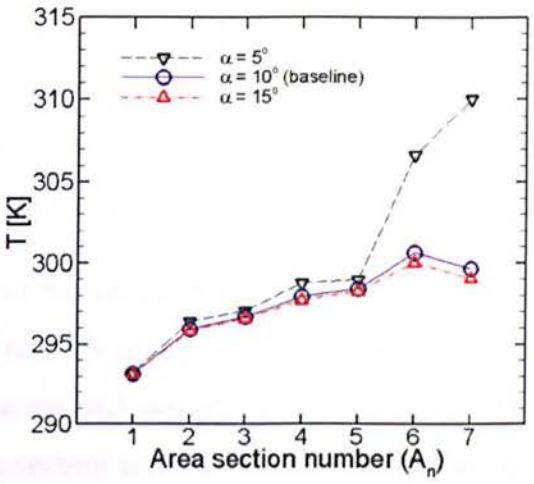

(b) Temperature

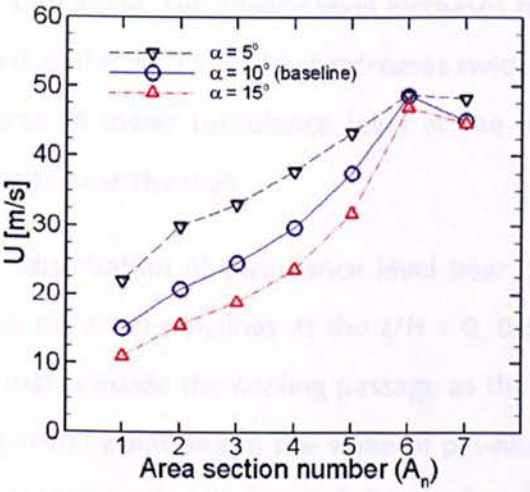

(c) Velocity

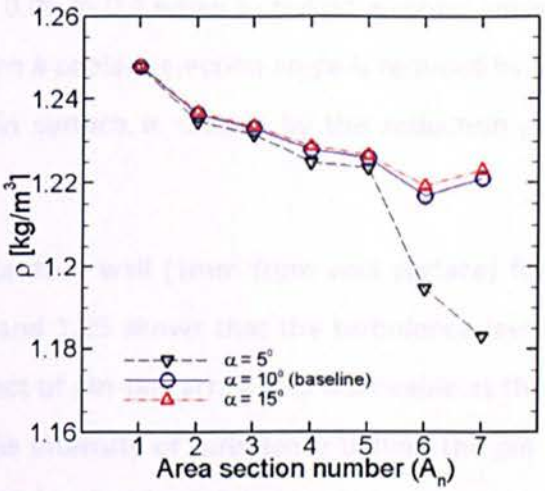

(d) Density

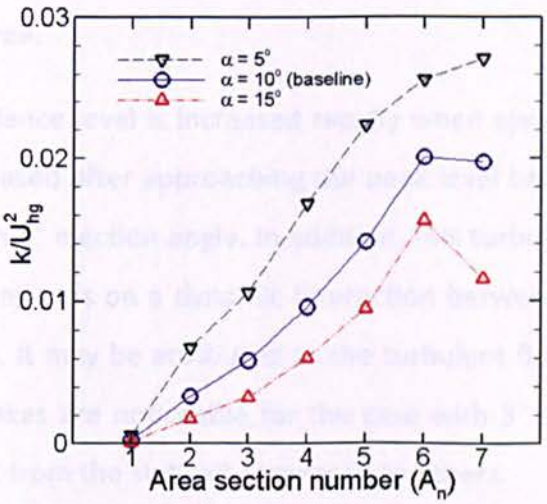

(e) Turbulence kinetic energy

Figure 8–5: Coolant properties inside the cooling passage.

8.5.2 Turbulence Characteristics

Figure 8–6 gives the characteristic of turbulence levels ($T_u = u'/U_\infty$) inside the cooling passage and along the blade TE cutback cooling for three coolant ejection angles. The u' velocity is based on a root mean square streamwise fluctuation flow velocity.

Inside the cooling passage, it has been found that the turbulence level of all three cases above are gradually increased along the cooling passage of wedge-shaped duct. Both the averaged-turbulence levels at the cross-section areas (A_n) and at the pin-fin surfaces (P_n) recognise those increases. The level at the cross-section areas is greater than at the pin-fin surfaces. It is more profound near the slot exit (A_7), mainly for the case with 5° ejection angle. Turbulence level increases from 0.05 to 0.2 when a coolant ejection angle is reduced from 15° to 5°. It increases twice when a coolant ejection angle is reduced by 5 degree. A lower turbulence level at the pin-fin surface is caused by the reduction of velocity near the wall.

The observation of turbulence level near the bottom wall (1mm from wall surface) for three different polylines at the z/H = 0, 0.625 and 1.25 shows that the turbulence level fluctuates inside the cooling passage as the effect of pin-fins array. It is noticeable at the stagnation point and in the wake of pin-fins. The intensity of turbulence behind the pin-fins is greater than in front of the pin-fins. This higher level is related to the recirculation vortices behind the pin-fins array, where both Karman vortex street and Horshoe vortex commonly exist in this area.

It is seen that the turbulence level is increased rapidly when ejecting coolant at the slot exit (A_7), and then decreased after approaching the peak level behind the lip region. It is obvious for the case with 5° ejection angle. In addition, this turbulence level grows along the mixing region that depends on a dynamic interaction between the mainstream flow and the coolant ejection. It may be attributed to the turbulent flow structures along the mixing region. Larger wakes are noticeable for the case with 5° ejection angle due to a stronger ejection coolant from the slot exit compared to others.

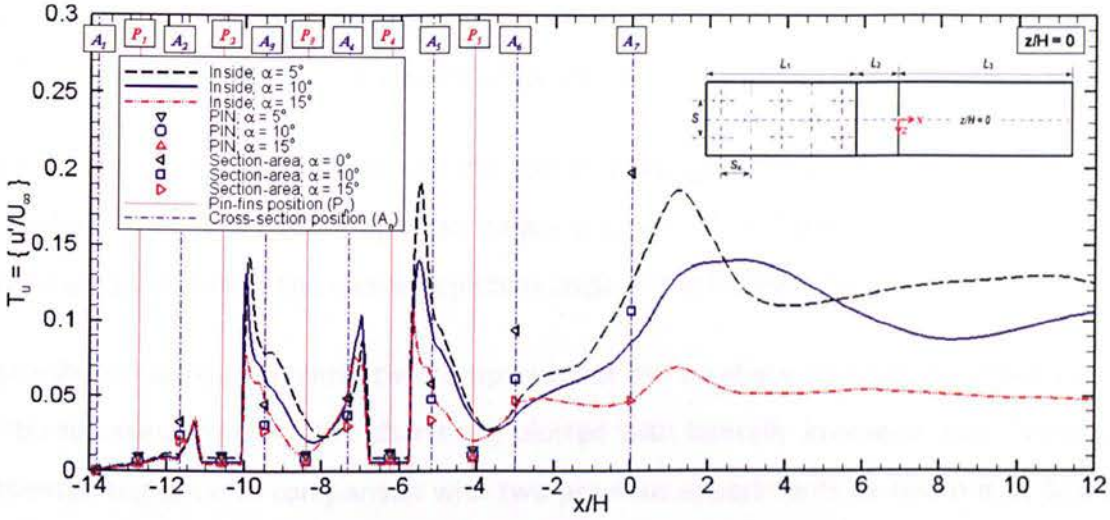

(a) $z/H = 0$

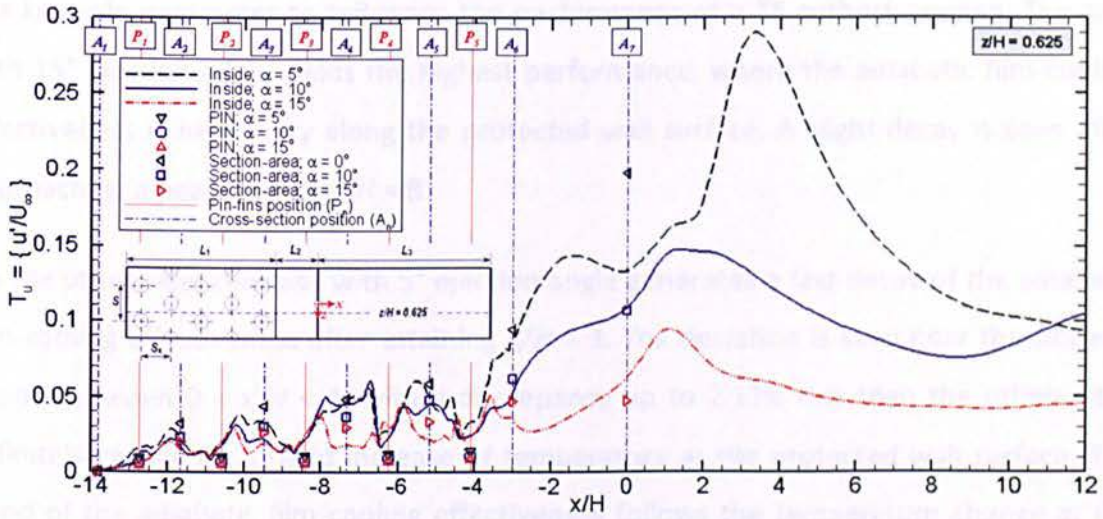

(b) $z/H = 0.625$

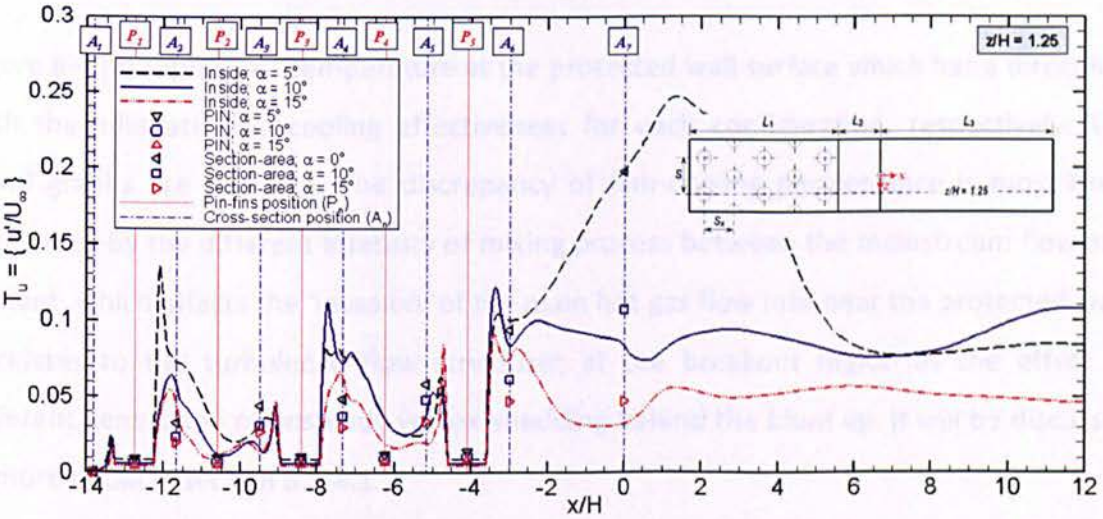

(b) $z/H = 1.25$

Figure 8–6: Turbulence levels.

8.5.3 Protected Wall/Cutback Surface

8.5.3.1 Laterally averaged film-cooling effectiveness:

Numerical study has been done with the aim to investigate the performance of the blade TE cutback cooling for three ejection angles (i.e. α = 5°, 10° and 15°). These cases are simulated by modifying the coolant ejection angle of the baseline model.

Figure 8–7(a) shows a quantitative comparison of the adiabatic film-cooling effectiveness for three cases. Similarly, the charts are plotted with laterally averaged data. These are presented together, in comparison with two previous experiments carried out by Martini *et al.* [4][5][23][24] and Horbach *et al.* [30]. It is confirmed that the coolant ejection angle is a key role parameter to influence the performance of a TE cutback cooling. The case with 15° ejection angle yields the highest performance, where the adiabatic film-cooling effectiveness is near unity along the protected wall surface. A slight decay is seen after approaching a peak level at x/H = 8.

On the other side, the case with 5° ejection angle generates a fast decay of the adiabatic film-cooling effectiveness after attaining x/H > 3. The deviation is seen near the slot-exit region between 0 < x/H < 4, with a discrepancy up to 2.12% less than the others. It is definitely caused by a rapid increase of temperature at the protected wall surface. The trend of the adiabatic film-cooling effectiveness follows the temperature change at the protected wall surface.

Figure 8–7(b) represents temperature at the protected wall surface which has a direct link with the adiabatic film-cooling effectiveness for each configuration, respectively. The trend graphs are opposite. The discrepancy of film-cooling performance is most likely influenced by the different intensity of mixing process between the mainstream flow and coolant, which affects the 'invasion' of the main hot gas flow into near the protected wall. It relates to the turbulence flow structures at the breakout region as the effect of different generation of unsteady vortex-shedding behind the blunt lip. It will be discussed in more detail in section 8.5.4.1.

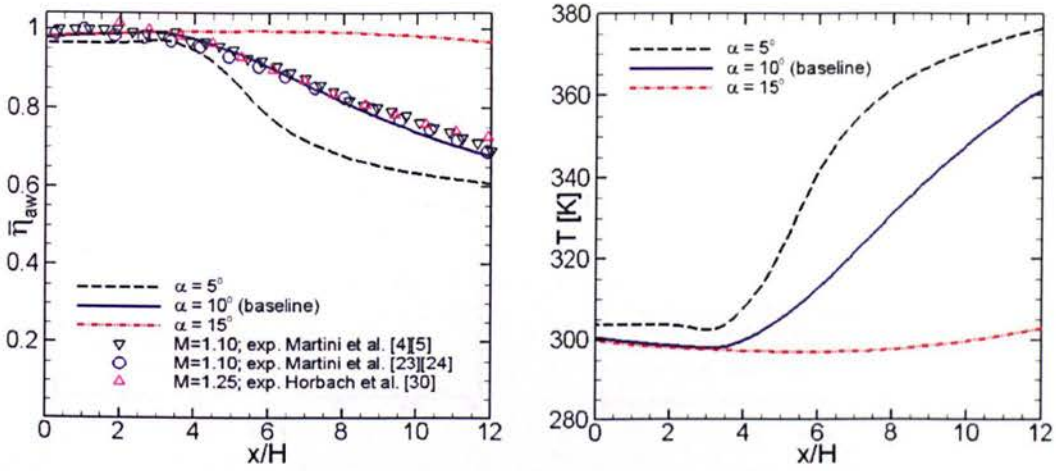

(a) Film-cooling effectiveness (b) Temperature

Figure 8–7: Properties at the protected wall.

8.5.3.2 Film-cooling effectiveness on various *z/H* position:

In order to complete the previous discussion above, Figure 8–8 gives the laterally averaged film-cooling effectiveness compared to the adiabatic film-cooling effectiveness at different *z/H* position (*z/H* = 1.25, 0 and -1.25). It is found that the distribution of the film-cooling effectiveness is non-uniform over the protected wall surface, mainly for the blade TE cutback with 5° ejection angle. It is very pronounced as indicated by the adiabatic film-cooling effectiveness at *z/H* = -1.25 and 1.25. The co-existence of the pin-fin array inside the cooling passage contributes on the generation of turbulent flow structures at the breakout region that influences the distribution of the adiabatic film-cooling effectiveness along the protected wall surface.

It has been found that the adiabatic film-cooling effectiveness at the centre line, mainly near the downstream region tends to decay rapidly compared to other *z/H* position. In addition, it decay exceeds the level of the averaged film-cooling effectiveness. It is likely affected by the layout of pin-fin array that causes a higher turbulent flow velocity along the centre location at *z/H* = 0, and then triggers a intensified thermal mixing process. Therefore, the invasion of main hot gas is stronger along this region.

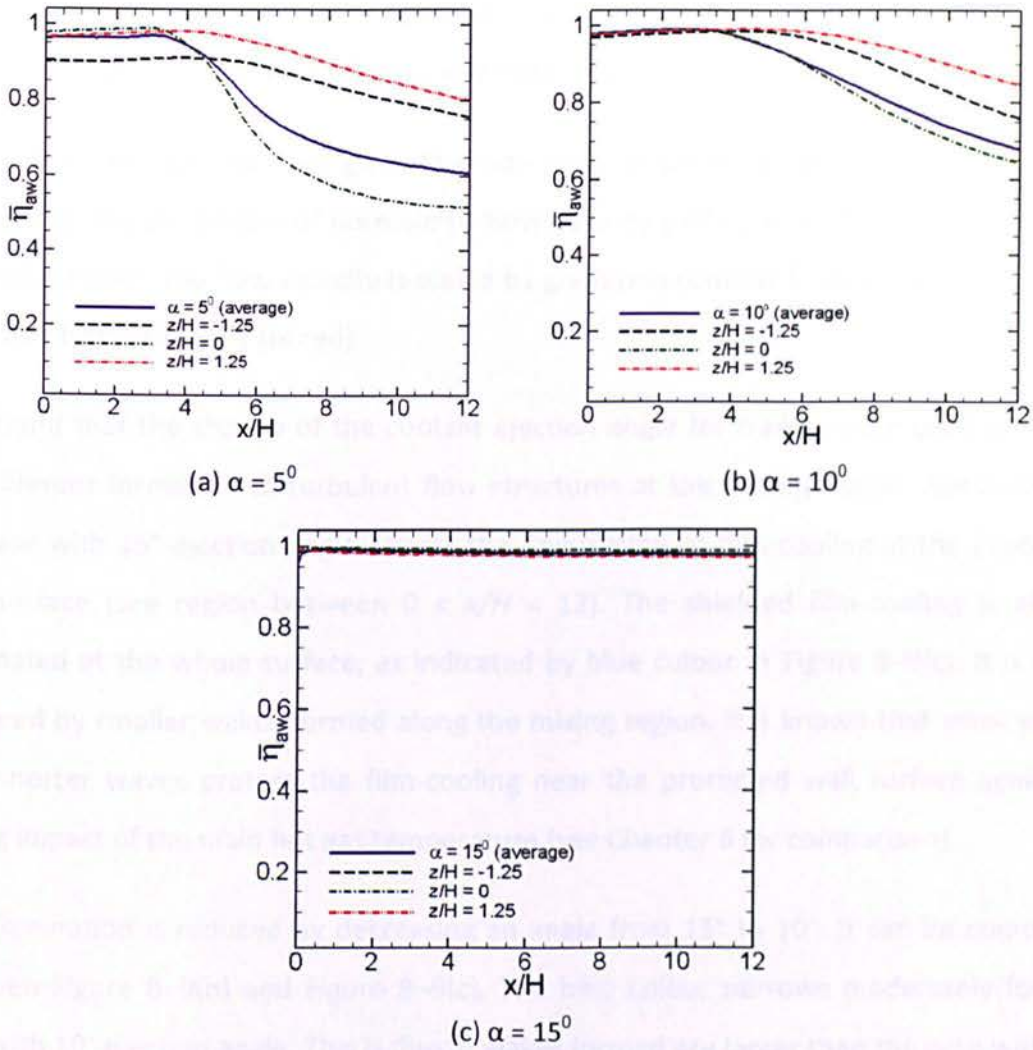

(a) $\alpha = 5^0$ (b) $\alpha = 10^0$

(c) $\alpha = 15^0$

Figure 8–8: Laterally averaged film-cooling effectiveness.

8.5.4 Mixing Region

8.5.4.1 Turbulent flow structures:

As mentioned in previous chapters 6 – 7, performance of a trailing-edge cutback cooling is related to the coherent structures at the mixing region. Figure 8–9 (the left figures) shows the distribution of turbulent flow structures at the mixing region for three different case studies, super-imposed by contour of the adiabatic film-cooling effectiveness at the protected wall and the non-dimensional temperature (θ) distribution at the *x-y* plane for a fixed *z/H* = -1.25. Similarly, these figures are presented by iso-contour of the vortex identification criterion Q as used by von Terzi *et al.* [137] and Schneider *et al.* [28][29]. The iso-surface is based on $\Omega^2 - S^2 = 10^5\ 1/s^2$ as applied by Egorov *et al.* [22]. The colour

indicates the non-dimensional temperature (θ) distribution of thermal mixing which is visualised by gradation contour from a low value of 0 (in red) to a high value of 1 (in blue)

Figure 8–9 (the right figures) gives the side view of turbulent flow structures, super-imposed by the streamline of normalized flow velocity (U/U_{hg}) from the mainstream and the coolant flow. The flow velocity is scaled by gradation contour from a low value of 0 (in blue) to a high value of 1 (in red).

It is found that the change of the coolant ejection angle for trailing-edge cooling causes the different formation of turbulent flow structures at the mixing region. Simulation of the case with 15° ejection angle affects the domination of film-cooling at the protected wall surface (see region between $0 < x/H < 12$). The shielded film-cooling is almost dominated at the whole surface, as indicated by blue colour in Figure 8–9(c). It is likely triggered by smaller wakes formed along the mixing region. It is known that small wakes with shorter waves protect the film-cooling near the protected wall surface against a strong impact of the main hot gas temperature (see Chapter 6 for comparison).

The domination is reduced by decreasing an angle from 15° to 10°. It can be compared between Figure 8–9(b) and Figure 8–9(c). The blue colour narrows moderately for the case with 10° ejection angle. This is due to wakes formed are larger than the case with 15° ejection angle, which trigger the penetration of main hot gas flow into the protected wall, mainly near the downstream region (see region between $6 < x/H < 12$). Therefore, a decay of the adiabatic film-cooling effectiveness is noticeable as shown in Figure 8–8(b).

A strange distribution of the adiabatic film-cooling effectiveness occurs for simulation of the case with 5° ejection angle. It can be seen clearly in Figure 8–9(a) that the distribution is asymmetric in spanwise orientation. Larger wakes are pronounced compared to others. Consequently, a strong thermal mixing occurs for this simulation case. The blue colour dominates at the left region between $0 < z/H < -1.25$, while the right region ($0 < z/H < -1.25$) is slightly less than the right one. The cause of this discrepancy could not be confirmed due to there is no available data of experiment for comparison.

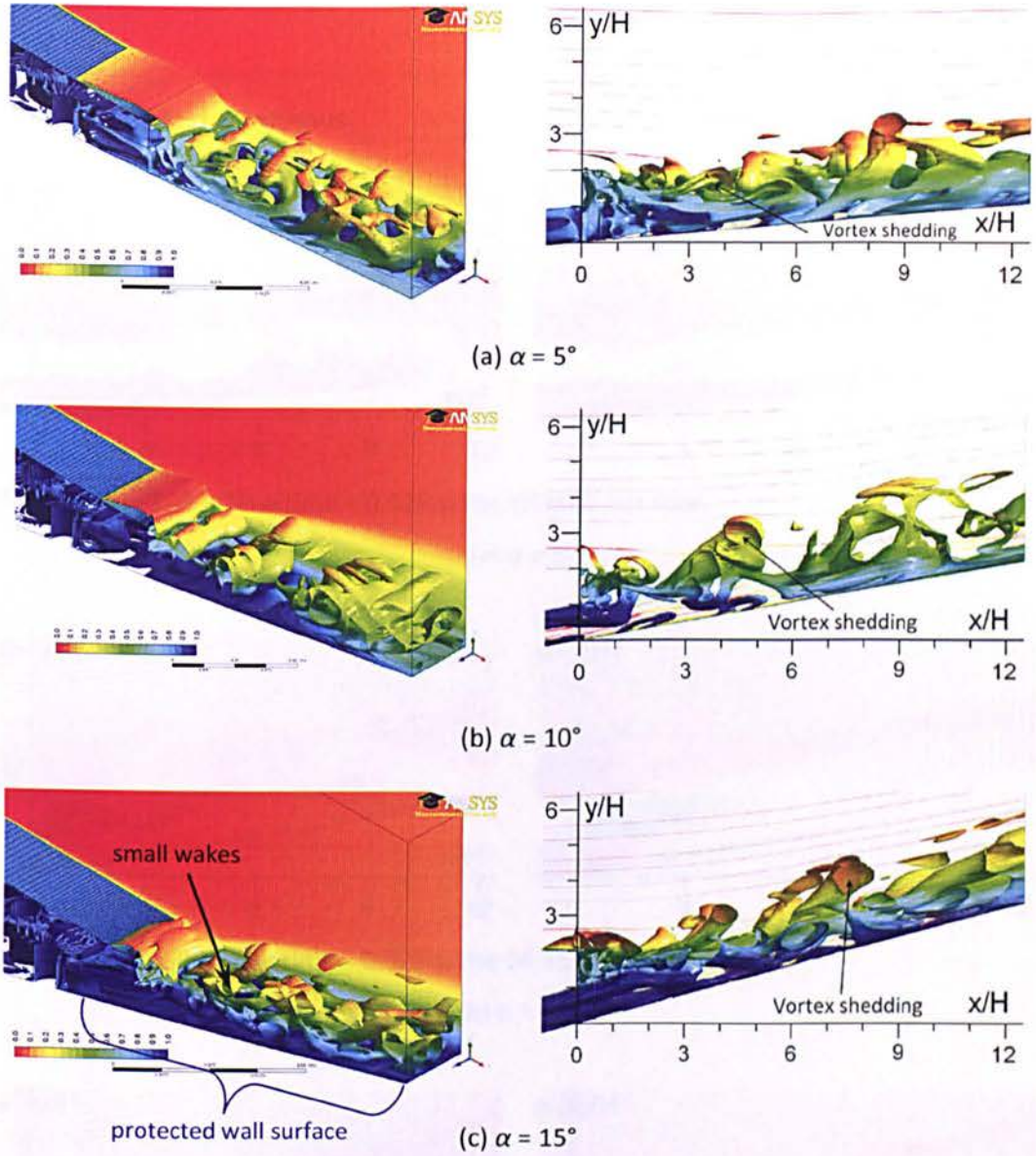

Figure 8–9: Turbulent flow structures

8.5.4.2 Distribution of velocity (U/U_{hg}):

Figure 8–10 shows the normalized instantaneous and time-averaged velocity (U/U_{hg}) along the mixing region at the x-y plane for a fixed z/H = 0. Both are presented by the gradation colour of velocity vector from a low value of 0 (in blue) to a high values of 1 (in red). It has been found that velocity drops significantly, as indicated blue colour around the shadow-triangle area. Superimposed by turbulent velocity fluctuations, the periodic pattern of vortex-shedding from the pressure side lip can be clearly captured for all configurations.

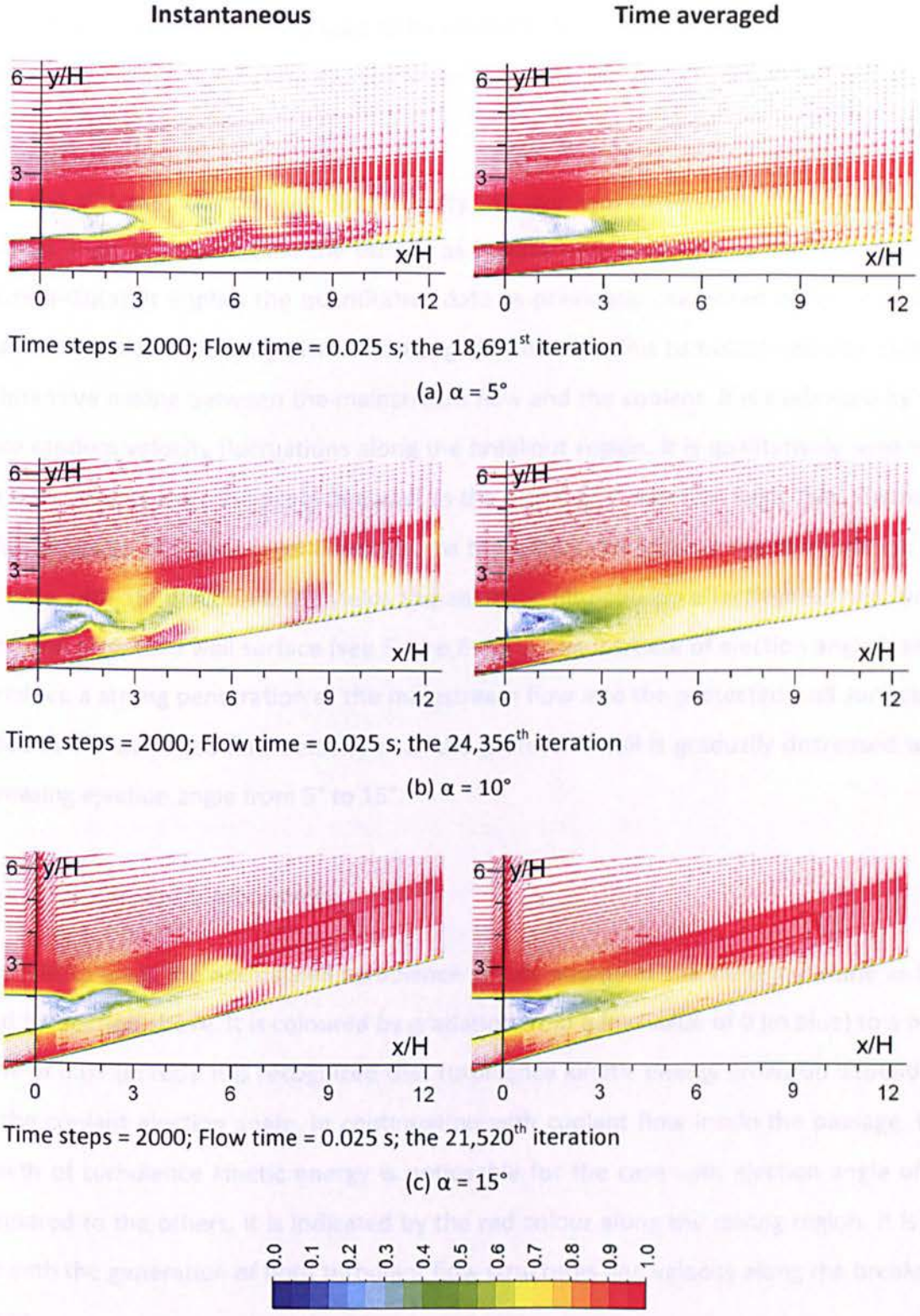

Figure 8–10: Distribution of velocity magnitude (U/U_{hg}) at the *x-y* plane of $z/H = 0$.

From Figure 8–10 (the left figures), the generation of unsteady vortex-shedding is most likely influenced by the periodic wake flow from the coolant slot, which is depending on the coolant ejection angle. It is seen to be more flat at the downstream for the case with higher ejection angle. In contrast, the velocity fluctuation is more obvious for the case with lower ejection angle.

Near the slot-exit, the coolant flow velocity (on average) resulted by the case with 5° ejection angle is greater than the others, as qualitatively indicated by the red colour in Figure 8–10(a). It implies the quantitative data as previously presented in Figure 8–5(c), where coolant flow velocity increases along the channel. This turbulent velocity triggers an intensive mixing between the mainstream flow and the coolant. It is evidenced by the more random velocity fluctuations along the breakout region. It is qualitatively seen that the flow velocity near the protected wall as the effect of 5° ejection angle (see Figure 8–10(a)) tends to at higher level compared to the others. Recall that the computation for the case with 15° ejection angle yields the adiabatic film-cooling effectiveness near unity along the protected wall surface (see Figure 8–8(c)). The increase of ejection angle is seen to reduce a strong penetration of the mainstream flow into the protected wall surface. It is due to the averaged flow velocity near the protected wall is gradually decreased with increasing ejection angle from 5° to 15°.

8.5.4.3 Turbulence kinetic energy:

Figure 8–11 gives the normalized turbulence kinetic energy at the same *x-y* plane as the used for section above. It is coloured by gradation from a low value of 0 (in blue) to a high value of 0.01 (in red). It is recognized that turbulence kinetic energy grows up depending on the coolant ejection angle. In continuation with coolant flow inside the passage, the growth of turbulence kinetic energy is noticeable for the case with ejection angle of 5° compared to the others. It is indicated by the red colour along the mixing region. It is in-line with the generation of both turbulent flow structures and velocity along the breakout region.

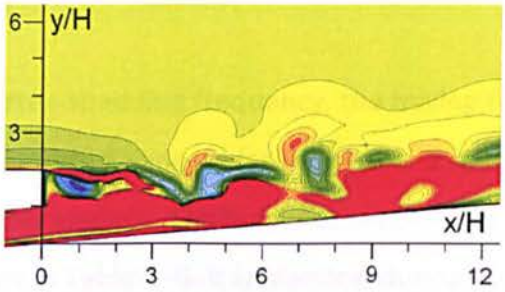

(a) $\alpha = 5^0$ (Time steps = 2000; Flow time = 0.025 s; the 18,691st iteration)

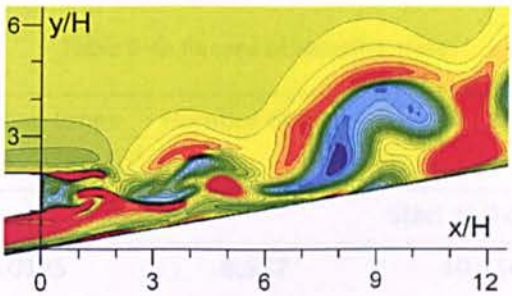

(b) $\alpha = 10^0$ (Time steps = 2000; Flow time = 0.025 s; the 24,356th iteration)

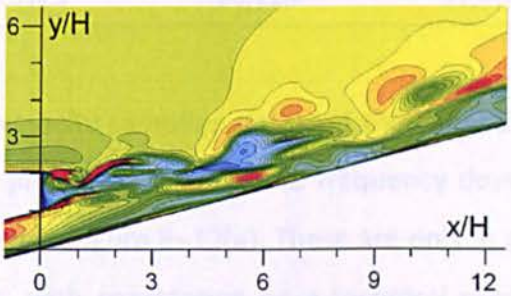

(c) $\alpha = 15^0$ (Time steps = 2000; Flow time = 0.025 s; the 21,520th iteration)

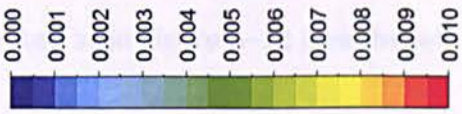

Figure 8–11: Distribution of turbulence kinetic energy (k/U_{hg}^2) at the *x*-*y* plane of $z/H = 0$.

Due to all these configurations are kept at the same lip thickness (t) and slow-height (H), the discrepancy of turbulence kinetic energy is likely affected by the generation of ejecting coolant from the slot exit. As previously mentioned, the change of ejection angle causes the change of the fitted area of wedge-shaped duct and the height of pin-fin array inside the cooling passage. This discrepancy creates a different generation of vortex horseshoe and Karman Vortex Street around the pin-fin array, mainly near the bottom wall inside the cooling passage. Therefore, this discrepancy triggers the generation of turbulence kinetic energy along the cutback region.

8.5.5 Shedding Frequency

In order to analyse the vortex-shedding frequency, the mixing flow velocity is recorded at two different monitoring points S_1 and S_2 (see Figure 4–2, page 66). Only the resultant velocity is monitored for this analysis. Similarly, the record data are taken in interval time of 0.0125 seconds, as given in Table 8–6. It is identical during 1000 time steps. These data then are processed by fast-Fourier Transform.

Table 8–6: Record of sampling data.

Ejection angle (α)	Sampling times	Number of data	Iterations	
			Start at 0.0125s	Stop at 0.025s
5	0.0125	8,577	10,114	18,691
10	0.0125	11,602	12,754	24,356
15	0.0125	10,116	11,404	21,520

Figure 8–12 shows both velocity sampling data and their shedding frequencies for three ejection angles, which is presented in time and frequency domain, respectively. Not all velocity data are presented in Figure 8–12(a). These are only in a selected range between 0.019 and 0.025 seconds, with considering on a technical presentation. Moreover, the period of oscillation could be captured clearly within this interval. Beating phenomenon also could be well demonstrated as in Figure 8–12 (see the left figures).

From Figure 8–12(a), the case with the coolant ejection angle of 15° causes lower amplitude of velocity compared to the others. The design of both angles at 5° and 10° yield similar amplitude with unique response, respectively. By comparing Figure 8–12(a) and Figure 8–12(b), it is found that the amplitude of monitoring points S_1 is less than at S_2. This discrepancy is most likely due to the effect of pin-fin array inside the cooling passage.

Beating phenomenon occurs at all variations within typical waves (see the left Figure 8–12). This phenomenon is clearly seen for the baseline model. The harmonic wave also forms another wave mode in a certain period. It looks a harmonic motion inside an envelope within a certain period. Almost three envelopes could be captured for the

baseline, in a range of sampling data between 0.019 and 0.025 seconds (see the blue colour of harmonic wave in Figure 8–12(a)).

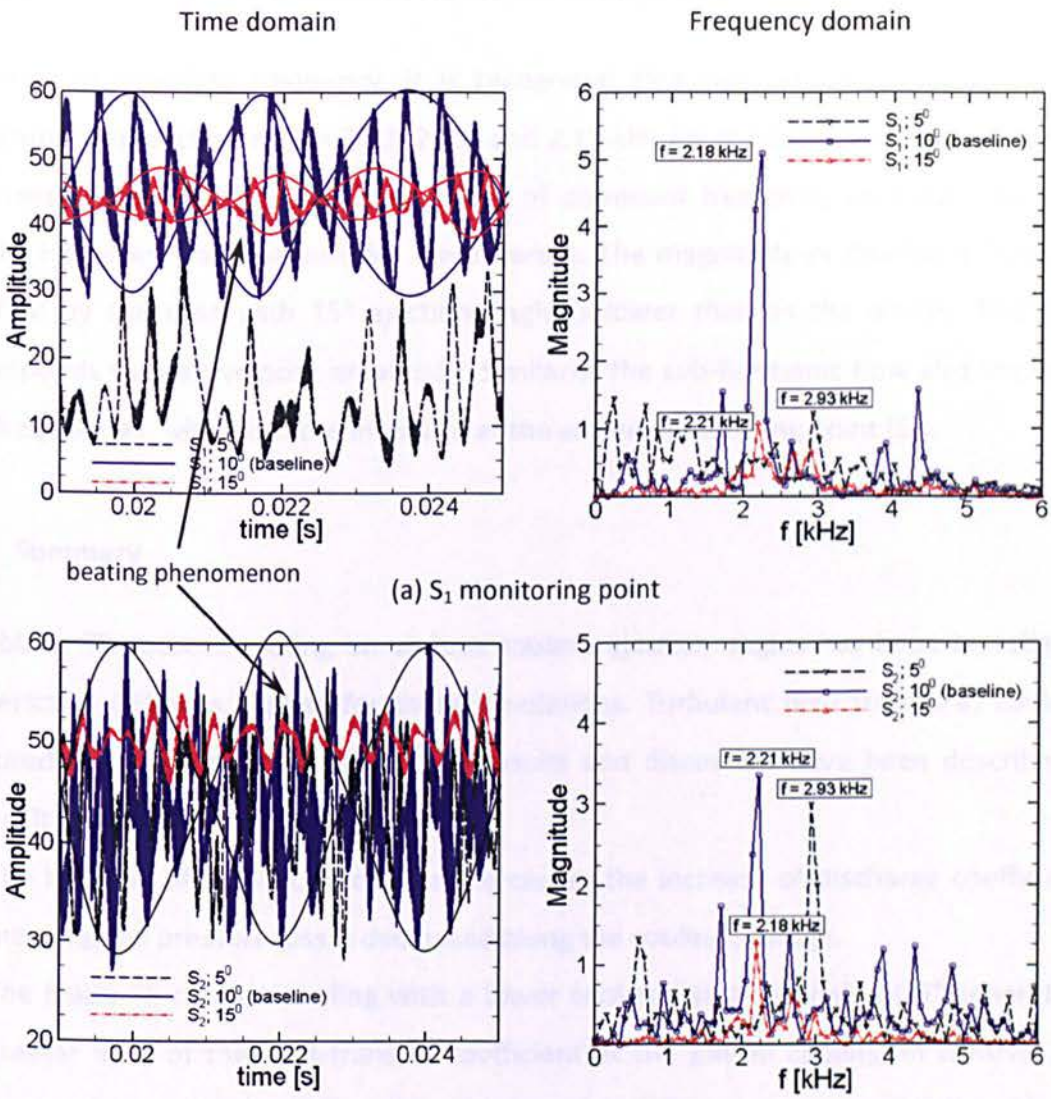

Figure 8–12: Shedding frequencies.

Beating may occur when the forcing frequency is close to the natural frequency of the system. In case of this study, beating phenomenon happens as the 3-D effect of turbulent flow motion from the mainstream flow and the coolant, which has a close frequency. The forcing frequency of both inflow regions probably has a similar natural frequency with mixing flow at the mixing region. It is known that mixing flow is followed by vortex shedding as the effect of lip construction. This vortex shedding illustrates a system that has a specific natural frequency. It is so-called as a characteristic system.

From the left Figure 8–12, it is seen that sub-harmonic response appears at all cases studied. Medic *et al.* [26] found the same sub-harmonic as in this study. It is very pronounced for the case with the coolant ejection angle of 10°.

In terms of shedding frequency, it is recognised (the right Figure 8–12(b)) that the spectrum frequencies are f_s = 2.93, 2.21, and 2.18 kHz for the cases with α = 5°, 10° and 15°, respectively. There is no discrepancy of dominant frequency on both monitoring points. However, both magnitudes are different. The magnitude of dominant frequency resulted by the case with 15° ejection angle is lower than as the others. This trend corresponds to their velocity amplitude. Similarly, the sub-harmonic flow also implicates sub frequencies, which is more intensive at the second monitoring point (S_2).

8.6 Summary

The blade TE cutback cooling on various coolant ejection angles has been investigated numerically. DES was applied for these simulations. Turbulent flow structures could be captured in this numerically study. The results and discussion have been described as above. It can be summarized as follows:

1. The increase of coolant ejection angle causes the increase of discharge coefficients, meaning the pressure loss is decreased along the cooling passage.
2. The blade TE cutback cooling with a lower coolant ejection angle of 5° generates a greater level of the heat-transfer coefficient at the pin-fin cooling. In contrast, the decay of the adiabatic film-cooling effectiveness is more pronounced as the effect of intensified mixing process between the mainstream flow and the coolant.
3. The distribution of the adiabatic film-cooling effectiveness at the protected wall is sensitive against the design of coolant ejection angle. The increase of ejection angle yields the cooling effectiveness near the unity almost along the adiabatic wall, whereas the decrease of ejection angle causes a drastic decay of cooling effectiveness after approaching the peak level.
4. The shedding frequencies are 2.93, 2.21 and 2.18 kHz for the blade TE cutback cooling with an ejection angle of 5°, 10° and 15°, respectively.

CHAPTER 9:

CASE IV: BLADE TRAILING-EDGE CUTBACK COOLING WITH PRESSURE-SIDE (PS) AND SUCTION-SIDE (SS) WALLS

This chapter contains a numerical study of the cooling performance of the trailing-edge (TE) cutback blade with pressure-side (PS) and suction-side (SS) wall surfaces (see Figure 9–1). Both upper and lower domains are considered in this case to provide a computational domain as seen in a real blade TE cooling condition, which is not addressed in the previous studies as presented in Chapters 5 – 8. The concept is to produce a finite thickness at same height of the coolant passage (H) to form a suction-side wall surface into the baseline model.

Another configuration of the simulations is that it is equipped with lands/partitions in an attempt to provide a proper shape as well as a recent design of gas turbine blade. Both computational domains are made within a double-pitch ($2S$) distance of pin-fin array.

The computations use a high quality grid to ensure a sufficiently fine spatial resolution with $\Delta y^+ < 1$ on all surfaces. The fine 'Mesh C' successfully validated in Chapter 5 is adopted to generate meshes for both configurations. The initial and boundary conditions are derived from the experiments carried out by Martini *et al.* [4][5][23][24] and Horbach *et al.* [30], same as the previous simulations (see Chapters 6, 7 and 8). Similarly, computations apply the SST k–ω turbulence model. It is simulated by employing DES simulation up to 2000 time steps, which is an acceptable iteration time to achieve a statistically stationary state condition. It is based on verification results during the validation stage. Both cases (i.e. blade TE cutback without and with lands) are simulated for four various blowing ratios, respectively.

9.1 Blade Trailing-edge Cutback Model with PS-SS Walls and Lands

In order to address the simulation test as well as in a real blade TE cooling condition, a model with pressure-side (PS) and suction-side (SS) wall surfaces has been proposed in the current computation. The blade cutback model studied so far are primarily based on the experimental configuration of Martini *et al.* [4][5][23][24] and Horbach *et al.* [30], which merely considers the pressure-side wall, meaning the blade TE cutback model is investigated by ignoring the influence of mainstream flow along the suction-side wall. Similarly, the previous computations as presented in Chapters 5 – 8 use models without the existence of suction-side wall.

As previously mentioned in Chapter 7, it is known that the pin-fin cooling is commonly integrated with the trailing-edge ejection cooling. Both pressure-side and suction-side walls exist in a real phenomenon. With respect to those aspects, the suction-side (SS) geometry is introduced into the current test model for this computation. The domain is realistically modelled compared to the previous case studies as described in Chapters 5 – 8. This geometry considers internal features inside the cooling passage in an attempt to have an integrated design of a TE cutback cooling system with a more realistic shape. Several blade TE cutback configurations such as Martini's [4][5][23][24], Horbach's [30], Joo's [27] and Ling's models [41] are considered to create the current test model. A combination of those models generates an integrated trailing-edge cutback cooling with circular pin-fin inside the cooling passage, which is completed by a suction-side wall from Joo's model [27].

Another important section in a pressure-side bleed cooled TE design is the structure of the land extensions as depicted in Figure 2–3 (see page 17). Lands are periodically constructed in spanwise direction following the regularity of internal features inside the cooling passage for structural strength orientation. In addition, this construction is expected to guide the ejecting coolant from the slot-exit in order to expand the reach of coolant ejection up to the downstream region. In case of a TE cutback with multi-ejection holes, regrouping of attached coolant jet also can be avoided by the lands, then the interaction of two/three coolant jets can be minimised. This is known that those

interactions are unexpected for a film-cooling effectiveness over the protected wall surface [15][16].

Several publications reported that the land extensions are used for a structural strength purpose. This becomes important to assess the performance of a TE cutback with the existence of lands. It is known that land extensions create blockages at the slot exit depending on their shape. An experimental study carried out by Horbach *et al.* [30] found that unsteady vortex shedding could be reduced using lands construction mainly at higher blowing ratios (for example at M = 1.25), meaning the effectiveness of film-cooling is increased. As commonly known, a higher film-cooling effectiveness would be expected along the breakout-slot [39]. A higher level of this parameter represents an optimum performance of a blade TE cutback cooling as previously explained in the literature review in Chapter 2.

The works of Ling *et al.* [41], Murata *et al.* [52] and Fiala *et al.* [74] provide a detailed study on performance of a blade TE cutback with land extensions. Fiala *et al.* [74] studied the impact of letterbox partitions on a trailing-edge against aerodynamic losses and heat transfer. Cutback surface and cooling flow slot for various geometries inside the cooling passage (i.e. short and long diffuser, rib and dimple) have been examined for various blowing ratios between 0.5 and 2.0. Film cooling effectiveness and land top surfaces were observed for the main-flow Reynolds number of 20,000 that was defined by the mean velocity and two times the channel height. The passage expansion caused the streamwise decrease of film-cooling effectiveness [52].

Two different land models of an airfoil have been investigated experimentally by Ling *et al.* [41]. This investigation considered the pin-fin array inside the cooling passage. It was recognised that the thinner lands give a much higher spanwise averaged film-cooling effectiveness on the breakout surface.

Using a similar model to that studied by Holloway, *et al.* [19][25], a critical mean flow structure which triggers a rapid mixing and low film-cooling effectiveness in a fully turbulent flow was successfully identified by Benson *et al.* [53]. The 3-D mean flow structures played a major role in controlling a film-cooling effectiveness. This finding was

in-line with the measurement performed by Chen *et al.* [39], who studied a turbine blade TE film-cooling breakout.

A recent experiment carried out by Yang *et al.* [6][37] highlighted that both blowing ratio and lands are keys important parameters to influence an effectiveness of film-cooling. In addition, the distribution of film-cooling effectiveness has a strong correlation with flow structures. It was based on experimental investigation of a TE cutback cooling at various blowing ratios between 0.4 and 1.6.

9.2 Computational Domain and Grids

There are two computational domains for the present simulation, i.e. the case without and with lands. Both are developed from the baseline model as previously used on the verification and validation stage in Chapter 5. Therefore, all the main dimensions between L_1 and L_3 region are totally kept the same as the baseline model, meaning internal features inside the cooling passage also use staggered circular pin-fins configuration (see Figure 4–2, page 66).

Figure 9–1(a) illustrates the 3-D computational domain after adding the suction-side (SS) wall region into model, with the aim is to provide a mainstream flow along the suction-side wall. This suction-side (SS) wall is placed in a distance of 4.8 mm below the protected wall, in parallel with the ejection angle. The suction-side wall region is modelled using the same height as the pressure-side wall region. The cutback region is extended up to 60 mm in x-direction, same as the length of L_3 region. The formed-lip between the protected wall and the suction-side wall is filleted by radius of 2.4 mm. The height of the outflow slot follows the intersection between pressure-side (PS) and suction-side (SS) wall regions. The computational domain is made within a double-pitch distance of pin-fin array in order to consider a space on designing a blade TE cutback with lands (see Figure 9–1(b)). Periodic boundary conditions are prescribed on the lateral planes.

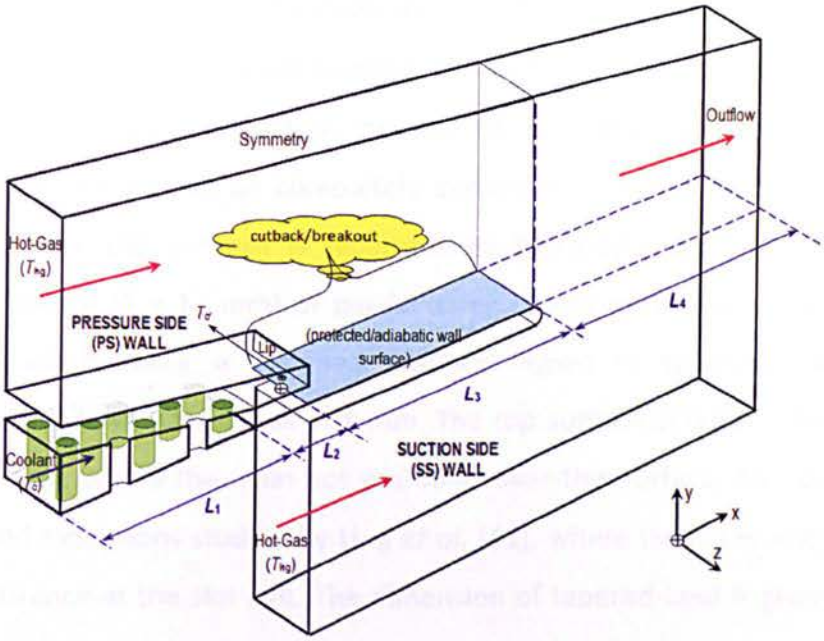

(a) Computational domain

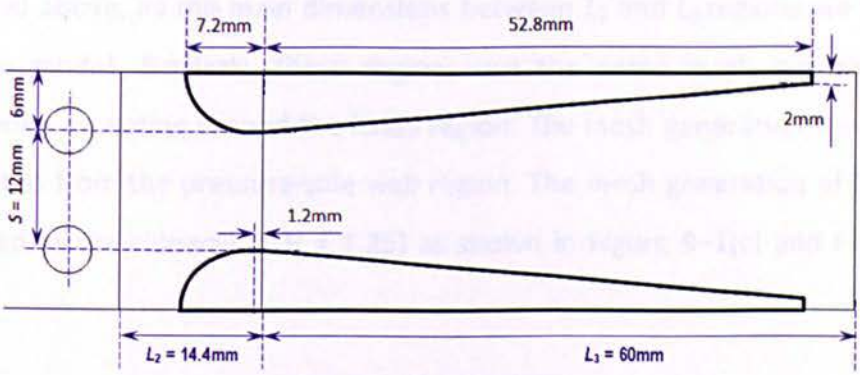

(b) Dimension of land extensions

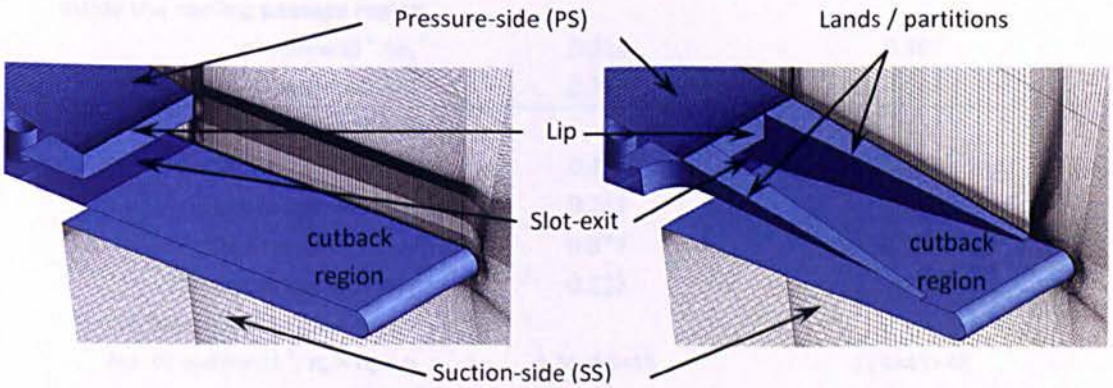

(c) TE breakout with PS-SS

(d) TE breakout with PS-SS and Lands

Figure 9–1: Domains and meshes.

Due to all main dimensions could be captured from the baseline model, this section only describes a few modification and dimensions for both computational domains as shown in Figure 9–1(c) and Figure 9–1(d). In the case of computational domain without land extensions, dimensions could be completely derived from Figure 9–1(a). In addition to domain with lands, the slot exit is separated by teardrop-shaped partitions in every single-pitch distance (S = 12 mm) of pin-fin array. These partitions are tapered at the downstream, which cause a widened cutback region in spanwise direction. The downstream lands have a thickness of 1 mm. The top surface of lands is in-line with the pressure-side wall, where the main hot gas flows over this surface. This design is made with airfoil land extensions studied by Ling *et al.* [41], where lands are installed in every single-pitch distance at the slot exit. The dimension of tapered-land is given in Figure 9–1(b).

As mentioned above, all the main dimensions between L_1 and L_3 regions are the same as the baseline model. Similarly, these regions use the same mesh generation as the baseline model, excepting around the lands region. The mesh generation for suction-side wall is adopted from the pressure-side wall region. The mesh generation of both models are portrayed at the sidewall (z/H = 1.25) as shown in Figure 9–1(c) and Figure 9–1(d), respectively.

Table 9–1: Mesh statistics.

TE breakout	with PS-SS	with PS-SS and lands
Inside the cooling passage region		
pin-fin wall [a] Δy_1^+	0.914	0.487
end-wall Δy_1^+	0.759	0.544
Mainstream region		
pressure side wall Δy_1^+	0.484	0.484
suction side wall Δy_1^+	0.281	0.280
The first lip wall Δy_1^+	0.878	0.761
The second lip wall Δy_1^+	0.226	0.199
TE breakout/cutback region		
No. of elements [b], $n_x \times n_y \times n_z$	124×48×48	124×48×48
protected wall Δy_1^+	0.344	0.204
average		
Δy_1^+	0.776	0.423

[a] an average of Δy_1^+ in the radial direction of pin-fins, [b] elements at the block of TE breakout-slot.

Table 9–1 shows the mesh statistics for both configurations above. These are generated with grid resolution of $\Delta y^+ < 1$ in order to assure a sufficiently fine spatial resolution. The interesting area (i.e. adiabatic/protected wall) is made within higher quality meshes with average $\Delta y^+ < 0.4$, as suggested by Nishino, *et al.* [126]. Mesh generation considers the growth of spacing in all directions as suggested by Spalart *et al.* [108] [123] and Joo *et al.* [27]. A boundary layer mesh is applied to all wall surfaces.

9.3 Boundary Conditions and Numerical Treatments

Same as the previous computational studies as explained in Chapters 6 – 8, simulations use exactly the same initial and boundary conditions as experiments worked out by Martini *et al.* [23][24]. The computational domain is designed to replicate the experimental setup. It is based on a realistic engine condition with mainstream Mach number of 0.125 (see Table 4–1, page 64). Boundary conditions for suction-side (SS) domain are adopted from pressure-side (PS) region. This numerical study is performed with low and high blowing ratios published by Martini *et al.* [23][24]. Simulations apply the SST $k-\omega$ turbulence model, as it is the best approach as previously achieved during verification and validation (see Chapter 5). Therefore, Detached-Eddy Simulation is employed for both case studies. The setting-up of simulations can be described as in Table 9–2.

Table 9–2: Setting-up of simulation.

Model	TE cutback cooling with PS - SS – configuration inside the cooling passage = an equilaterally staggered array of five rows of cylindrical pin fins; – lip-thickness to slot height ratio, $t/H = 1$; – ejection angle, $\alpha = 10^0$
Domain size	Double pitch of pin-fin array
Turbulence model	SST $k-\omega$
Wall temperature (T_w)	325 K
Time step sizes	1.25×10^{-5} seconds
Initial and boundary conditions	see Figure 4–3 (page 68)

The same setting-up of simulation is also applied for the case with land extensions. The land walls are set to be adiabatic conditions as at the protected wall. The effects of blowing ratios are examined ranging from M = 0.42 to 1.83 for case without lands and M = 0.36 to 2.68 for case with lands. Each configuration is simulated for four different blowing ratios. Due to blowing ratio is obtained after doing a simulation; four variations are highly dependent upon the definition of coolant flow velocity at inflow region (u_c). With respect to these variations, the definition of coolant flow velocity as used on the validation stage is referred on the computations for the case without lands. Blowing ratios of 0.42, 0.89, 1.35 and 1.83 must be related to boundary condition of coolant flow velocity at the inflow region for u_c of 4.75, 10, 15 and 20 m/s.

In terms of blowing ratio for simulation of the configuration with lands, 15 m/s coolant flow velocity is used at the first time by assuming the computation would achieve the same blowing ratio of 1.35 as obtained for the configuration without lands. In fact, it has been found that simulation results in a higher blowing ratio at M = 2.68. It is likely caused by a reduction of the slot exit due to an extending lands construction into coolant slot. Therefore, a range discrepancy of blowing ratios for both configurations could not be hindered. Table 9–3 and Table 9–4 give the calculations of blowing ratios for both cases without and with land extensions, respectively. In addition, it is known that the density ratio of the previous test condition is around 1.67. This ratio has been verified in the present computations as inserted in Table 9–3 and Table 9–4, which is seen to agree well with experimental data.

Table 9–3: Calculation of blowing ratios (TE without lands)

Coolant inflow	u_c (m/s)	4.75	10	15	20
Slot-exit[a]	$u_{c'}$ (m/s)	14.439563	30.248104	45.497765	60.334805
	$\rho_{c'}$ (kg/m^3)	1.2113689	1.2189772	1.2230598	1.2250682
Mainstream flow	u_{hg} (m/s)	55.999996	55.999996	55.999996	55.999996
	ρ_{hg} (kg/m^3)	0.73166305	0.73166305	0.73166305	0.73166305
Blowing ratio	$M = (\rho_{c'}u_{c'})/(\rho_{hg}u_{hg})$	**0.426905077**	**0.899900701**	**1.354121439**	**1.833968833**
Density ratio	$\rho_{c'}/\rho_{hg}$	1.65563766	1.666036299	1.67161619	1.674361169
Re[b]	$(u.d_{hyd})/v$	4,027	8,487	12,722	17,045

[a] It is based on the properties at the slot exit (A_7), [b] It is based on the properties at the section A_6 (see Figure 5–10, page 92).

Table 9–4: Calculation of blowing ratios (TE with lands)

Coolant inflow	u_c (m/s)	2	4.75	7.5	15
Slot-exit [c]	$u_{c'}$ (m/s)	12.227798	28.722885	45.048161	89.576591
	$\rho_{c'}$ (kg/m^3)	1.2142811	1.2169057	1.2202832	1.2255787
Mainstream flow	u_{hg} (m/s)	55.999996	55.999996	55.999996	55.999996
	ρ_{hg} (kg/m^3)	0.73166305	0.73166305	0.73166305	0.73166305
Blowing ratio	$M = \rho_{c'}u_{c'}/\rho_{hg}u_{hg}$	**0.362383438**	**0.853072289**	**1.34164788**	**2.679394027**
Density ratio	$\rho_{c'}/\rho_{hg}$	1.659617907	1.663205078	1.667821274	1.675058895
Re [d]	$(u \cdot d_{hyd})/\nu$	1,744	4,062	6,428	12,833

[c] It is based on the properties at the slot exit (A_7), [d] It is based on the properties at the section A_6 (see Figure 5–10, page 92).

9.4 Results and Discussion

Once a proper computational domain and grid of the blade TE cutback with PS – SS have been created within a double-pitch distance of the pin-fin array inside the cooling passage, simulations are run by DES for four blowing ratios. Similar to the previous simulations as presented in Chapters 6 – 8, data could be collected after approaching a statistically stationary state up to 2000 time steps. The results are analysed and interpreted in a similar manner with the experiments carried out by Martini *et al.* [4][5][23][24] and Horbach *et al.* [30], and three quantities will be used for assessment.

Another case considers the coexistence of land extensions as mentioned earlier. This computation uses the same treatments as the case without lands. Similarly, data collection and post-processing are worked out after approaching a flow time of 0.025 seconds, which is equal to computation times of 720 hours. It should be related to the statistically stationary state computation mentioned above.

The simulation results of both cases (see Figure 9–1) are presented on four blowing ratios, respectively. Three quantities: film-cooling effectiveness (η_{aw}), discharge coefficient (C_D), and shedding frequency (f_s) are used as the study parameters in an attempt to assess the performance of both cases.

9.4.1 Internal Cooling Passage

Two configurations, with and without lands, have been simulated within four blowing ratios. The coolant flow behaviour along the cooling channel due to the effect of blowing ratios is investigated for both cases. This flow behaviour is likely to be related to a dynamic interaction between the mainstream flow and the coolant at mixing region.

9.4.1.1 Discharge coefficient:

Figure 9–2 shows a CFD prediction of discharge coefficients (C_D) for both studies, in comparison with the available data of experimental measurements carried out by Martini *et al.* [23][24] and Horbach *et al.* [30] including a previous computation performed by Martini *et al.* [23][24]. The predicted data are plotted against blowing ratios. In general, the level of discharge coefficient increases gradually when blowing ratios is increased. It has been found that the CFD data for the case with PS-SS matches with that of the experiments mentioned above, as well as the CFD data carried out by Martini *et al.* [23][24]. The use of both cases with and without suction-side walls yield a similar level of discharge coefficient in the range of 0.58 – 0.64 for various blowing ratios simulated. This finding is seen to be consistent with the measurement data found by Horbach *et al.* [30]. However, it is noted that both previous experiments use a full domain of blade TE cutback with pressure-side (PS), whilst these computations apply a partial domain with double pitch distance of pin-fin array. The slot-height (H) used by Horbach *et al.* [30] is lower than the other models, but they keep the same t/H ratio as the works of Martini *et al.* [23][24] including the present study. These facts imply that adding suction-side (SS) wall and the domain size does not affect significantly on the discharge coefficient. Both simulations of the cases with PS and PS-SS wall yield the same level of discharge coefficient as experiment performed by Horbach *et al.* [30]. It is highly reasonable due to the discharge coefficient representing the pressure losses inside the cooling passage. It is known that all domains have the same internal features as the baseline model.

In regards to the case with lands, it can be seen clearly that the discharge coefficient for the case with land extensions is greater than that of for the baseline, with an average discrepancy up to 20% (see Figure 9–2(a)). This finding is contradictive with the work of

Horbach *et al.* [30], which leads to a nearly constant decrease approximately 4% within the whole range of blowing ratios. The reason of this discrepancy is most likely caused by the different reference of the slot-exit area for calculating the discharge coefficients. The current numerical study computes them with the slot-exit area in each design. It is known that the slot-exit area reduces up to 50% as the existence of land constructions as shown in Figure 9–1. In the experiments, Horbach *et al.* [30] does not explain the slot-exit area used on their calculation. No clarification is provided concerning their experiments. Their calculation is probably done by keeping a constant area for both different cases. An evaluation of discharge coefficient in this numerical study would give a similar order as found by Horbach *et al.* [30], if both calculations use the same slot-exit area. The discharge coefficients for the use of land extensions into the reference cooling becomes a relatively lower than the cases with PS-SS wall and the baseline (see Figure 9–2(b)). The discrepancy is obvious between the present computation and the experiment done by Horbach *et al.* [30]. This may be attributed to the different design of land extensions by these two studies.

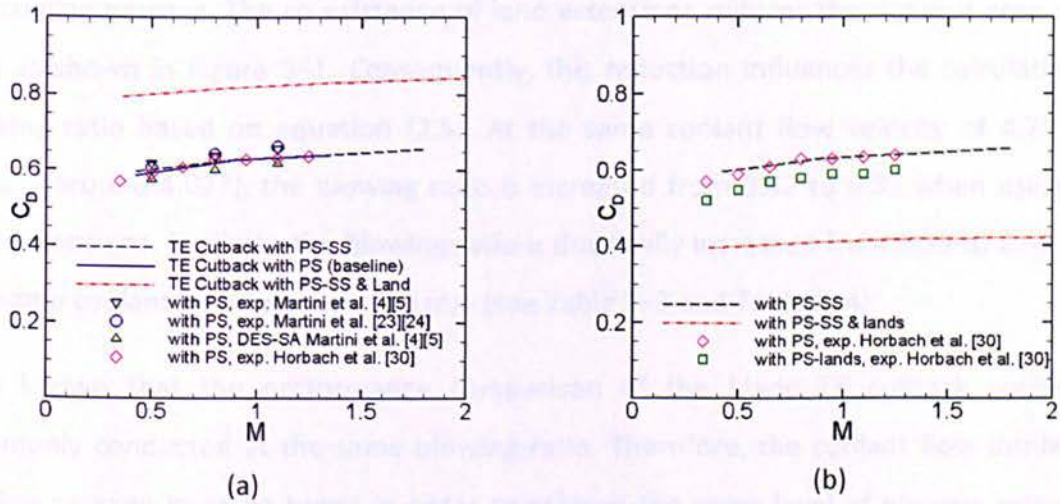

Figure 9–2: Discharge coefficients.

9.4.1.2 Heat transfer coefficient of the pin-fins array:

Figure 9–3 shows the averaged heat-transfer coefficient (HTC) at the surface of the pin-fin array on varying blowing ratios for both cases, with and without lands. Both use the same position of pin-fin rows ($P_1 - P_5$) as previously defined in Figure 5–10. It has been found

that the averaged heat-transfer coefficient is increased gradually along the cooling passage depending on the blowing ratio. Due to all case studies are kept at the same main hot gas flow velocity of 56 m/s, the blowing ratio follows the change of Reynolds number at the coolant slot, which is known as the throat section (A_6) (see Figure 5–10, page 92). The heat-transfer coefficient almost remains unchanged at lower blowing ratios, for example at M = 0.42 or Re_{throat} = 4,027 as shown in Figure 9–3(a). The heat-transfer coefficient is seen to have a higher level by rising more than two times of Reynolds number. The increase of heat-transfer coefficient is obvious near the slot exit. This is more noticeable when increasing Reynolds number. This can be captured at Re_{throat} = 12,722 and 17,045 for the case without lands. A similar rise is also seen for the case with lands as shown in Figure 9–3(b). The previous experiment carried out by Tarchi *et al.* [13] yielded a similar increase as this finding. They used seven rows of staggered pin-fins inside the wedge-shape duct. The internal pin-fin cooling was not coupled with trailing-edge cutback. This boundary condition was very different from the present computation.

As previously described, both computational models have the same pin-fin array inside the cooling passage. The co-existence of land extensions reduces the slot-exit area up to 50% as shown in Figure 9–1. Consequently, this reduction influences the calculation of blowing ratio based on equation (2.5). At the same coolant flow velocity of 4.75 m/s (Re_{throat} around 4,027), the blowing ratio is increased from 0.42 to 0.85 when using the land extensions. Similarly, the blowing ratio is drastically increased from 1.35 to 2.68 with the same coolant flow velocity of 15 m/s (see Table 9–3 and Table 9–4).

It is known that the performance comparison of the blade TE cutback cooling is commonly conducted at the same blowing ratio. Therefore, the coolant flow inside the cooling passage must be tuned in order to achieve the same level of blowing ratio. For example, the coolant flow velocity must be decreased a half times from 15 to 7.5 m/s when installing land extensions as in Figure 9–1(b), in an attempt to keep the same level of blowing ratio around 1.3. This velocity is equal to a decreasing Reynolds number from Re_{throat} 12,722 to 6,428.

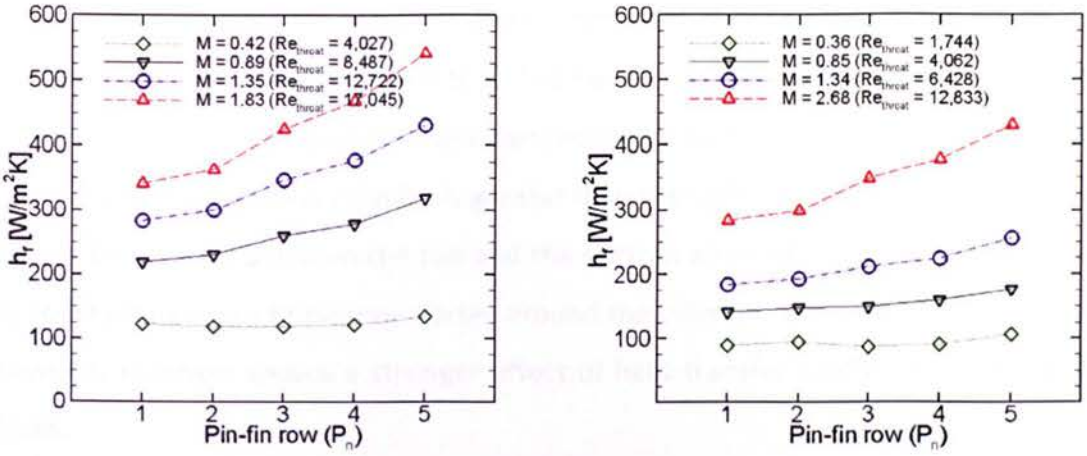

(a) TE breakout with PS-SS top

(b) TE breakout with PS-SS and Land

Figure 9–3: HTC at the pin-fin surfaces.

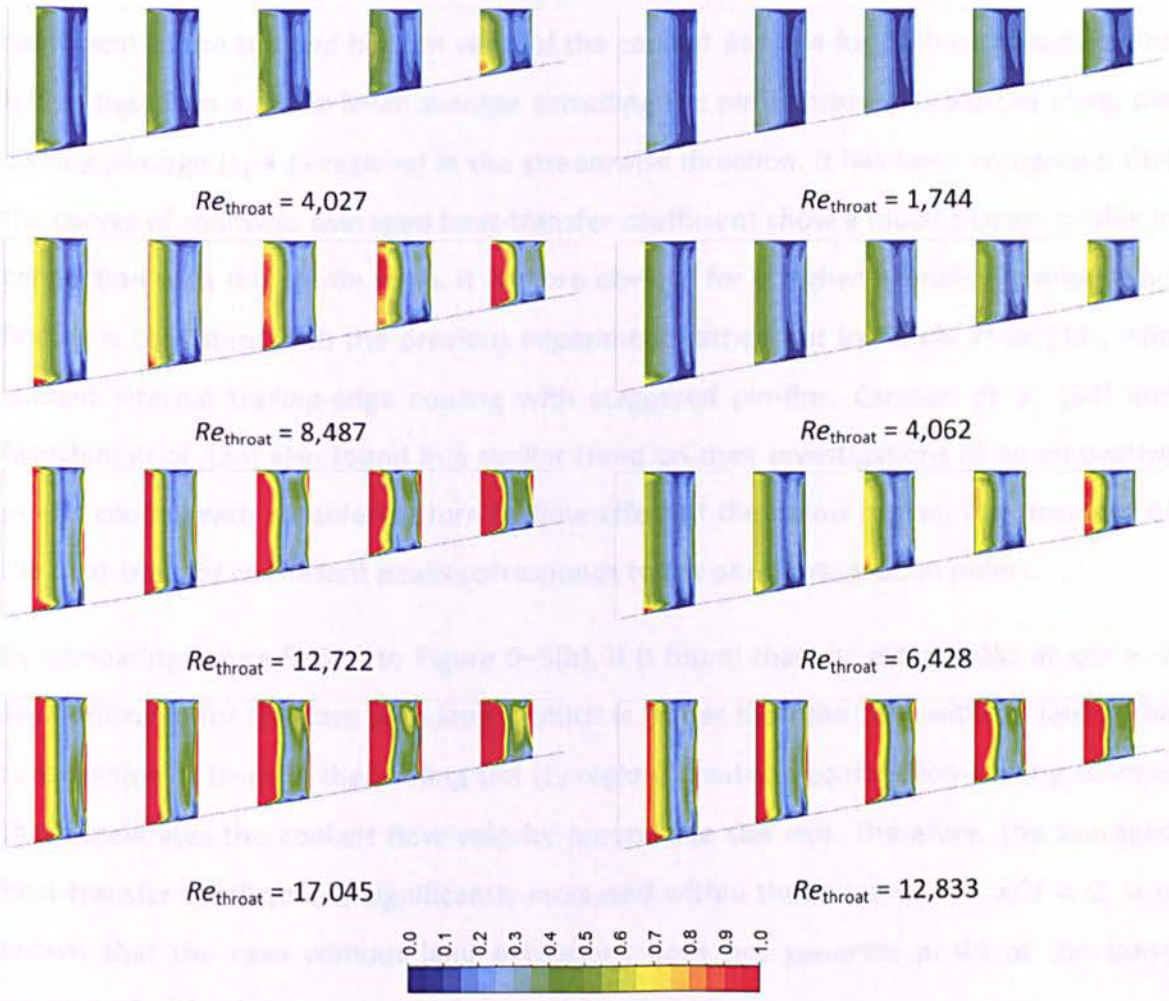

(a) without lands

(b) with lands

Figure 9–4: HTC contour at the pin-fin surfaces.

Figure 9–4 gives the contour of heat-transfer coefficient at the surface of the pin-fin array as quantitatively presented in Figure 9–3. The heat-transfer coefficient is non-uniform at the pin-fin surface due to different flow behaviour along the coolant passage. The HTC in the left area of each vertical cylinder is greater than the right regions. A slight discrepancy is seen to be obvious between the top and the bottom areas of the vertical cylinder. It is likely to be related to a horseshoe vortex around the cylinder. It is seen that the increase of Reynolds numbers causes a stronger effect of heat-transfer coefficient on the pin-fin surfaces.

9.4.1.3 Heat transfer coefficient at the coolant wall duct:

Figure 9–5 shows the quantitative comparison of the spanwise averaged heat-transfer coefficient at the top and bottom walls of the coolant passage for both case studies. The HTC is based on a direct linier average excluding the pin imprint. It is plotted along the cooling passage (L_1 + L_2 regions) in the streamwise direction. It has been recognised that the curves of spanwise averaged heat-transfer coefficient show a much sharper profile in connection with the pin-fin rows. It is more obvious for a higher Reynolds number. This finding is consistent with the previous experiment carried out by Tarchi *et al.* [13], who studied internal trailing-edge cooling with staggered pin-fins. Carcasci *et al.* [34] and Bianchini *et al.* [33] also found in a similar trend on their investigations of an innovative pin-fin cooling with considering turning flow effect at the inflow region. The presence of the heat-transfer coefficient peaks corresponds to the pin-fin stagnation points.

By comparing Figure 9–5(a) to Figure 9–5(b), it is found that the extra peaks at x/H = -2 are noticeable for the case with lands, which is higher than the case without lands. The construction of lands in the cooling slot (L_2 region) creates a constriction-cooling channel that accelerates the coolant flow velocity around the slot exit. Therefore, the averaged heat-transfer coefficient is significantly increased within the range of $-4 < x/H < -2$. It is known that the case without land extensions does not generate peaks at the same position of x/H = -2.

From Figure 9–5(c) and Figure 9–5(d), there are no available data within the range of $-3 < x/H < 0$. The bottom wall of L_2 region is set to be adiabatic as suggested by Martini *et al.*

[4][5]. By comparing Figure 9–5(a) with Figure 9–5(c), it is seen that the spanwise averaged heat-transfer coefficient at the top wall is greater than that of at the bottom wall. It is likely triggered a different horseshoe vortex between them. This finding is reasonable due to the bottom wall has the same inclination as the protected wall with a 10^{o} ejection angle.

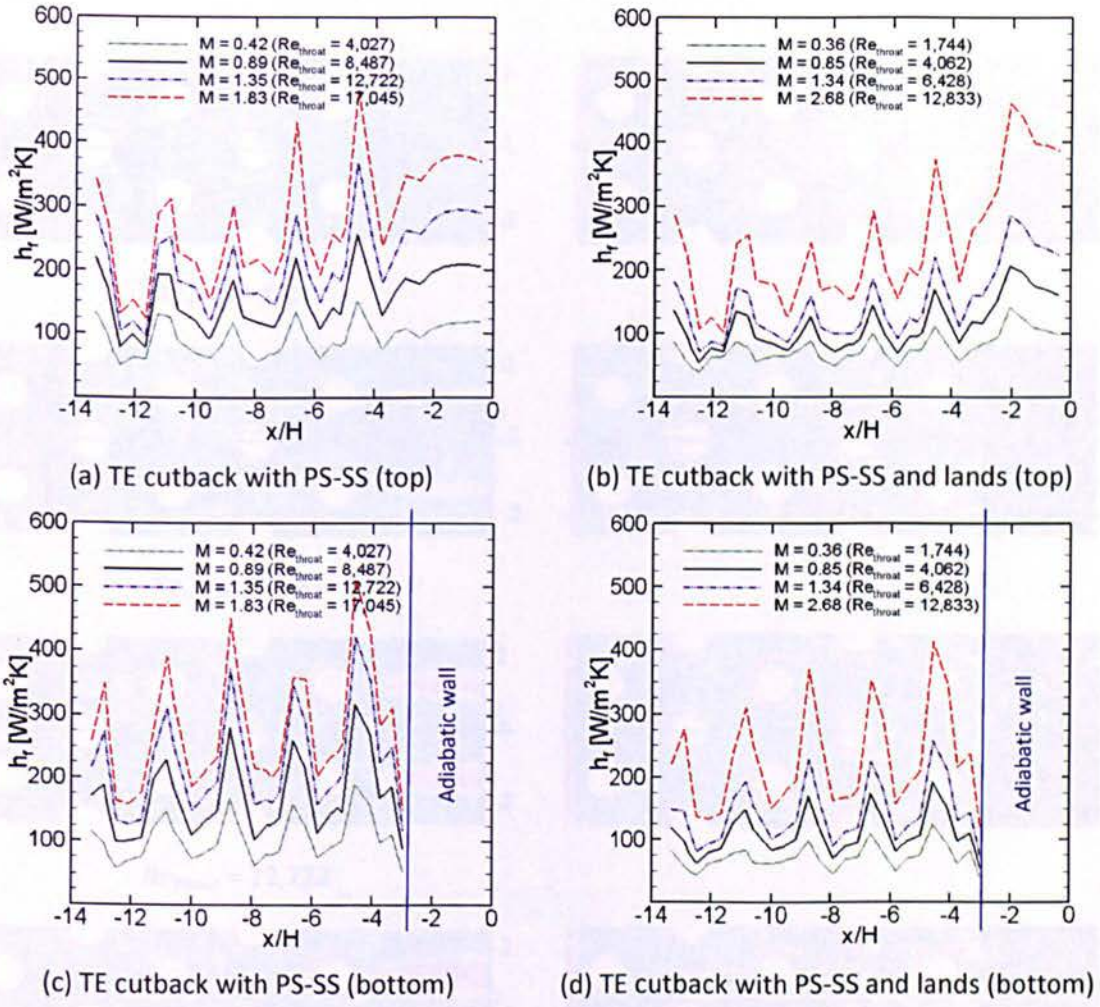

(a) TE cutback with PS-SS (top)

(b) TE cutback with PS-SS and lands (top)

(c) TE cutback with PS-SS (bottom)

(d) TE cutback with PS-SS and lands (bottom)

Figure 9–5: Spanwise-averaged HTC at the coolant passage walls.

Figure 9–6 and Figure 9–7 show the qualitative comparison in an effort to complete the quantitative heat-transfer coefficient as previously explained in Figure 9–5. It has been found that the distribution of heat-transfer coefficient is symmetric in the staggered arrays. A stagnation region is present in front of each pin-fin array. It is indicated by the red colour in the left position for each pin-fin row. The red colour is seen to be obvious near the slot exit position (x/H = 0). The increase of blowing ratio causes a significant

effect on the intensity of the red colour. It is more pronounced for higher blowing ratios or higher Reynolds numbers of the coolant inside the cooling passage. This finding is seen to be in-line with the work of Tarchi *et al.* [13]. The blue colour within the range of -3 < *x/H* < 0 at the bottom wall indicates the adiabatic boundary condition in this region. It relates to a zero heat-transfer coefficient at the bottom wall (see Figure 9–5(c) and Figure 9–5(d)).

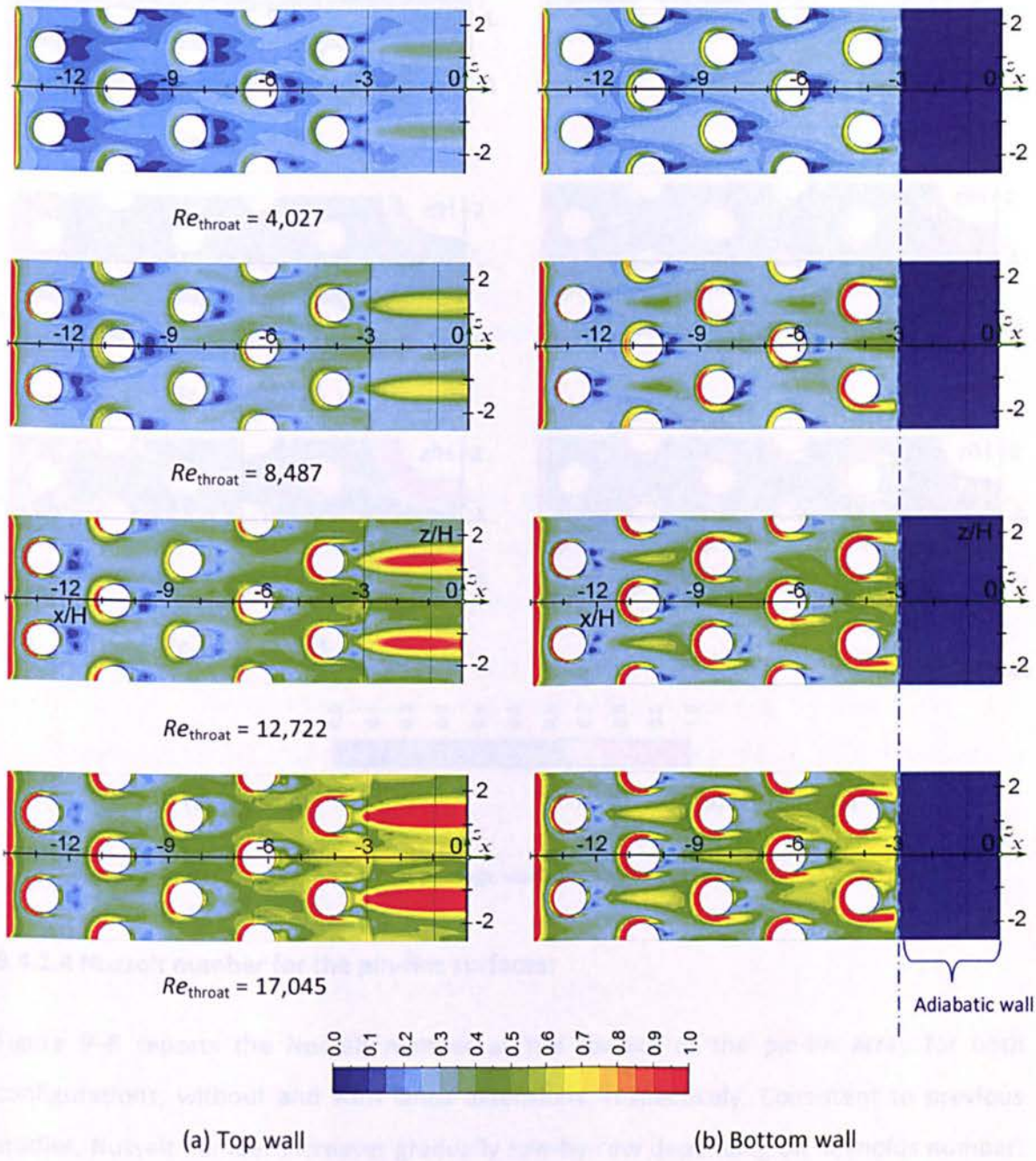

Figure 9–6: HTC map at the coolant passage walls for the TE cutback with PS-SS.

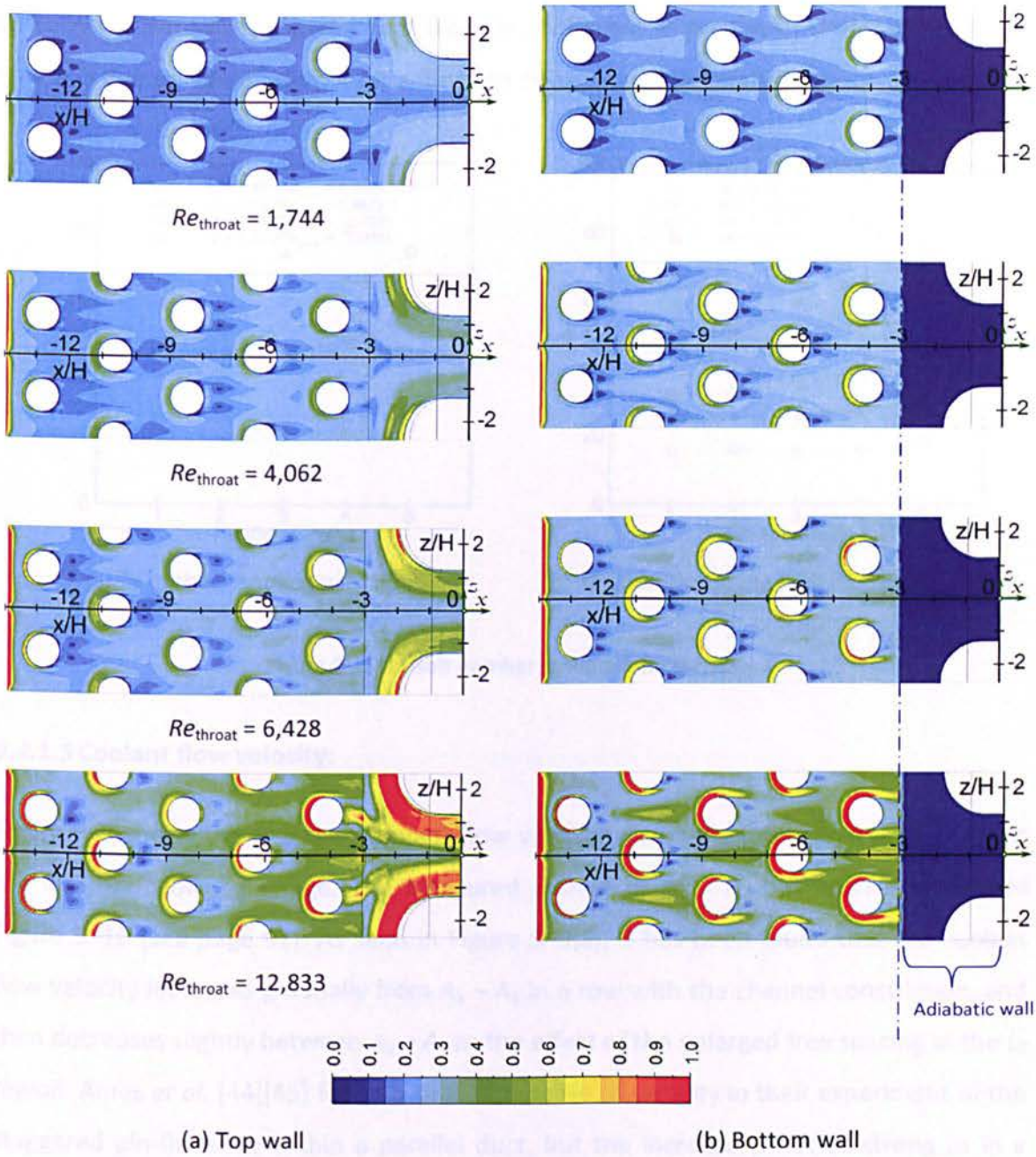

Figure 9–7: HTC map at the coolant passage walls for the TE cutback with PS-SS and lands.

9.4.1.4 Nusselt number for the pin-fins surfaces:

Figure 9–8 reports the Nusselt number at the surface of the pin-fin array for both configurations, without and with lands extensions, respectively. Consistent to previous studies, Nusselt number increases gradually row-by-row depending on Reynolds number. A higher Reynolds number causes a rapid increase of Nusselt number. This change is seen

to be in-line with the averaged heat-transfer coefficient as previously presented in Figure 9–4. It is due to Nusselt number is a function of heat-transfer coefficient.

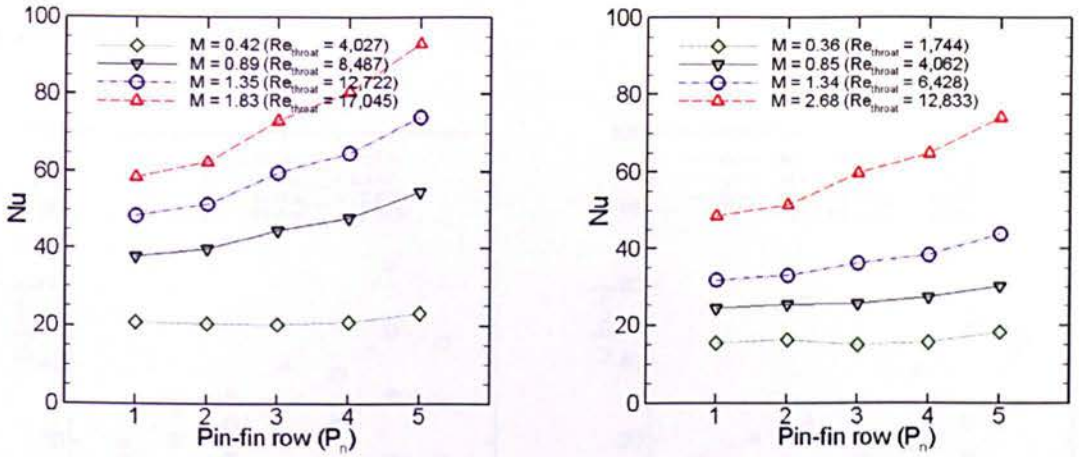

(a) TE cutback cooling with PS-SS

(b) TE cutback cooling with PS-SS and lands

Figure 9–8: Nusselt number at the pin-fin surfaces.

9.4.1.5 Coolant flow velocity:

Figure 9–9 shows the averaged coolant flow velocity across the inter-pin-fins ($A_1 - A_7$) at the internal cooling passage. The measured section of $A_1 - A_7$ has been described in Figure 5–10 (see page 92). As seen in Figure 9–9(a), it has been found that the coolant flow velocity increases gradually from $A_1 - A_6$ in a row with the channel constriction, and then decreases slightly between $A_6 - A_7$ as the effect of the enlarged free spacing at the L_2 region. Ames *et al.* [44][45] found a similar increase of velocity in their experiment of the staggered pin-fin array within a parallel duct, but the increase is not as strong as in a wedge-shaped duct. The increase of velocity is more noticeable at a higher Reynolds number than at the lower one.

For the case with PS-SS and land extensions, the coolant flow velocity increases drastically due to the constriction channel at the slot exit. It is very pronounced for the case with a higher Reynolds number (see Figure 9–9(b)), where the increase is about five times from the inflow region to the slot exit. The coolant flow velocity plotted in Figure 9–10(b) also confirms this quantitative data.

By comparing Figure 9–9(a) with Figure 9–9(b), it can be stated that the blockages of land extensions cause a different intensity of coolant flow velocity at the slot exit that probably trigger a different dynamic flow between the coolant and the mainstream flow at the mixing region.

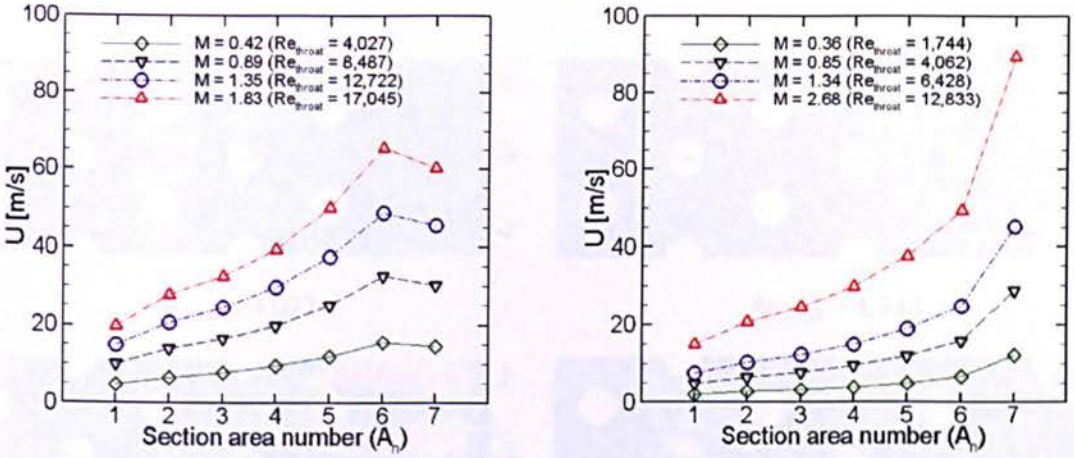

(a) TE breakout with PS-SS

(b) TE breakout with PS-SS and lands

Figure 9–9: Coolant flow velocity inside the cooling passage.

Figure 9–10 shows the contour plots of coolant flow velocity inside the cooling passage. These visualisations confirm the growth of coolant flow velocity along the channel. This is obvious in the region between two pin-fins. The wedge-shaped duct triggers that generation. It is noticeable for higher Reynolds numbers.

As deeply discussed in Chapter 7, the fast increase of coolant flow velocity is most likely caused by a contraction channel rather than the existence of pin-fin array. It has been demonstrated on the computation using a blade TE cutback with empty duct inside the wedge-shaped duct. However, the existence of pin-fin array could not be neglected on the raising of the coolant flow velocity. In fact, their growth is more noticeable after replacing the pin-fin array inside the cooling passage.

Based on Figure 9–10 a separation bubble with a lower coolant flow velocity is seen behind each of the pin-fins in the uniform flow-field. The flow separation pattern of the last pin-fin row seems to have a feedback effect from the slot at L_2 region. This is indicated by a long recirculation for the case without lands, and an asymmetric

recirculation for the case with lands. Both stagnation point in front of pin-fins and the recirculation behind each pin-fin are in-line with the coolant flow direction. The two counter-rotating vortexes in the recirculation downstream spread up to the next pin-fin row and then interact with the stagnation area of each row. This creates more periodic flow pattern along the constriction coolant passage.

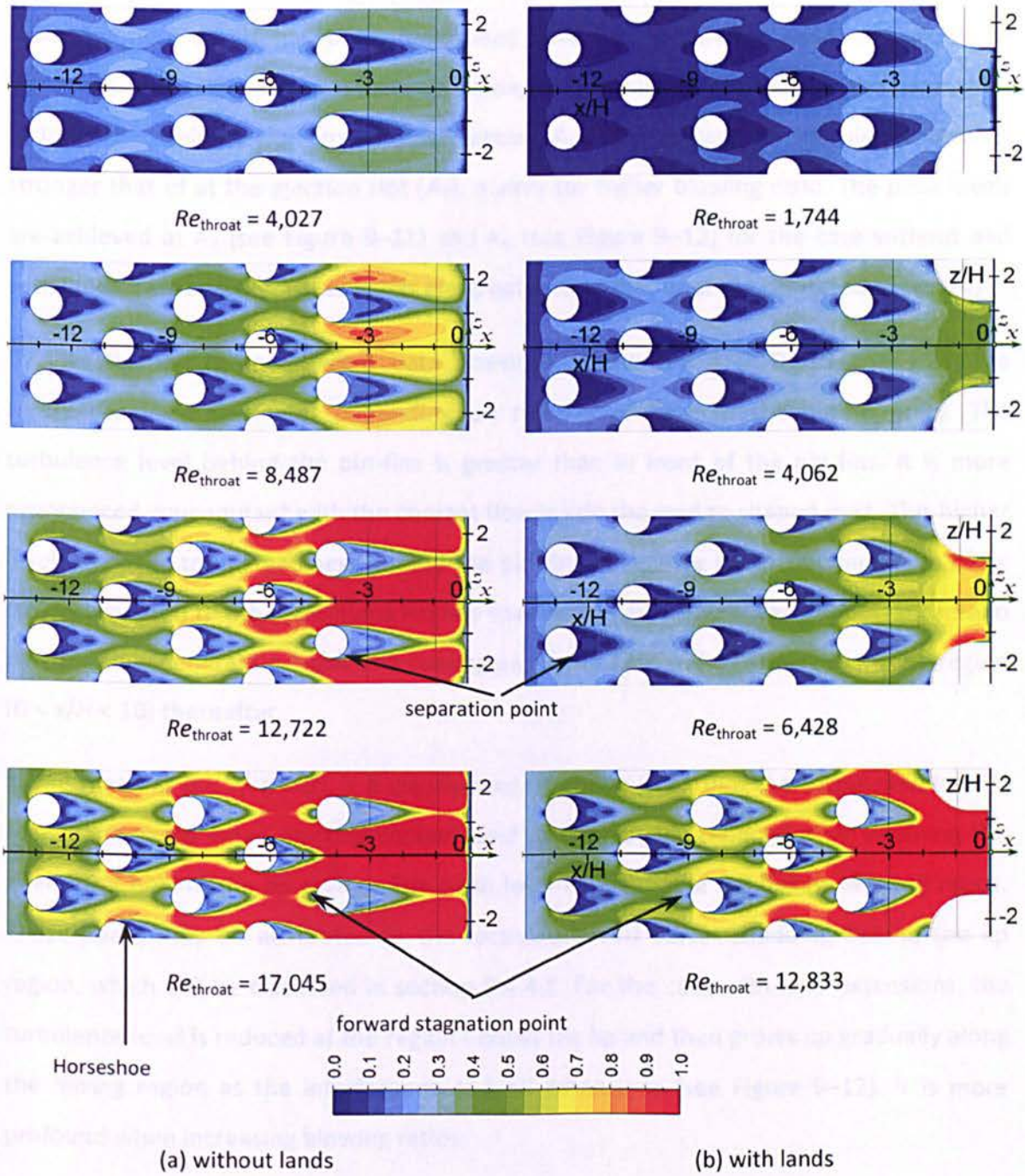

Figure 9–10: Coolant flow velocity (U/U_{hg}) contour around the pin-fins array inside the cooling passage.

9.4.2 Turbulence Characteristics

Similar position as previously used in Chapters 6 – 8, Figure 9–11 shows the characteristic of turbulence levels ($T_u = u'/U_\infty$) for various blowing ratios. Two groups of data are separately presented for four different blowing ratios. The u' velocity is based on the root mean square streamwise fluctuation flow velocity.

From Figure 9–11, it has been recognised that the turbulence levels are gradually increased along the internal cooling passage as clearly indicated by the averaged-turbulence levels at the cross-section areas (A_n). The growth of turbulence level is stronger that of at the ejection slot (A_7), mainly for higher blowing ratio. The peak levels are achieved at A_7 (see Figure 9–11) and A_6 (see Figure 9–12) for the case without and with lands, respectively. These levels are greater than that of at the pin-fin surfaces (P_n).

By investigating three different data positions at the z/H = 0, 0.625 and 1.25, the turbulence level fluctuates depending on relative position to the pin-fin array. The turbulence level behind the pin-fins is greater than in front of the pin-fins. It is more pronounced concomitant with the coolant flow inside the wedge-shaped duct. This higher level is related to unsteadiness behind the pin-fins. A relative lower fluctuation at z/H = 0.625 compared to other positions implies that the pin-fin array is a key important role to play the flow generation inside the cooling passage ($-14 < x/H < 0$) and the mixing region ($0 < x/H < 10$) thereafter.

In the range of $0 < x/H < 10$, it is clearly seen in Figure 9–11 that the turbulence level is rapidly increased when ejecting coolant, and then gradually reduced after attaining the peak level behind the lip region. The peak level is noticeable for higher blowing ratios. These peaks may be attributed to the recirculation of vortex-shedding behind the lip region, which will be discussed in section 9.4.4.1. For the case with land extensions, the turbulence level is reduced at the region behind the lip and then grows up gradually along the mixing region as the interference of land extensions (see Figure 9–12). It is more profound when increasing blowing ratios.

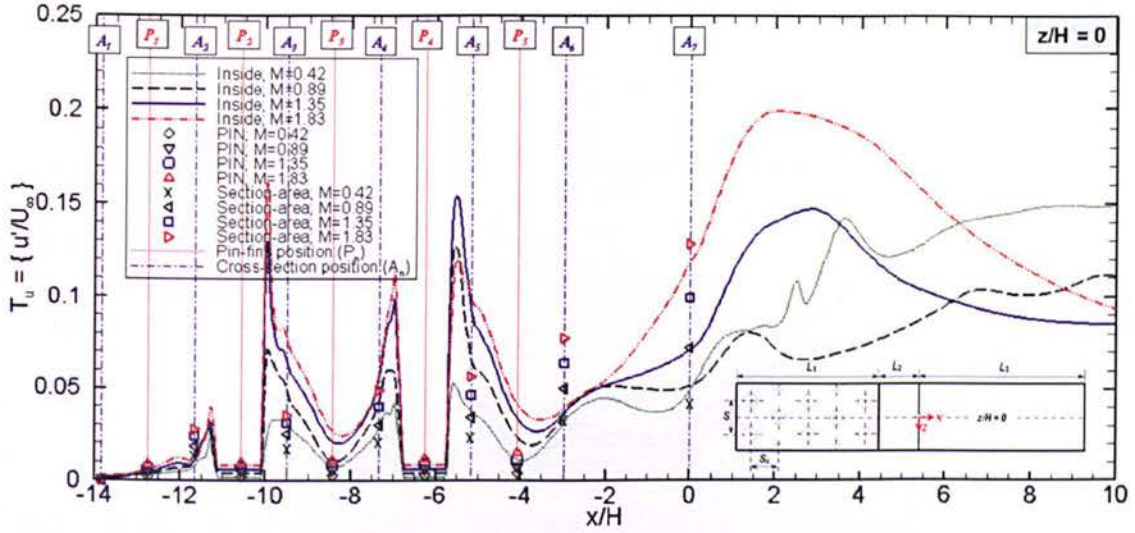

(a) $z/H = 0$

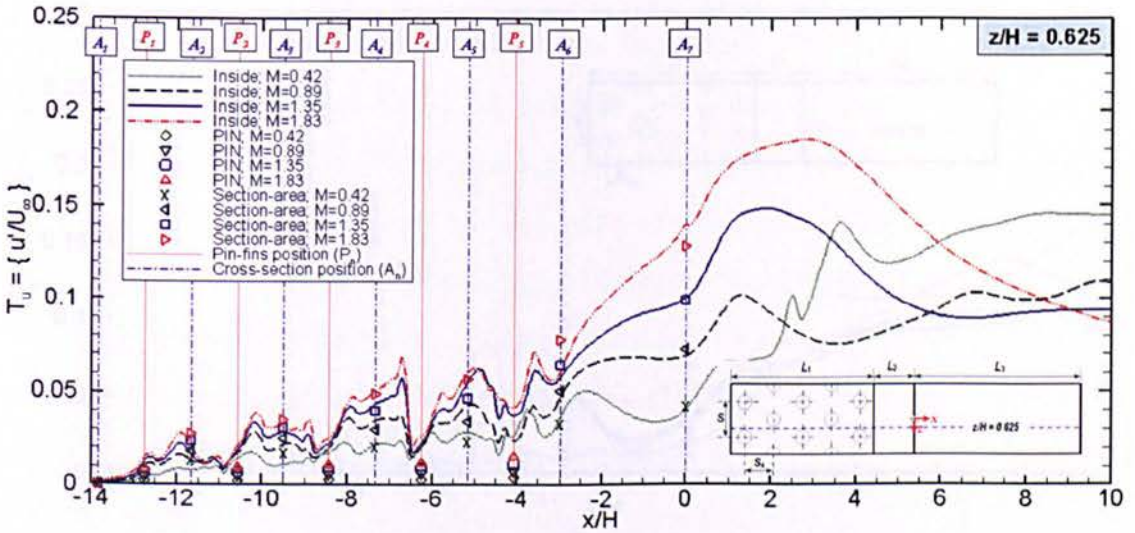

(b) $z/H = 0.625$

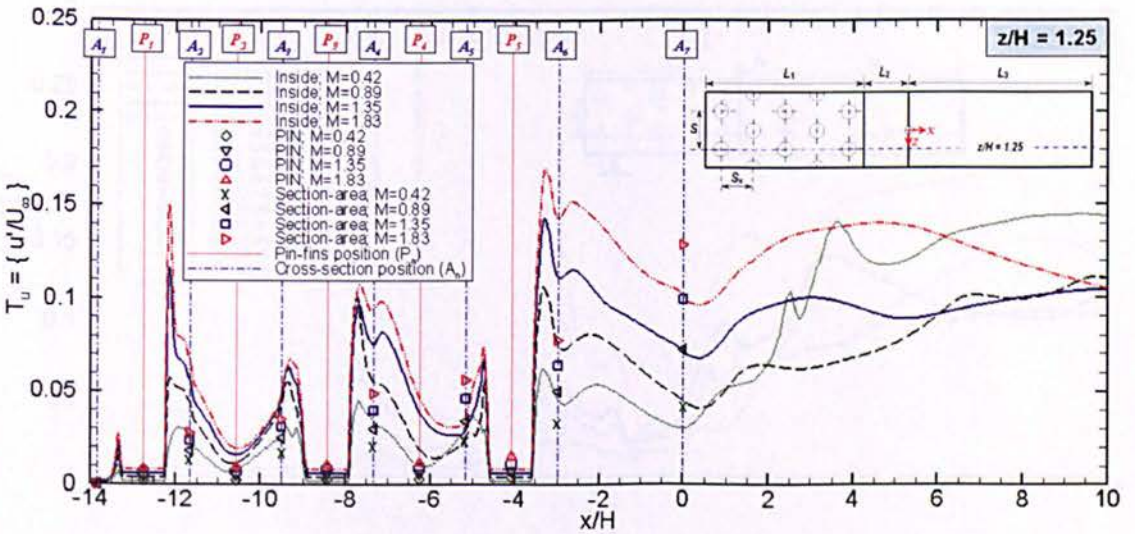

(c) $z/H = 1.25$

Figure 9–11: Turbulence levels for the cases without lands.

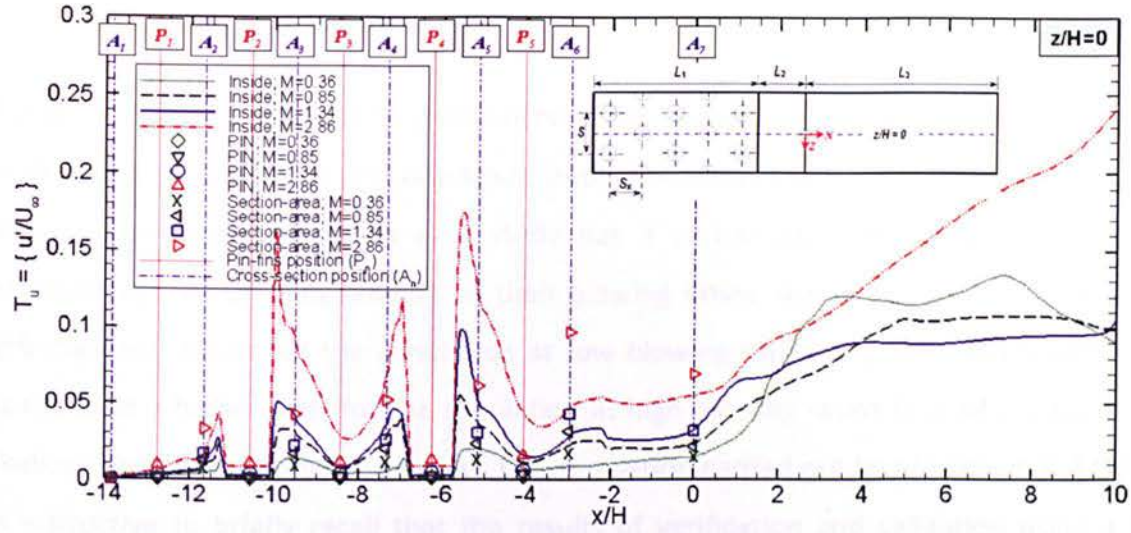

(a) $z/H = 0$

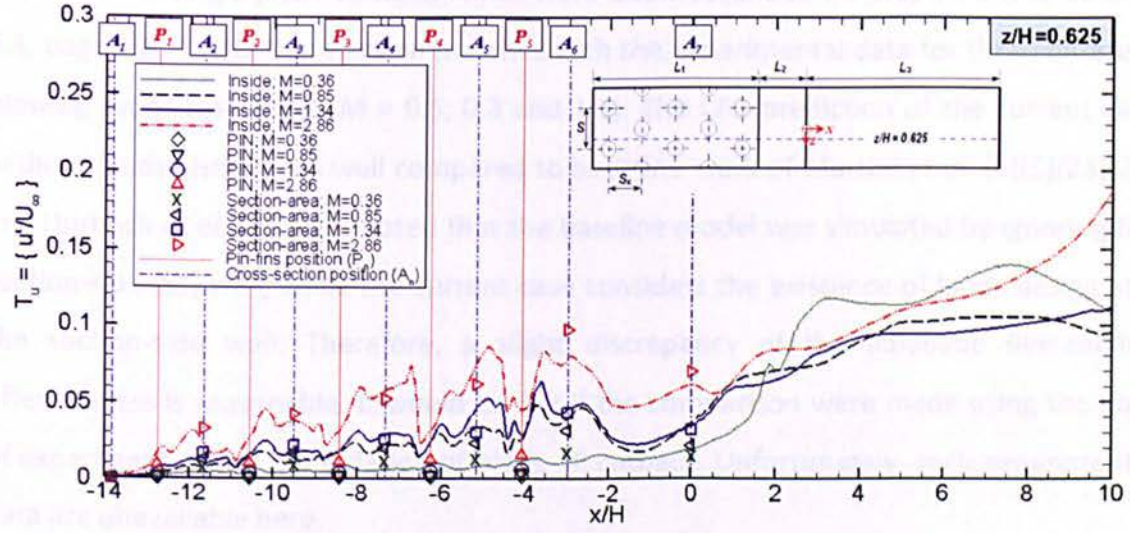

(b) $z/H = 0.625$

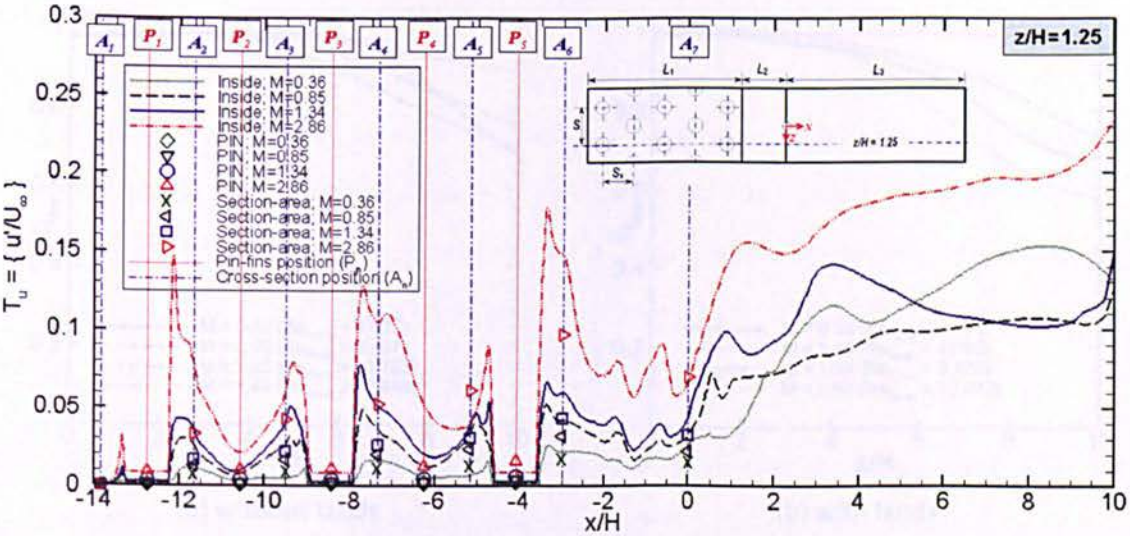

(c) $z/H = 1.25$

Figure 9–12: Turbulence levels for the cases with lands.

9.4.3 Film-cooling Effectiveness

Figure 9–13 gives a quantitative comparison of the averaged film-cooling effectiveness for both TE cutbacks, without and with lands. Both are varied at four different blowing ratios. It has been found that each case study has a typical characteristic of film-cooling effectiveness, which is depending on their blowing ratios. A rapid decay of film-cooling effectiveness occurs for the simulation at low blowing ratios (e.g. M = 0.42), whilst it tends to at a higher level for the simulation at high blowing ratios (e.g. M = 1.83). This finding is consistent with the previous DES simulation carried out by Martini *et al.* [20]. It is instructive to briefly recall that the results of verification and validation using a TE cutback with single-pitch domain, which have been described in Chapter 5 (see section 5.4, page 99). The CFD prediction matches with the experimental data for three different blowing ratios tested (i.e. M = 0.5, 0.8 and 1.1). The CFD prediction of the current case without lands also agrees well compared to both the work of Martini *et al.* [4][5][23][24] and Horbach *et al.* [30]. It is noted that the baseline model was simulated by ignoring the suction-side (SS) wall, while the current case considers the existence of lands design and the suction-side wall. Therefore, a slight discrepancy of the adiabatic film-cooling effectiveness is reasonable. It would be fair if the comparison were made using the data of experiment at the same design of blade TE cutback. Unfortunately, such experimental data are unavailable here.

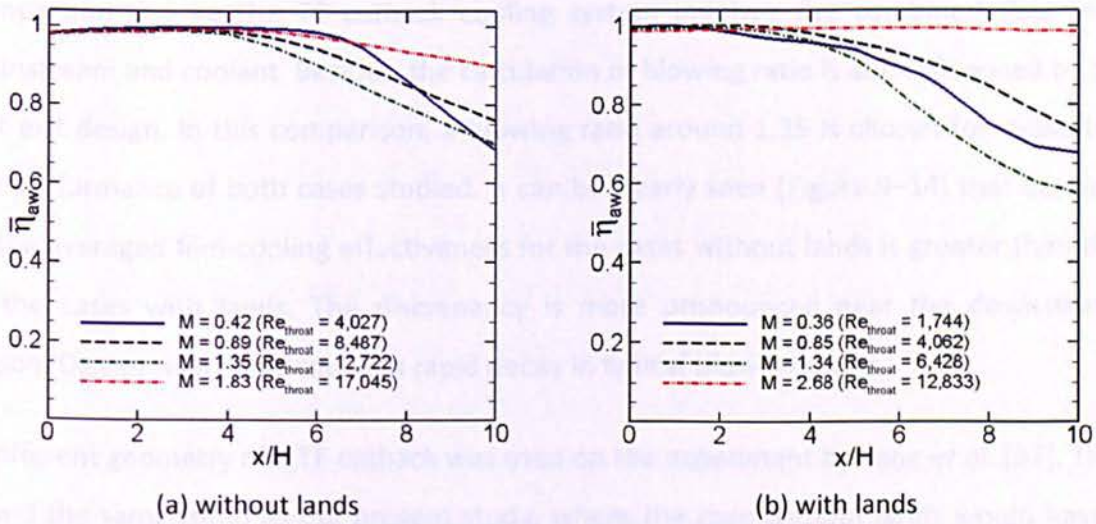

(a) without lands (b) with lands

Figure 9–13: Laterally averaged film-cooling effectiveness.

As previously discussed on the verification and validation stage in section 5.4 (see Chapter 5), anomalous phenomena occurs when a case is simulated around intermediate blowing ratio. The order of the graph trend does not follow the order of the blowing ratio. The experiment carried out by Horbach *et al.* [30] found the same trend as the present study. Using LES simulation, Schneider *et al.* [28][29] noted the counter-intuitive behaviour of film-cooling effectiveness. They found a fast decay of film-cooling effectiveness at higher blowing ratios. The decay of the case with higher blowing ratios (M = 1.1) is faster than the decay at M = 0.5. The counter-intuitive behaviour in the current study is indicated by the trend at M = 0.89 and 1.35, where the case with higher blowing ratios yields a lower film-cooling effectiveness near the downstream region after attaining $x/H > 4$.

In connection with the effectiveness, Holloway *et al.* [19][25] also noted an anomalous phenomenon on their investigations of the unsteady transonic pressure-side bleed film cooling on the trailing edge of a turbine blade. As the blowing ratio increased from 0 to 0.8, the effectiveness increased. For intermediate blowing ratios, the effectiveness decreased. For the blowing ratios greater than 1.25, the effectiveness increased once again.

In order to reveal the design effect of the blade TE cutback without and with lands on the film-cooling effectiveness over the protected wall, it can be seen from Figure 9–13 at the same blowing ratio. Reynolds number of the coolant is not enough as a reference comparison due to the TE cutback cooling system involves the combined flow from mainstream and coolant. Besides, the calculation of blowing ratio is also influenced by the slot exit design. In this comparison, a blowing ratio around 1.35 is chosen for evaluating the performance of both cases studied. It can be clearly seen (Figure 9–14) that the level of the averaged film-cooling effectiveness for the cases without lands is greater than that of the cases with lands. The discrepancy is more pronounced near the downstream region. Design with lands causes a rapid decay in typical blowing ratios.

A different geometry of a TE cutback was used on the experiment by Yang *et al.* [37]. They found the same trend as the present study, where the case without lands would have a higher overall-averaged film-cooling effectiveness up to 10% discrepancy than that of the

case with lands. The comparison of overall averaged film-cooling effectiveness at the protected wall is presented in Figure 9–14(b). Performance of the case without lands is better than that of the case with lands by discrepancy up to 18% in terms of overall-averaged film-cooling effectiveness. These data are obtained by spatially averaging the all measurements over the test plate surface. It has been found that both the current computation and those experimental data are seen to agree well in terms of the trend and the peak values that reach at the blowing ratio of M = 0.6 – 0.8. The disagreement of both data may be attributed to the different models and boundary conditions used by the two studies.

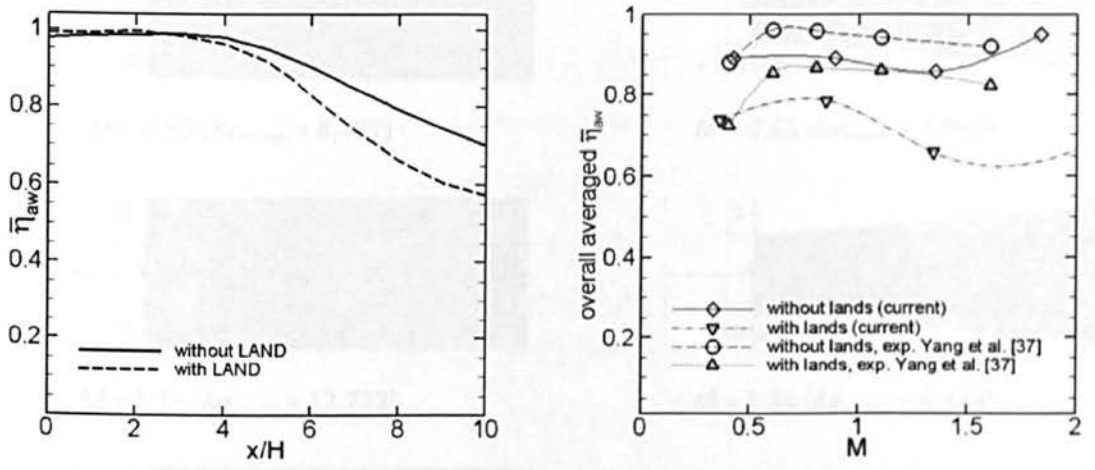

(a) M = 1.35 (b) η_{aw} versus M

Figure 9–14: The comparison of the averaged film-cooling effectiveness

Figure 9–15 shows a qualitative comparison of the adiabatic film-cooling effectiveness at the protected wall, in an effort to complete the charts expression in Figure 9–13. It has been found that each distribution of the adiabatic film-cooling effectiveness is un-uniform. A half surface of the protected wall is dominated by high film-cooling effectiveness nearly unity, mainly close to the slot exit. It tends to form in a symmetrical pattern for each typical blowing ratio. This is strongly influenced by the layout of pin-fin array. The increase of blowing ratio causes a uniformity of distribution as the combined effect of the pin-fin layout and blowing ratio. In case of lower blowing ratios, the adiabatic film-cooling effectiveness tends to decay rapidly. Corresponding to the core region of the coolant jet flows, the area with higher film-cooling effectiveness becomes

longer and longer with increasing blowing ratios. It is obvious for the case with lands (see Figure 9–15(b)). Moreover, high film-cooling effectiveness is almost dominated at all surface of the protected wall for the case with the highest blowing ratio of M = 2.86.

M = 0.42 (Re_{throat} = 4,027)

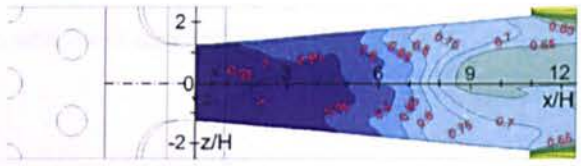

M = 0.36 (Re_{throat} = 1,744)

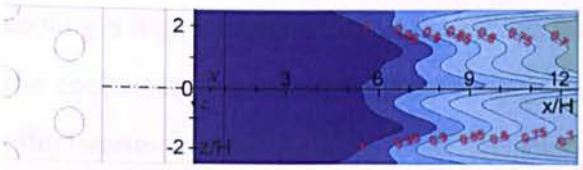

M = 0.89 (Re_{throat} = 8,487)

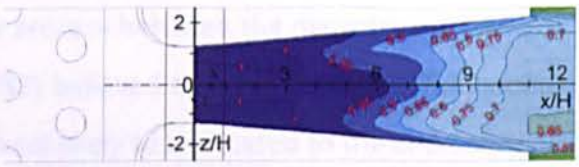

M = 0.85 (Re_{throat} = 4,062)

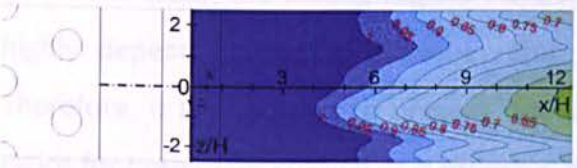

M = 1.35 (Re_{throat} = 12,722)

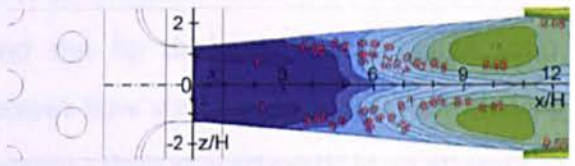

M = 1.34 (Re_{throat} = 6,428)

M = 1.83 (Re_{throat} = 17,045)

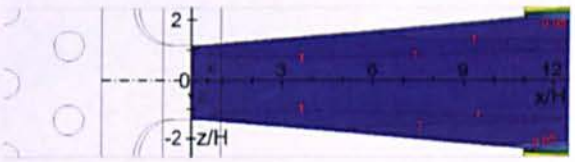

M = 2.86 (Re_{throat} = 12,833)

(a) without lands (b) with lands

Figure 9–15: Film-cooling effectiveness map at the protected wall.

As discussed in the previous chapters, the formation of the film-cooling effectiveness at the protected wall is strongly affected by the turbulent flow structures formed at the mixing region. The blowing ratio is a key important role to play a mixing process between the mainstream flow and the ejecting coolant, if domain and boundary conditions remain unchanged. In this case, the blowing ratio is only depending on the change of the coolant flow due to fixed mainstream flow as has been defined in Chapter 4. Therefore, the

formation of the turbulent-flow structures follows the velocity of the ejecting coolant from the slot exit. The coolant flow can reach up to the downstream region when increasing the velocity of the ejecting coolant. In contrast, the decrease of the coolant velocity reduces the reach of the ejecting coolant and delays a mixing process with mainstream gas. The turbulent-flow structures will be discussed in section 9.4.4.1.

9.4.4 Mixing Region

As explained previously in Chapters 5 – 8, the performance of the blade TE cutback cooling is highly dependent on the mixing flow process between the mainstream flow and the coolant at the mixing region. Yang *et al.* [37] believed that the adiabatic film-cooling effectiveness at the protected wall surface is most likely to be related to the characteristic of mixing flow over the cutback region. It links to the formation of turbulent-flow structures along the mixing region. Holloway *et al.* [19][30] noted that unsteadiness is highly dependent on the blowing ratios and the lip thickness-to-slot height ratio. Therefore, it is important to present the turbulent-flow structures on different blowing ratios for both cases studied. It is expected to capture their characteristic in an attempt to interpret the relationships between the film-cooling effectiveness and the turbulent-flow structures.

9.4.4.1 Turbulent flow structures:

Figure 9–16 gives a qualitative visualisation of the turbulent flow structures for both cases studied, super-imposed by the contour of the adiabatic film-cooling effectiveness at the protected wall and the temperature distribution at the internal pin-fin cooling. It represents a dynamic mixing process between the mainstream flow and the coolant. Four blowing ratios are used in the current study. The turbulent flow structures are illustrated by the iso-contours of the vortex identification criterion Q, as suggested by von Terzi *et al.* [137] and Schneider *et al.*[28][29]. The visualisation of iso-surface (i.e. $\Omega^2 - S^2 = 10^5$ $1/s^2$) from Egorov *et al.* [22] is adopted here. The colour indicates the non-dimensional temperature (θ) distribution of mixing, which is expressed by the gradation from a low value of 0 (in red) to a high value of 1 (in blue).

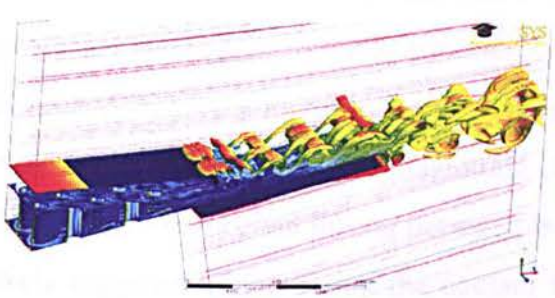

M = 0.42 (Re_{throat} = 4,027)

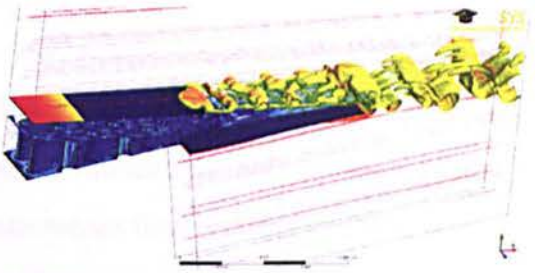

M = 0.36 (Re_{throat} = 1,744)

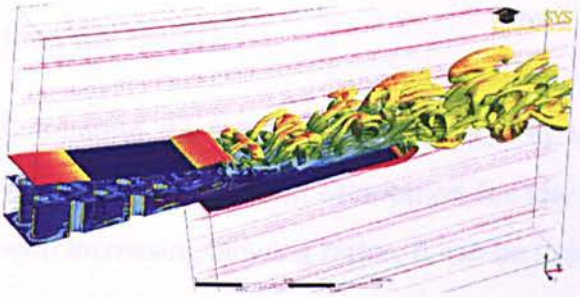

M = 0.89 (Re_{throat} = 8,487)

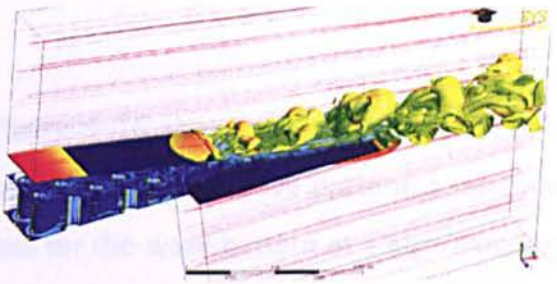

M = 0.85 (Re_{throat} = 4,062)

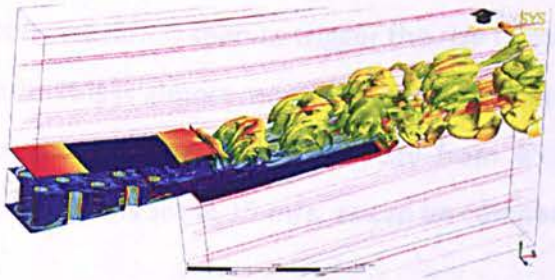

M = 1.35 (Re_{throat} = 12,722)

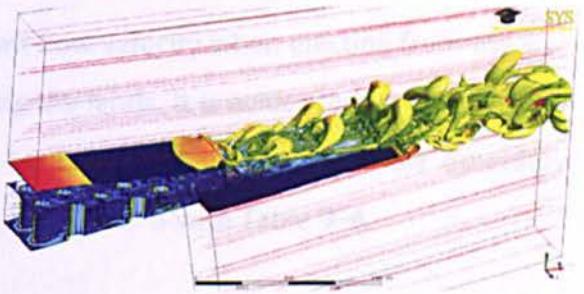

M = 1.34 (Re_{throat} = 6,428)

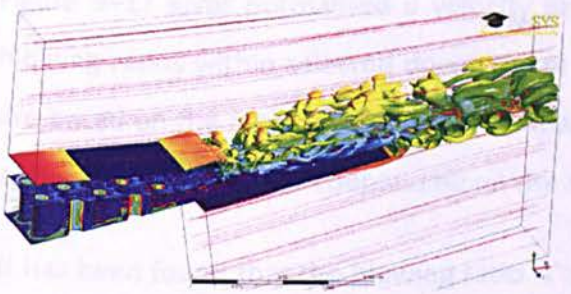

M = 1.83 (Re_{throat} = 17,045)

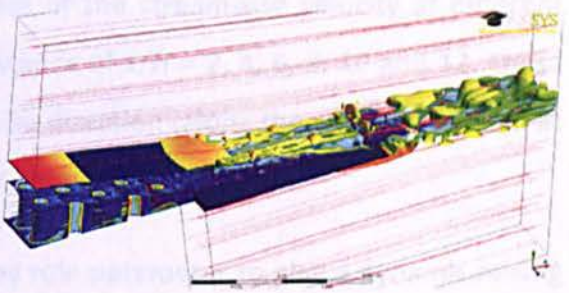

M = 2.86 (Re_{throat} = 12,833)

(a) without lands

(b) with lands

Figure 9–16: Turbulent flow structures.

As explained above, the characteristic of the turbulent flow structures demonstrates a significant correlation to the distribution of the adiabatic film-cooling effectiveness at the protected wall. It is found that the turbulent flow structures are more noticeable when increasing blowing ratios. The magnitude of wakes is reduced for higher blowing ratios as the effect of intensified mixing between the mainstream flow and the coolant. It is most likely triggered by increasing the coolant flow velocity. It can be seen clearly from the growth of waves along the mixing region as shown in Figure 9–16. A mixing process is more intensive for higher blowing ratios as the regeneration effect of the coolant flow from the slot exit.

Comparing the turbulent flow structures in Figure 9–16 shows that the crests of the waves are clockwise in orientation for low blowing ratios. The wave pattern is random with increasing blowing ratios. It can be indicated for the wave pattern at a high blowing ratio of 1.83 (see Figure 9–16(a)).

The co-existence of land extensions causes the constriction passage at the slot exit. This construction is seen to trigger the rise of coolant flow velocity when ejecting from the slot exit. This is almost more than twice by installing the lands. It is evidenced by the increase of the ejecting coolant velocity from 45.50 to 89.58 m/s when the inflow boundary condition is set at 15 m/s, as can be compared to Table 9–3 with Table 9–4.

9.4.4.2 Transverse velocity profiles:

Figure 9–17 gives normalised u velocity profiles of the streamwise velocity at different blowing ratios within selected downstream distance of x/H = 2, 4, 6, 8, 10 and 12. These are based on the averaged u velocity at spanwise direction (along the width of domain at a specific z-axis direction depending on the x/H position).

It has been found that the blowing ratio is a key role parameter to play a dynamic mixing process along the breakout region. It is evidenced by a stronger flow velocity when blowing ratio is increased from 0.42 to 1.83. The left-curve and the right-curve discrepancy of the averaged u velocity near the protected wall are noticeable as indicated by Figure 9–17(a). The change of u velocity profile is more pronounced around the slot

exit region, for example at x/H = 2. The distance of the left-curve and the right-curve reduces near the downstream region, for instance at x/H = 12 (see Figure 9–17(f)). A gradual change of u velocity profiles is presented for each blowing ratio tested as shown in Figure 9–18. Each blowing ratio has a typical pattern. The u velocity profiles are dominated by the mainstream flow with $u/U_{hg} > 1$ after approaching $x/H > 6$.

A larger discrepancy between the left-curve and the right-curve at x/H = 2 is likely caused by a combined effect of vortex-shedding behind the lip and ejecting coolant. The ejecting coolant from the slot exit causes the right-curvature (see region $0 < y\text{-}y_{ow}/H < 1$), and the recirculation of vortices affects a reduction of u velocity as indicated by the left-curvature (see region $1 < y\text{-}y_{ow}/H < 2$). Near the protected wall, the u velocity is increased concomitant with a regeneration of turbulence flow structures along the breakout region. The mainstream flow velocity is seen to influence a gradual increase of this u velocity within the range of $4 < x/H < 12$. It is more noticeable for a low blowing ratio of 0.42 (see Figure 9–18(a)).

The previous investigation carried out by Holloway *et al.* [19][25] found that unsteadiness is highly dependent on the blowing ratios. The current finding is seen to yield similar results compared to that experiment. In fact, the pattern of u velocity profile is gradually changed as shown in Figure 9–18. The evolution of mixing flow velocity is changed by various blowing ratios. This profile is likely caused by a different flow mixing process between the mainstream flow and the cooling stream. The intensity of ejecting coolant is seen to play this dynamic mixing process due to all geometries and the boundary conditions of mainstream flow velocity remain unchanged. Therefore, the coolant flow velocity is a key parameter against this discrepancy. The increase of coolant flow velocity causes the rise of blowing ratio. This influences in increasing of the coolant stream momentum that has a stronger power to force the mainstream flow away from the protected wall. In addition, these u velocity profiles are in-line with the previous experiment performed by Yang *et al.* [6] using a different test model and boundary conditions. Joo *et al.* [27] found the same trend as these findings.

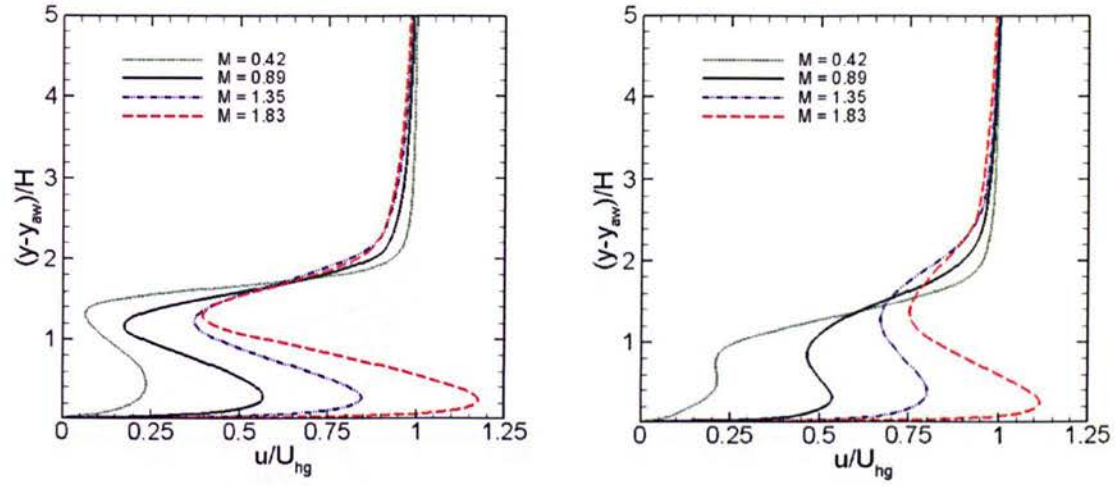

(a) $x/H = 2$ (b) $x/H = 4$

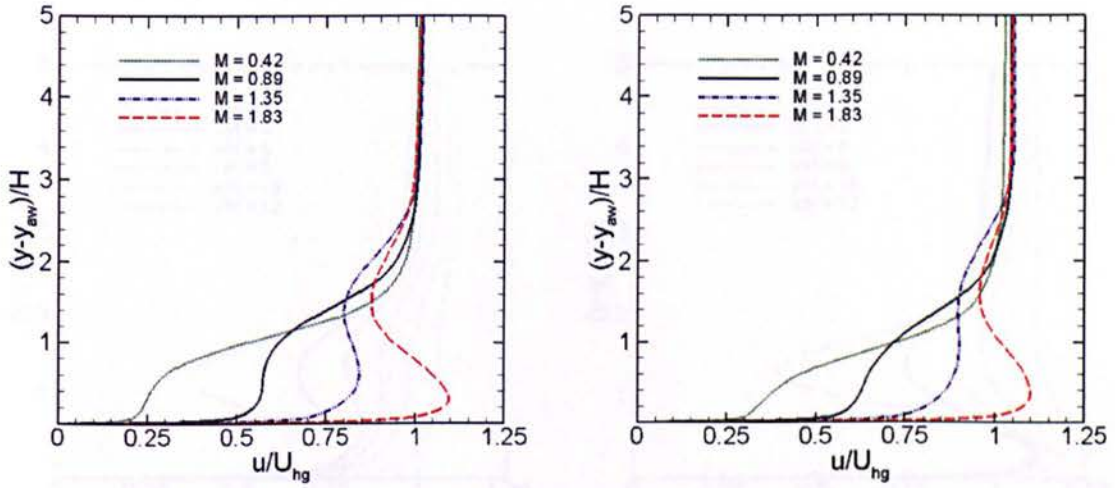

(c) $x/H = 6$ (d) $x/H = 8$

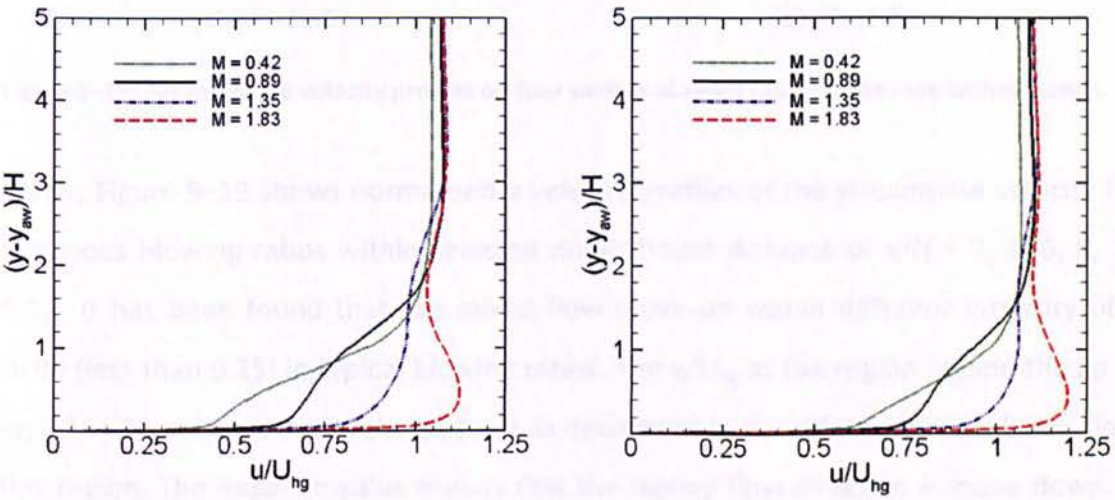

(e) $x/H = 10$ (f) $x/H = 12$

Figure 9–17: Normalised *u* velocity profiles at different downstream locations for the case without lands.

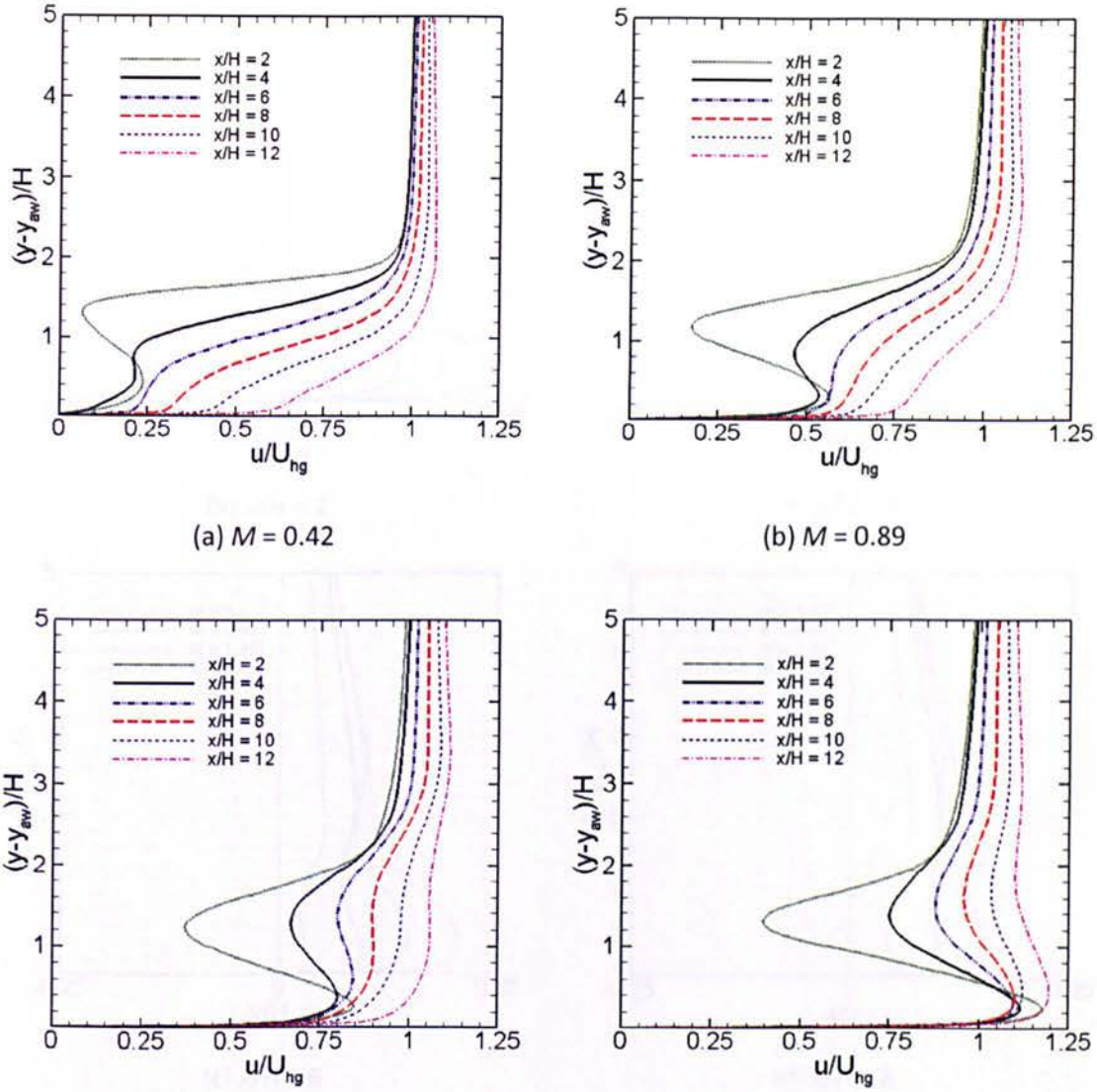

(a) $M = 0.42$ (b) $M = 0.89$

(c) $M = 1.35$ (d) $M = 1.83$

Figure 9–18: Normalised *u* velocity profiles on four various blowing ratio for the case without lands.

Similarly, Figure 9–19 shows normalised *v* velocity profiles of the streamwise velocity for four various blowing ratios within selected downstream distance of x/H = 2, 4, 6, 8, 10 and 12. It has been found that the mixed-flow move-up within different intensity of *v* velocity (less than 0.25) in typical blowing ratios. The v/U_{hg} at the region behind the lip ($1 < y\text{-}y_{aw}/H < 2$), mainly close to the slot exit, is decreased as the effect of recirculation flow in this region. The negative value means that the mixing flow direction is move down. A gradual change of *v* velocity profiles is given in each blowing ratio simulated as seen in Figure 9–20.

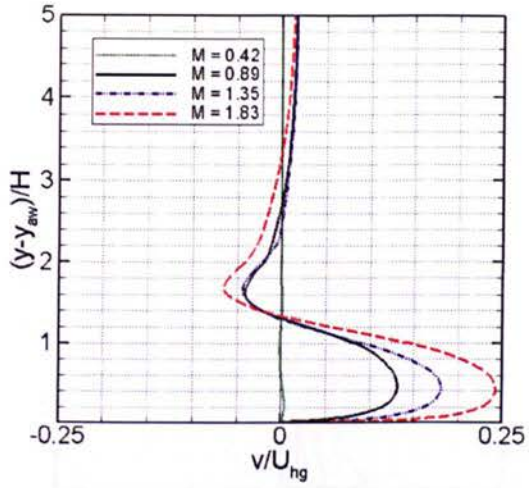

(a) $x/H = 2$

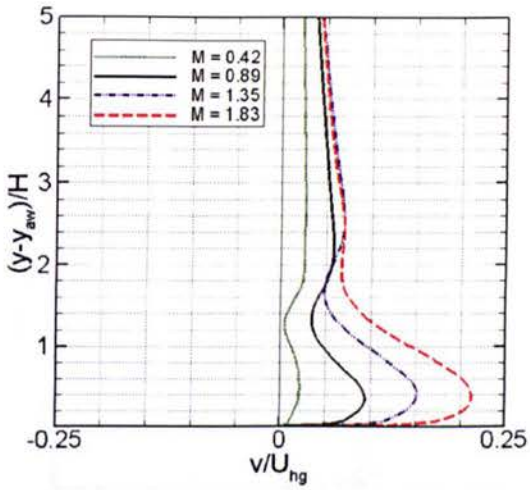

(b) $x/H = 4$

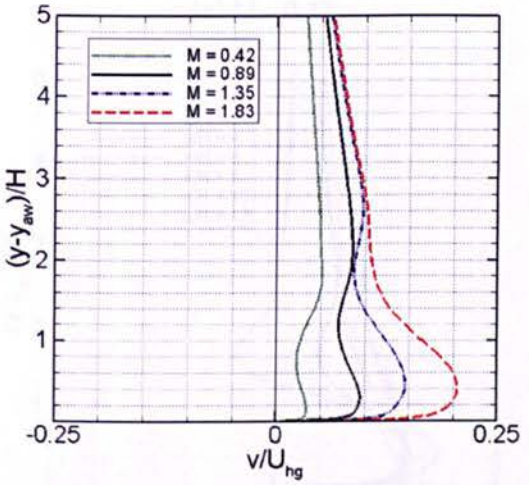

(c) $x/H = 6$

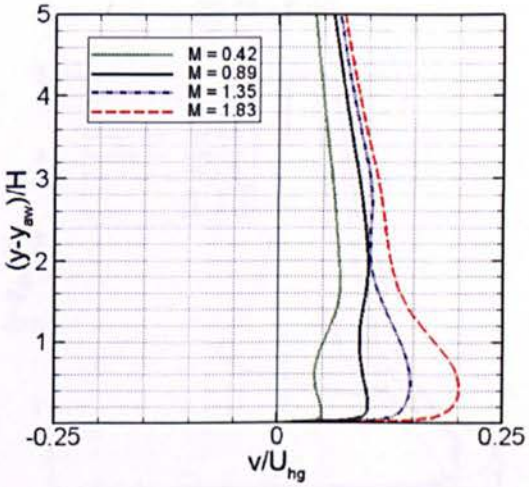

(d) $x/H = 8$

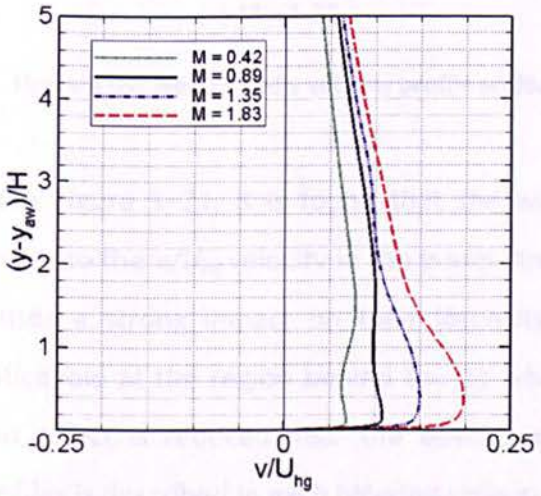

(e) $x/H = 10$

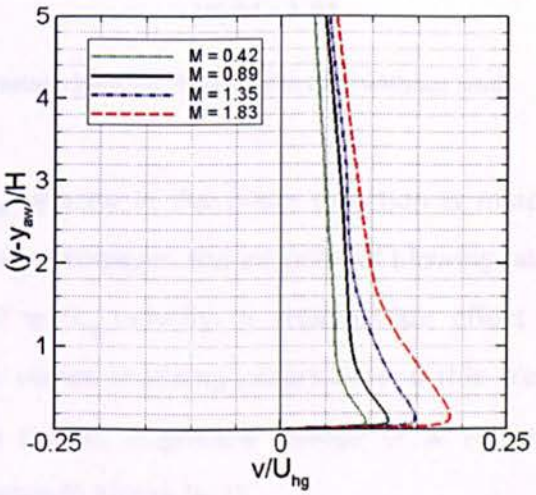

(f) $x/H = 12$

Figure 9–19: Normalised *v* velocity profiles at different downstream locations for the case without lands.

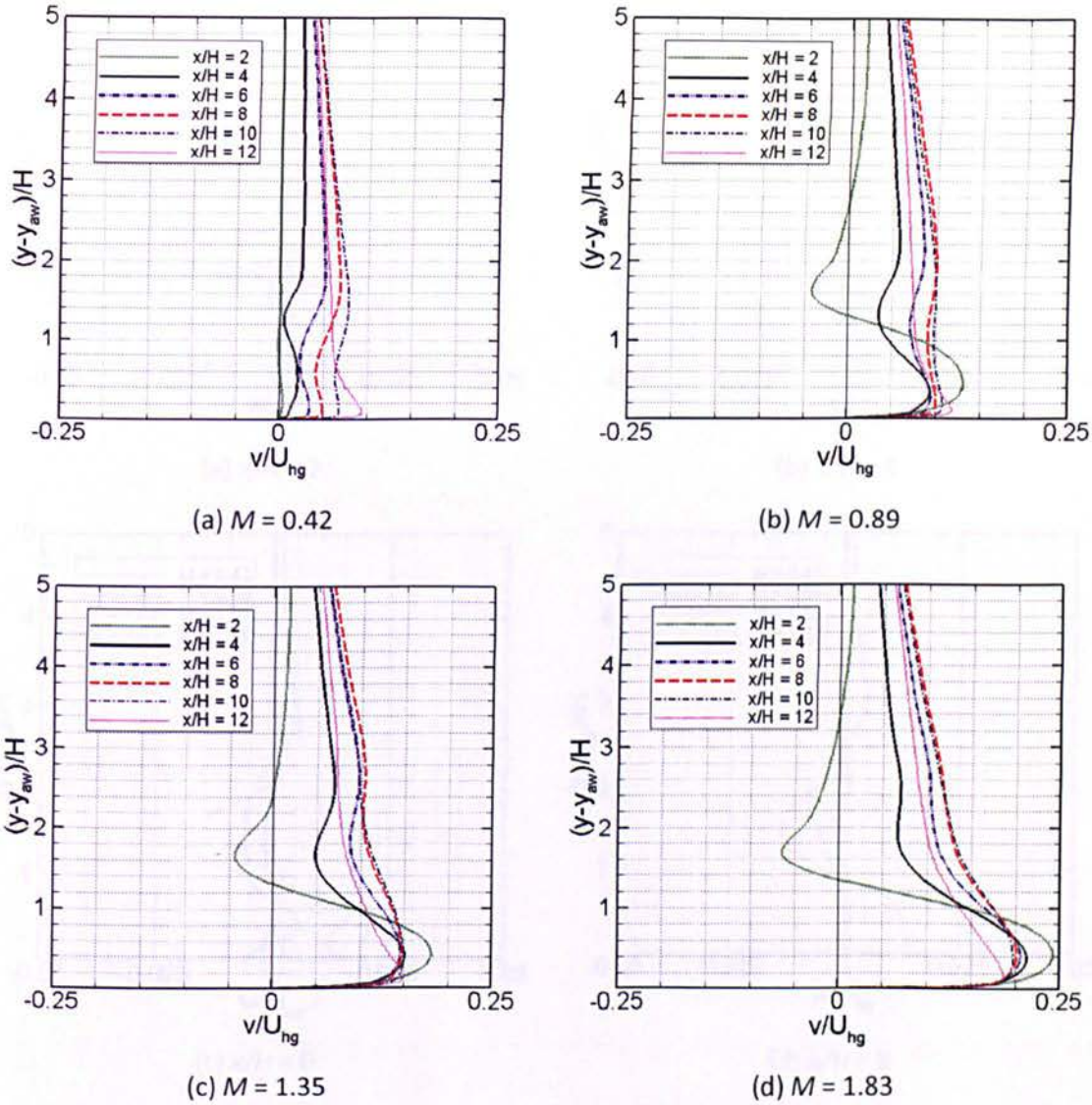

(a) $M = 0.42$ (b) $M = 0.89$

(c) $M = 1.35$ (d) $M = 1.83$

Figure 9–20: Normalised v velocity profile on four various blowing ratio for the case without lands.

From Figure 9–21, it is found that the w/U_{hg} velocity in the z-axis direction is minor, similar to the v/U_{hg} velocity in the y-axis direction. However, the increase of blowing ratio causes a strong impact on their intensity of w/U_{hg} velocity. A recirculation effect is noticeable at the region behind the lip where vortex-shedding occurs around this area. This effect is reduced near the downstream region. A gradual change of w velocity profiles is described in each blowing ratio as shown in Figure 9–22.

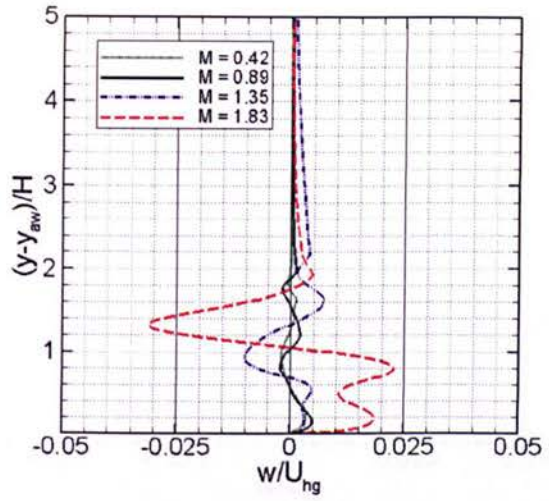

(a) $x/H = 2$

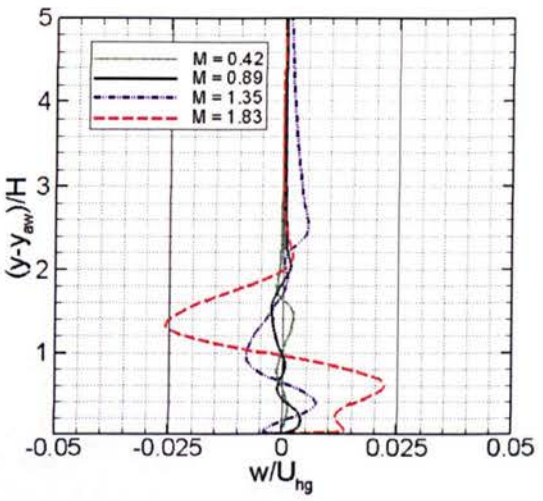

(b) $x/H = 4$

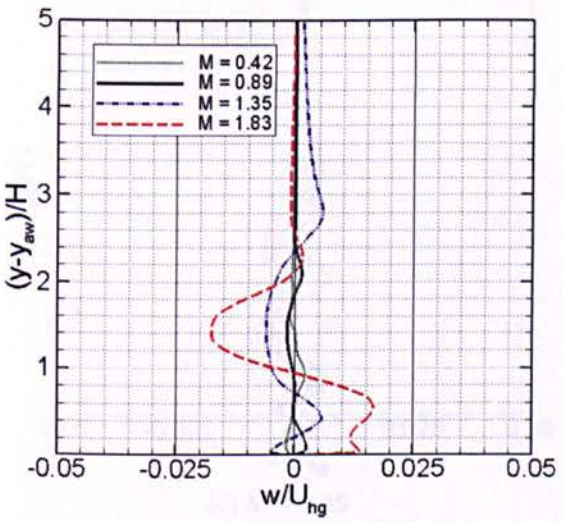

(c) $x/H = 6$

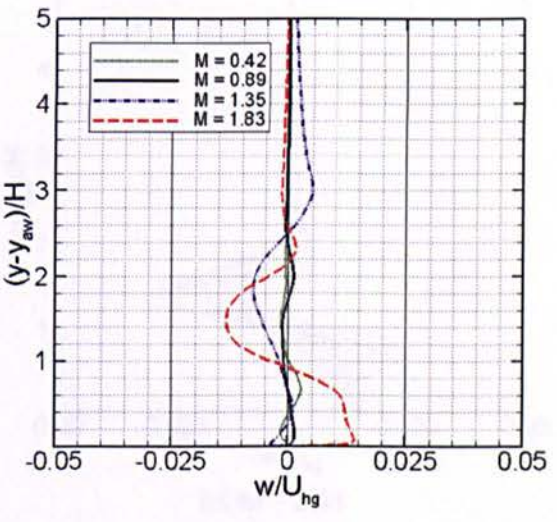

(d) $x/H = 8$

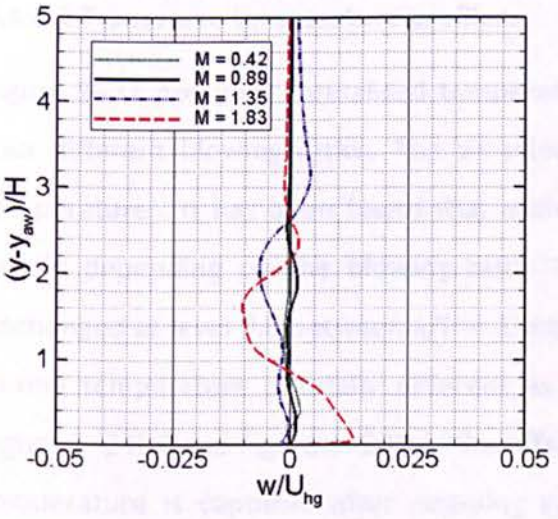

(e) $x/H = 10$

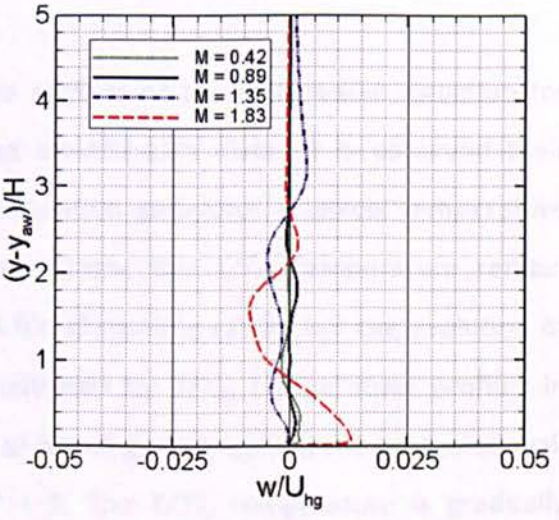

(f) $x/H = 12$

Figure 9–21: Normalised *w* velocity profiles at different downstream locations for the case without lands.

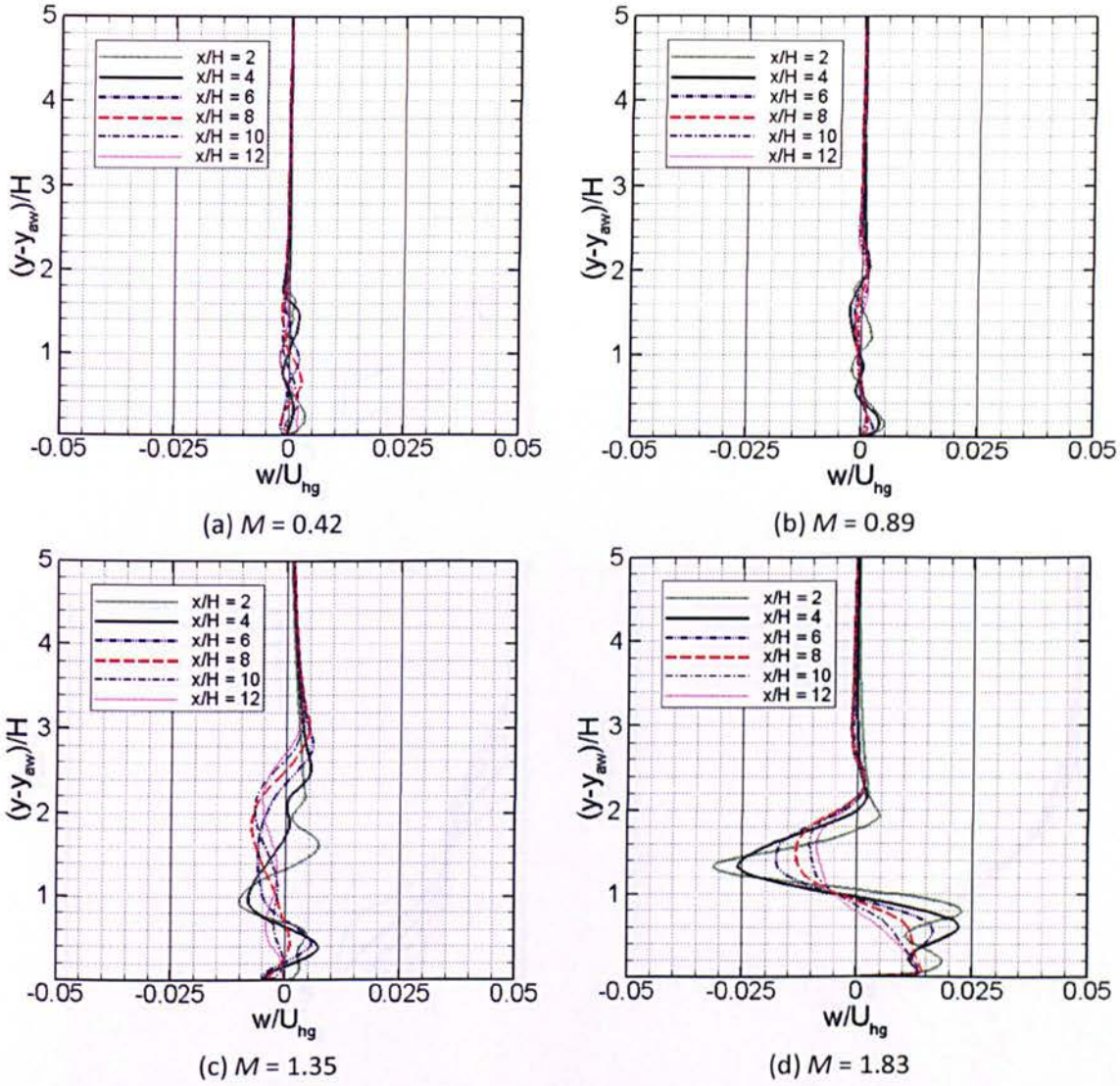

(a) $M = 0.42$ (b) $M = 0.89$

(c) $M = 1.35$ (d) $M = 1.83$

Figure 9–22: Normalised *w* velocity profiles on four various blowing ratio for the case without lands.

9.4.4.3 Transverse temperature profiles:

Figure 9–23 provides normalised temperature profiles of the streamwise direction for four different blowing ratios. The six-selected downstream distance is observed their temperatures. It has been found that each simulation generates a typical temperature profile depending on the blowing ratio. Interestingly, the T/T_{hg} temperature remain unchanged at level 0.6 between x/H = 2 and 4 for all blowing ratios, but the evolution of mixing temperature is totally different as illustrated by T/T_{hg} temperature profiles in Figure 9–24(a) and Figure 9–24(b). The effect of blowing ratio against the protected wall temperature is captured after attaining x/H = 6. The T/T_{hg} temperature is gradually increased in typical intensity depending on the coolant flow velocity from the slot exit due to the boundary condition of main hot gas flow remain unchanged.

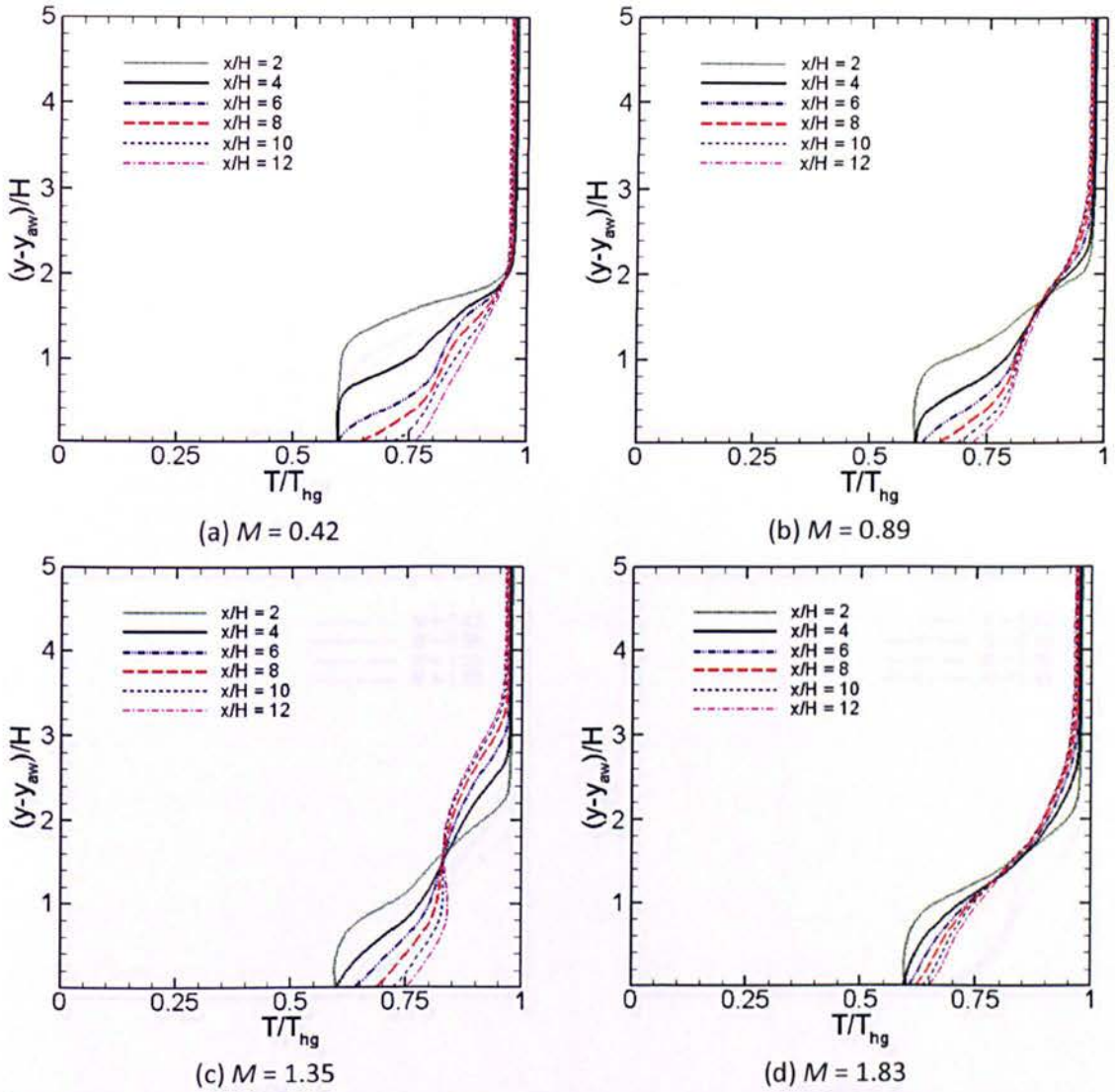

Figure 9–23: Normalised temperature profiles on four various blowing ratio for the case without lands.

It is clearly seen that the evolution of T/T_{hg} temperature is nonlinear as predicted as the effect of different thermal mixing process along the breakout region. It is most likely related to the turbulent flow structure as previously discussed in Figure 9–16. A regeneration of those structures probably influences an intensified thermal mixing, which causes a different evolution from the middle region into the protected wall surface. Indeed, the growth of turbulent flow structures involves various size of wakes and intensity of flow movement which affects heat-transfer process along the mixing region. Therefore, the invasion of mainstream flow into the region near the protected wall is dependent on turbulence flow structures resulted for various blowing ratio.

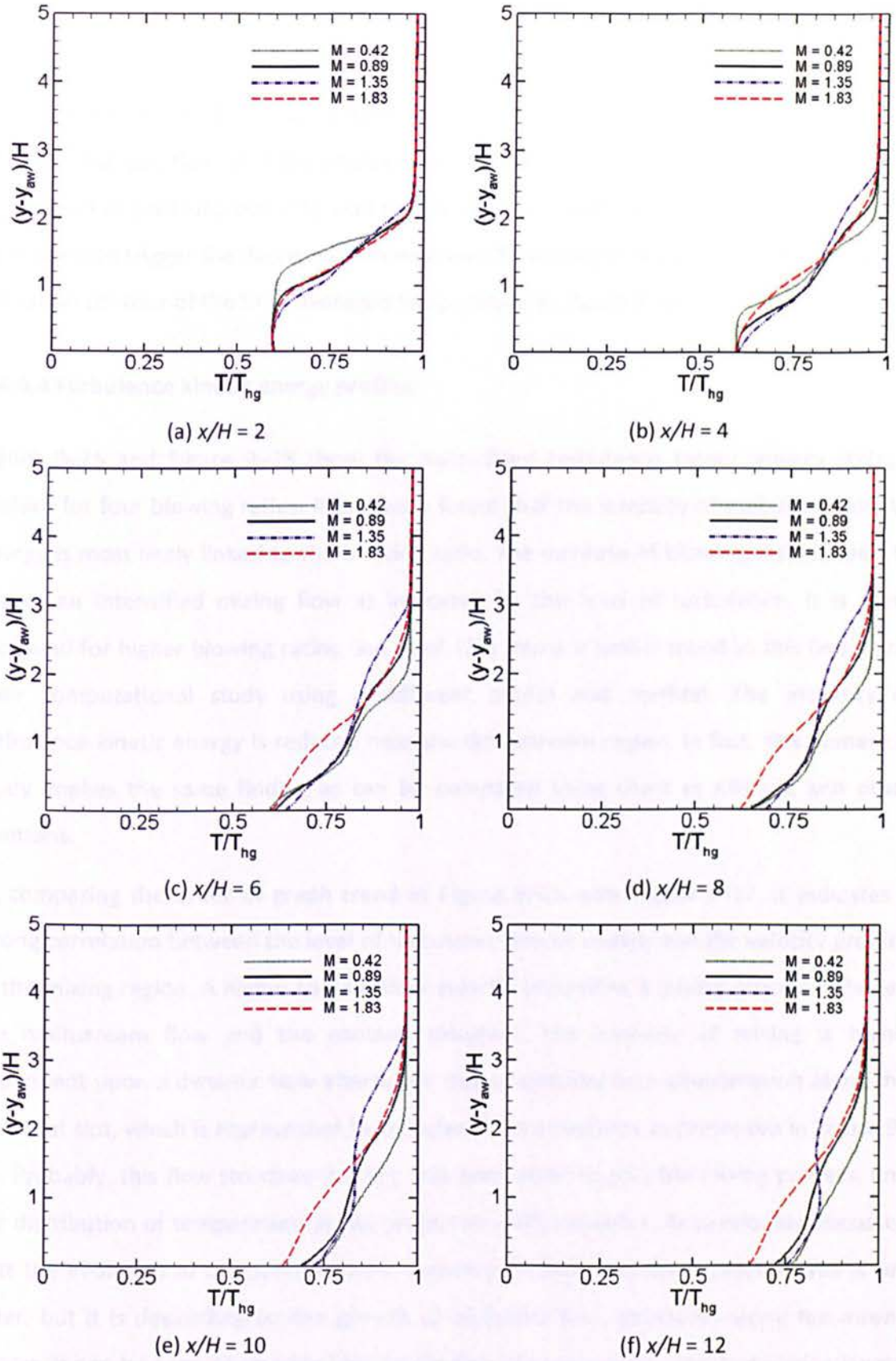

(a) $x/H = 2$ (b) $x/H = 4$

(c) $x/H = 6$ (d) $x/H = 8$

(e) $x/H = 10$ (f) $x/H = 12$

Figure 9–24: Normalised temperature profiles at different downstream locations.

Similar to the velocity profiles discussed above, the normalised T/T_{hg} tends to remain constant away from the protected wall. The normalised T/T_{hg} is equal to 0.95 at region $y-y_{ow}/H > 4$. This is for all various blowing ratios. This proves that this area is dominated by the main hot gas flow. A slight decrease of mainstream temperature is influenced by a lower level of pressure-side (PS) wall temperature and thermal mixing with the coolant. Both seem to trigger the decrease of mainstream flow temperature. This is indicated by a gradation contour of the time-averaged temperature in Figure 9–27.

9.4.4.4 Turbulence kinetic energy profiles:

Figure 9–25 and Figure 9–26 show the normalised turbulence kinetic energy (k/U_{hg}^2) profiles for four blowing ratios. It has been found that the intensity of turbulence kinetic energy is most likely linked to the blowing ratio. The increase of blowing ratio is seen to trigger an intensified mixing flow as indicated by the level of turbulence. It is more profound for higher blowing ratios. Joo *et al.* [27] found a similar trend as this finding on their computational study using a different model and method. The intensity of turbulence kinetic energy is reduced near the downstream region. In fact, this numerical study implies the same finding as can be compared using chart at $x/H = 2$ and other positions.

By comparing the order of graph trend in Figure 9–25 with Figure 9–17, it indicates a strong correlation between the level of turbulence kinetic energy and the velocity profiles at the mixing region. A higher coolant flow velocity intensifies a mixing process between the mainstream flow and the coolant. However, the intensity of mixing is highly dependent upon a dynamic flow interaction due to unsteadiness phenomenon along the breakout slot, which is represented by turbulent flow structures as presented in Figure 9–16. Probably, this flow structure is a key role parameter to play the mixing process, and the distribution of temperature at the protected wall thereafter. As previously discussed that the evolution of temperature from mainstream flow into the protected wall is un-linier, but it is depending on the growth of turbulent flow structures along the mixing region. It can be seen comparing the distribution of temperature and turbulence kinetic energy at the mixing region as shown in Figure 9–24 and Figure 9–25, respectively.

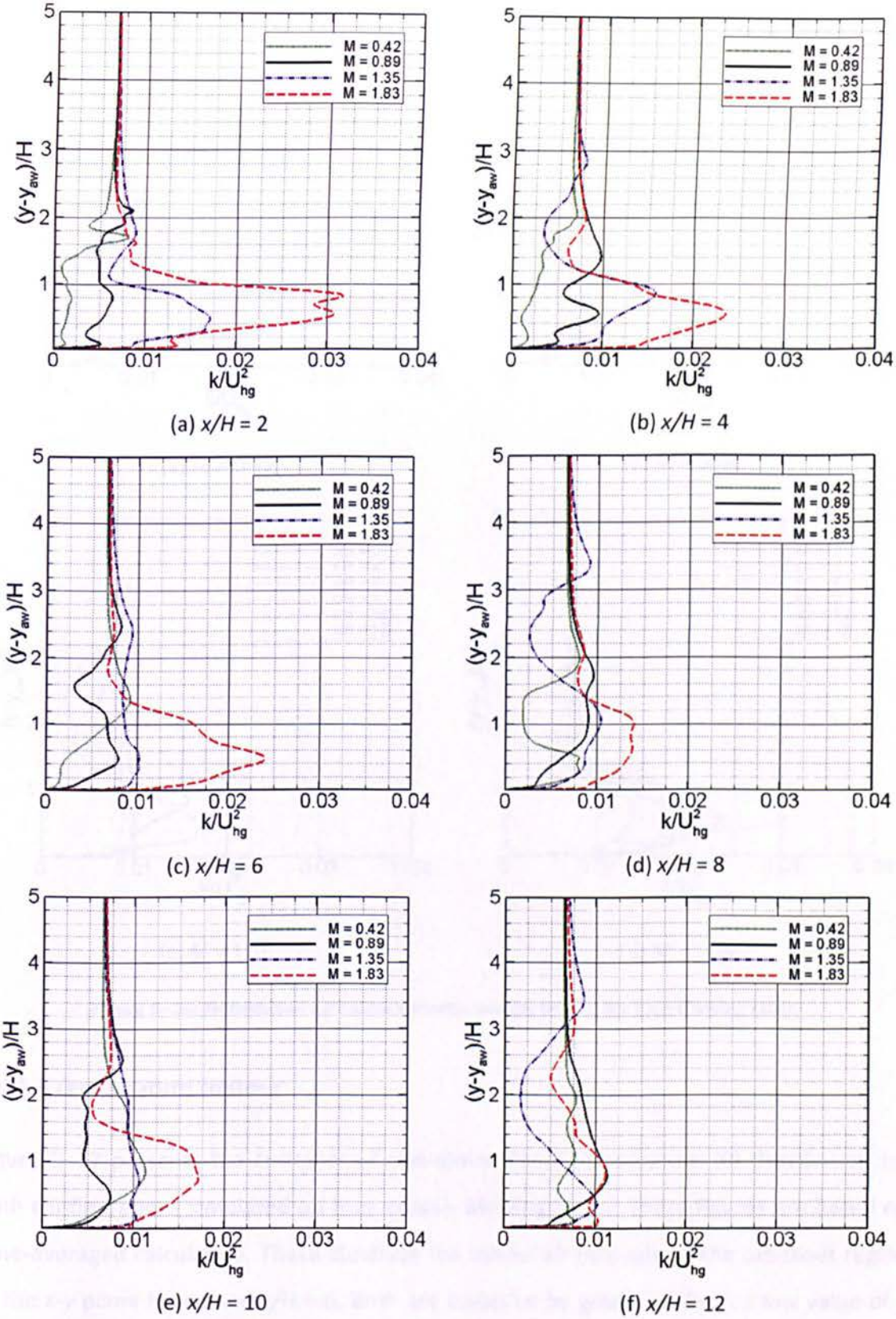

(a) $x/H = 2$ (b) $x/H = 4$

(c) $x/H = 6$ (d) $x/H = 8$

(e) $x/H = 10$ (f) $x/H = 12$

Figure 9–25: Normalised turbulence kinetic energy profile at different downstream locations.

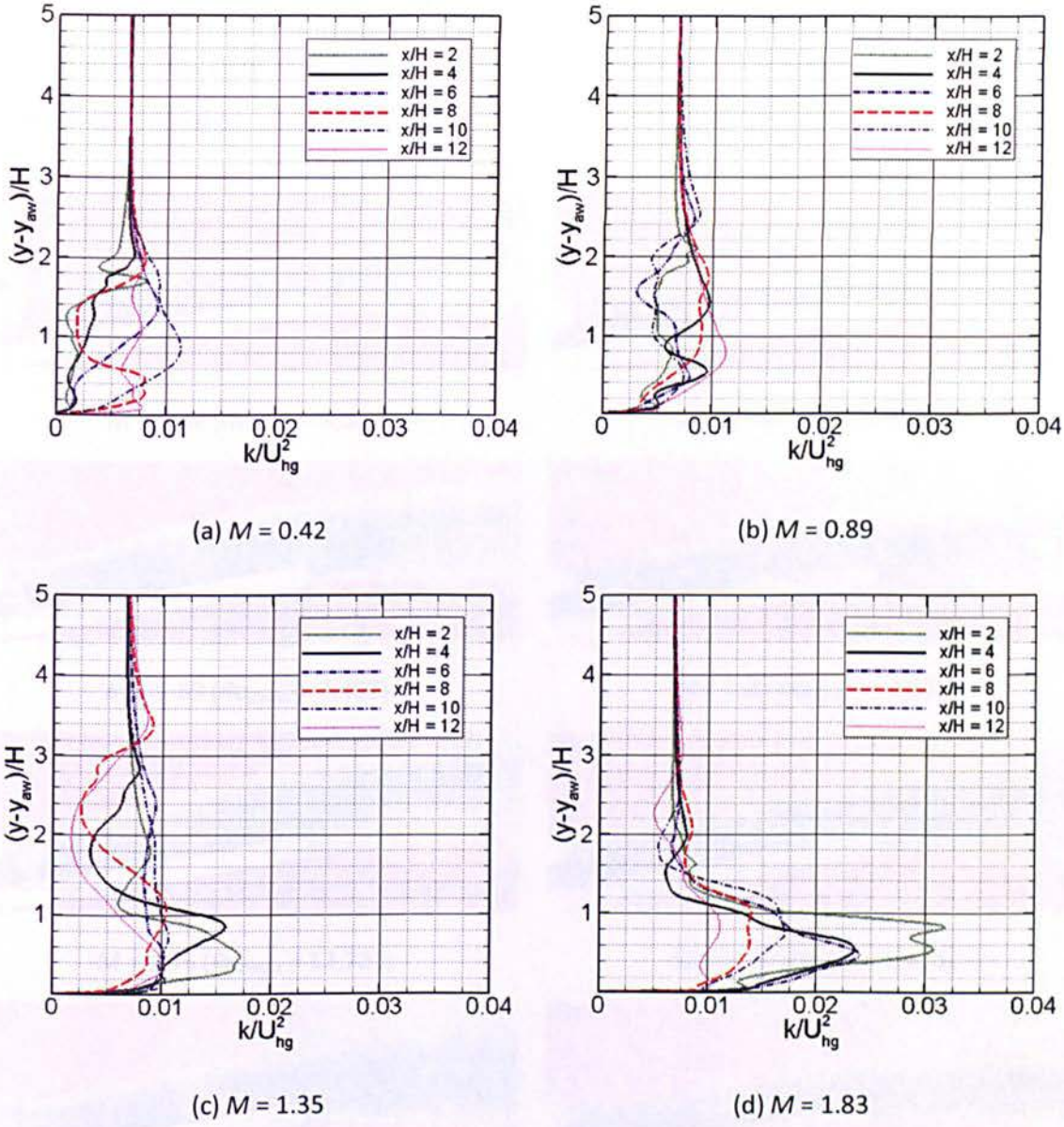

(a) $M = 0.42$ (b) $M = 0.89$

(c) $M = 1.35$ (d) $M = 1.83$

Figure 9–26: Normalised turbulence kinetic energy profile for four blowing ratio.

9.4.4.5 Temperature contour:

Figure 9–27 presents the contours of non-dimensional temperature (θ) distribution for both configurations simulated on four various blowing ratios. These figures are based on time-averaged calculation. These illustrate the mixed-air throughout the breakout region at the *x-y* plane for a fixed $z/H = 0$. Both are coloured by gradation from a low value of 0 (in red) to a high value of 1 (in blue). The red colour means that the mixed-air is dominated by the mainstream flow (hot gas), whilst the blue colour illustrates the domination of the coolant air. It has been found that the ejecting coolant is able to

expand the reach of ejection up to the downstream region by increasing blowing ratio as indicated by the blue colour. However, it is rather bias to interpret the evolution of temperature from M = 0.89 to 1.35.

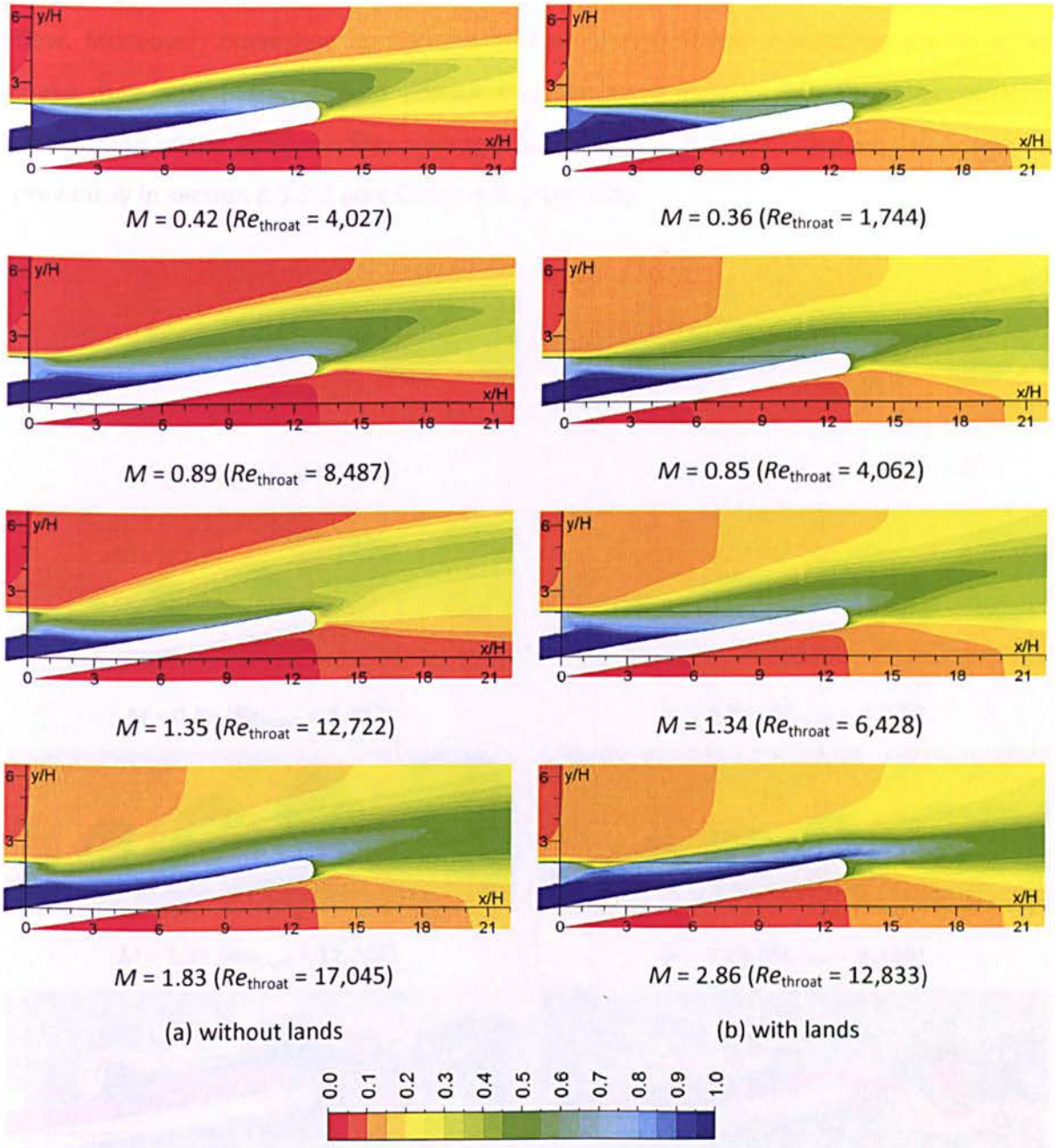

Figure 9–27: Distribution of non-dimensional temperature (θ) at the *x-y* plane of *z/H* = 0

9.4.4.6 Turbulence kinetic energy:

Figure 9–28 shows the normalised turbulence kinetic energy (k/U_{hg}^2) at the *x-y* plane for z/H = 0. It is coloured by gradation from a low value of 0 (in blue) to a high value of 0.01

(in red) on typical scale. It is recognized that turbulence kinetic energy increases in typical characteristic in each case simulated. The increase of blowing ratio is seen to trigger the growth of turbulent flow with sporadic movement. The combined effect of pin fin array and a higher coolant velocity at the inflow boundary condition causes a big unsteadiness flow. Moreover, horseshoe vortex and Karman Vortex Street around the pin-fin array make their flow patterns more complicated. All these aspects may cause asymmetric distribution of the adiabatic film-cooling effectiveness at the protected wall as discussed previously in section 8.5.3.2 (see Chapter 8, page 188).

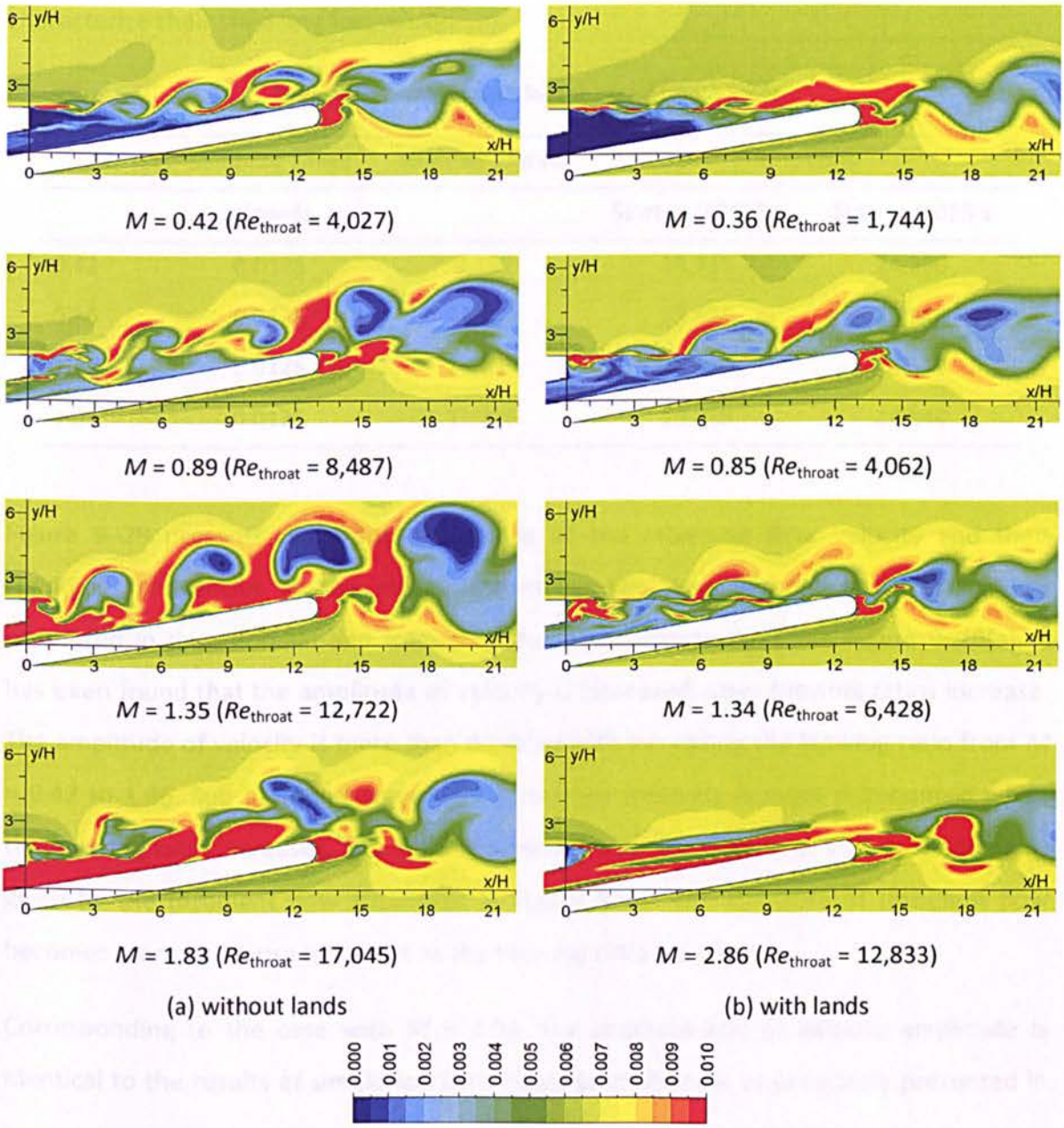

Figure 9–28: Distribution of turbulence kinetic energy (k/U_{hg}^2) at the *x-y* plane of *z/H*=0.

9.4.5 Shedding Frequency

In order to analyse the frequency of vortex-shedding, the mixing flow velocity of both case studies is recorded at two monitoring points S_1 and S_2 (see Figure 4–2, page 66). These positions are adopted from Martini's investigation [23][24]. Only the velocity magnitude is monitored in the current computation. The record data are taken in a range of flow times between 0.0125 and 0.025 seconds, as given in Table 9-5. Table 9–5 shows the iterations record in each blowing ratios studied corresponding to the duration of sampling times above. Based on this data, the fast-Fourier Transform is used to characterize their shedding frequency.

Table 9–5: Iteration data for the case without lands.

M	Sampling times	Number of data	Iterations	
	seconds		Start at 0.0125 s	Stop at 0.025 s
0.42	0.0125	9,159	15,131	24,290
0.86	0.0125	12,402	13,586	25,988
1.35	0.0125	13,939	14,610	28,549
1.83	0.0125	11,756	13,088	24,844

Figure 9–29 presents the truncated record of the mixed-air flow velocity and their shedding frequencies at the mixing region for the case without lands, which are presented in time domain and frequency domain, respectively. From Figure 9–29(a), it has been found that the amplitude of velocity is increased when blowing ratios increase. The amplitude of velocity is more than doubled with increasing the blowing ratio from M = 0.42 to 1.86. Sub harmonic wave with a stronger intensity is more pronounced when the blowing ratio increases. This finding matches with the growth of vortex-shedding as given by the turbulent flow structures in Figure 9–16. The structure of turbulent flow becomes more and more turbulent as the blowing ratio increases.

Corresponding to the case with M = 1.34, the characteristic of velocity amplitude is identical to the results of simulation with single pitch domain as previously presented in

section 6.5.8 (see Figure 6–19(c), page 137) It implies that both the use of domain could be considered acceptable for this prediction.

Similar to the previous investigations as presented in Chapters 5 – 8, a beating phenomenon is clearly captured in these case studies, mainly at higher blowing ratios. The increase of blowing ratio is identical to the increase of coolant flow velocity as the mainstream flow velocities are kept constant for this simulation. The increase of the coolant velocity inside the cooling passage is seen to trigger the growth of turbulence before ejecting the coolant from the slot-exit. The ejecting coolant is stronger with increasing the coolant velocity. Therefore, the mixing process between the mainstream flow and the coolant is more intensive along the mixing region, as indicated by increasing the amplitude of velocity in the left Figure 9–29(a). Certainly, the different coolant velocity causes different intensity of mixing which influences the natural frequency resulted in each blowing ratio. As previously discussed in section 8.5.5 (see page 194), beating may occur when the forcing frequency is close to the natural frequency of the system. The characteristic of beating phenomenon represents turbulent flow at the mixing region, which has a typical pattern in each blowing ratios.

The right figures (Figure 9–29(b)) show the shedding frequencies corresponding to the left figures (Figure 9–29(a)). It is found (the right Figure 9–29(b)) that the dominant frequencies are 1.71, 2.23, 2.17, and 2.93 kHz for the cases with blowing ratios of 0.42, 0.89, 1.35, and 1.83, respectively. The increase of dominant frequency is reasonable as the intensity effect of turbulent flow when blowing ratios increase. The ejecting coolant is more intensive when mixing with mainstream flow due to the increase of coolant velocity from the slot exit. The layout of pin-fin array inside the cooling passage also influences the turbulent flow pattern that affects the distribution of mixing flow velocity along the cutback region. In addition, the multiple effects of the horseshoe vortex near to the end-wall and the Karman vortex street around the middle pin-fins array affect a complicated turbulent flow at the mixing region. It can be indicated by different amplitude of velocity between the monitoring point positions; S_1 and S_2 (see the left Figure 9–29(a)). Therefore, each blowing ratio causes a different dominant frequency as discussed above.

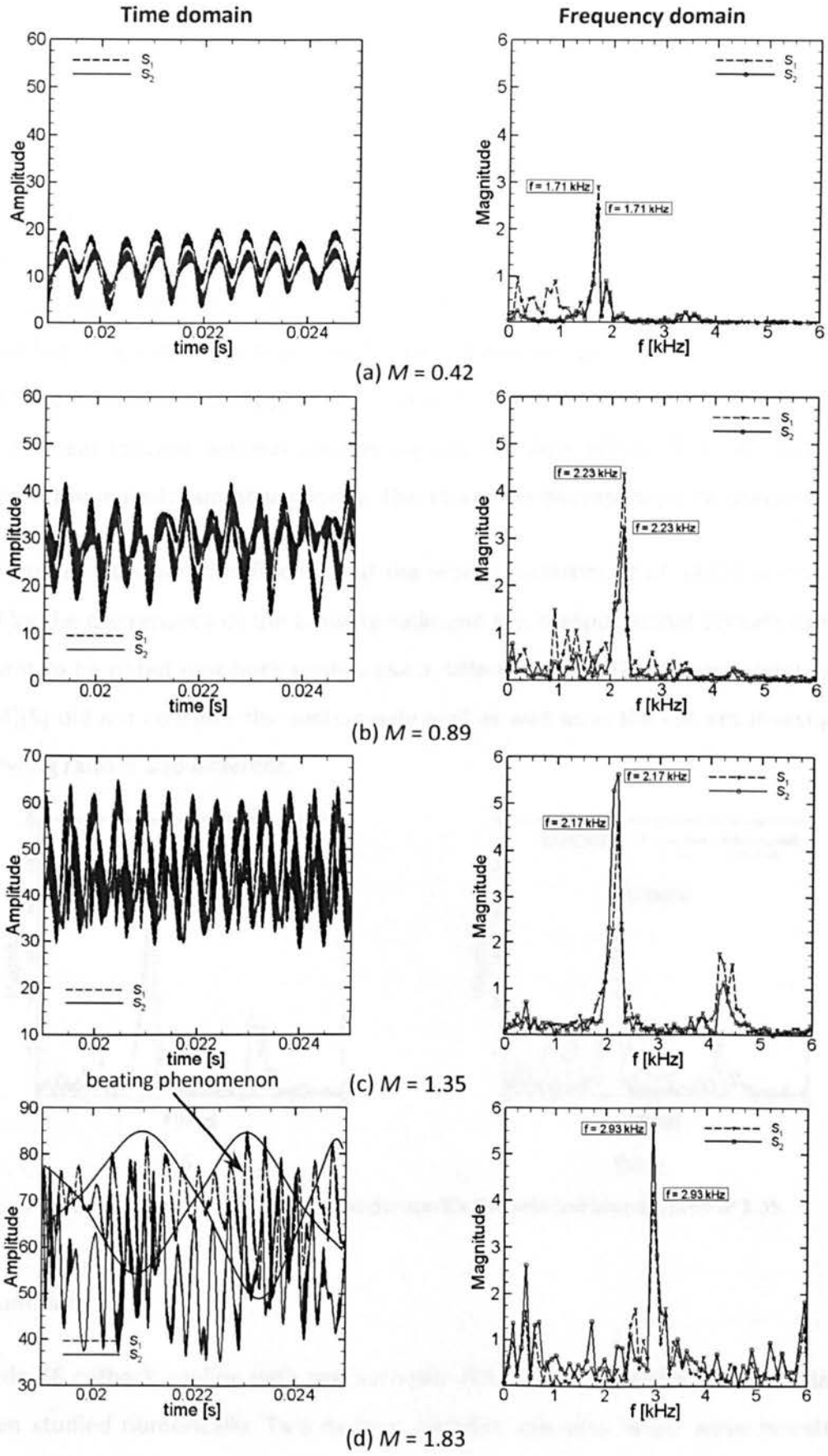

Figure 9–29: Shedding frequencies for the blade TE cutback without lands.

Figure 9–30 shows the comparison of shedding frequency for the selected blowing ratio of 1.35. It has been found that both designs yield a similar level of the shedding frequency as indicated by two monitoring points at S_1 and S_2. Both shedding frequencies are 2.17 and 2.20 kHz for the cases without lands and with lands, respectively. Each shedding frequency represents vortex shedding at the mixing region. This finding is seen to be close to the previous investigation carried out by Martini *et al.* [4][5] at the blowing ratio of 0.8, where a predicted frequency was around 2.36 kHz. Their analytical calculation noted that the shedding frequency should be about 2.4 kHz based on the effective lip thickness of 5 mm and the mainstream velocity at u_{hg} = 56 m/s. Of course, this solution was calculated within an ideal concept without considering the 3-D flow effect. That calculation only considered the mainstream flow velocity. Therefore, the discrepancy is reasonable.

The difference between this finding and the work of Martini *et al.* [4][5] is most likely caused by the discrepancy of the blowing ratio and the computational domain used. It is important to be noted that both studies use a different blade TE cutback model. Martini *et al.* [4][5] did not consider the suction-side wall as well as in the current investigation. The blowing ratio is also different.

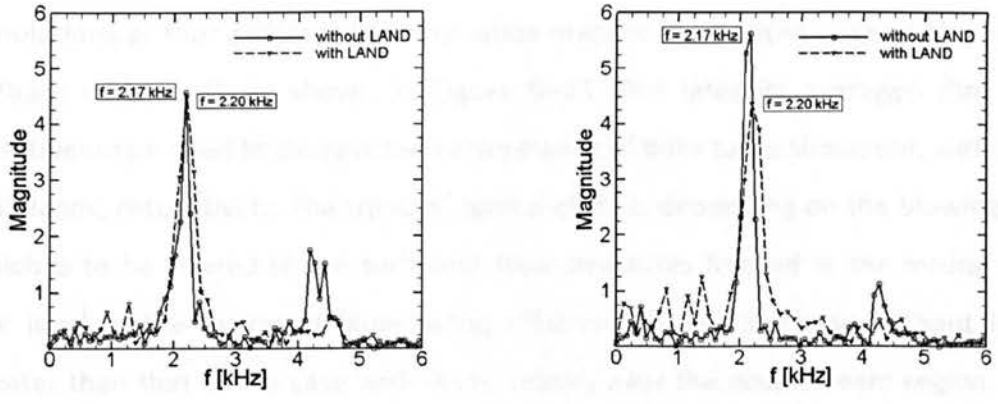

Figure 9–30: Shedding frequency comparison for the selected blowing ratio of 1.35.

9.5 Summary

The blade TE cutback cooling with pressure-side (PS) and suction-side (SS) wall surfaces has been studied numerically. Two designs, without and with lands, were investigated here. Similar to chapters 6 – 8, DES simulation was applied for these simulations. The

results and discussion have been presented comprehensively as above. Accordingly, the following points can be concluded:

1. The discharge coefficients for the insertion of land extensions into the reference blade TE cutback cooling is relatively greater than that of the case without lands with an average increase up to 20%. The use of both configurations, without and with suction-side (SS), yields the same level of discharge coefficient in a range of 0.58 – 0.64 for various blowing ratios simulated. This finding proves that the size of domain does not influence the discharge coefficient significantly.
2. The averaged heat-transfer coefficient of the pin-fin array increases gradually in typical the characteristic depending on blowing ratios. The increase of coolant flow velocity inside the cooling passage causes a rapid increase of heat-transfer coefficient as a combined effect of the pin-fin array and the turbulence. It is more noticeable for higher Reynolds numbers. The level of heat-transfer coefficient is significantly increased when raising Reynolds number. The change of coolant flow at the inflow region is sensitive to the turbulent flow structures at the mixing region. Correspondingly, Nusselt number increases row-by-row in-line with the averaged heat-transfer coefficient.
3. Simulations at four different blowing ratios present the performance of the blade TE cutback with PS-SS as shown in Figure 9–13. The laterally averaged film-cooling effectiveness is used to express the performance of both cases simulated, without and with lands, respectively. The trend of typical chart is depending on the blowing ratios, which is to be related to the turbulent flow structures formed at the mixing region. The level of the averaged film-cooling effectiveness for the case without lands is greater than that of the case with lands, mainly near the downstream region. Design with land extensions causes a fast decay in typical blowing ratios.
4. The dominant frequencies of the case without lands are 1.71, 2.23, 2.17 and 2.93 kHz for simulation at blowing ratios of 0.42, 0.89, 1.35 and 1.83. The comparison of shedding frequency for the selected blowing ratio of 1.35 shows that, both configurations yield a similar level of the shedding frequency. Both are 2.17 and 2.20 kHz for the cases without lands and with lands, respectively.

CHAPTER 10:

CONCLUSIONS AND FUTURE WORK

10.1 Conclusions

The phenomenon of mixing in a gas turbine blade trailing-edge cutback has been studied computationally. The shear-stress transport (SST) $k-\omega$ turbulence model was used in this simulation. Flow interaction between the internal cooling (i.e. pin-fin cooling) and the external cooling (i.e. TE cutback cooling) arising from the effects of features inside the cooling passage, the ratio of lip thickness to slot height (t/H), the coolant ejection angle (α), and the coexistence of the suction-side (SS) wall were comprehensively investigated. The evolutions of turbulent flow structures and vortex shedding at the mixing region were modelled. The effects of blowing ratio and film-cooling effectiveness as key technologies for improving thermal efficiency in gas turbine engines were studied in detail.

The results obtained and presented in this work are in good agreement with available experimental data. It has been proven by the agreement of predicted performance for the baseline model of the TE cutback in terms of discharge coefficient, film-cooling effectiveness and shedding frequency. Based on the results and discussion presented from Chapters 5 to 9 (inclusive), the following conclusions can be drawn.

1. The Detached Eddy Simulation (DES) method is capable of acquiring an advanced level of mixing unlike that of the unsteady RANS. This limitation with the unsteady RANS method could explain the anomaly found at the intermediate blowing ratio. Furthermore, steady RANS cannot simulate turbulent flow structures, which can be captured by both unsteady RANS and DES.
2. The steady RANS, unsteady RANS and DES methods can all be used to accurately predict the discharge coefficient (C_D), but not for predicting both film-cooling effectiveness (η_{aw}) and shedding frequency (f_s).

3. In order to achieve an appropriate prediction as obtained by DES method, computations must apply high quality grids with $\Delta y^+ < 1$ on all surfaces and small time-step sizes. Both time-step sizes of 2.5×10^{-5} and 1.25×10^{-5} seconds are considered acceptable for these case studies. However, time-step sizes of 1.25×10^{-5} seconds is a realistic value for this prediction in order to satisfy three study parameters as mentioned in the second conclusion.

4. The size of domain is not a crucial issue in the simulation of a TE cutback with a periodic pin-fin configuration in the lateral direction. Both single-pitch and double-pitch domains are considered acceptable for prediction.

5. The ejection lip thickness has a pronounced effect on the thermal mixing process between the mainstream flow and the coolant. Simulations carried out for four different *t/H* ratios indicate that the increase of lip thickness triggers intensified unsteady vortex shedding from the blunt lip. It enhances the mixing process of the film-cooling, which causes a rapid decay of effectiveness near the downstream region. Performance of TE cutback cooling could be maximised by designing thinner lip thickness. This design causes small wakes with shorter period at the mixing region that shield film-cooling near the protected wall from the mainstream flow. However, it is noted that a thinner lip thickness is challenging when related to manufacturing process.

6. In regards to the blade TE cutback with various lip thickness as explained in conclusion 5, the dominant frequency is decreased by increasing the *t/H* ratios from 0.25 to 1.5.

7. Based on results from simulations for three different internal cooling designs, performance of a TE cutback cooling could be improved by installing the elliptical pin-fin array inside the cooling passage. The film-cooling effectiveness is increased by up to 2.53% (on average) when the circular pin-fin configuration is replaced with the elliptical pin-fins array incorporating a streamwise orientation of the array. Aside from their functions for enhancing heat-transfer along the cooling channel, the streamwise pin-fin orientation is able to increase the level of discharge coefficient by

up to 10%. It means that the pressure loss in the cooling passage could be minimised to a lower level in an attempt to reduce the power of the coolant flow.

8. The distribution of the adiabatic film-cooling effectiveness at the protected wall is strongly influenced by the design of the coolant ejection angle. A decrease of the ejection angle causes a decay of the averaged film-cooling effectiveness. It is noticeable after approaching the peak level. Shedding frequency is seen to follow the change of ejection angle, where a shedding frequency is increased in-line with a decrease of ejection angle

9. Numerical studies of the TE cutback cooling with pressure-side (PS) and suction-side (SS) wall show that performance of the case without lands is greater than that of the case with lands, mainly near the downstream region. A design, which incorporates land extensions, causes a rapid decay of the averaged film-cooling effectiveness. Anomalous chart order is seen for both case studies. For the case with lands, the effectiveness increases gradually when increasing blowing ratios from 0.36 to 0.85. The effectiveness of film-cooling decreases for intermediate blowing ratio of 0.85 then increases once again. This phenomenon also occurs for the case without lands in typical blowing ratio. It can be stated that the film-cooling effectiveness is predominantly affected by blowing ratio. In terms of the discharge coefficient, it increases by up to 20% after installing land extensions

10.2 Future Work

As discussed in this thesis, not at all of the various cases could be simulated perfectly by considering the existence of a suction-side (SS) wall in real conditions, in order to provide a computational domain. Due to the large amount of time required for each simulation with double pitch of pin-fin distance to obtain a statistically converged solution (up to 720-hours), the blowing ratio could only be varied within a limited range. As a result, only four different blowing ratios are provided in this computation, i.e. blowing ratios of 0.42, 0.89, 1.35 and 1.83 for the case without lands; and blowing ratios of 0.36, 0.85, 1.34 and 2.86 for the case with lands.

In several previous studies, the research teams have evaluated the performance a TE cutback without the existence of suction-side (SS) wall as mentioned in open literatures. The results and conclusions presented in Chapters 5 – 8 of this thesis have been performed using the same parameters. Whilst, these results are valid and can add significantly to the body of knowledge compared to the existing experiments.

In real fact, the results of this investigation found that the use of both designs (TE cutback with PS versus TE cutback with PS-SS) does not affect significantly. The size of domain also is not a crucial issue for this simulation. The design of domain without considering the suction-side wall as described in Chapter 5 – 8 are considered acceptable in this investigation as used by various researchers.

Based on the discussion in this thesis, it is suggested in the future works as follow:

1. The cases presented in chapters 5 – 8 should be simulated within the range used in this study but considering the existence of suction-side (SS) wall. Experiment by developing a trailing-edge cutback with the existence of suction-side (SS) wall is very useful in an attempt to validate simulation at exactly the same design as presented in Chapter 9.
2. As stated in conclusion number eight and mentioned by several researchers in open literature regarding the effectiveness of film-cooling, performance of the blade TE cutback cooling is predominantly determined by blowing ratios. Therefore, it is important to simulate cases above in more detail in terms of blowing ratio variations. It is expected to explain an anomalous order of film-cooling effectiveness mainly around an intermediate blowing ratio, which is still unclear in terms of that range.
3. Improvement of the capability of hardware-and-software is needed concomitant with refining the mesh resolution and expanding the domain size as suggested in point number-1 about a computational domain with the existence of suction-side (SS).
4. The application of other turbulence models, e.g. DES based on the Spalart-Allmaras, DES based on the realisable $k-\varepsilon$ model, to simulate the cases presented in this work for comparative purposes.

REFERENCES

[1] J. C. Han and S. Ekkad, "Recent Studies in Turbine Blade Film Cooling," *J. Rotating Machinery,* vol. 7, no. 1, p. 21–40, 2001.

[2] J. C. Han, "Recent Studies in Turbine Blade Cooling," *J. Rotating Machinery,* vol. 10, no. 6, p. 443–457, 2004.

[3] B. Facchini, B. Innocenti and L. Tarchi, "Pedestal and Endwall Contribution in Heat Transfer in Thin Wedge Shaped Trailing Edge," in *ASME Paper No. GT-2004-53152,* Vienna, Austria, 2004.

[4] P. Martini, A. Schulz and H. -J. Bauer, "Film Cooling Effectiveness and Heat Transfer on The Trailing Edge Cutback of Gas Turbine Airfoils with Various Internal Cooling Designs," in *ASME Paper No. GT-2005-68083,* 2005.

[5] P. Martini, A. Schulz and H. -J. Bauer, "Film Cooling Effectiveness and Heat Transfer on The Trailing Edge Cutback of Gas Turbine Airfoils with Various Internal Cooling Designs," *J. Turbomachinery,* vol. 128, no. 1, p. 196–206, 2006.

[6] Z. Yang and H. Hu, "An Experimental Investigation on the Trailing-edge Cooling of Turbine Blades," *J. Propulsion and Power Research,* vol. 1, no. 1, p. 36–47, 2012.

[7] B. Facchini, F. Simonetti and L. Tarchi, "Experimental Investigation of Turning Flow Effects on Innovative Trailing Edge Cooling Configurations with Enlarged Pedestals and Square or Semicircular Ribs," in *ASME Paper No. GT-2009-59925,* Orlando, Florida, USA, 2009.

[8] J. Choi, S. Mhetras, J. -C. Han, S. Lau and R. Rudolph, "Film Cooling and Heat Transfer on Two Cutback Trailing Edge Model with Internal Performance Blockages," *J. Heat Transfer,* vol. 130, no. 1, p. 012201, 2008.

[9] A. L. Brundage, M. W. Plesniak, P. B. Lawless and S. Ramadhyani, "Experimental Investigation of Airfoil Trailing Edge Heat Transfer and Aerodynamic Losses," *J. Experimental Thermal and Fluid Science,* vol. 31, no. 3, p. 249–260, 2007.

[10] J. C. Han and A. P. Rallabandi, "Turbine Blade Film Cooling Using PSP Technique," *Frontier in Heat and Mass Transfer,* vol. 1, 2010.

[11] B. Facchini, M. Surace and S. Zecchi, "A New Concept of Impingement Cooling for Gas Turbine Hot Parts and Its Influence on Plant Performance," in *ASME Paper No. GT-2003-38166*, Atlanta, Georgia, USA, 2003.

[12] J. Han, S. Dutta and S. Ekkad, Gas Turbine Heat Transfer and Cooling Technology, Second ed., London: CRC Press, Taylor and Francis Group, 2013.

[13] L. Tarchi, B. Facchini and S. Zecchi, "Experimental Investigation of Innovative Internal Trailing Edge Cooling Configurations with Pentagonal Arrangement and Elliptic Pin Fin," *J. Rotating Machinery,* 2008.

[14] J. Krueckels, M. Gritsch and M. Schneider, "Design Consideration and Validation of Trailing Edge Pressure Side Bleed Cooling," in *ASME Paper No. GT-2009-59161*, 2009.

[15] P. Martini, A. Schulz and S. Wittig, "Experimental and Numerical Investigation of Trailing Edge Film Cooling by Circular Wall Jets Ejected from a Slot with Internal Rib Arrays," in *ASME Paper No. GT-2003-38157*, 2003.

[16] P. Martini and A. Schulz, "Experimental and Numerical Investigation of Trailing Edge Film Cooling by Circular Wall Jets Ejected from a Slot with Internal Rib Arrays," *J. Turbomachinery,* vol. 126, no. 2, p. 229–236, 2004.

[17] T. Schobeiri, "Optimum Trailing Edge Ejection for Cooled Gas Turbine Blades," *J. Turbomachinery,* vol. 111, no. 4, p. 510–514, 1989.

[18] F. J. Cunha and M. K. Chyu, "Trailing-Edge Cooling for Gas Turbines," *J. Propulsion and Power,* vol. 22, no. 2, p. 286–300, 2006.

[19] S. D. Holloway, J. H. Leylek and F. A. Buck, "Pressure-Side Bleed Film Cooling: Part I - Steady Framework For Experimental and Computational Results," in *ASME paper No GT-2002-30471*, Amsterdam, The Netherlands, 2002.

[20] P. Martini, A. Schulz, C. F. Whitney and E. Lutum, "Experimental and Numerical Investigation of Trailing Edge Film Cooling Downstream of a Slot with Internal Rib Arrays," in *Proc. Inst. Mech. Eng., Part A, 217*, 2003.

[21] M. Effendy, Y. Yao and J. Yao, "Comparison Study of Turbine Blade with Trailing-Edge Cutback Coolant Ejection Designs," in *51st AIAA Aerospace Sciences Meeting, Texas, 2013-0548*, 2013.

[22] Y. Egorov, F. R. Menter, R. Lechner and D. Cokljat, "The Scale-Adaptive Simulation Method for Unsteady Turbulent Flow Predictions. Part 2: Application to Complex Flows," *J. Flow, Turbulence and Combustion,* vol. 85, no. 1, p. 139–165, 2010.

[23] P. Martini, A. Schulz, H. -J. Bauer and C. F. Whitney, "Detached Eddy Simulation of Film Cooling Performance on The Trailing Edge Cutback of Gas Turbine Airfoils," in *ASME Paper No. GT-2005-68084,* 2005.

[24] P. Martini, A. Schulz, H. -J. Bauer and C. F. Whitney, "Detached Eddy Simulation of Film Cooling Performance on The Trailing Edge Cutback of Gas Turbine Airfoils," *J. Turbomachinery,* vol. 128, no. 2, p. 292–300, 2006.

[25] S. D. Holloway, J. H. Leylek and F. A. Buck, "Pressure-Side Bleed Film Cooling: Part II - Unsteady Framework for Experimental and Computational Results," in *ASME paper No. GT-2002-30472,* Amsterdam, The Netherlands, 2002.

[26] G. Medic and P. A. Durbin, "Unsteady Effects on Trailing Edge Cooling," *J. Heat Transfer,* vol. 127, no. 4, p. 388–392, 2005.

[27] J. Joo and P. Durbin, "Simulation of Turbine Blade Trailing Edge Cooling," *J. Fluid Engineering,* vol. 131, no. 2, pp. 021102-1 – 021102-14, 2009.

[28] H. Schneider, D. von Terzi and H. -J. Baurer, "Large-Eddy Simulations of Trailing-Edge Cutback Film Cooling at Low Blowing Ratio," *J. Heat and Fluid Flow,* vol. 31, no. 5, p. 767–775, 2010.

[29] H. Schneider, D. von Terzi and H. -J. Baurer, "Turbulent Heat Transfer and Large Coherent Structures in Trailing-edge Cutback Film Cooling," *J. Flow, Turbulence and Combustion,* vol. 88, no. 1-2, p. 101–120, 2012.

[30] T. Horbach, A. Schulz and H. -J. Bauer, "Trailing Edge Film Cooling of Gas Turbine Airfoils – External Cooling Performance of Various Internal Pin Fin Configurations," *J. Turbomachinery,* vol. 133, no. 4, pp. 041006-1 – 041006-9, 2011.

[31] N. E. Taslim, S. D. Spring and B. P. Mehlmann, "Experimental Investigation of Film Cooling Effectiveness for Slot of Various Exit Geometries," *J. Thermophysics and Heat Transfer,* vol. 6, no. 2, p. 302–307, 1992.

[32] M. Effendy, Y. Yao, J. Yao and D. R. Marchant, "Predicting Film Cooling Performance of Trailing–Edge Cutback Turbine Blades by Detached–Eddy Simulation," in *52st AIAA Aerospace Sciences Meeting,* Maryland, 2014.

[33] C. Bianchini, B. Facchini, F. Simonetti and L. Tarchi, "Numerical and Experimental Investigation of Turning Flow Effects on Innovative Pin Fin Arrangements for Trailing Edge Cooling Configurations," in *ASME Paper No. GT-2010–23536*, Glasgow, UK, 2010.

[34] C. Carcasci and F. Simonetti, "Experimental Investigation of Turning Flow Effects on Innovative Trailing Edge Cooling Configurations with Elliptic Pin Fins," Antalya, Turkey, *2009*.

[35] T. Horbach, A. Schulz and H. -J. Bauer, "Trailing Edge Film Cooling of Gas Turbine Airfoils – Effect of Ejection Lip Geometry on Film Cooling Effectiveness and Heat Transfer," in *International Symposium on Heat Transfer in Gas Turbine Systems, Antalya, Turkey, 42-TE*, 2009.

[36] Y. Hepeng, Z. Huiren and K. Manzhao, "Effect of Blowing Ratio Measured by Liquid Crystal on Heat Transfer Characteristic of Trailing Edge Cutback," *Chinese J. Aeronautics,* vol. 21, no. 6, p. 488–495, 2008.

[37] Z. Yang and H. Hu, "An Experimental Investigation on the Trailing-edge Cooling of Turbine Blades by Using PIV and PSP Techniques," in *41st AIAA Fluid Dynamic Conference and Exhibit*, Honolulu, Hawai, 2011.

[38] Z. Yang and H. Hu, "Study of Trailing-Edge Cooling Using Pressure Sensitive Paint Technique," *J. Propulsion and Power,* vol. 27, no. 3, p. 700–709, 2011.

[39] Y. Chen, C. G. Matalanis and J. K. Eaton, "High Resolution PIV Measurements around a Model Turbine Blade Trailing Edge Film Cooling Breakout," *J. Experiments in Fluids,* vol. 44, no. 2, p. 199–209, 2007.

[40] N. Fiala, J. Johnson and F. Ames, "Aerodynamics of a Letterbox Trailing Edge : Effects of Blowing Rate, Reynolds Number, and External Turbulence on Aerodynamics Losses and Pressure Distribution," *J. Turbomachinery,* vol. 132, no. 4, pp. 041011-1–041011-11, 2010.

[41] J. Ling, S. Yapa, M. Benson, C. Elkins and J. Eaton, "Three-Dimensional Velocity and Scalar Field Measurements of an Airfoil Trailing Edge with Slot Film Cooling: The Effect of an Internal Structure in the Slot," *J. Turbomachinery,* vol. 135, no. 3, pp. 031018-1 – 031018-8, 2013.

[42] J. -C. Han, "Fundamental Gas Turbine Heat Transfer," *J. Thermal Science and Engineering Applications,* vol. 5, no. 2, pp. 021007-1, 2013.

[43] G. Delibra, K. Hanjalic, D. Borello and F. Rispoli, "Vortex Structures and Heat Transfer in a Wall-bounded Pin Matrix: LES with a RANS Wall-Treatment," *J. Heat and Fluid Flow,* vol. 31, no. 5, p. 740–753, 2010.

[44] F. E. Ames, L. A. Dvorak and M. J. Morrow, "Turbulent Augmentation of Internal Convection Over Pins in Staggered Pin-fin Arrays," *J. Turbomachinery,* vol. 127, no. 1, p. 183–190, 2005.

[45] F. E. Ames and L. A. Dvorak, "Turbulent Transport in Pin-fin Arrays: Experimental Data and Predictions," *J. Turbomachinery,* vol. 128, no. 1, p. 71–81, 2006.

[46] F. E. Ames, C. A. Nordquist and L. A. Dvorak, "Endwall Heat Transfer Measurements in a Staggered Pin-fin array with an Adiabatic Pin," in *ASME Paper No. GT-2007-27432*, Montreal, Canada, 2007.

[47] C. P. Lee, "Turbine Blade Trailing Edge Cooling Openings and Slots". Patent EP 1 065 344 A2, 2001.

[48] J. -L. Bacha, E. Berche and T. Brusq, "Cooled Turbine Blade for Gas Turbine Engine". Patent US2013142668 A1, 2013.

[49] D. E. Demers, R. F. Manning and P. J. Acquaviva, "Turbine Blade for a Gas Turbine and Method of Cooling Side Blade". Patent EP1205636 B1, 2012.

[50] V. Bregman and M. Petukhovskiy, "Gas Turbine Blade". Patent US20130209268 A1, 2013.

[51] M. Schobeiri and K. Pappu, "Optimization of Trailing Edge Ejection Mixing Losses: A Theoritical and Experimental Study," *J. Fluid Engineering,* vol. 121, no. 1, p. 118–125, 1999.

[52] A. Murata, S. Nishida, H. Saito, K. Iwamoto, Y. Okita and C. Nakamata, "Effect of Surface Geometry on Film Cooling Performance at Airfoil Trailing Edge," *J. Turbomachinery,* vol. 134, no. 5, pp. 051033-1 – 051033-8, 2012.

[53] M. Benson, C. Elkins and J. Eaton, "Measurements of 3D Velocity and Scalar Field for a Film-Cooled Airfoil Trailing Edge," *J. Experiments in Fluids,* vol. 51, no. 2, p. 443–455, 2011.

[54] M. Benson, C. Elkins, S. Yapa, J. Ling and J. Eaton, "Effects of Varying Reynolds Number, Blowing Ratio, and Internal Geometry on Trailing Edge Cutback Film Cooling," *J. Experiments in Fluids,* vol. 52, no. 6, p. 1415–1430, 2012.

[55] M. Benson, S. Yapa, C. Elkins and J. Eaton, "Experimental-Based Redesigns for Trailing Edge Film Cooling of Gas Turbine Blades," *J. Turbomachinery,* vol. 135, no. 4, July 2013.

[56] N. E. Taslim, S. D. Spring and B. P. Mehlmann, "An Experimental Investigation of Film Cooling Effectiveness for Slot Various Exit Geometries," in *AIAA Paper No. 90-2266,* 1990.

[57] S. Kacker and J. Whitelaw, "The Effect of Slot Height and Slot-Turbulence Intensity on the Effectiveness of the Uniform Density, Two Dimensional Wall Jet," *J. Heat Transfer,* vol. 90, no. 4, p. 469–475, 1968.

[58] S. C. Kacker and J. H. Whitelaw, "An Experimental Investigation of Slot Lip Thickness on Impervious Wall Effectiveness of the Uniform Density, Two-Dimensional Wall Jet," *J. Mass and Heat Transfer,* vol. 12, no. 9, p. 1196–1201, 1969.

[59] S. Sivasegaram and J. Whitelaw, "Film Cooling Slots: The Importance of Lip Thickness and Injection Angle," *J. Mechanical Engineering Science,* vol. 11, no. 1, p. 22–27, 1969.

[60] W. Burns and J. Stollery, "The Influence of Foreign Gas Injection and Slot Geometry on Film Cooling Effectiveness," *J. Heat and Mass Transfer,* vol. 12, no. 8, p. 935–951, 1969.

[61] K. Viswanathan, M. Schur, P. R. Spalart and M. Strelets, "Flow and Noise Predictions for Single and Dual Stream Beveled Nozzles," *J. AIAA,* vol. 46, no. 3, p. 601–626, 2008.

[62] A. Viswanathan and D. K. Tafti, "Detached-Eddy Simulation of Flow and Heat Transfer in Fully Developed Rotating Internal Cooling Channel with Normal Ribs," *J. Heat and Fluid Flow,* vol. 27, no. 1, p. 351–370, 2006.

[63] A. Viswanathan, K. Klismith, J. Forsythe and R. Squires, "Detached-Eddy Simulation around a Forbody at High Angle of Attack," in *AIAA Paper No. 2003-263,* 2003.

[64] A. Viswanathan and D. K. Tafti, "Detached-Eddy Simulation of Turbulent Flow and Heat Transfer in a Two-Pass Internal Cooling Duct," *J. Heat and Fluid Flow,* vol. 27, no. 1, p. 1–20, 2006.

[65] C. H. K. Williamson and R. Govardhan, "Vortex-induced Vibration," *Annual Review of Fluid Mechanics,* vol. 36, p. 477–539, 2004.

[66] A. Roshko, "Perspectives on Bluff Body Aerodynamics," *J. Wind Engineering and Industrial Aerodynamics,* vol. 49, no. 1-3, p. 79–100, 1993.

[67] D. You and M. R. Choi, "Control of Flow Induced Noise behind a Circular Cylinder using Splitter Plates," *J. AIAA,* vol. 36, no. 11, p. 1961–1967, 1998.

[68] Y. Hwang and H. Choi, "Sensitivity of Global Instability of Spatially Developing Flow in Weakly and Fully Nonlinear Regimes," *J. Physics of Fluids,* vol. 20, 2008.

[69] H. Choi, W. P. Jeon and J. Kim, "Control of Flow over a Bluff Body," *Annual Review of Fluid Mechanics,* vol. 40, p. 113–139, 2008.

[70] Y. J. Chen and C. P. Shao, "Suppresion of Vortex Shedding from Rectangular Cylinder at Low Reynolds Number," *J. Fluids and Structures,* vol. 43, p. 15–27, 2013.

[71] C. P. Shao and Q. D. Wei, "Control of Vortex Shedding from a Square Cylinder," *J. AIAA,* vol. 46, no. 2, p. 397–407, 2008.

[72] C. L. J. Shao, "Control of Vortex Shedding from a Plate at Incidence Angles in the Range of 0-90 deg," *J. Fluids Engineering,* vol. 131, no. 11, p. 1–9, 2009.

[73] R. Hiramoto and H. Higuchi, "Vortex Shedding behind a Nonparallel Pair of Circular Cylinders," *J. Fluids and Structures,* vol. 18, pp. 131-141, 2003.

[74] N. Fiala, I. Jaswal and F. Ames, "Letterbox Trailing Edge Heat Transfer: Effects of Blowing Rate, Reynolds Number, and External Turbulence on Heat Transfer and Film Cooling Effectiveness," *J. Turbomachinery,* vol. 132, no. 1, pp. 011017-1 – 011017-9, 2009.

[75] P. Chakraborty, S. Balachandar and R. J. Adrian, "Kinematics of Local Vortex Identification Criteria," *J. Visualization,* vol. 10, no. 2, p. 137–140, 2007.

[76] Y. You, H. Lüdeke and V. Hannemann, "Detached Eddy Simulation of Base Flows under Subsonic Free Stream Conditions," 2010.

[77] H. K. Versteeg and W. Malalasekera, An Introduction to Computational Fluid Dynamics, Pearson, 2007.

[78] J. Bredberg, S. -H. Peng and L. Davidson, "An Improved k-ω Turbulence Model Applied to Recirculating Flows," *J. Heat and Mass Transfer,* vol. 23, no. 6, p. 731–743, 2002.

[79] Z. Yang and T. H. Shih, "New Time Scale Based k-ε Model for Near Wall Turbulence," *J. AIAA,* vol. 31, no. 7, p. 1191–1993, 1993.

[80] K. Abe, T. Kondoh and Y. Nagano, "A New Turbulence Model for Predicting Fluid Flow and Heat Transfer in Sparating and Reattaching Flows - I. Flow Field Calculation," *J. Heat and Mass Transfer,* vol. 37, no. 1, p. 139–151, 1994.

[81] W. P. Jones and B. E. Launder, "The Prediction of Laminarization with a Two-Equation Model of Turbulence," *J. Heat and Mass Transfer,* vol. 15, no. 2, p. 301–314, 1972.

[82] K. Y. Chien, "Predictions of Channel and Boundary-Layer Flows with a Low-Reynolds-Number Turbulence Model," *J. AIAA,* vol. 20, no. 1, p. 33–38, 1982.

[83] B. E. Launder and B. I. Sharma, "Application of the Energy-Dissipation Model of Turbulence to the Calculation of Flow Near a Spinning Disc," *Letters in Heat and Mass Transfer,* vol. 1, no. 2, p. 131–138, 1974.

[84] C. B. Hwang and C. A. Lin, "Improved Low-Reynolds-Number k-ε Model Based on Direct Numerical Simulation Data," *J. AIAA,* vol. 36, no. 1, p. 38–43, 1998.

[85] M. M. Rahman and T. Siikonen, "Improved Low-Reynolds-Number k-ε Model," *J. AIAA,* vol. 38, p. 1298–1300, 2000.

[86] M. Wolfshtein, "The Velocity and Temperature Distribution in One-dimensional Flow with Turbulence Augmentation and Pressure Gradient," *J. Heat and Mass Transfer,* vol. 12, no. 3, p. 301–318, 1969.

[87] C. G. Speziale, R. Abid and E. C. Anderson, "Critical Evaluation of Two-equation Models for Near-Wall Turbulence," *J. AIAA,* vol. 30, no. 2, p. 324–331, 1992.

[88] P. A. Durbin, "Near-Wall Turbulence Closure Modelling without Damping Functions," *J. Theoretical and Computational Fluid Dynamics,* vol. 3, no. 1, p. 1–13, 1991.

[89] K. Suga, M. Nagaoka, N. Horinouchi, K. Abe and Y. Kondo, "Application of a Three Equation Cubic Eddy Viscosity Model to 3-D Turbulent Flow by the Unstructured Grid Nethod," *In K. Hanjalic, Y.Nagano, and T.Tsuji, editors, 3rd Int. Symp. on Turbulence, Heat and Mass Transfer,,* p. 370–381, 2000.

[90] D. C. Wilcox, "Reassessment of the Scale-Determining Equation for Advanced Turbulence Models," *J. AIAA,* vol. 26, no. 11, p. 1299–1310, 1988.

[91] D. C. Wilcox, "Comparison of Two-equation Turbulence Models for Boundary Layers with Pressure Gadient," *J. AIAA,* vol. 31, no. 8, p. 1414–1421, 1993.

[92] D. C. Wilcox, Turbulence Modelling for CFD, DCW Industries Inc., 2006.

[93] S. -H. Peng, L. Davidson and S. Holmberg, "A Modified Low-Reynolds-Number k-ω Model for Resirculating Flows," *J. Fluids Engineering,* vol. 119, no. 4, p. 867–875, 1997.

[94] F. R. Menter, "Two-Equation Eddy-Viscosity Turbulence Models for Engineering Applications," *J. AIAA,* vol. 32, no. 8, p. 1598–1605, 1994.

[95] FLUENT-ANSYS, "Theory Guide Release 13.0, ANSYS Inc., Chapter 4, Canonsburg, PA.," 2010, p. 61–102.

[96] N. N. Sorensen and J. A. Michesles, "Aerodynamic Prediction for the Unsteady Aerodynamic Experiment Phase-II at the National Renewable Energy Laboratory," in *AIAA Paper No. 2000-0037*, 2000.

[97] M. Breurer, "Large Eddy Simulation of the Subcritical Flow Past a Circular Cylinder: Numerical and Modeling Aspects," *J. Numerical Methods in Fluids,* vol. 28, no. 9, p. 1281–1302, 1998.

[98] K. Watanabe and T. Takahashi, "LES Simulation and Experimental Measurement of Fully Developed Ribbed Channel Flow and Heat Transfer," in *ASME Paper No. GT-2002-30203*, Amsterdam, The Netherland, 2002.

[99] A. Viswanathan and D. K. Tafti, "Large-Eddy Simulation in a Duct with Rounded Skewed Ribs," in *ASME Paper No. GT-2005-68117*, 2005.

[100] E. A. Sewall and D. K. Tafti, "Large Eddy Simulation of the Developing Region of a Stationary Ribbed Internal Turbine Blade Cooling Channel," in *ASME Paper No. GT-2004-53832*, Vienna, Austria, 2004.

[101] E. A. Sewall and D. K. Tafti, "Large Eddy Simulation of the Developing Region of a Rotating Ribbed Internal Turbine Blade Cooling Channel," in *ASME Paper No. GT-2004-53833*, Vienna, Austia, 2004.

[102] E. A. Sewall and D. K. Tafti, "Large Eddy Simulation of Flow and Heat Transfer in the 180° Bend Region of a Stationary Gas Turbine Ribbed Internal Cooling Duct," *J. Turbomachinery,* vol. 128, no. 4, p. 763–771, 2006.

[103] E. A. Sewall and D. K. Tafti, "Large Eddy Simulation of Flow and Heat Transfer in the Developing Flow Region of a Rotating Gas Turbine Blade Internal Cooling Duct with Coriolis Forces and Bouyancy Forces," in *ASME Paper No. GT 2005-68519*, 2005.

[104] S. Abdel-Wahab and D. K. Tafti, "Large Eddy Simulation of Flow and Heat Transfer In a 90° Ribbed Duct with Rotation - Effect of Coriolis and Centrifugal Bouyancy Forces," *J. Turbomachinery,* vol. 126, no. 4, p. 627–636, 2004.

[105] S. Abdel-Wahab and D. K. Tafti, "Large Eddy Simulation of Flow and Heat Transfer in a Staggered 45° Ribbed Duct," in *GT 2004-53800, ASME Turbo Expo*, Vienna, Austria, 2004.

[106] P. R. Spalart, W. H. Jou, M. Strekets and S. R. Allmaras, "Comments on the feasibility of LES for Wings, and on a hybrid RANS/LES approach," in *The 1st AFOSR International Conference on DNS/LES*, Ruston, LA, 1997.

[107] P. R. Spalart, "Strategies for Turbulence Modelling and Simulations," *J. Heat Fluid Flow,* vol. 21, no. 3, p. 252–263, 2000.

[108] P. R. Spalart, S. Deck, M. L. Shur, K. D. Squires, M. K. Strelets and A. Travin, "A New Version of Detached Eddy Simulation, Resistant to Ambiguous Grid Densities," *J. Theoretical and Computational Fluid Dynamics,* vol. 20, no. 3, p. 181–195, 2006.

[109] M. Strelets, "Detached Eddy Simulation of Massively Separated Flows," in *AIAA Paper No. 2001-0879,* 2001.

[110] B. Wang and G. C. Zha, "Detached-Eddy Simulation of Transonic Limit Cycle Oscillations Using High Order Schemes," in *the 47th AIAA*, Orlando, Florida, 2009.

[111] X. Chen, B. Wang and G. C. Zha, "Delayed Detached Eddy Simulation of 3-D Wing Flutter with Fully Coupled Fluid-Structural Interaction," in *the 48th AIAA*, Orlando, Florida, 2010.

[112] A. Tarvin, M. Shur, M. Strelets and P. Spalart, "Detached-Eddy Simulations Past a Circular Cylinder," *J. Flow Turbulence and Combustion,* vol. 63, no. 1-4, p. 293–313, 1999.

[113] R. P. Hansen and J. R. Forsythe, "Large and Detached Eddy Simulation of a Circular Cylinder using Unstructured Grids," in *AIAA Paper No. 2003-0775*, 2003.

[114] C. Xu, L. Chen and X. Lu, "Large-Eddy and Detached-Eddy Simulations of the Separated Flow around a Circular Cylinder," *J. Hydrodynamics, Ser. B,* vol. 19, no. 5, p. 559–563, 2007.

[115] B. Wang and G. -C. Zha, "Detached Eddy Simulation of a Circular Cylinder Using a Low Diffusion E-CUSP and High-order WENO Scheme," in *AIAA Paper No. 2008-3855*, 2008.

[116] K. D. Squires, V. Krishnan and J. R. Forsythe, "Prediction of the Flow over a Circular Cylinder at High Reynolds number using Detached-Eddy Simulation," *J. Wind Engineering and Industrial Aerodynamics,* vol. 96, no. 10-11, p. 1528–1536, 2008.

[117] J. R. Forsythe, K. Hoffman, K. D. Cummings and R. M. Squires, "Detached-eddy Simulation with Compressibilty Corrections Applied to Supersonic Axisymmetric Base Flow," *J. Fluids Engineering,* vol. 124, no. 4, p. 911–923, 2002.

[118] K. D. Squires, "Detached Eddy Simulation: Current status and Perspectives," in *Direct and Large-Eddy Simulation V, ERZCOFTAC Series*, vol. 9, Springer Netherlands, 2004, p. 465–480.

[119] S. Kapadia, S. Roy and K. Wurtlzer, "Detached Eddy Simulation over a Reference Ahmed Car Model," in *AIAA Paper No. 2003-0857*, 2003.

[120] J. R. Forsythe, K. D. Squires, K. E. Wurtzler and P. R. Spalart, "Detached-eddy Simulation of Fighter Aircraft at High Alpha," in *AIAA Paper No. 2002-0591*, 2002.

[121] A. Viswanathan and D. K. Tafti, "Detached-Eddy Simulation of Turbulent Flow and Heat Transfer in Duct," *J. Fluids Engineering,* vol. 127, no. 1, p. 888–896, 2005.

[122] A. Viswanathan and D. K. Tafti, "Detached-Eddy Simulation of Turbulent Flow and Heat Transfer in a Stationary Internal Cooling Duct with Skewed Ribs," in *ASME Paper No. GT-2005-68118*, 2005.

[123] P. R. Spalart, "Young-Person's Guide to Detached-Eddy Simulations Grids," Boeing Commercial Airplane Group, Seattle, WA USA, 2001.

[124] F. R. Menter and M. Kuntz, "Development and Application of a Zonal DES Turbulence Model for CFX-5," ANSYS CFX Validation Report, Vol.CFX-VAL17/0703, 2001.

[125] F. R. Menter, M. Kuntz and R. Langtry, "Ten Years of Industrial Experience with the SST Turbulence Model," *Turbulence, Heat and Mass Transfer 4 , edited by K. Hanjalic, Y. Nagano, and M. Tummers, Begell House, Inc,* p. 625–632, 2003.

[126] T. Nishino, G. T. Roberts and X. Zhang, "Unsteady RANS and Detached-eddy Simulations of Flow around a Circular Cylinder in Ground Effect," *J. Fluids and Structures,* vol. 24, no. 1, p. 18–33, 2008.

[127] F. P. Incropera and D. P. DeWitt, Fundamentals of Heat and Mass Transfer, John Wiley & Sons, 1996.

[128] F. P. Incropera and D. P. DeWitt, Introduction to Heat Transfer, John Wiley & Sons., 2002.

[129] D. E. Metzger, C. S. Fan and S. W. Haley, "Effects of Pin Shape And Array Orientation on Heat Transfer and Pressure Loss in Pin Fin Arrays," *J. Engineering for Gas Turbines and Power,* vol. 106, no. 1, p. 252–257, 1984.

[130] C. H. Sieverding and H. Heinemann, "The Influence of Boundary Layer State on Vortex Shedding from Flat Plates and Turbine Cascades," *J. Turbomachinery,* vol. 112, no. 2, p. 181–187, 1990.

[131] D. R. Boldman, P. F. Brinich and M. E. Goldstein, "Vortex Shedding from a Blunt Trailing Edge with Equal and Unequal External Mean Velocities," *J. Fluid Mechanics,* vol. 75, no. 4, p. 721–735, 1976.

[132] R. J. Goldstein, "Film Cooling," *J. Advance Heat Transfer,* vol. 7, p. 321–379, 1971.

[133] D. E. Metzger, R. A. Berry and J. P. Bronson, "Developing Heat Transfer in Rectangular Ducts with Staggered Arrays of Short Pin Fins," *J. Heat Transfer,* vol. 104, no. 4, p. 700–706, 1982.

[134] S. A. Lawson, K. A. Thrift, A. Thole and A. Kohli, "Heat Transfer from Multiple Row Arrays of Low Aspect Ratio Pin-fins," *J. Heat and Mass Transfer,* vol. 54, no. 17-18, p. 4099–4109, 2011.

[135] M. K. Chyu, Y. C. Hsing, T. I. -P. Shih and V. Natarajan, "Heat Transfer Contributions of Pins and Endwall in Pin-fin Arrays: Effects of Thermal Boundary Condition Modeling," *J. Turbomachinery,* vol. 121, no. 2, p. 257–263, 1999.

[136] J. F. Mitre, L. M. Santana, R. B. Damina, J. Su and P. L. C. Lage, "Numerical Study of Turbulent Heat Transfer iln 3D Pin Fin Channels: Validation of a Quick Procedure to Estimate Mean Values in Quasi-Periodic Flows," *J. Applied Thermal Engineering,* vol. 30, no. 17-18, p. 2796–2803, 2010.

[137] D. A. von Terzi, R. D. Sandberg and H. F. Fasel, "Identification of Large Coherent Structures in Supersonic Axisymmetric Wakes," *J. Computers and Fluids,* vol. 38, no. 8, p. 1638–1650, 2009.

[138] O. Atsushi, "Strouhal Numbers of Rectangular Cylinders," *J. Fluid Mechanics,* vol. 123, p. 379–398, 1982.

[139] O. Uzol and C. Camci, "Elliptical Pin Fins as an Alternative to Circular Pin-fins for Gas Turbine Blade Cooling Applications Part 1: Endwall Heat Transfer and Total Pressure Loss Characteristics," in *ASME Paper No.GT-2001-0180,* New Orleans, LA, USA, 2001.

[140] O. Uzol and C. Camci, "Elliptical Pin Fins as an Alternative to Circular Pin-fins for Gas Turbine Blade Cooling Applications Part 2:Wake Flow Field Measurements and Visualization using Particle Image Velocimetry," in *ASME Paper No. GT-2001-181,* New Orleans, LA, USA, 2001.

[141] Q. Li, Z. Chen, U. Flechter and H. J. Warnecke, "Heat Transfer and Pressure Drop Characteristic in Rectangular Channels with Elllliptic Pin-fins," *J. Heat and Fluid Flow,* vol. 19, no. 3, p. 245–250, 1998.

[142] K. S. Yang, W. H. Chu, I. Y. Chen and C. C. Wang, "A Comparative Study of the Airside Performance of Heat Sinks Having Pin-fin Configurations," *J. Heat and Mass Transfer,* vol. 50, no. 23-24, p. 4661–4667, 2007.

[143] O. Sara, "Performance Analysis of Rectangular Ducts with Staggered Square Pin-fins," *J. Energy Conversion and Management,* vol. 44, no. 11, p. 1787–1803, 2003.

[144] A. K. Saha and S. Acharya, "Parametric Study of Unsteady Flow and Heat Transfer in Pin-fin Heat Transfer," *J. Heat and Mass Transfer,* vol. 46, no. 20, p. 3815–3830, 2003.

[145] G. Tanda, "Heat Transfer and Pressure Drop in a Rectangular Channel with Diamond-shaped Elements," *J. Heat and Mass Transfer,* vol. 44, no. 18, p. 3529–3541, 2001.

[146] T. Jeng, "Thermal Performance of In-line Diamond-Shaped Pin-fins in Rectangular Duct," *J. Heat and Mass Transfer,* vol. 33, no. 9, p. 1139–1146, 2006.

[147] Z. Chen, Q. Li, D. Meier and H. -J. Warnecke, "Convective Heat Transfer and Pressure Loss in Rectangular Ducts with Drop-Shaped Pin-fins," *J. Heat and Mass Transfer,* vol. 33, no. 3, p. 219–224, 1997.

[148] B. Facchini and L. Tarchi, "Investigation of Innovative Trailing Edge Cooling Configurations with Enlarged Pedestals and Square or Semicircular Ribs. Part 1 - Experimental Results," in *ASME Paper No. GT-2008-51047*, 2008.

[149] J. C. Telisinghe, P. T. Ireland, J. T. V, B. D and C. Son, "Comparative Study between a Cut-back and Conventional Trailing-Edge Film Cooling System," in *ASME Paper No. GT-2006-91207*, 2006.

[150] S. C. Lau, J. C. Han and T. Batten, "Heat Transfer, Pressure Drop, Mass Flow Rate in Pin-fin Channels with Long and Short Trailing-edge Ejection Holes," *J. Turbomachinery,* vol. 111, no. 2, p. 116–123, 1989.

[151] S. Y. Won, G. I. Mahmood and P. M. Ligrani, "Spatially-Resolved Heat Transfer and Flow Structure in Rectangular Channel with Pin-fins," *J. Heat and Mass Transfer,* vol. 47, no. 8-9, p. 1731–1743, 2004.

[152] G. Su, H. C. Chen and J. C. Han, "Computation of Flow and Heat Transfer in Rotating Rectangular Channel (AR=4:1) with Pin-fins by a Reynolds Stress Turbulence Model," *J. Heat Transfer,* vol. 129, no. 6, p. 685–696, 2007.

[153] G. Delibra, D. Borello, K. Hanjalic and F. Rispoli, "URANS of Flow and Endwall Heat Transfer in a Pinned Passage Relevant to Gas Turbine Blade Cooling," *J. Heat and Fluid Flow,* vol. 30, no. 3, p. 549–560, 2009.

[154] R. Yu, W. Chaoyi and Z. Shusheng, "Transitional Flow and Heat Transfer Characteristic in a Rectangular Duct with Staggered-array Short Pin-fins," *Chinese J. of Aeronautics,* vol. 22, no. 3, p. 237–242, 2009.

[155] J. -J. Hwang, D. -Y. Lai and Y. -P. Tsia, "Heat Transfer and Pressure Drop in Pin-fin Trapezoidal Ducts," *J. Turbomachinery,* vol. 121, no. 2, p. 264–271, 1999.

[156] J. -J. Hwang and C.-C. Lui, "Detailed Heat Transfer Characteristic Comparison in Straight and 90-deg Turned Trapezoidal Ducts with Pin-fin Arrays," *J. Heat and Mass Transfer,* vol. 42, no. 21, p. 4005–4016, 1999.

[157] J. -J. Hwang and C. -C. Lui, "Measurement of Endwall Heat Transfer and Pressure Drop in Pin-fin Wedge Duct," *J. Heat and Mass Transfer,* vol. 45, no. 4, p. 877–889, 2002.

[158] T. M. Jeng and S. C. Tzeng, "Pressure Drop and Heat Transfer of Square Pin-fin Arrays in In-line and Staggered Arrangements," *J. Heat and Mass Transfer,* vol. 50, no. 11-12, p. 2364–2375, 2007.

[159] G. Barigozzi, A. Armellini, C. Mucignat and L. Casarca, "Experimental Investigation of the Effect of Blowing Conditions and Mach Number on the Unsteady Behaviour of Coolant Ejection through a Trailing Edge Cutback," *J. Heat and Fluid Flow,* vol. 37, p. 37–50, 2012.

[160] M. Effendy and Y. Y. J. Yao, "Effect of Mesh Topologies on Wall Heat Transfer and Pressure Loss Prediction of a Blade Coolant Passage," *J. Applied Mechanics and Materials,* vol. 315, p. 216–220, 2013.

[161] G. J. Van Fossen, "Heat Transfer Coefficients for Staggered Arrays od Short Pin-fins," *J. Engineering Gas Turbines Power,* vol. 104, no. 2, p. 268–274, 1982.

[162] M. K. Chyu, "Heat Transfer and Pressure Drop for Short Pin-fin Arrays with Pin-Endwall Fillet," *J. Heat Transfer,* vol. 112, no. 4, p. 926–932, 1990.

[163] S. S. Papell, "Effect of Gaseous Film Cooling Injection Through Angled Slots and Normal Holes," NASA Report No. TN-D-299, 1960.

[164] S. M. Aminossadati and J. D. Mee, "An Experimental Study on Aerodynamic Performance of Turbine Nozzle Guide Vanes with Trailing-Edge Span-Wise Ejection," *J. Turbomachinery,* vol. 135, no. 3, 2013.

Table A-1: Thermophysical Properties of Air at Atmpospheric Pressure

T (K)	ρ (kg/m^3)	Cp (kJ/kg·K)	μ·10^7 (N·s/m^2)	ν·10^6 (m^2/s)	k·10^3 (W/m·K)	α·10^3 (m^2/s)	Pr
100	3.5562	1.032	71.1	2.00	9.34	2.54	0.786
150	2.3364	1.012	103.4	4.426	13.8	5.84	0.758
200	1.7458	1.007	132.5	7.590	18.1	10.3	0.737
250	1.3947	1.006	159.6	11.44	22.3	15.9	0.720
300	1.1614	1.007	184.6	15.89	26.3	22.5	0.707
350	0.9950	1.009	208.2	20.92	30.0	29.9	0.700
400	0.8711	1.014	230.1	26.41	33.8	38.3	0.690
450	0.7740	1.021	250.7	32.39	37.3	47.2	0.686
500	0.6964	1.030	270.1	38.79	40.7	56.7	0.684
550	0.6329	1.040	288.4	45.57	43.9	66.7	0.683
600	0.5804	1.051	305.8	52.69	46.9	76.9	0.685
650	0.5356	1.063	322.5	60.21	49.7	87.3	0.690
700	0.4975	1.075	338.8	68.10	52.4	98	0.695
750	0.4643	1.087	354.6	76.37	54.9	109	0.702
800	0.4354	1.099	369.8	84.93	57.3	120	0.709
850	0.4097	1.110	384.3	93.80	59.6	131	0.716
900	0.3868	1.121	398.1	102.9	62.0	143	0.720
950	0.3666	1.131	411.3	112.2	64.3	155	0.723
1000	0.3482	1.141	424.4	121.9	66.7	168	0.726
1100	0.3166	1.159	449.0	141.8	71.5	195	0.728
1200	0.2902	1.175	473.0	162.9	76.3	224	0.728
1300	0.2679	1.189	496.0	185.1	82	238	0.719
1400	0.2488	1.207	530.0	213	91	303	0.703
1500	0.2322	1.230	557.0	240	100	350	0.685
1600	0.2177	1.248	584.0	268	106	390	0.688
1700	0.2049	1.267	611	298	113	435	0.685
1800	0.1935	1.286	637	329	120	482	0.683
1900	0.1833	1.307	663	362	128	534	0.677
2000	0.1741	1.337	689	396	137	589	0.672
2100	0.1658	1.372	715	431	147	646	0.667
2200	0.1582	1.417	740	468	160	714	0.655
2300	0.1513	1.478	766	506	175	783	0.657
2400	0.1448	1.558	792	547	196	869	0.630
2500	0.1389	1.665	818	589	222	960	0.613
3000	0.1135	2.726	955	841	486	1570	0.536